Universidade de Aveiro
(2020)

Alena Kuznetsova

Hidróxidos Duplos Lamelares (HDL) como nanoreservatórios versáteis para aplicação em revestimentos multifuncionais

Layered Double Hydroxides (LDH) as versatile nanoreservoirs for application in multi-functional coatings

2020

Universidade de Aveiro
2020

Alena Kuznetsova

Hidróxidos Duplos Lamelares (HDL) como nanoreservatórios versáteis para aplicação em revestimentos multifuncionais

Layered Double Hydroxides (LDH) as versatile nanoreservoirs for application in multi-functional coatings

Tese apresentada à Universidade de Aveiro para cumprimento dos requisitos necessários à obtenção do grau de Doutor em Ciência e Engenharia de Materiais, realizada sob a orientação científica do Doutor João André da Costa Tedim, Professor Auxiliar do Departamento de Engenharia de Materiais e Cerâmica da Universidade de Aveiro e do Professor Doutor Mikhail Larionovich Zheludkevich, Investigador Principal Convidado.

Apoio financeiro do POCTI no âmbito do III Quadro Comunitário de Apoio.

O trabalho da tese foi realizado pelo apoio financeiro da FCT, referência SFRH/BD/89490/2012 e do FSE no âmbito do III Quadro Comunitário de Apoio

Dedico este trabalho à minha família pelo incansável apoio.

o júri

presidente

Doutor Nuno Miguel Gonçalves Borges de Carvalho,
Professor Catedrático, Universidade de Aveiro

Doutor Joaquim Manuel Vieira
Professor Catedrático, Universidade de Aveiro

Doutor Fernando Jorge Mendes Monteiro
Professor Catedrático, Universidade do Porto

Doutora Marta Mohedano Sanchez
Investigadora, Universidade Complutense de Madrid

Doutor Christian Rone Simon
Investigador Coordenador, SINTEF Industry, de Oslo

Doutor João André da Costa Tedim (Orientador)
Professor Auxiliar, Universidade de Aveiro

agradecimentos

Os meus agradecimentos vão para os meus orientadores Prof. Dr. João Tedim e Prof. Dr. Mikhail Zheludkevich, pela orientação e o apoio incondicional, em todos os momentos. Ao Professor Mário G.S. Ferreira, Dr. Tiago L.P. Galvão, Dr. Aleksey Lisenkov, Dr. Maksim Starykevich, Dr. Jorge Carneiro, Eng.º Artur Ricardo Mesquita Sarabando, Eng.ª Célia Cristina Moreira Pereira Miranda, Eng.ª Ana Sofia Marques Ribeiro, Eng.ª Maria Celeste Coimbra de Azevedo, Manon Wilhelm e a todos os meus colegas do grupo de SECOP pela ajuda e a colaboração.

Agradeço ainda à minha Professora da química Tatiana Pavlovna Kutikova e a Professora da biologia Liliya Vyacheslavovna Konovalova na escola (cidade Kurgan, Rússia) e as minhas orientadoras na Universidade Estatal de Kurgan Dr. Lidiya Vitalievna Mostalygina e Elena Yurievna Kolobova pelos conhecimentos, amor, inspiração e as minhas escolhas do caminho científico e do caminho da vida.

Por último agradeço à minha família, ao meu marido e a todos os meus amigos pelo amor, apoio e a inspiração enorme.

Agradeço à FCT pela bolsa de investigação de doutoramento com a referência SFRH/BD/89490/2012. O presente trabalho foi realizado no âmbito do projeto SELMA (ref. P2020-PTDC/QEQ-QFI/4719/2014), e financiado pelo Promover a Produção Científica e Desenvolvimento Tecnológico e a Constituição de Redes Temáticas e fundo FEDER pelo COMPETE 2020, Programa Operacional Competitividade e Internacionalização (POCI). Eu também agradeço o projeto europeu NANOBARRIER No.: 280759, o projeto SMARCOAT-645662-H2020-MSCA-RISE-2014 Ref. Ares(2014)3789766 e o projeto SMARTAQUA (FCT, ref. MARTTERA/0004/2017), Conselho de Investigação da Noruega (RCN-284002), Conselho de Ciência e Tecnologia de Malta (MCST), e co-fundo pelo União Europeu Horizon 2020 de programa de investigação e inovação no âmbito de ERA-NET Cofund MarTERA (Maritime and Marine Technologies for a new Era) pelo suporte financiado.

palavras-chave

Hidróxidos duplos lamelares, síntese, difração de raios-X, libertação de espécias ativas, modelos cinéticos de libertação e adsorção, revestimentos multifuncionais.

resumo

O objetivo do presente trabalho consistiu na síntese e caracterização de nanoreservatórios inorgânicos baseados em hidróxidos duplos lamelares (HDL) com diferentes espécies ativas imobilizadas, nomeadamente inibidores de corrosão e indicadores de pH. Uma das características mais relevantes associada com o HDL é a sua capacidade de permuta aniónica. Apesar dos inúmeros trabalhos que descrevem a utilização do HDL para aplicações em revestimentos protetores contra a corrosão, o estudo relacionado com a imobilização e consequente libertação das espécies aniónicas é algo limitado. Além disso, não existem estudos sistemáticos na literatura que correlacionem a estrutura dos nanocontentores com as propriedades (perfis e condições de libertação controlada) e o efeito correspondente nos revestimentos.

Neste trabalho, várias metodologias foram aplicadas para a preparação dos HDL. A estrutura, morfologia, propriedades coloidais e texturais dos nanocontentores resultantes foram caracterizadas por difração de raios-X (DRX), espectroscopia no infravermelho por transformada de Fourier (FTIR), microscopia eletrónica de varrimento (SEM), dispersão dinâmica de luz (DLS), análise termogravimétrica (TG) e isotérmicas de adsorção - desadsorção de azoto. Atenção especial foi prestada aos estudos de libertação de diferentes espécies ativas imobilizadas em HDL, nomeadamente as condições experimentais que podem levar à libertação das espécies ativas (ex.: pH, presença de sais), estabelecimento de modelos cinéticos e definição de mecanismos de libertação, recorrendo à espetrofotometria de UV-Visível. Além disso, o processo de adsorção de espécies ativas foi investigado para tentar perceber o que ocorre durante a síntese de diferentes composições de HDL bem como avaliar o impacto na aplicação prática de nanoreservatórios em revestimentos multifuncionais.

Os resultados obtidos permitem concluir que, de forma geral, a libertação de espécies ativas é determinada pela difusão, com possibilidade de reação de permuta aniónica, quando espécies aniónicas estão presentes no ambiente. No entanto, os perfis de libertação, extensão da mesma e adsorção de espécies ativas em HDL dependem do método de síntese, bem como da estrutura e propriedades das espécies ativas. Igualmente relevante, é que as diferentes composições de HDL apresentam capacidade de libertar as espécies ativas imobilizadas em resposta à presença de aniões na solução (ex.: cloretos, hidróxidos, carbonatos), mesmo quando não intercaladas nas galerias do HDL, encontrando-se apenas adsorvidas na superfície externa do HDL. Além disso, a tendência dos materiais de HDL à dissolução ou reação sob condições extremas de pH, em combinação com alterações nas propriedades da superfície, tem influência no maior ou menor grau de aglomeração e/ou agregação das partículas, podendo afetar a adsorção e libertação das diferentes espécies.

Atendendo às propriedades dos materiais obtidos, concluiu-se que vários HDL estudados são candidatos promissores para aplicação em revestimentos multifuncionais. Para além disso o presente trabalho pode ser usado como suporte na elaboração e validação de modelos computacionais que visam prever a captação e libertação de espécies ativas do HDL.

keywords

Layered double hydroxides, synthesis, X-ray diffraction, release of active species, kinetic models of release and adsorption, multi-functional coatings.

abstract

The objective of the present work is synthesis and characterization of inorganic nanoreservoirs based on layered double hydroxides (LDH) loaded with active species, namely corrosion inhibitors and pH indicators. The most attractive feature of LDH is the anion-exchange ability. Despite the countless studies that describe the use of LDH for applications in protective coatings for anti-corrosion applications, the study related to immobilization and consequent release of anionic species is somewhat limited. Besides, there is still a lack of systematic studies correlating the structure of nanocontainers with properties (release profiles, triggering conditions) and the corresponding effect in coatings.

In this work, several methodologies were used for preparation of LDH. Structure, morphology, colloidal and textural properties of resulting nanocontainers have been characterized by X-ray diffraction (XRD), Fourier transform infrared spectroscopy (FTIR), scanning electron microscopy (SEM), dynamic light scattering (DLS), thermogravimetric analysis (TG) and nitrogen adsorption-desorption isotherms. Particular attention has been paid to the release studies of active species immobilized in LDH, determination of triggering conditions, establishment of kinetic models and definition of release mechanisms by UV-Visible spectrophotometry. Additionally, the adsorption of active species in LDH was investigated to understand how the active species are immobilized during the synthesis, as well as for evaluation of its impact on the application of nanoreservoirs in multi-functional coatings.

In general, the release of active species is rate-limited by diffusion with possibility of anion-exchange reaction when anionic species are presenting in the environment. However, the release profiles, extent of release and adsorption of active species are strongly dependent on the method of synthesis and on the structure and properties of the active species. In addition, the LDH compositions studied were found to release the active species in response to the presence of anions in solution (e.g. chlorides, hydroxides, carbonates), even when the active species are not intercalated into the LDH galleries, but adsorbed onto the external surface of the particles. Besides, the propensity of LDH to dissolution or reaction under extreme pH conditions, in combination with changes in the surface properties, can play a role in the agglomeration and/or aggregation of the particles, thereby affecting adsorption and release of different species.

Taking into account the properties of the materials obtained, it is possible to conclude that several LDH compositions studied in this work are prospecting additives for application in multi-functional coatings. Moreover, the present work can be used as some sort of library of experimental data to support the building and validation of computational models, to aid on the prediction of the uptake and release of active species from LDH.

Contents

List of Symbols

2-mercaptobenzothiazole (**MBT**)

60 ^{0}C (**HT**)

90 % of sampled particles (**D90**)

anion exchange capacity (**AEC**)

Barrett, Joyner and Halenda (**BJH**) method

Brunauer-Emmett-Teller (**BET**) analysis

charge density (**c.d.**)

correlation coefficient (**CC**)

cross-sectional area (**CSA**)

Derjaguin-Landau-Verwey-Overbeek (**DLVO**) theory

dynamic light scattering (**DLS**)

energy dispersive spectroscopy (**EDS**)

fluorescein (**FSS**)

formula weight (**FW**)

Fourier transform infrared spectroscopy (**FTIR**)

gluconate (**Glu**)

layer-by-layer methodology (**LbL**)

layered double hydroxide(s) (**LDH**)

layered double oxide (**LDO**)

phenolphthalein (**PhPh**)

room temperature (**RT**)

scanning electron microscopy (**SEM**)

sodium dodecyl sulphate (**SDS**)

standard deviation (**S**)

standard error (**s.e.**)

synthetic hydrotalcite (**SH**)

thermal gravimetry (**TG**)

thymol blue (**TB**)

tributyltin (**TBT**)

X-ray diffraction (**XRD**)

List of Figures

List of Tables

1. INTRODUCTION

Chemical research and mountaineering have much in common. If the goal or the summit is to be reached, both initiative and determination, as well as, perseverance are required. But after the hard work it is a great joy to be at the goal or the peak with its splendid panorama.

Wittig, Georg

In Tore Frängsmyr (ed.)

Nobel Lectures

Chemistry 1971–1980

Nobel Lecture of Peter Mitchell

8 December 1978 (p. 368)

Due to ubiquitous application of metals and corresponding alloys in everyday' s life, corrosion and corrosion protection have been crucial topics in materials science and engineering. There are three main arguments of their significance: economics, safety and conservation. In industrially developed countries the cost of corrosion is approximately 3 – 4 % of the Gross National Product (GNP). Moreover, corrosion can be the reason of contamination of products by metal ions, which is extremely dangerous in the case of food transportation in metallic containers, or it may lead to the failure of structures and vehicles causing accidents with unpredictable consequences for human lives (Revie and Uhlig 2008).

The vast majority of objects surrounding us consists of coated materials. Coatings change the surface properties of different substrates (metal, wood, glass and ceramics) and can be classified according to the main function they render: decorative, protective (corrosion-protective) and functional (which add to the system a complementary functionality) (Ghosh 2006). Actually, the application of organic coatings, commonly termed as 'paints', is one of the most common ways of protecting metals and corresponding alloys against unwanted reactions with the environment. For instance, organic coatings are used to provide a dense barrier against 'aggressive' species, isolating the metallic substrate from the environment. However, as a result of exposure during service-life, the coatings tend to lose its barrier effect, with the opening of small pores and cracks due to a paraphernalia of conditions which may occur, separately or in conjunction: degradation by electromagnetic radiation,

large thermal gradients, mechanical defects (e.g. scratches), wet/drying cycles, etc. Thus, the presence of additional 'defence strategies' embedded in the coating is crucial if its protective action is to be extended over time. Traditionally, this was accomplished with the impregnation of anti-corrosion pigments such as $SrCrO_4$, whose main role was to release small species (so-called *corrosion inhibitors*), which acted directly on the exposed metal/solution interface to inhibit corrosion processes. However, with the ban of Cr(VI)-derived species arising from its carcinogenic effects (Wang, et al. 2017), the challenge of obtaining of equally effective protective coatings rapidly spreads throughout coating industry. Similar issues have been found in anti-fouling coatings with the prohibition of tributyltin (TBT), which was a potent but very toxic biocide used formerly in antifouling paints for ship hulls (Antizar-Ladislao 2008).

The development of multi-functional coatings based on nanocontainers with ability to release active species in a controlled manner, is one of the leading strategies to obtain environmentally friendly, yet high-performing coatings. Most of the works available in the literature are focused on the protective effect provided by different coatings modified with nanocontainers for corrosion protection (Khramov, et al. 2005); (Shchukin, et al. 2006); (Calle, et al. 2010). However, there is still a lack of systematic studies correlating the structure of nanocontainers with properties (release profiles, triggering conditions) and the corresponding effects in coatings. Simultaneously, there is an unexplored field for use of the nanocontainers to confer other functionalities such as sensing or biocidal effects.

In the present PhD work, layered double hydroxide (LDH) nanocontainers loaded with different active species (corrosion inhibitors and sensing species/dyes) were synthesized using several methodologies and characterized by different techniques, paying particular attention to the release studies of the active species immobilized in LDH, determination of triggering conditions, establishment of kinetic models and definition of release mechanisms. Also, the detailed evaluation of LDH textural properties (surface area, porosity) and surface charge in different media was investigated as well, to unveil possible effects on the release of active species.

The selection of active species for this work was done with the goal of providing different functionalities to coatings, specifically corrosion protection, sensing and biocidal activity.

The specific objectives associated with the present thesis are:

1) Synthesis of LDH nanoreservoirs by different methodologies and intercalation of different active species. The selection of anionic species was based on the purpose to confer the desired functionality: corrosion protection, biocide, and sensing.

2) Assessment of parameters relevant for coating technology: anion-exchange capacity, particle size distribution, textural properties and colloidal stability in various media.
3) Evaluation of adsorption of active species on LDH after their release.
4) Release studies of the active species in different conditions relevant for the occurrence of substrate/coating degradation.
5) Determination of loading capacity and definition of triggering conditions for the release of species from LDH materials.
6) Establishment of kinetic models for the release of anionic active species from LDH nanoreservoirs.
7) Critical assessment of the experimental findings toward application of LDH materials in multi-functional anticorrosion, antifouling and sensing coatings.

2. STATE OF THE ART

2.1 A short introduction to corrosion

A destructive environmental attack on a metal through chemical or electrochemical reaction is called *corrosion* (Revie and Uhlig 2008).

Corrosion, as an electrochemical process, requires the presence of the following elements: anode, cathode, electrolyte (conductive solution), external circuit between anode and cathode (metal itself or wire between different metals) and species that can be reduced, receiving electrons from the oxidised metal (i.e. H_2O or O_2). All the mentioned elements form a corrosive cell (corrosion battery). Corrosion can happen only if these elements are present (Munger and Vincent 1999).The process of corrosion of metal M in an aqueous solution is shown schematically in **Figure 1.** Cathodic processes include both H_2O and O_2 reduction reactions (Bardal 2004); (Cicek and Al-Numan 2011).

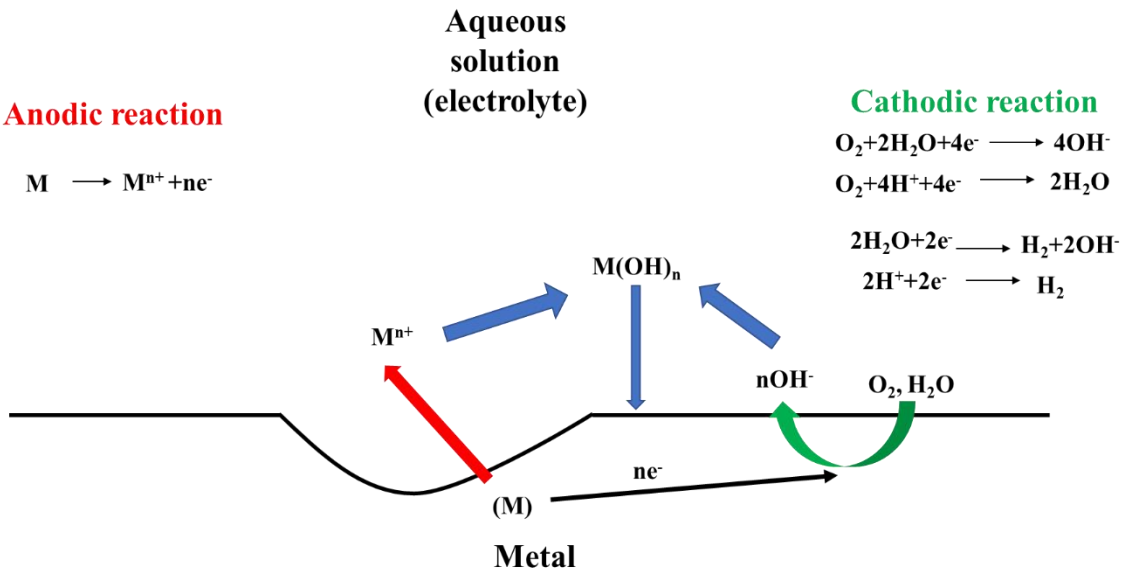

Figure 1. Corrosion of metal M in an aqueous electrolyte

In general, the corrosion of metals under environmental conditions takes place in fresh water, sea water, salt solutions and alkaline or acidic media. In almost all these environments, corrosion occurs significantly in the presence of oxygen, because of its oxidizing nature.

2.2 Corrosion protection via coatings

Coatings have been used for thousands of years, even before consideration of their protective properties, mainly for decorative and identification purposes. Any material, consisting of synthetic resins or inorganic silicate polymers, which after treatment creates a continuous surface resistant coating on the substrate under industrial and marine environment, is known as *protective coating* (Munger and Vincent 1999).

In general, preventive measures which can impede or reduce to some extent corrosion processes include (Munger and Vincent 1999):

- ✓ the selection of a corrosion-resistant material in the actual environment.
- ✓ the addition of anti-corrosion chemicals – inhibitors.
- ✓ the design of a barrier for prevention of water/electrolyte contact with metal surface.
- ✓ the application of cathodic or anodic protection.

Each of these measures is not universal, with its effectiveness depending upon different factors such as the type of metal alloy, environment and targeted application, among others. In addition, they may be applied jointly to achieve a high level of protection at an acceptable cost. One example is the combination of cathodic protection with protective coatings impregnated with corrosion inhibitors (M. Zheludkevich 2009).

The most common and cost-effective way of protecting of metallic substrates against corrosion is by application of organic coatings. The application of coatings is generally known as a *passive* type of *corrosion protection* since the coating works as a physical barrier against the ingress of aggressive species. During service life, most coatings degrade due to weathering conditions, thereby opening pores, cracks, defects, which enable the entrance of electrolyte species and ultimately leads to the onset of corrosion at the metal/coating interface. However, addition of anti-corrosion pigments (low-soluble inorganic salts) and/or corrosion inhibitors (organic molecules) to the coating matrix results in *active corrosion protection*. When the coating fails, they directly react or adsorb on the metallic surface, decreasing the rate of corrosion.

The concept of s*elf-healing coatings* has been central in the development of novel coating technologies in the last 20 years, contributing for the rise of a class of coatings currently termed as *smart coatings* (White, et al. 2001); (Brown, White and Sottos 2005); (Cho, et al. 2006); (Yin, et al. 2007). The classical definition of *self-healing* is the complete recovery of the coating mechanical integrity due to a real healing of the defect. Since in the case of corrosion prevention it is not necessary to recover all the properties of the film as long as the metallic substrate is kept protected, the main aim is to block the corrosion activity in the defect using inhibitors. This healing of defects can be understood as some sort of *functional self-healing* on its own (M. Zheludkevich 2009).

It is worth to note that in situations where degradation of metals by corrosion is a possibility, the recovery of the coating matrix integrity does not preclude the occurrence of corrosion on its own. Indeed, corrosion can occur under undamaged coatings or in the place of healed defects, as a result of electrolyte penetration (M. Zheludkevich 2009). For these applications, a multi-level protection approach based on the combination of triggered release of corrosion inhibitors from the coating layer, for achievement of adequate quantity of inhibitor at the corrosion site with the reconstruction of the protective coating in the defects, has been advocated (Hughes, et al. 2007). Thus, the 'smart' release of corrosion inhibitors and other species such as water displacing agents and polymerizing agents, can afford a long-term protection and block further propagation of corrosion reactions on the metal surface. Among the 'smart' systems under development, one relevant area of active investigations has been based upon the studies of nano- and microcontainers for controlled release of corrosion inhibitors (Khramov, et al. 2005); (Shchukin, et al. 2006); (Calle, et al. 2010). These approaches will be described in detail in the next section.

2.3 Micro- and Nanocontainers for corrosion protection

Self-healing coatings based on active protection have existed for many decades. One the most notable and industrially-relevant example has been based upon organic primers loaded with Cr(VI) pigments such as strontium chromate. The action of this pigment is based upon limited yet sufficient solubility of the pigment with leaching of the corrosion inhibitor to the sites on the metallic surface. However, the high toxicity of Cr(VI)-derived species led to its prohibition in new coating systems, prompting active research in the attempt of looking for effective solutions (Makhlouf 2011).

Various types of corrosion inhibitors have been suggested as environmentally friendly approaches (also known as *'chrome-free' technologies*). Nevertheless, the direct dispersion of 'green' inhibitors in coating matrices can lead to unwanted interactions between inhibitor and coatings. Also, the active protection functionality can be negatively affected by the high solubility of inhibitors, with occurrence of osmotic blistering and spontaneous leaching of inhibitors, that overall jeopardize long-term protection. The minimization of these issues can be achieved by loading of active species in inert hosting structures that are capable to release corrosion inhibitors, only under specific conditions in the surrounding media during initiation of corrosion process, specifically under pH changes and presence of aggressive species like chloride or sulphate anions (Zheludkevich, Salvado and Ferreira 2005). These hosting structures have been designated as micro/nanocontainers or reservoirs.

There are several other examples of containers available in the literature for corrosion inhibitors, including mixed oxide nanoparticles and hollow propylene fibres (Shchukin, et al. 2006). Such oxide

nanoparticles are used for adsorption of corrosion inhibitors on their surface. Additionally, oxide nanoparticles can be applied as reinforcements for the coating matrix and for improvement of barrier properties. Hollow propylene fibres can be also loaded with organic or inorganic corrosion inhibitors (M. Zheludkevich 2009).

Another way of incorporating organic corrosion inhibitors into hybrid coatings is based on physical entrapment of the inhibitor within the coating material at the stage of film formation and cross-linking. Afterwards, the entrapped corrosion inhibitor can diffuse out of the host material in the corrosive electrolyte. A reversible chemical equilibrium of either ion-exchange of the inhibitor with the coating material or through cyclodextrin-assisted molecular encapsulation provides a sustained release of the inhibitor with the aim of continuous delivery of the inhibitor to corrosion sites and continuing corrosion prevention (Khramov, et al. 2005).

An attractive method for the entrapment of corrosion inhibitors between polyelectrolyte multilayers, is based on the *layer-by-layer* (LbL) *methodology* (Shchukin, et al. 2006); (Zheludkevich, Shchukin, et al. 2007); (Ozin, Arsenault and Cademartiri 2008). Due to pH-dependency of polyelectrolytes permeability, these are attractive systems for exploration in the frame of corrosion protection as the cathodic and anodic reaction processes may generate distinct pH conditions and thus trigger the release of inhibitor when it is necessary.

Corrosion indication is certainly a desired functionality to be added to protective coatings, as it allows the early detection of corrosion processes, thereby triggering cost-effective maintenance measures. An interesting approach for indication of corrosion protection is based upon the encapsulation of pH-indicators into inorganic or organic particles which are latter added to protective coatings (Calle, et al. 2010); (Maia, et al. 2014). Thus, the use of various types of sensing species and finding ways of their encapsulation results in the opening of a novel branch of coating research in what corrosion signalling concerns.

Another family of materials studied intensively by different groups as possible nanocontainers for controlled release of species is ion-exchangers. The release from these host structures depends on the presence of ions in the environment. Similar to the relevance of pH for corrosion processes, the presence of aggressive species such as chlorides or formation of metal cations as a result of metal oxidation are among the possible triggers which can be used to release corrosion inhibitors. Among ion-exchangeable materials, different anion- and cation-exchangers have been studied in the context of corrosion, namely layered double hydroxide (LDH) (R. Buchheit, et al. 2003); (McMurray and Williams 2004); (Imanieh and Afshar 2019) and bentonite (Buchheit, Chrisanti and Mahajanam 2004); (Jlassi, et al. 2018), respectively.

LDH is known as environmentally friendly, low-cost material, possessing the ability of intercalation of different anions, inorganic as well as organic ones. Recent studies confirmed successful application of LDH for corrosion protection (Poznyak, et al. 2009); (Tedim, et al. 2010). LDH materials with various corrosion inhibitors like, 2-benzothiazolylthio-succinic acid molybdates, phosphates, 2-mercaptobenzothiazole, gluconate and many others were successfully prepared with evaluation of their efficiency in terms of corrosion protection (Ghotbi, et al. 2009); (Poznyak, et al. 2009); (Tedim, et al. 2010); (Zheludkevich, Poznyak, et al. 2010); (Hang, et al. 2012); (Montemor, et al. 2012); (Zadeh, et al. 2018); (Imanieh and Afshar 2019).

In spite of the massive amount of works reporting LDH structures for corrosion applications, most of them tends to focus on the application and results in terms of corrosion inhibition, while little is mentioned in terms of release profiles, triggering conditions and kinetics of release (Yang, et al. 2007); (Panda, Srivastava and Bahadur 2009); (Hussein, et al. 2010); (Kong, et al. 2010). Therefore, it is key to investigate further the conditions and mechanisms associated with ion-exchange in LDH if a deeper understanding of the release is targeted, which is the main goal of this PhD thesis. Hopefully, it will contribute to increase knowledge on LDH materials, fostering the increase of their efficiency as controlled release systems in the field of coating technology. The next sections include detailed information about structure, preparation, main properties and areas of application of LDH.

2.4 LDH as nanocontainer

As mentioned earlier, LDH is structure which exhibits promising properties in the field of coating technologies. This section is divided into structural features of LDH, methods of preparation and properties.

2.4.1 LDH structure

LDH structure is based on brucite ($Mg(OH)_2$), with small polarizing cations and polarizable anions, where hydroxides surround octahedrally magnesium cations (**Figure 2**). Spatially infinite layers are formed through edge-sharing of octahedral units with the hydroxides located perpendicularly to the plane of layers. The three-dimensional structure corresponds to the stacking of these layers on the top of each other. From close packing point of view, brucite can be described as close-packed panels of hydroxyl anions located in triangular lattice. However, in real structures a distortion from idealized values of local geometry around the metal and close packing of hydroxides is detected. Nevertheless, distortion of brucite layers does not change the hexagonal symmetry, giving the lattice parameters as $a_0=b_0=0.3142$ nm, $c_0=0.4766$ nm, $\gamma=120^0$ and space group $P\bar{3}m1$. a_0 value corresponds to the nearest

neighbour Mg-Mg distance parallel to the plane. The direction of O-H bond is along to three-fold axes towards the vacant tetrahedral site in the neighbour layers (Evans and Slade 2006).

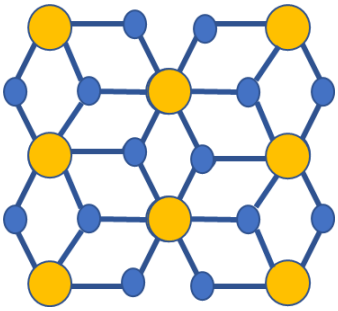

Figure 2. Scheme of brucite structure (*magnesium cations are yellow and hydroxides are blue coloured circles)*

The LDH structure can be obtained through partial substitution of divalent cation of brucite by trivalent cations, giving rise to a positive charge in the layer. For charge neutralization, intercalation of negatively charged anions and water molecules takes place (**Figure 3**). A large range of LDH materials with general formula $[M^{II}_{1-x}M^{III}_{x}(OH)_2]^{x+}[A^{n-}]_{x/n}\cdot yH_2O$ can be prepared, where *x* stands for the ratio of cations $(M^{3+}/(M^{2+}+M^{3+}))$, A^{n-} is an anion with valence n^-, and *y* is amount of water molecules (Newman and Jones 1998); (Evans and Slade 2006).

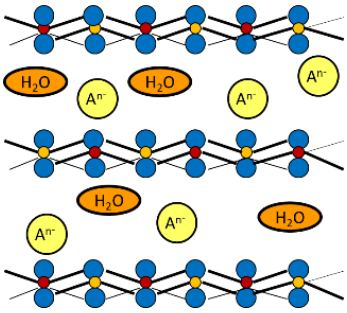

Figure 3. Scheme of LDH structure

Authors suggest that LDH structures with different divalent and trivalent cations are obtained according to the following mechanism: initial formation of amorphous hydroxides, followed by long period of layers ordering, cations substitutions and final attachment of metal hydroxide sheets by interlayer anions. Vucelic and co-workers mentioned the existence of a long-range cation ordering for Li/Al LDH only (Vucelic, Jones and Moggridge 1997). The lack of long-range ordering for other

LDH compositions can be explained by the large difference in size between divalent and trivalent cations. The latter especially concerns to LDH containing Al^{3+}. Local cation ordering demands specific structural conditions. When the ratio M(II)/M(III) is 2, each M(II) cation is surrounded by 3 M(II) and 3 M(III), while M(III) cations are surrounded by 6 M(II). A shift in this ratio also changes the theoretical local order (Forano, et al. 2006). Nevertheless, Vucelic and co-authors also mentioned the presence of anions ordering within the interlayer galleries. The position of anions should be resolved by geometric considerations and hydrogen bonding optimization, instead of maximum coulombic attractions to the positive charged layers (Vucelic, Jones and Moggridge 1997).

The *basal spacing* of LDH is known as the distance from the centre of one layer to the neighbouring one. Due to presence of interlayer anions and molecules of water this parameter is higher for LDH when compared to the brucite structure (c_0= 0.4766 nm). The value of LDH basal spacing depends on the layer's composition, anion size and extent of hydration (Evans and Slade 2006). Thus, the difference in basal spacing can be ascribed to the difference in height of the interlayer galleries (Evans and Slade 2006).

In general, the maximum water content of the interlayers depends on the number of remaining vacancies between hydroxide sheets and anions. For anions like hydroxides, carbonates, nitrates, chlorides and sulphates only trigonal prismatic voids are available, meaning only n vacancies from n OH positions. Moreover, only half of vacancies can be filled by anions or water at the same time due to effective volumes of the void-filling atoms (Hofmeister and Von Platen 1992). In general, all LDH structures can be classified in three groups, depending on swelling and water sorption (Evans and Slade 2006), namely:

- ✓ Type 1 represents significant expandable basal spacing (0.15-0.30 nm).
- ✓ Type 2 shows slightly expandable basal spacing (lower 0.05 nm), but significant interlayer water exchange.
- ✓ Type 3 possesses not expandable basal spacing with small interlayer water exchange.

There is an indication of metal-oxygen octahedra compression along the c axis in LDH exactly as O-M-O bond angles are distorted (7-8^0) from ideal octahedral arrangement in brucite. The value of a_0 (0.3142 nm) parameter of brucite mentioned above is equivalent to the mean distance between adjacent cations centres in the close-packed sheets and its value correlates with average radii of the metal cations in the LDH sheets. According to *Vegard's law* an ideal atomic arrangement of cations is estimated as $a_0 = \sqrt{2d(M-O)}$, where d (M - O) is a metal-oxygen bond length, which is related with ionic radii by the follow equation:

$$d(M-O) = (1-x)r(M^{II}) + xr(M^{III}) \quad (1)$$

The values of a_0 for $Mg_{1-x}Al_x$ LDH (~ 0.302-0.307 nm) is lower compared to the brucite structure due to the Shannon crystal radius of Al^{3+} being smaller than the radius of Mg^{2+} (0.0675 and 0.0860 nm, respectively). For example, Shannon crystal radius of Zn^{2+} is 0.088 nm and a_0 value parameter for ZnAl LDH is in the range of 0.306-0.311 nm, depending on cations ratio M^{2+}/M^{3+}. The lack of correlation between the value of a_0 and the apparent composition of LDH can be an indication of the presence of non-LDH phases (Evans and Slade 2006).

There are different possibilities of stacking of brucite layers that results in appearance of 3 layer - *rhombohedral* (3R) or 2 layer - *hexagonal* (2H) symmetry polytypes (Evans and Slade 2006). For example, $MgAlCO_3$ LDH corresponds to 3R polytype, which is typical for most carbonate containing LDH compositions. This is due to the prismatic structure of hydroxyl groups assisted by hydrogen bonding with the oxygen atoms of the carbonate anion and the interlayer water molecules. However, due to sensitivity of reflections to the interlayer anion, the polytype distinction is a difficult process. In fact, stacking faults and disorders can take place during crystallization process. Besides, anion-exchange reaction results in obtaining of LDH with high degree of order, if incoming anions are carbonate or chlorides and, oppositely, formation of interstratified phase when incoming anion is nitrate. Moreover, it can lead to turbostratic disorder (broadening of *h0l* reflections) when the incoming anion is sulphate (Xu and Xu 2017).

The interlayer galleries of LDH can be described as a complex network of hydrogen bonds between layer hydroxides, intercalated anions and molecules of water. Moreover, the interlayers are strongly disarranged with a continuous flux of hydrogen bonds. There is a combination of electrostatic effects and hydrogen bonding to connect the octahedral layers. In general, hydroxide groups bonded to trivalent cations are strongly polarized and connected with interlayer anions. Besides, every anion should counterbalance excessive positive charges on both sandwiching octahedral layers, which are electrically balanced by two adjacent interlayers. Adjacent with the higher charged cations the hydrogen atoms of hydroxides are delocalized away from the octahedral layers and bounded to the negatively charged anions of the interlayer, meaning the electrostatic bonding between positive octahedral layers and negative interlayers by local hydrogen bonds (Evans and Slade 2006).

The LDH structure can be stabilized through fitting of hydroxide layers with effective volumes of all anions. The latter condition readily works with intercalating anions like hydroxides, carbonates, nitrates or sulphates, because they present an effective surface created by the atoms with volumes

similar to their adjacent host anions of the octahedral layers (hydroxides). Chloride anion has a greater volume due to polarization, leading to increase of interlayer distance. The interlayer spacing of hydrotalcite-like materials is in the range of 0.3-0.4 nm, depending on the volume of intercalating anions. Larger anions can increase the interlayer spacing up to 0.6-0.65 nm (Hofmeister and Von Platen 1992).

In general, there is a strong interaction between oxoanions with hydroxide surface groups, resulting in a dense packing of anions. The latter is a result of symmetry compatibility between oxoanions polyhedra and octahedral layers of LDH. Moreover, hexagonal or rhombohedral LDH stacking forms octahedra, prismatic and tetrahedral interlayer crystallographic sites, that can host monomeric oxoanions. In addition, authors claim that the basal spacing of oxopolyanions can be around 1.4 nm. The intercalation of organic anions into LDH is accompanied by strong hydrogen bonds interaction of their anionic groups as $-COO^-$, $-SO_3^-$, $-PO_3^{2-}$, $-OSO_3^-$, $-OPO_3^{2-}$ with surface hydroxyl groups, whereas hydrophobic hydrocarbon chains are located far away from the hydrophilic sheets surface to guarantee the lowest energy conformation. However, dianionic molecules are able to connect to two neighbouring layers with final basal spacing equal to the length of the hydrocarbon chain. Bilayer or interdigitated geometry can be formed for monovalent long-chain anions, as well. The latter results in basal spacing values greater than 1.5 nm. Thus, relation between the charge and size of organic molecule and equivalent area of the layer influences on the packing type within the interlayer (Evans and Slade 2006); (Forano, et al. 2006).

The structural characterization of LDH can be evaluated through analysis of X-ray diffraction patterns obtained by *X-ray diffraction* (XRD). The reflections of LDH in XRD patterns can be split into three groups (Evans and Slade 2006):

- Strong basal (00*l*) reflections series at low 2 Theta angle is used for direct estimation of basal spacing (c_0), which is normal to (00*l*) plane and is equal to the thickness of brucite layer plus one interlayer. For n-layer polytype the unit cell parameter c is estimated as $c=n\cdot c_0$ and the lowest angle reflection is indexed as (00n), though its spacing always corresponds to c_0. Higher (00*l*) reflections demonstrate spacings equal to $c_0/2$; $c_0/3$, … . In the case of variation in composition and ordering in the interlayers, the mentioned consequence is broken. Moreover, the basal reflection is shifted to slightly lower angles due to the small coherent scattering domains from very thin LDH platelets in the c direction, resulting in apparent spacing, which is greater compared to true value of c_0 calculated from high order basal reflections.
- (110) reflection (occurring around 60^0 for 2 Theta using CuK_α radiation) is applied for determination of a_0 parameter: $a_0=2d(110)$. Thus, a_0 coincides with the distance between

metal cations and this value reflects the cations radii. Commonly, this reflection can be weak and broad, sometimes overlapping with the neighboring (113) reflection, so accurate determination of a_0 parameter can be complicated.

- Positions of (01*l*) and (10*l*) reflections in the intermediate 2 Theta angles is applied for determination of stacking arrangement of the layers. Knowing a_0 and c_0 parameters, the number of layers packed along c-axis can be estimated from calculation of the values d(*hkl*) for each possible value c (c_0, $2c_0$, $3c_0$ and so on) through the following equation:

$$1/d(hkl)^2 = 4(h^2 + hk + k^2)/3a_0^2 + l^2/c^2 \qquad 2$$

The correct c value shows similar calculated and experimental values for positions of (01*l*) and/or (10*l*) reflections within experimental error. Besides, presence or absence of reflections can be an indication of hexagonal or rhombohedral structure. For example, for rhombohedral stacking reflections are systematically absent, except of $-h+k+l$ =3n, where n is integer and *hkl* are Miller indices, while presence of strong reflections with $-h+k+l \neq 3n$ is a sign of hexagonal symmetry. For rhombohedral symmetry with space group $R\bar{3}m$ the basal repeat distance is $c_0 = c/3$. For hexagonal symmetry with space group ($P6_3/mmc$) the basal spacing c_0 is equal to c/2.

Many synthetic LDH materials show an XRD pattern with low intensities of non-basal reflections and only information about basal spacing from (00*l*) reflections can be extracted. The lines can be indexed as a one-layer polytype. However, many similar XRD patterns can be indexed as 3R sequence. Thus, diffraction patterns of prepared LDH compositions can be refined in $R\bar{3}m$ space group and in rhombohedral symmetry (Evans and Slade 2006); (Forano, et al. 2006).

Besides, XRD peaks from LDH can be broaden. Line broadening results from comparatively small domain size, particularly in (00*l*) direction. For example, stacking faults (position of cations in neighbouring layers which are not correlated relatively c-axis) can be a reason of XRD peak broadening. If there is a small number of such stacking faults in $3R_1$ polytype the positions, intensities and widths of (11*l*) reflections do not change. However, the intensity of (10*l*) reflections is decreased, lines are broadened, and reflections are shifted to lower 2 theta angles. If the amount of such faults is excessive, (10*l*) reflections present “shark fin” shape associated with turbostratic structures. Moreover, broadening of (01*l*) and (10*l*) peaks can be attributed to intergrowth of rhombohedral and hexagonal polytypes in synthetic LDH materials. Thus, stacking faults and turbostratic distortions relate to a mismatch in geometry of layers and interlayer anions, preventing ideal packing of the LDH

slabs. Moreover, distribution of electrostatic charges can result in the occurrence of microstrain, rising local distortions within LDH platelets (Evans and Slade 2006).

The gallery height is usually calculated through subtraction of brucite like layer thickness (~0.48 nm) from the basal spacing determined from XRD pattern, namely $d_{basal}= 0.48+l_{anion}$, where l_{anion} is van de Waals radii of external atoms of the anion. Nevertheless, for carboxylate and sulfonates the latter equation is transformed into $d_{basal}=l_{layer}+2l_{O\text{-}H\text{-}O}+l'_{anion}$, l_{layer} is 0.21 nm (interlayer of O…O distance perpendicular to the brucite sheet), $l_{O\text{-}H\text{-}O}$ is 0.27 nm (length of strongly hydrogen bonded O-H-O unit), l'_{anion} – anion length, leading to $d_{basal}= 0.75+ l'_{anion}$ (Evans and Slade 2006).

It is important to note, that intensity of LDH basal reflections are dependent on intercalated anion type. Thus, if intercalated anions do not have atoms with large scattering power, the intensity of basal reflections are influenced by the X-ray intensity of scattered cations in the LDH sheets, resulting in decreasing of intensity with *l* value increase in (00*l*) plane. For example, positions of (006) reflection can be close to (003) peak in presence of impurities such as LDH-Cl/NO_3 or LDH-CO_3 through uptake of atmospheric carbon dioxide. However, anomalous intensities can be detected even for some organic anions. The second (006) reflection can be more intense compared to (003) in the case of a metal complex anion being the intercalated specie, due to increased electron density at the centre of interlayers, where the metal is placed. Inversion of intensities is also observed for polyoxometalate anions, resulting also in presence of additional broad peak between first and second basal reflections, because of partial hydrolysis of polyoxometalates. Broadening of (006) reflection can be ascribed to the formation of polymeric chains and loss of periodicity of (00*l*) planes, as well (Evans and Slade 2006).

Another technique widely used to investigate structure and composition of LDH and other clay-like materials, especially those containing organic anions, is *Fourier-transform infrared spectroscopy* (FTIR). This technique is based on the absorption of IR radiation as a result of vibrations of atoms. The interpretation of FTIR spectra is simplified by the fact that bands that occur can be assigned to particular parts of a molecule, producing group frequencies (Stuart 2004). The most common group frequency is the so-called *mid-IR region* (4000-400 cm^{-1}), which can be divided into the *X-H stretching region* (4000-2500 cm^{-1}), the *triple-bond region* (2500-2000 cm^{-1}), the *double bond region* (2000-1500 cm^{-1}) and the *fingerprint region* (1500-600 cm^{-1}). The band position (wavenumber), the shape and relative intensity are usually analysed qualitatively. Generally, during interpretation of an IR spectrum, the region between 4000 and 1500 cm^{-1} is analysed first to ascribe the measuring compound to a defined class of compounds. Then, the fingerprint region can be analysed for final determination of the compound structure. Moreover, descriptions such as broad, sharp, weak,

medium and strong for peak depth and strength characterization are applied for analysis of IR spectrum (Kenkel 2014).

The normal vibrations that occur in a complex molecule can be divided into *stretching vibrations* (change in the bond lengths) and *bending vibrations* (planar and non-planar), that change the bond angles with constant bond lengths. Further distinctions between vibrations is based on *symmetry grounds* like *symmetric vibrations* (s), which retain of the full molecule symmetry; *antisymmetric vibrations* (as), with distortion of one or more symmetry elements; and *degenerate vibrations* (e). Besides, *localized vibrations*, which in first approximation only affect one bond in the molecule, are the most important for IR spectrum analysis. Thus, localized vibrations are specified on *stretching or bonding vibrations* (υ); *deformation or bending vibrations* (δ); *out of plane deformation vibrations* (γ) and *torsional vibration* with change of torsion angle (τ). For example, CH_2 vibrations can be determined as υ_s (CH_2); υ_{as} (CH_2) or δ_s (CH_2) and δ_{as} (CH_2) **Figure 4** (Hesse, Meier and Zeeh 1997).

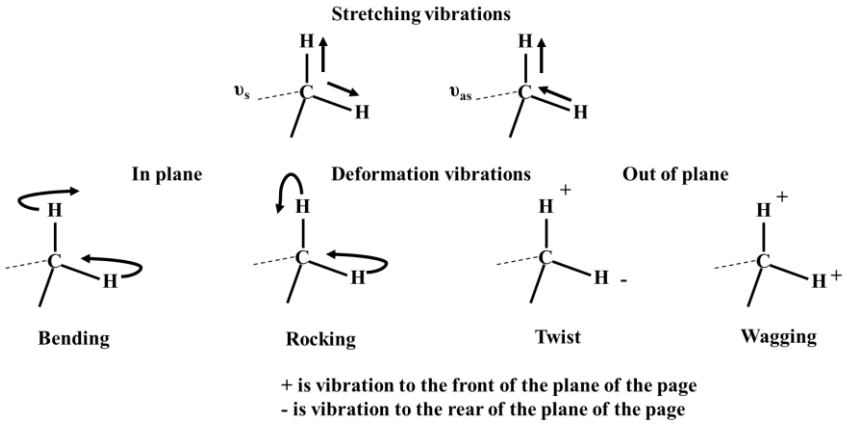

Figure 4. Types of vibrations of a molecule

The most typical IR groups associated with LDH structure give rise to vibrations with bands occurring at 4000-3000 cm^{-1} (O-H stretching mode of layered hydroxides and interlayer water molecules) and at 1650-1620 cm^{-1} (bending mode of water molecules). Bands occurring at wavenumbers lower than 600 cm^{-1} are usually ascribed to Metal-O and Metal-OH modes (Rives and Kannan 2000); (Ghotbi, et al. 2009); (Poznyak, et al. 2009). Vibrations in the range of 1410-1350 cm^{-1} can be attributed to the presence of inorganic anions in the structure, including nitrates or carbonates. If organic molecules are immobilized in LDH, their functional groups can lead to additional vibration modes whose bands may occur down to 1000 cm^{-1} (Hesse, Meier and Zeeh 1997).

Thus, LDH structure is usually studied by combination of XRD and FTIR techniques. The former allows evaluation of synthesis success, determination of unit cell parameters, polytype symmetry and crystallinity. The latter is widely applied for studies of vibration bands after intercalation processes or thermal treatment and estimation of catalytic activity of LDH (Forano, et al. 2006).

2.4.2 Methods for preparation of LDH

There are LDH structures which be found in nature, such as hydrotalcite ($[Mg_6Al_2(OH)_{16}CO_3 \cdot 4H_2O]$) and pyroaurite ($[Mg_2Fe_2(OH)_{16}CO_3 \cdot 4H_2O]$), but the majority of LDH materials used for different applications are synthesized. Reports show that LDH was firstly prepared by Feitknecht in 1942, from a diluted aqueous metal salt solutions under basic conditions (Newman and Jones 1998).

A wide range of divalent and trivalent cations can be used for the preparation of LDH compositions, including Mg^{2+}, Zn^{2+}, Fe^{2+}, Co^{2+}, Cu^{2+}, Ni^{2+}, Cd^{2+}; Al^{3+}, Cr^{3+}, Ga^{3+}, Fe^{3+} (Newman and Jones 1998); (Evans and Slade 2006). Nevertheless, more exotic LDH structures consisting of mixture of divalent and trivalent metals or rare-earth metals can be successfully prepared as well (Porta and Morpurgo 1995); (Chang, et al. 2006). On the other hand, naturally occurring LDH materials generally contain carbonate anions within the interlayer galleries. However, LDH can be prepared with a broad range of possible anions for intercalation: from inorganic anions to metal complexes as hexacyanoferrates II/III, vitamins, large biomolecules and pharmaceuticals (Crespo, et al. 1997); (Newman and Jones 1998); (Khan and O'Hare 2002); (He, et al. 2006).

The synthesis of LDH materials can be performed using the following methods: coprecipitation; ion-exchange; calcination-rehydration; thermal reaction; urea hydrolysis; separate nucleation and aging steps method; coprecipitation reaction in reverse microemulsion method; ‘chimie douce’ method, exfoliation of LDH sheets (Newman and Jones 1998); (Li, et al. 2005); (He, et al. 2006); (Abellán, et al. 2010).

The most widespread method for preparation is *coprecipitation*. It can be readily scaled up and allows synthesis of LDH with both organic and inorganic anions (Newman and Jones 1998); (He, et al. 2006). This route is based on the growth and nucleation of hydroxide layers from an aqueous solution with salts of the corresponding anions to be incorporated into LDH structure. The synthesis may be performed under controlled pH for simultaneous precipitation of cations. To obtain LDH, pH should be identical or higher than the pH at which the most soluble hydroxide is precipitated **Table 1** (He, et al. 2006).

Coprecipitation arises because of the condensation of hexaaquo complexes in solution, which allows the arrangement of uniformly distributed metal cations and solvated interlamellar anions. However,

competing reactions can occur if pH is not carefully controlled, generating undesired phases. The preparation of pure-phase LDH is usually obtained when the ratio of divalent to trivalent metal cations is maintained between 2 and 4. When the ratio is lower than 2, the presence of M^{3+} high density octahedra in the hydroxide layer acts as a nuclei for formation of M^{3+} hydroxide, whereas when the ratio is higher than 4, $M(OH)_2$ can be obtained as unwanted phase (Newman and Jones 1998).

Table 1. pH values of precipitation of some metal hydroxides

Cation	pH at 0.01M	pH at 0.0001M	pH at which hydroxides re-dissolve
Al^{3+}	3.9	8.0	9.0-12.0
Cr^{3+}	5.0	9.5	12.5
Cu^{2+}	5.0	6.5	-
Zn^{2+}	6.5	8.0	14.0
Ni^{2+}	7.0	8.5	-
Fe^{2+}	7.5	9.0	-
Co^{2+}	7.5	9.0	-
Mn^{2+}	8.5	10.0	-

Hydrothermal treatment is a crucial stage after the coprecipitation, for improvement of particles crystallinity, typically under the temperatures ranging 0-100 ^{0}C during several hours up to several days (He, et al. 2006). Instead of hydrothermal treatment, application of microwave radiation has been suggested (Benito, Labajos and Rives 2009).

The *ion-exchange route* can be used to prepare different types of LDH, especially those loaded with organic molecules. This method is applied when the reaction between cations and the guest anion (unwanted reaction) occurs preferentially. The ion-exchange process is based on electrostatic interactions between positively-charged LDH sheets and exchangeable anions and in some extent on changes in the free energy of hydration (He, et al. 2006). Consequently, when the entering anions have a high charge density, the exchange reaction is favoured. The exchange between anions occurs in the following sequence (Forano, et al. 2006):

$$OH^- > F^- > Cl^- > Br^- > NO_3^- > I^- \quad (3)$$

$$CO_3^{2-} > C_{10}H_4N_2O_8S^{2-} > SO_4^{2-} \quad (4)$$

HPO_4^{2-}; $HAsO_4^{2-}$ > CrO_4^{2-} > SO_4^{2-} > MoO_4^{2-} **5**

The most convenient precursors for ion-exchange reactions are LDH structures intercalated with chlorides or nitrates. Due to the high affinity of LDH towards carbonates, the synthesis of LDH should be performed in CO_2 – free environment for intercalation of the desired anions. The most important factors for successful preparation of LDH in this way are stability of anions at the pH of exchange and constant ratio between the cations during reaction for stability of hydroxide layers (He, et al. 2006).

The *rehydration of calcined LDH precursor* results in intercalation of anions, that differ from LDH precursor, especially when the LDH precursor has carbonate anions in the structure (though some of carbonates can still remain in the rehydrated LDH) (Clause, et al. 1991). The incorporation of large guest species like organic chromophores, surfactants, aminoacids and peptides by this methodology is also possible (He, et al. 2006). It is based on the calcination of LDH-precursor in the range of temperatures between 500-800^{0}C, which leads to formation of mixed metal oxides. Then, they rehydrate and reconstruct the LDH framework in the presence of the guest anion and water (Newman and Jones 1998). The rehydration time depends on the calcination temperature and chemical composition of LDH sheets. Moreover, during calcination-rehydration procedure changes of crystal symmetry and sorption capacity of LDH can occur (Stanimirova, et al. 2004).

Although the thermal stability of LDH is function of the chemical composition of the mixed-metal hydroxide sheets as well as the type of intercalating anion (Forano, et al. 2006), the thermal behaviour of LDH as a function of temperature follows a similar trend, regardless of differences in the chemical composition of the hydroxide sheets. Representatively, the thermal analysis of $MgAlCO_3$ LDH, obtained by thermogravimetric analysis, shows the following regions: between 150-250 ^{0}C the weight loss detected is related to the loss of interlayer water; in the interval 250-450^{0}C the weight loss is associated with decomposition of hydroxide layers and carbonates; the formation of magnesium oxide MgO phase formation occurs in the range 400-850 ^{0}C; for temperatures higher than 1000 ^{0}C the formation of pure MgO and $MgAl_2O_4$ occurs (Forano, et al. 2006). The thermal decomposition of $MgAlCO_3$ scheme suggested by Stanimirova and co-authors is presented in **Figure 5** (Stanimirova, et al. 2004).

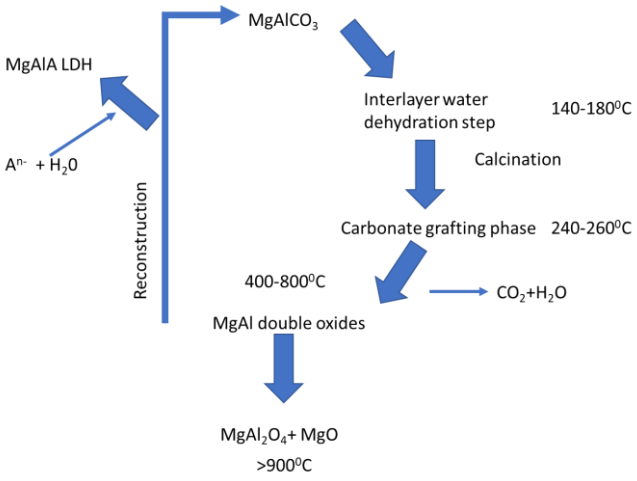

Figure 5. Decomposition and reconstruction of $MgAlCO_3$ LDH

However, steps in the range of temperatures 140-800 ^{0}C (**Figure 5**) are more complex in reality. The decomposition of LDH results in the formation of single-phase rock salt-type solid solution before segregation in divalent cation oxide and spinel phases with further rise in temperature. The obtained mixed oxides maintain some structural homogeneity. Additionally, models of local ordering or local segregation in the calcined materials with formation of *layered double oxide* (LDO) has been suggested. LDO maintains the possibility to obtain LDH via reconstruction with intercalation of guest anions (Hudson, Carlino and Apperley 1995).

The *urea hydrolysis* method is based on the properties of urea. For many decades urea has been applied in gravimetric analysis for precipitation of a few metal cations as hydroxides or as insoluble salts in presence of a suitable anion. Urea is a very weak Brønsted base with pK_b=13.8. It is soluble in water with possibility to control its hydrolysis rate through temperature regulation. Two steps of urea hydrolysis are presented below:

$$CO(NH_2)_2 \rightarrow NH_4CNO \quad (6)$$

$$NH_4CNO + 2H_2O \rightarrow 2NH_4^+ + CO_3^{2-} \quad (7)$$

The second step of hydrolysis (**7**) corresponds to formation of ammonia and carbonate with pH around 9, depending on temperature, which is suitable for precipitation of a broad range of metal hydroxides (He, et al. 2006). Several types of LDH structures have been prepared by this method with variation of temperature, total metal concentration, molar fraction of metals and molar fraction of urea/metals by Costantino and co-authors (Costantino, Marmottini, et al. 1998), (Oh, Hwang and

Choy 2002), (Ogawa and Kaiho 2002), (Adachi-Pagano, Forano and Besse 2003). Nevertheless, LDH synthesized by this route usually contain carbonate anions, which may restrict this method for some applications.

The methodology of *separate nucleation and aging steps* was suggested by Zhao and colleagues (Zhao, et al. 2002). The crucial specificity of this approach is based on fast mixing and nucleation process in a colloid mill with further separate aging. It allows obtaining of LDH with higher crystallinity, smaller crystallites with high aspect ratio, narrower crystallite size distribution compared to LDH particles synthesized by regular coprecipitation. During conventional coprecipitation formation of crystallites is a complex process, including crystal growth, agglomeration, breakage and Ostwald ripening and all mentioned reactions are prolonged in time. Thus, after aging LDH crystallite size distribution is very wide. However, application of the methodology and equipment suggested by Zhao and co-authors allows the completion of growth and nucleation stages in a short period of time and separation of LDH with further aging. Moreover, extreme forces applied during nucleation in a colloidal mill prevent agglomeration of LDH particles and result in uniform, small size nuclei.

More recently, Hu and O'Hare (Hu and O'Hare 2005) suggested the modification of the conventional coprecipitation method, carrying out the *coprecipitation reaction in reverse microemulsion*. This method gives rise to the transformation of platelet-like LDH particles morphology into belt-like and rod-like (**Figure 6)**.

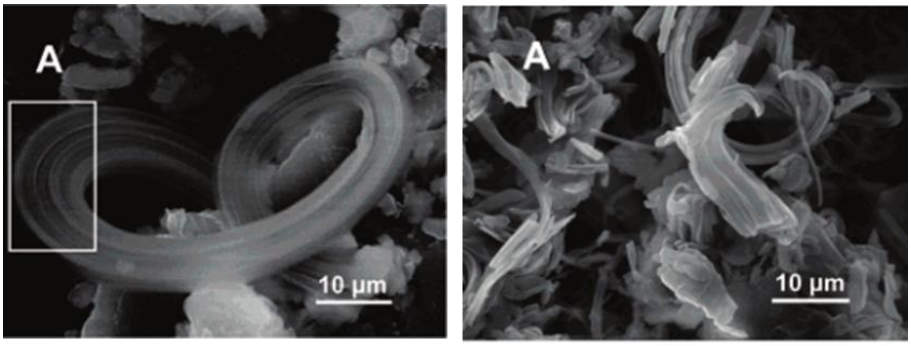

Figure 6. Belt-like (left image) and rod-like (right image) of $MgAlNO_3$ LDH "Reprinted (adapted) with permission from (Hu and O'Hare 2005). Copyright (2020) American Chemical Society"

The *chimie douce* methodology was suggested by Delmas and co-authors (Delmas and Borthomieu 1993); (Han, Guerlou-Demourgues and Delmas 1996) and allows overcoming the difficulties of conventional coprecipitation method like poor crystallinity of the obtained LDH particles and

compositional fluctuations because of pH difference of divalent and trivalent hydroxides, at which their precipitation takes place. It consists of synthesis of high crystalline γ -oxyhydroxide precursor through high temperature oxidizing hydrolysis from initial oxides mixture (for example, $NiO/Co_3O_4/Na_2O$) in presence of sodium hypochlorite and potassium hydroxide, followed by reduction reaction in presence of mixture of hydrogen peroxide and ammonium vanadate with formation of LDH particles. This methodology allows preparation of LDH with inorganic anions like carbonate, sulphate, nitrate, hydroxide and metavanadate.

The *exfoliation of LDH* on positively-charged nanosheets (Li, et al. 2005); (Abellán, et al. 2010) is another attractive path for preparation of materials based on self-assembly and LbL routes. Exfoliated LDH can be prepared by different methods like treatment of LDH materials with alcohol with reflux at 120 ^{0}C, common mixing with formamide, mixing of water and LDH prepared in alcohols, mixing of LDH with acrylate monomers at 70 ^{0}C (Forano, et al. 2006).

2.4.3 Surface properties, morphology and porosity of LDH particles

Particles with dimensions raging between 10 Å and 1μm are usually referred to as *colloids*. Due to the relevance of solid LDH particles in aqueous media in this thesis, this section is directed to the particular cases of colloidal dispersions consisting of solid particles distributed within a liquid (continuous phase).

In general, particles in aqueous medium have an interfacial charge. Any charged surface contains an associated electrostatic potential at the particle surface while the concentration of counter-ions (cations) in the diffuse layer decreases exponentially from the surface into bulk solution (Vincent 2005). The combination of the particle surface charge with oppositely charged ions in the solution is known as the *electrical double layer*. **Figure 7** shows a scheme of *electrical double layer*, where specifically adsorbed ions lose part of their hydration water and are in direct contact with charged surface. On the right side of dotted line, the ions (positive/negative) are diffusely distributed in the solution (Norde 2003).

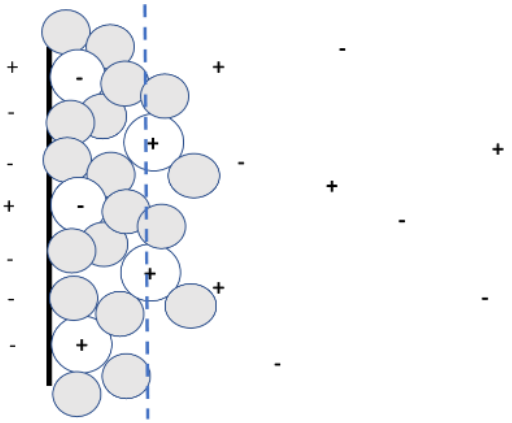

Figure 7. Scheme of electrical double layer

Particles behave individually in dilute dispersions, because they are sufficiently isolated. Several forces act on the particles: *inertial forces* from solvent molecules, rising *Brownian motion*, *external field forces* from the Earth gravitational field (for small particles diffusion is predominating process under sedimentation and opposite for large particles), *electrophoretic motion* in applied electrical field, *shear forces* and *inter-particle forces*.

The following parameters should be controlled in dispersions of particles with double layer interaction for their stabilization: high surface or Stern potential (*zeta potential*); high surface charge; low electrolyte concentration and low valency of counter-ions and co-ions. Zeta potential is an important characteristic of the dispersion. It is calculated from the particle mobility, which can be easily measured by application of Smoluchowski treatment, Hückel equation or Henry's treatment, estimating the particles shape as spherical and electrolyte concentration (Tadros 2011). Zeta potential is an important practical parameter for estimation of colloidal stability and tendency to coagulation (higher value of zeta potential more stable the system). The evaluation of stability and the agglomeration of dispersions follows the Derjaguin-Landau-Verwey-Overbeek (DLVO) principles, which are based on the sum of attractive (van der Waals forces) and repulsive forces between the particles: an increase in zeta potential and thickness of electrical double layer enhances electrostatic repulsive interaction and the dispersion is thus more stable. However, for non-spherical particles, zeta potential is only a sign of external charge and the description of electrokinetic properties should be done by presenting the value of electrophoretic mobility instead.

LDH structures are known as clay-like materials (Forano, et al. 2006). The main structural concepts related to clay materials are presented in **Figure 8**. An assembly (stack) of layers is called a *particle* and an assembly of particles is named *aggregate*. Interlayer, interparticle and interaggregate pores

are all present in clay materials. The arrangement of particles can result in various morphologies such as plates, tubules, laths and fibres (Bergaya and Lagaly 2006).

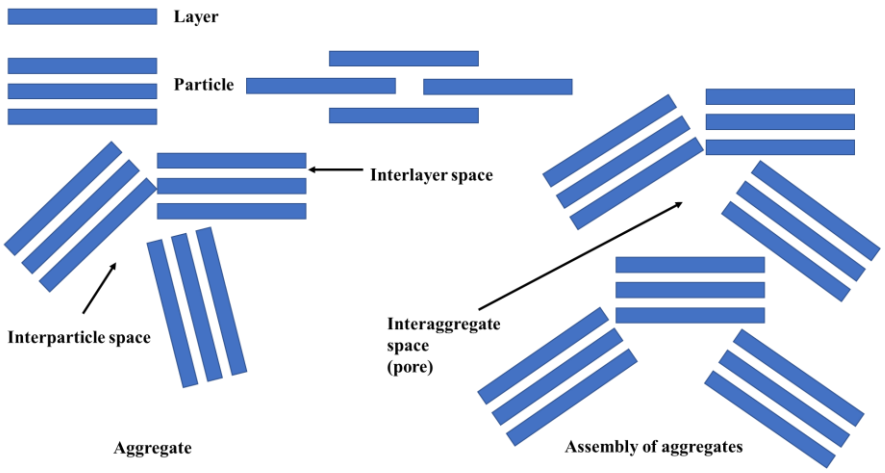

Figure 8. Structural concepts of clay materials

The aggregation of clays can be described by two main mechanisms: *card-house* (edge-face contacts) and *band-type* (face-face contacts). Card-house mechanism is observed for clays with positively charged edges in slightly alkaline medium above the critical salt concentration (Lagaly 2006). Dried LDH aggregates tend to show the card-house structure (**Figure 9)**. Such stone-like aggregates cannot be easily re-dispersed in water or undergo anion-exchange reactions when compared to LDH materials that have never been dried. Moreover, this structure results in formation of *interparticle porosity*, which is common for all clay materials (Gursky, et al. 2006).

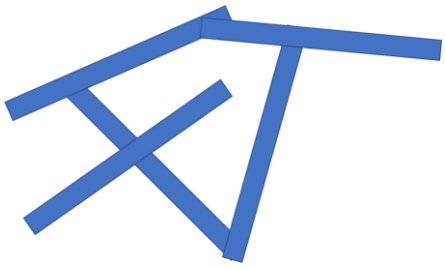

Figure 9. Scheme of the house-of-cards structure of LDH particles

The shape of LDH particles is influenced by the chemical composition as well as by the synthesis method (Forano, et al. 2006). Standard coprecipitation method, where growth and nucleation of

particles occur simultaneously, results in crystalline plate like particles with hexagonal shape and wide range of particle sizes. The coprecipitation method with long time aging is favourable for obtaining LDH structures with sand-rose morphology, whilst coprecipitation at variable pH leads to formation of mesoporous fine-grained LDH particles with rough-surfaces and relatively high surface area. Coprecipitation at constant pH results in the preparation of large, regular hexagonal-shaped particles with a narrow mesoporous size distribution.

The urea hydrolysis method is effective for particle size control during hydrothermal treatment or homogeneous precipitation. However, the size of obtained particles is larger compared to LDH materials synthesized by other routes. LDH structures with rod-like and belt-like morphologies can be obtained by coprecipitation reaction in reverse microemulsion, as suggested by Hu and O'Hare (Hu and O'Hare 2005).

As highlighted above, the surface area of colloidal particles is an important parameter to understand how particles interact with the surrounding media and play an important role in processes such as adsorption/desorption of chemical species. The *specific surface area* of LDH can be estimated as presented in equation **8** (Forano, et al. 2006):

$$S = a^2\sqrt{3}\,10^{-18}N/M \qquad \mathbf{8}$$

N- Avogadro's number ($6.022\cdot10^{23}$)

a – cell parameter (nm)

M – molecular weight of the unit formula (FW)

The formula weight can be calculated using equation **9:**

$$FW = (M_{MII} + 46) + x(M_{MIII} + M_x - M_{MII}) \qquad \mathbf{9}$$

FW- formula weight

M_x – molar mass of anion

The ideal composition of LDH can be presented as $M^{II}_{1-x}M^{III}_{x}(OH)_2X\cdot0.66\ H_2O$, where x =0.2 for (4:1 cations ratio); 0.25 (3:1) and 0.33 (2:1). FW corresponds to full occupancy (2/3) of interlayer crystallographic sites by water molecules ($0.66H_2O$/metal). Additionally, it is possible to calculate

LDH *charge density* (c.d.) -equation **10**, free cross sectional area (nm^2/charge) -equation **11,** and LDH *anion exchange capacity* (AEC) (cmol/kg) -equation **12**.

$$c.d. = \left(a^2\sqrt{3}/2x\right)^{-1} \quad \textbf{10}$$

$$S_{free\ cross\ sectional\ area} = \frac{1}{c.d.} \quad \textbf{11}$$

$$AEC = \frac{x \cdot 10^5}{FW} \quad \textbf{12}$$

The charge density values for LDH materials are in the range of 2.5-4.0 charge/nm^2 and free cross-sectional area (CSA) 0.25-0.40 nm^2/charge. The usual values of AEC for LDH structures are 200-400 cmol/kg (meq/100g) (Forano, et al. 2006). The specific surface area estimated using equation **8** can give values like 800-1300 m^2/g. However, experimentally obtained data are much smaller due to internal surfaces of LDH are not being accessible to adsorptive gases such as N_2 (Forano, et al. 2006) and as a result values of specific surface area reported for LDH are smaller than 100 m^2/g (Hussein, et al. 2012); (Kuhl, et al. 2012). Nitrogen adsorption-desorption isotherms of LDH typically contain narrow hysteresis, showing, that LDH particles are mesoporous without microporosity (Leroux and Besse 2001); (Forano, et al. 2006).

2.5 Incorporation of active species into LDH for application in functional coatings

Taking into account the range of mixed-metal hydroxides that can be prepared, as well as the inorganic and organic anions that can be incorporated into LDH, it is no surprise that LDH materials have been applied in different fields including catalysis, electrochemistry, biology and corrosion.

Various types of LDH structures composed of zinc, magnesium, nickel and aluminium cations and carbonate have been used as supports for Ziegler catalysts in the polymerization of olefins. Besides, application of LDH materials intercalated with polyoxometalates for selective adsorption and oxidation catalysis can be found in the literature (Newman and Jones 1998). Also, there is a possibility of preparation of thin-film electrodes based on CoAl and MgAl LDH structures and modification of glassy carbon electrode with LDH for investigation of bisphenol A oxidation (Wang, et al. 2008); (Yin, et al. 2010). The LDH materials have been used in the field of medicine and biology as well, as antacids and stabilizers. Reports detailing the loading of various biologically-relevant species, namely vitamins, drugs, aminoacids, peptides and genes within LDH are available in literature (Kwak, et al. 2002); (del Hoyo 2007); (Shafiei, et al. 2008).

Several studies have confirmed the possibility of using of LDH materials as host structures for corrosion inhibitors (Buchheit, et al. 2003); (Poznyak, et al. 2009); (Tedim, et al. 2010). In particular, ZnAl- and MgAl LDH nanocontainers intercalated with divanadates were studied for replacement of carcinogenic chromates in primers used in the aeronautical industry. These systems exhibited promising results for corrosion protection of aluminium alloy 2024 (Zheludkevich, Poznyak, et al. 2010). Other works revealed the successful intercalation of different biocides like sodium paeonolsilate, cinnamate and anionic surfactants into LDH, which can be important for preparation of antifouling coatings (Badawi, et al. 2010); (Wang and Zhang 2015); (Sun, et al. 2016). Besides, LDH structures loaded with different organic dyes and pH indicators have been prepared (Forano, et al. 2006), which raises the possibility of preparing sensors for humidity and pH based on these materials.

From the amount of work available in the literature, it is clear that the incorporation of chemical species in the form of anions/molecules into the LDH structure brings additional benefits to the properties of organic coatings, when compared to the free form of the active species: (i) LDH can release the active molecules in response to specific triggers (e.g. chlorides), (ii) they impart additional thermal and chemical stability to the active organic species and (iii) the easiness and cost-effectiveness of preparation, size, morphology and mechanical robustness as compared to other hosting structures such as polymeric capsules, which makes LDH a reliable nanocontainer to introduce functionalities such as active corrosion protection and detection, and biocidal action into protective coatings (Tedim, et al. 2010); (Maia, Tedim, et al. 2014); (Cruz, et al. 2018). Below, the species used as guest anions/molecules in LDH structures in the present work are described in more detail.

Gluconate (Glu) is a salt of *D*-gluconic acid (**Figure 10**), widely applied in pharmaceutical, food, detergent, textile, leather, photographic and concrete industries (Liu, et al. 2003). Moreover, the last explorations of Hakeem and colleagues showed successful application of calcium gluconate for corrosion protection of aluminium (Hakeem, Rajendran and Pascal Regis 2014).

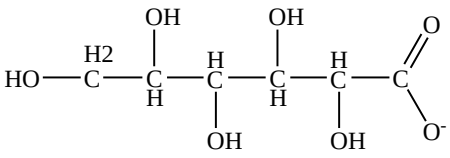

Figure 10. Structure of D-gluconate

2-mercaptobenzothiazole (MBT) is a heterocyclic thioamide, which belongs to a group of molecules containing nitrogen and sulphur as electron donor atoms in the structure (**Figure 11**). It forms complexes with different metal ions and has been widely investigated due to its ability to form hydrophobic complexes with many metals and, thus, its use as a corrosion inhibitor and chelant for metal ions has been proposed (Poznyak, et al. 2009). Additionally, MBT can be used in the manufacture of tyres, rubber shoes and other rubber articles. It is also applied as a preservative and biocide (Kuznetsova, et al. 2017) and is commonly employed as a copper corrosion inhibitor in recirculating water systems (Rai, et al. 2006); (Feng and Chen 2007).

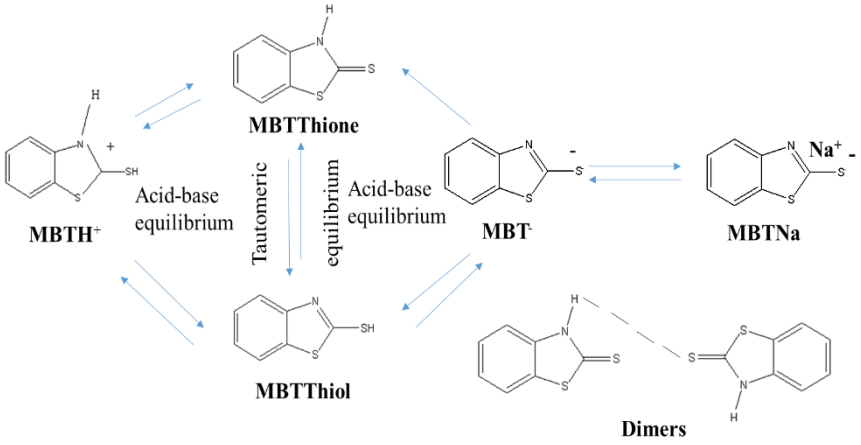

Figure 11. MBT tautomeric and equilibrium forms presenting in solution

With the goal of possible preparation of coatings with corrosion detection functionalities, different pH indicators were chosen for intercalation into the LDH structures, namely fluorescein, phenolphthalein and thymol blue. These compounds can be used to detect occurrence of corrosion processes, as evidenced in the works available in the literature (Galvão, et al. 2018); (Sousa, Quevedo, et al. 2020).

Fluorescein (FSS) is used as an extrinsic fluorescence probe in bioscience. It demonstrates high extinction coefficient, large fluorescent quantum yield and well-studied conjugation chemistry to various biomolecules. FSS is pH sensitive and susceptible to photobleaching (Wang, et al. 2001). Besides, Büchler and co-authors showed possibility of FSS application as indicator of localized corrosion on aluminium alloys (Büchler, Watari and Smyrl 2000). The structure of FSS in solution is pH-dependent and can be distinguished in univalent cation (pH<1), neutral lactonoid (pH=3), univalent anion (pH=5-6) and bivalent anion (pH>8) **Figure 12** (Chen, Nakamura and Tamura 1979).

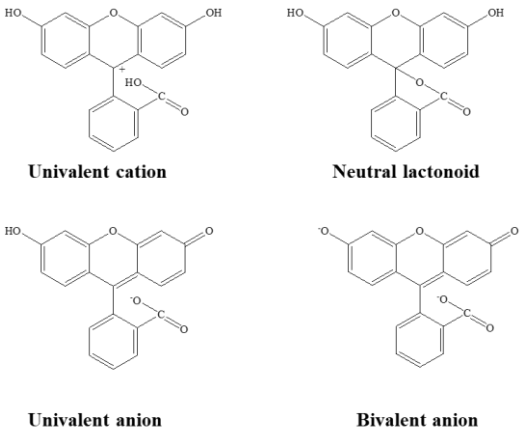

Figure 12. FSS forms in solution

Phenolphthalein (PhPh) is a well-known acid-base indicator. Proton dissociation results in indicator colour change. Colourless lactone form (H_2PhPh) is the predominating specie at pH lower than 8. In the pH range between 8 and 10 dissociation of both phenolic protons takes place with formation of PhPh dianion form ($PhPh^{2-}$). Red-pink colour quinonoid form of PhPh ($PhPh^{2-}$/Q) is formed at pH higher than 10. Further pH increase results in formation of colourless carbinol ($PhPh(OH)^{3-}$). PhPh can exist in benzenoid (B) or quinonoid (Q) forms, depending on the pH value (**Figure 13**) (Kunimoto, et al. 2001). Besides, PhPh can be applied as indicator of corrosion initiation on aluminium and magnesium alloys (Maia, et al. 2014); (Galvão, et al. 2018).

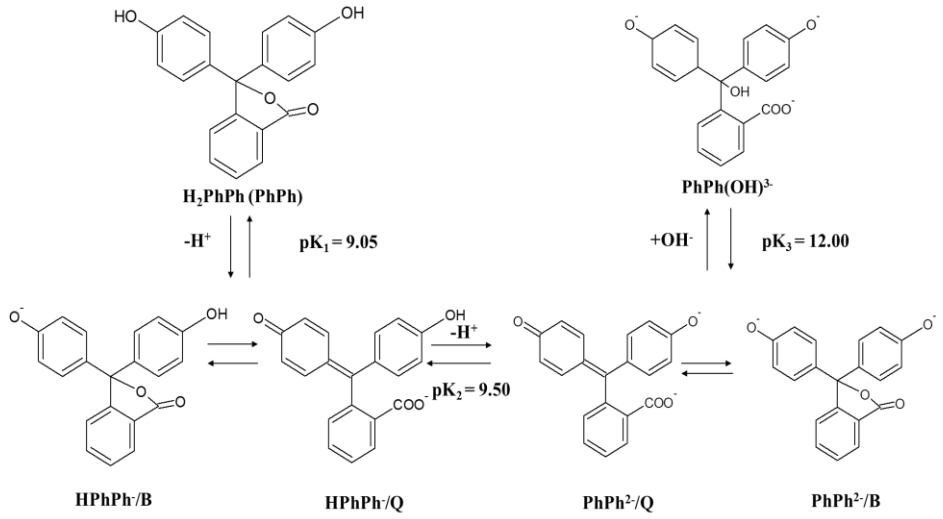

Figure 13. Proton dissociation equilibria of PhPh

Thymol Blue (TB) is a pH indicator dye from the family of the sulphonephtalein, that is broadly applied in the end-point volumetric determinations, in particular in the quantitative determination of proteins (γ- globulin, bovine serum albumin), in proton exchange in organic reactions, for production of the biosensors, for determination of active substances in pharmaceutical preparations, in development of culture media for microorganisms like Escherichia Coli (Zaggout, et al. 2006); (Balderas-Hernández, et al. 2007), and as carbon dioxide sensor (Nakamura and Amao 2003); (Puligundla, Jung and Ko 2012). TB molecule contains three points with pH dependent protonation, as shown in **Figure 14**.

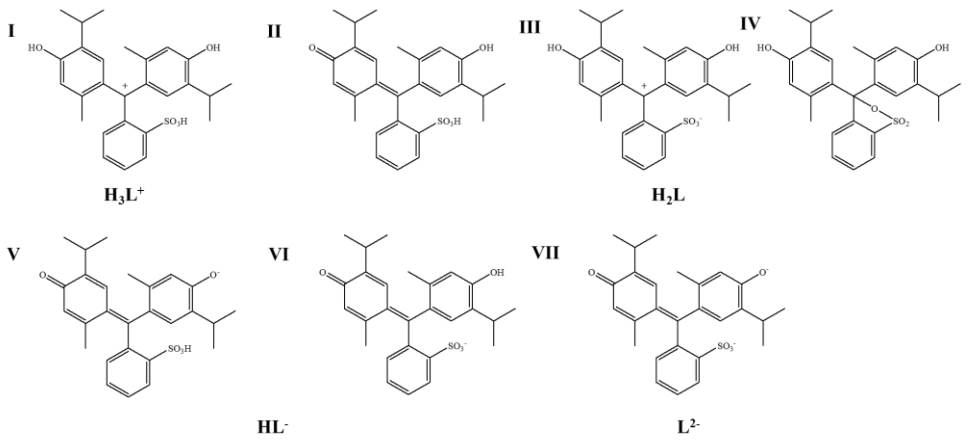

Figure 14. Tautomeric structures for various protonation states of TB, where L is non-protonated structure

2.6 Thermodynamic and kinetic considerations on uptake and release of species from LDH

LDH have been reported as materials with ability to release in a controlled way intercalated species. This controlled release has been associated with an ion-exchange reaction between anions intercalated with anions available in solution (Yang, et al. 2007); (Panda, Srivastava and Bahadur 2009); (Hussein, et al. 2010); (Kong, et al. 2010). In order to go deeper into the understanding of this process, it is necessary to consider both thermodynamic and kinetic aspects associated with adsorption of species from solution in LDH, as well as the kinetic insights associated with the ion-exchange reaction itself. Later in the results section, it will become apparent the need to investigate how species not intercalated but present in LDH interact with its surface (physisorption vs. chemisorption), as well as the need to investigate the kinetics associated with the ion-exchange reaction (in cases where intercalation of guesting anions was successful).

2.6.1 Adsorption isotherms

The attachment of molecules or other chemical species at the surface can be achieved in two ways:

- ✓ Physisorption
- ✓ Chemisorption

Physisorption is based on van der Waals interaction between adsorbate and substrate. The energy released when a molecule is physisorbed is of the same order of magnitude as the enthalpy of condensation (the values are in the range of −20 $kJmol^{-1}$). The enthalpy of physisorption can be measured, from one side, by monitoring of the rise in temperature of a sample of known heat capacity or by observation of the temperature dependence of the parameters, that occur in the adsorption isotherm (Atkins and de Paula 2010). As a rule, physisorption is a reversible process, that happens at temperature lower or close to the critical temperature of adsorbed substance (Dabrowski 2001).

Chemisorption is based on the formation of chemical bonds (usually covalent ones) between adsorbate and substrate with the tendency of maximization of coordination number with substrate. The enthalpy of chemisorption is much more negative than for physisorption, and typical values are in the region of −200 $kJmol^{-1}$. The distance between the surface and the closest adsorbate atom is also typically shorter for chemisorption than for physisorption (Atkins and de Paula 2010). Furthermore, chemisorption occurs only as monolayer, contrary to physisorption (Adamson 1990). Moreover, there is substantial change in the electron density of both the adsorbate and the substrate, that corresponds to the chemical bond formation for chemisorption reaction (Davis and Dykstra 2012).

In most cases physisorption and chemisorption can be distinguished by the rates with which these processes occur. For instance, achievement of equilibrium in physisorption is normally fast and the process is readily reversible. On the other hand, chemisorption may not happen at an appreciable rate at low temperatures due to the presence of an activation energy barrier. The rate of chemisorption reaction speedily grows with rise in temperature. Besides, in chemisorption the bonding may be so strong that the original species may not be recovered (Davis and Dykstra 2012).

The rate of adsorption is proportional to the amount of surface positions available to adsorb onto. These surface positions are called *sites of adsorption*. The extent of adsorption can be calculated by the ratio of number of occupied adsorption sites to the number of available adsorption sites (*fractional coverage*) (Atkins and de Paula 2010); (Ball 2015). The fractional coverage of the surface depends on the pressure of the overlying gas. For gas-solid adsorption the variation of coverage (θ) with pressure at chosen constant temperature is known as *adsorption isotherm*. Besides, for liquid–solid adsorption systems, the adsorption isotherm is an important model for description of adsorption

behaviour. At equilibrium, a saturation point is reached, meaning that no further adsorption can occur. The adsorption isotherm in this case shows the relationship between the mass of adsorbate adsorbed per unit mass of adsorbent and the liquid-phase equilibrium concentration of adsorbate (Atkins and de Paula 2010). Thus, the adsorption isotherm can be seen as the relationship between the concentration of a solute on the surface of an adsorbent to the concentration of the solute in the contact liquid at a constant temperature (Selim 2015).

Table 2 lists adsorption isotherms models considered in this work. q_e corresponds to the amount of adsorbate adsorbed at equilibrium and can be calculated from the experimental data using equation **13** (X. Chen 2015).

$$q_e = \frac{(C_o - C_e) \cdot V}{m} \qquad \textbf{13}$$

C_0 - initial adsorbate concentration (mgL^{-1})

C_e – equilibrium adsorbate concentration (mgL^{-1})

q_e – the amount of adsorbate adsorbed at equilibrium (mgg^{-1})

V-volume of adsorbate solution (L)

m - mass of adsorbent (g)

Table 2. Adsorption isotherm models

Model	Equation	Model's description
Langmuir isotherm	$q_e = \frac{q_m \cdot K_L \cdot C_e}{1 + K_L \cdot C_e}$ q_e - amount of adsorbate adsorbed at equilibrium (mgg^{-1}) q_m - maximum monolayer adsorption capacity of the adsorbent (mgg^{-1}) C_e - equilibrium concentration of adsorbate (mgL^{-1}) K_L - Langmuir adsorption constant related to the free energy adsorption (Lmg^{-1})	The adsorbed layer is one molecule thick (monolayer adsorption). Adsorption occurs at specific homogeneous sites within the adsorbent. After occupation of a site by a molecule, no further adsorption can take place at that site. Adsorption energy is constant and does not depend on the degree of occupation of adsorbent's active sites. The strength of the intermolecular attractive forces falls off fast with distance. The adsorbent has a finite capacity for the adsorbate (at equilibrium, a saturation point is reached where no further adsorption can occur). All sites are identical and energetically equivalent. The adsorbent is structurally homogeneous (Gimbert, et al. 2008). The essential feature of the Langmuir isotherm can be expressed by means of R_L, a dimensionless constant referred to a separation factor. Its value is used for description of adsorption process (Hall, et al. 1966); (Mahmoud, Salleh and Karim 2012): Unfavourable (R_L >1); Linear (R_L =1); Favourable (0< R_L <1); Irreversible (R_L = 0).

Table 2. Adsorption isotherm models (cont.)

Model	Equation	Model's description
Langmuir isotherm (cont.)	Linear forms of equation (Gimbert, et al. 2008): $$\frac{C_e}{q_e} = \frac{1}{q_m \cdot K_L} + \frac{1}{q_m} \cdot C_e$$ $$\frac{1}{q_e} = \frac{1}{q_m} + \frac{1}{q_m \cdot K_L \cdot C_e}$$ $$q_e = q_m - \frac{q_e}{K_L \cdot C_e}$$ $$\frac{q_e}{C_e} = K_L \cdot q_m - q_e \cdot K_L$$ $$\frac{1}{C_e} = \frac{K_L \cdot q_m}{q_e} - K_L$$ Equilibrium parameter: $$R_L = \frac{1}{1 + K_L \cdot C_0}$$ C_0-the highest initial adsorbate concentration (mgL^{-1})	
Freundlich isotherm	$$q_e = K_F \cdot C_e^a$$ $$a = \frac{1}{n}$$ $$n > 1$$ K_F - adsorption capacity parameter ($(mgg^{-1})(Lmg^{-1})^{-1/n}$) n- adsorption intensity parameter a=1/n - characteristic of strength of adsorption q_e – equilibrium solid state concentration (mgg^{-1}) C_e – equilibrium liquid state concentration (mgL^{-1}) The linear form (Voudrias, Fytianos and Bozani 2002) (Tosun 2012): $$lnq_e = lnK_F + \frac{1}{n} \cdot lnC_e$$	Empirical equation for adsorption on heterogeneous surfaces. The model describes the non-ideal, reversible and multilayer adsorption, based on the energetic surface heteroigenity (X. Chen 2015). If n = 1 then the partition between the two phases are independent of the concentration. If value of 1/n is lower than 1, it indicates a *normal adsorption*. If 1/n is higher than 1, it shows *cooperative adsorption* (Mohan and Karthikeyan 1997).
Dubinin-Radushkevich isotherm	$$q_e = q_m \cdot \exp(-K_{DR} \cdot \varepsilon^2)$$ $$\varepsilon = R \cdot T \cdot \ln(1 + \frac{1}{C_e})$$ q_m – constant, adsorption capacity (mgg^{-1}) K_{DR} – constant related to the mean free energy of adsorption (mol^2J^{-2}) R – the universal gas constant 8.314 ($Jmol^{-1}\ K^{-1}$) T- absolute temperature (K) The linear form (X. Chen 2015): $$lnq_e = lnq_m - K_{DR} \cdot \varepsilon^2$$	Adsorption process occurs by a *pore filling mechanism*. Adsorption at both homogeneous and heterogeneous surfaces with Gaussian energy distribution (Dabrowski 2001); (X. Chen 2015).

Table 2. Adsorption isotherm models (cont.)

Model	Equation	Model's description
Temkin isotherm	$q_e = \frac{R \cdot T}{b} \cdot \ln (A_T \cdot C_e)$ $q_e = \frac{R \cdot T}{b} \cdot lnA_T + \frac{R \cdot T}{b} \cdot lnC_e$ A_T – Temkin isotherm equilibrium binding constant (Lmg^{-1}) b – Temkin isotherm constant ($Jmol^{-1}K^{-1}$) R -universal gas constant (8.314 $Jmol^{-1}K^{-1}$) T- absolute temperature (K) (Temkin and Pyzhev 1940)	The model assumes adsorbent–adsorbate interactions. In the intermediate range of concentrations, the model estimates that heat of adsorption (function of temperature) of all molecules in the layer decreases linearly rather than logarithmically with coverage (Temkin and Pyzhev 1940).
Flory-Huggins isotherm	$\frac{\theta}{C_0} = K_{FH} \cdot (1-\theta)^{n_{FH}}$ $\theta = 1 - \frac{C_e}{C_0}$ K_{FH}- Flory-Huggins isotherm equilibrium constant (Lmg^{-1}) n_{FH} - Flory-Huggins isotherm exponent (number of solute molecules on the adsorbent surface) θ – degree of surface coverage C_e – equilibrium liquid state concentration (mgL^{-1}) C_0 – initial concentration of a solute (mgL^{-1}) (Ismadji, Soetaredjo and Ayucitra 2015)	The model correlates the adsorption experimental data in order to estimate the coverage characteristic degree of the solute on the surface of adsorbent. It also can express the feasibility and spontaneous nature of an adsorption process (Ismadji, Soetaredjo and Ayucitra 2015).

2.6.2 Kinetics of adsorption

The prediction of rate and mechanism of reaction can be obtained from analysis of kinetic information. Knowledge of rate of reaction, dependence of reactant concentration from temperature and other parameters of kinetic modelling is important in fields such as food science and drug delivery (Dash, et al. 2010); (Marangoni 2017). In corrosion science, although not much addressed in what concerns nanocontainers loaded with active species, this information can be valuable if long-term protection is the aim. In published literature devoted to use of LDH materials with corrosion inhibitors, there has been confirmation of release of active species and anion-exchange with chlorides in solution, performed by techniques such as ICP analysis (Buchheit, Chrisanti and Mahajanam 2004); (Li, et al. 2011). However, there is a lack of more detailed analysis, though some articles may present profiles of release of corrosion inhibitors for different timescales, from 4 hours (Carneiro, et al. 2015) up to 600 hours (Yasakau, et al. 2018).

Kumar determined that the nature of the sorption process is dependent on physical or chemical characteristics of the adsorbent systems and on the system conditions in general (Kumar 2006). Nevertheless, the explanation of adsorption kinetics is a complicated problem compared to the theoretical description of adsorption equilibria. Besides, the physical nature of solid-liquid systems

is much more complicated than solid-gas system. However, solid-liquid systems are the adsorption systems of crucial importance for life and for a variety of important technological processes (Rudzinski and Plazinski 2006).

The formulation of a general expression for description of adsorption kinetics on solid surfaces for the solid-liquid adsorption systems was attempted several times (Y.-S. Ho 2004). Kinetic models in general represent slow reactions, when the amount of solute sorption or transformation is measured as a function of contact time (Selim 2015). If one of the processes happens slower than others, it can be determined as *rate-limiting step* for the entire sequence, so mathematically only this *slow process should be considered* (Siepmann and Siepmann 2008); (Siepmann and Siepmann 2012).

Several mathematical models have been suggested for description of adsorption data during last decades. They can be distinguished as *adsorption reaction models* and *adsorption diffusion models*. Pseudo-first and pseudo-second order kinetic equations are known as adsorption reaction models. They are originated from chemical reaction kinetics and are based on the whole process of adsorption. First order kinetics is known as *Freundlich kinetics* and second order is known as *Langmuir kinetics* (Selim 2015). Pseudo-second-order rate equation is based on chemical adsorption (chemisorption). However, it was wrongly applied for description of organic pollutants adsorption onto several non-polar polymeric adsorbents, which corresponds to physisorption by different authors (Meng 2005). Thus, along with careful application of pseudo-first and pseudo-second-order rate models depending on adsorption mechanism, it is necessary to apply other models which consider also boundary conditions (Qiu, et al. 2009).

Adsorption diffusion models are based on the following consecutive steps (Lazaridis and Asouhidou 2003); (Plazinski, Rudzinski and Plazinska 2009):

- ✓ transport of solute in the bulk of the solution
- ✓ diffusion across the liquid film, which surrounds the adsorbent particles (external diffusion or film diffusion)
- ✓ diffusion of the liquid in the pores and/or along the pore walls (internal diffusion or intraparticle diffusion)
- ✓ adsorption and desorption between the adsorbate and active sites (mass action) or, in other words, adsorption and desorption of solute molecules on/from the adsorbent surface (also called as ‘the surface reaction’)

The main adsorption kinetic models are presented in **Table 3** and the mechanisms are described later on. For calculation of adsorption kinetic equations the main parameters should be initially determined according to equations **13, 14** and **15** (SenGupta 2017) .

$$q_t = \frac{V}{m} \cdot (C_0 - C_t) \quad \textbf{14}$$

C_0 - initial adsorbate concentration (mgL^{-1})

C_t –adsorbate concentration at time t

q_t – the amount of adsorbate adsorbed at time t (mgg^{1})

V-volume of adsorbate solution (L)

m - mass of adsorbent (g)

$$F = \frac{q_t}{q_e} \quad \textbf{15}$$

F -fractional uptake

q_e-calculated from **13**

q_t-calculated from **14**

Table 3. Adsorption kinetic models

Model	Equation	Model's description
Zero order	$C_t = C_0 - k \cdot t$ $C_t - C_0 = -k \cdot t$ C_t – concentration of reactant at time t C_0 – initial concentration of reactant at t=0	Model is based on zero order rate kinetics (Sparks 2003).
First order	$ln\frac{C_t}{C_0} = -k \cdot t$ C_t – concentration of reactant at time t C_0 – initial concentration of reactant at t=0	Typical first order rate reaction (Qiu, et al. 2009).
Second order	$\frac{1}{C_t} = \frac{1}{C_0} + k \cdot t$ $\frac{1}{C_t} - \frac{1}{C_0} = k \cdot t$ C_t – concentration of reactant at time t C_0 – initial concentration of reactant at t=0	Typical second order rate reaction (Qiu, et al. 2009).
Pseudo-first order	$\ln(q_e - q_t) = lnq_e - k \cdot t$ q_e and q_t (mgg^{-1}) are the adsorption capacities at equilibrium and at time t respectively	Model is based on Lagergren equation (Ismadji, Soetaredjo and Ayucitra 2015).
Pseudo-second order	$\frac{t}{q_t} = \frac{1}{q_e} \cdot t + \frac{1}{k_2 + q_e^2}$ q_e and q_t (mgg^{-1}) are the adsorption capacities at equilibrium and at time t respectively	Model is based on situation when the rate of direct adsorption or desorption process controls the overall sorption kinetics (Ismadji, Soetaredjo and Ayucitra 2015).
Elovich	$q_t = \alpha \cdot \ln(a \cdot \alpha) + \alpha \cdot lnt$ q_t -adsorption capacity at time t a-desorption constant α- the initial adsorption rate (Qiu, et al. 2009)	Initially the model was used for description of heterogeneous chemisorption of gases on solid surfaces and afterwards extended for description of bulk and surface diffusion (Sparks 2003).

Table 3. Adsorption kinetic models (cont.)

Model	Equation	Model's description
Parabolic diffusion	$F = k \cdot t^{0.5}$ F-fractional uptake k- constant	This model is indication of diffusion-controlled phenomena as rate-limiting step (Sparks 2003). In other articles it is also called as Weber Morris and intraparticle diffusion models. In Weber-Morris model, if the plot initiates from the origin, the intraparticle diffusion is the single limiting step. Nevertheless, adsorption kinetics can be controlled by simultaneous intraparticle and film diffusion and the slope can differ from zero (Qiu, et al. 2009); (Dawodu, Akpomie and Ogbu 2012). Intraparticle diffusion assumes that external mass transfer occurs in the initial step with further intraparticle pore diffusion into macropores, mesopores and micropores (Cooney 1999); (Ismadji, Soetaredjo and Ayucitra 2015).
Power function	$q = a \cdot t^{k}$ q - amount of sorbate per unit of sorbent (mgg^{-1}) a – constant; k- constant, lower 1	Empirical model, when k=0.5, equation starts to be equal to parabolic diffusion, Weber Morris and intraparticle diffusion models (Sparks 2003).

Adsorption and solute transport were intensively investigated for soils and clays. However, this knowledge is also useful for understanding adsorption mechanisms and kinetics of other solid-liquid systems. It was determined that the actual chemical reaction at the surface as adsorption is usually very fast and is not rate limiting. In contrast to empirical models, in most geochemical models, sorption processes are often considered as instantaneous, when equilibrium conditions are attained in a relatively short time (minutes or several hours). Transport processes (**Figure 15**) can be separated on transport in the solution phase (1), which is fast and, in the laboratory is eliminated through rapid mixing; transport across a liquid film at the particle/liquid interface (film diffusion) (2); transport in liquid-filled macropores (>2 nm), all of which are nonactivated diffusion processes and occur in mobile regions (3); diffusion of a sorbate along pore wall surfaces (surface diffusion) (4); diffusion of sorbate occluded in micropores (<2 nm—pore diffusion) (5); diffusion processes in the bulk of the solid (6), all of which are activated diffusion processes. Pore and surface diffusions are also called as *interparticle diffusion*, whereas diffusion in the solid is *intraparticle diffusion* (Selim 2015).

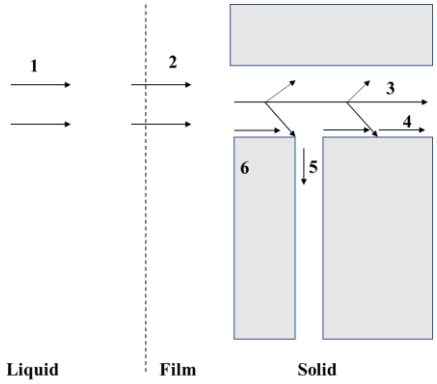

Figure 15. Transport properties in solid-liquid soil reactions

The transport of dissolved chemicals in soils is governed by active and passive transport mechanisms. For example, diffusion is an active mechanism (it takes place regardless of presence or absence of water flow in the system). Diffusion of ions or molecules results from random thermal motion of molecules in solution. Diffusion leads to a net transfer of molecules from regions of higher to lower concentrations. A common description of the diffusion is *Fick's law of diffusion* when solute flux is proportional to the concentration gradient. A passive mechanism is known as *mass transport (mass flow or convection)* and *dispersion*, they occur only in presence of water flow. Mass transport is based on the movement of dissolved chemicals in water flow. Dispersion is a unique characteristic mechanism for porous media. Dispersion (mechanical or hydrodynamic) is based on solute-spreading mechanisms, that are different from molecular diffusion and are associated with the geometry and flow characteristics of porous media. There are interconnected pores with various size diameters and various proportions in porous media. The latter leads to different water velocities due to the different pore diameters or the pore size distribution of the porous medium. Thus, solutes in large pores pass to a greater distance than solutes in small pores. Additionally, even within an individual pore, according to *Poiseuille's law*, there is a variation in velocity from the centre of a pore (maximum value) to zero at the solid surface. Thus, a velocity distribution develops over time with an increase in the advance or spreading of a solute front. Fluctuation of the flow direction due to curvature of the porous medium is another significant factor, that results in solute spreading. However, dispersion is effective only during fluid movement. Thus, for a static water condition (water flow is near zero), molecular diffusion is the dominant mixing process for solute transport in soils (Selim 2015).

2.6.3 Ion-exchange reactions

Ion-exchange represents a complex set of several inter-related processes, that may be influenced by the individual or combined effects of ion exchanger properties (capacity, functional groups, porosity); external fluid dynamics (Reynolds number); fluid properties (concentration, pH, temperature); counterion properties (diffusivity, sorption affinity, hydrophobicity); concentration and electric charge gradients in both phases. Ion exchange is based on sorption of one counterion, that is accompanied by desorption of equivalent amounts of other counterions. It is an instantaneous and a fully reversible process. Ion-exchange process includes six main steps (as an example of exchange of ions A^+ and B^+) (**Figure 16**) (SenGupta 2017):

- ✓ Transport of the counter ion A^+ from the bulk phase into the ion exchange liquid film layer
- ✓ Diffusion of A^+ across the film layer to the surface of the ion exchanger
- ✓ Intraparticle diffusion of A^+ within the ion exchanger to the functional group R^-
- ✓ Ion exchange at the fixed sites of the ion exchanger
- ✓ Intraparticle diffusion of B^+ to the film layer of the ion exchanger
- ✓ Transport of B^+ from the film layer to the bulk solution phase

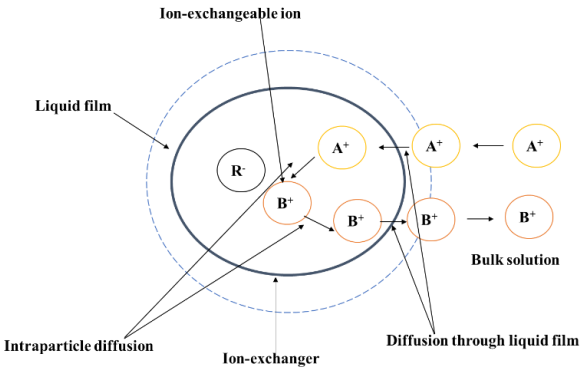

Figure 16. Ion-exchange reaction and transport of counterions between the liquid and ion-exchanger (solid phase)

A selective ion-exchange process (such as in ion-exchange resins, that are suitable for removal of specific compounds) is governed by transport of counterions within the exchanger, namely, intraparticle diffusion (rate-limiting step). Thus, selectivity, water content, porosity, cross-linking and intraparticle diffusivity are factors that influence the ion-exchange process. However, external film diffusion and chemical reaction can also be a rate-limiting step.

For determination of the rate-limiting step an empirical approach is used, performed in several stages: estimation of the limiting steps of ion exchange; approximation of mathematical solutions and

linearization of them in terms of concentration versus time plots; performance of ion exchange testing; determination of the prevailing mechanism based on the best fit of the experimental data and the model prediction. Experiments should be carried out at a single temperature with minimum imprecisions in data collection. The knowledge of activation energy value – kilojoule per mole of the reactant – in a chemical process is the most crucial determinant in identifying the rate-limiting step. However, in most cases ion-exchange reaction is a diffusion-controlled process with activation energy values much more below 100 $kJmol^{-1}$ (SenGupta 2017).

As mentioned above, all the sorption processes are fast and not rate-limiting. However, the following effects can decrease the sorption rates: transport of ion species from bulk solution to the reaction sites on mineral surfaces and chemical kinetics of reactions such as ion exchange, formation of inner-sphere surface complexes, precipitation into distinct solid phases or surface precipitation on minerals.

2.6.4 Models for release of active species

There are several models for description of release processes, especially in the field of drug delivery, because controlled drug release from dosage forms is a fundamental topic. The suggested models can be divided into empirical and semi-empirical, including also mechanistic/realistic ones. In general, empirical/semi-empirical models reveal poor predictive power. However, they can be useful for comparison of various types of drug release profiles using a specific parameter (for instance, an apparent release rate constant for experimental design analysis). But for quantitative predictions such mechanistic conclusions should be done with great precaution. In contrast, *mechanistic mathematical theories* are based on real phenomena, such as diffusion, dissolution, swelling, erosion, precipitation and/or degradation, allowing determination of drug release mechanisms. Thus, various mass transport processes can be included in the control of drug release from a dosage form, namely, the diffusion of water into the system, drug diffusion out of the device, drug dissolution, polymer swelling, matrix former erosion, osmotic effects (Siepmann and Siepmann 2008); (Siepmann and Siepmann 2012).

All theories for description of drug release kinetics are based on the following assumptions (Siepmann and Siepmann 2012):

- ✓ Diffusional mass transport (generally the drug) is the release-rate limiting step
- ✓ The diffusion coefficient of the diffusing species is constant
- ✓ Perfect sink conditions (sink condition is the volume of dissolution environment, with or without a solubiliser, for complete dissolution of the expected amount of drug present in the product) are provided in the release medium during the entire time period

- ✓ The device is not significantly swelling (or swells very rapidly upon contact with body fluids and then reaches an equilibrium state)
- ✓ The device is not significantly eroding during drug release
- ✓ Mass transfer resistance due to liquid unstirred boundary layers on the surface of the system is negligible

Moreover, the type and geometry of a drug delivery system and drug concentration versus drug solubility should be considered, while selecting the appropriate mathematical model. The main drug release models are shown in **Table 4,** using the following parameters (Chandrasekaran, et al. 2011); (Donato, et al. 2012):

$$M = \frac{C \cdot V \cdot f}{1000} \quad (16)$$

M - amount of drug released (g)

C – concentration of drug released (mgL^{-1}/ppm)

V – dissolution bath volume (L)

f- dilution factor

$$P = \frac{M_t}{M_i} \cdot 100 \quad (17)$$

P – percentage of drug released

M_t – amount of drug released at time t (g)

M_i – initial amount of drug (g)

$$Q = \frac{V\ of\ sample\ withdrawn}{V\ of\ bath} \cdot (P_{t-1} + P_t) \quad (18)$$

Q – cumulative release (%)

P_{t-1} – percentage release at time previous to time t

P_t – percentage release at time t

Table 4. Release kinetic models

Model	Equation	Model's description
Zero order	$Q_t = Q_0 + K_0 \cdot t$ Q_0 – initial amount of drug in solution (most time is equal to 0); Q_t – cumulative amount of drug dissolved at time t; K_0 (concentration $time^{-1}$) - zero order release constant; t-time (min)	Drug dissolution and release happens slowly without aggregation (Libo and Reza 1996). Some authors apply cumulative release masses for data fitting (Narashimhan, Mallapragada and Peppas 1999).

Table 4. Release kinetic models (cont.)

Model	Equation	Model's description
First order	$-\ln(1-\frac{M_t}{M_i}) = K \cdot t$ M_i – initial amount of drug; M_t –amount of drug released at time t	The model is based on first order rate kinetics that explains adsorption and/or elimination of some drugs (Narashimhan, Mallapragada and Peppas 1999); (Dash, et al. 2010); (Donato, et al. 2012).
Higuchi	$Q_t = K_H \cdot t^{0.5}$ K_H - Higuchi dissolution constant	The model describes release of a drug from planar, porous and materials with different geometry (Siepmann and Siepmann 2012).
Power function	$M_t = a \cdot t^k$ a - constant;k- constant, lower 1	Havlin and Westfall used this model for description of potassium release from soils (Sparks 2003). In other papers the same model is called as Korsmeyer-Peppas (Ritger-Peppas) model and used for drug release description from a polymeric system. The value of release exponent explains the type of release mechanism (Dash, et al. 2010). Or it is also called modified Freundlich model for expression of the release from a flat surface with heterogeneous sites based on a diffusion-controlled process (Panda, Srivastava and Bahadur 2009); (Kong, et al. 2010).
Kopcha	$Q = A \cdot t^{0.5} + B \cdot t$ A – diffusion term; B – erosion term	The model determines if diffusion or erosion processes are predominating during release. If A/B = 1, it means that ratios of diffusion and erosion are equal. If it is higher than 1, diffusion is predominating. If it smaller than 1, erosion predominates (Liu, Desai, et al. 2006).
Bhaskar's equation	$-\ln(1-\frac{M_t}{M_i}) = K \cdot t^{0.65}$	This model is applied for description of release from resinates. It is used for description of drug diffusion through the resins and inorganic materials (Ngawhirunpat, et al. 2010).
Pseudo-second order	$\frac{t}{M_i - M_t} = \frac{1}{K_2 \cdot M_{eq}^2} + (\frac{1}{M_{eq}}) \cdot t$ M_{eq} – concentration of drug in LDH matrix at equilibrium	This model is based on second order rate kinetics (Hussein, et al. 2010).

Table 4. Release kinetic models (cont.)

Model	Equation	Model's description
Elovich	$1 - \frac{M_t}{M_i} = a \cdot \ln(t) + b$ a, b – constants	The model describes the processes including bulk and surface diffusion (Yang, et al. 2007).

As mentioned in **Table 4**, the Power function model is also called modified Freundlich model or Korsmeyer (Ritger) Peppas model in literature. It does not have any restrictions on the values of k constant, except to be lower than 1. However, Siepmann and Peppas expressed physical realistic meanings of Power function equation for two specific cases: when k= 0.5 (transformation into Higuchi equation) and k=1. k=0.5 is an indication of diffusion-controlled drug release and k=1 is swelling-controlled drug release. Values between them are the sign of overlapping of both phenomena (anomalous transport). However, these extreme values are only valid for slab geometry, namely thin films. For spheres and cylinders these parameters are different. In the case of cylindrical tablets, if k=0.45 the mechanism corresponds to Fickian diffusion; 0.45< k < 0.89 – non-Fickian transport (anomalous transport); k= 0.89 – case II relaxational transport (zero-order release); n> 0.89 – Supercase II transport. For spheres, if k=0.43 the mechanism corresponds to Fickian diffusion; 0.43< k < 0.85 – non-Fickian transport (anomalous transport); k= 0.85 – case II relaxational transport (zero-order release) (Siepmann and Siepmann 2012).

The applicability of different models depends on different factors such as size and morphology, type of materials (polymer, clay), among others which shape the physico-chemical processes behind the release of active species. For instance, in Higuchi, Korsmeyer (Ritger) Peppas/Modified Freundlich/Power function models the mechanism of release is based on diffusion process and all of them have the same mathematical nature.

Moreover, the following factors should be taken into consideration for selection of best fitting model: material matrix (its stability), shape of particles (morphology), swelling and degradation; conditions of the release medium (temperature, pH, ionic strength); properties of immobilized species (solubility; stability; charge and interaction with matrix) (Fu and Kao 2010).

Diffusion, swelling and erosion are mainly rate-limiting factors for most commercially available controlled release devices. The most essential factors of diffusion process control are (Yang, et al. 2007); (Siepmann and Siepmann 2012):

- ✓ Geometry of particles: one-dimensional transport (thin films and flat planar devices) or three-dimensional (cylindrical tablets)
- ✓ Composition and particle size of host material

- ✓ Chemical interaction between host and guest structures
- ✓ Packing density of guest species

Additionally, Sparks and Kong with co-authors showed that the ion-exchange process cannot be the rate-limiting step (Sparks 2003); (Kong, et al. 2010), which is important for studies of ion-exchangeable materials like LDH. As mentioned in the previous paragraph, diffusion or degradation (swelling or erosion) can be found among the main rate-limiting steps in release systems. Thus, models such as Higuchi, Power function, Elovich and Kopcha from **Table 4** can be useful for determination of rate limiting step based on diffusion or erosion.

In existing articles devoted to the release of drugs from LDH materials, authors used the following models for evaluation of rate-limiting step of the release process: zero order, first order and pseudo-second order kinetics, modified Freundlich or Power function model and parabolic diffusion model (the latter model can be transformed into Higuchi model equation) (Yang, et al. 2007); (Panda, Srivastava and Bahadur 2009); (Hussein, et al. 2010); (Kong, et al. 2010). In these works, the authors found that the release is mainly controlled by diffusion. Nevertheless, studies of this nature cannot be found in literature for LDH used for coating applications.

2.6.5 Data analysis

In addition to the need of taking into account the physico-chemical properties of the release system, as described in the previous sections, analysis of the release data can play an important role on the selection of the most appropriate release model.

The success of fitting of experimental release data can be assessed via linear and non-linear regression analysis. *Least-Squares Minimization* or *Regression Analysis* (linear or non-linear) estimates the equation parameters by determination of parameter values for which the sum of squared residuals is at a minimum. Regression analysis comprises several crucial assumptions about the chosen function and the error structure of the data, namely:

- ✓ The correct equation is used
- ✓ Only dependent variables are subjected to error, while independent variables are known exactly
- ✓ Errors are normally distributed with zero mean, the same for all responses (homoscedastic errors) and uncorrelated (zero covariance)
- ✓ The correct weighting is used

However, a linear function of parameters does not result in a straight line. A model is linear if the first partial derivative of the function corresponding to the parameter is independent of such parameter, consequently, higher order derivatives would be zero. Moreover, *the reduced chi square* (χ^2) parameter is applied for estimation of the fitting quality of a model to experimental data. The reduced chi-square value should be roughly equal to the number of degrees of freedom, if the model is correct, χ^2 ~1. For instance, the number of degrees of freedom is calculated like (n-p-1), where n is the total number of data values and p is the number of parameters for estimation. The *correlation coefficient* (CC) is another most appropriately used statistic parameter to linear regression. It serves as indication of the closeness of the approximation of a linear relationship between dependent and independent variables. Values for the CC can range from −1 to +1. A CC value close to +/−1 is a signal of a strong correlation. Additionally, r-square statistic (r^2), which is close to ±1 is the indication that the model accounts for most of the variability in the data (for linear regression). For non-linear functions, however, the situation is more complex. Iterative methods are used in this case, when parameter values are changed simultaneously or one at a time, in a prescribed mode until reaching a global minimum. The applied algorithms include the Levenberg-Marquardt method, the Powell method, the Gauss-Newton method, the steepest-descent method, simplex minimization and their combinations. The *F-test* is the most common statistical tool for understanding if a model fits the data better than another. Comparable models are fitted to data with calculation of reduced χ^2 values. The ratio of the χ^2 gives the F-statistic value. Application of standard statistical tables allows estimation, if the fits of the models to the data are significantly different from each other at a certain level of statistical significance (Marangoni 2017).

The above-mentioned parameters can be estimated using ORIGIN program. The final report in the program includes the following results: values of r-squared correlation coefficient; R-squared coefficient of determination; the reduced chi square (χ^2); Pearson's correlation coefficient; Adj. R-Square. The last parameter is a modified version of R-square, which is adjusted for the number of predictors in the fitted line. For instance, if the number of predictors is greater than 1, Adj.R-square is always smaller than R-square (OriginLab 2019). Moreover, the final report in ORIGIN also presents the ANOVA parameters like F value and Prob. F.

F is a ratio of two mean squares, which can be computed by dividing the mean square of fitted model by the mean square of error. The more this ratio deviates from 1, the stronger is the evidence for the fitted model to differ significantly from the model, where Y=constant (namely, flat line with zero slope). Prob.F is a p-value for F-test with the range from 0 to 1. For example, the p-value for F-test lower than the significant level alpha (usually is 5% or 0.05) indicates that the fitted model is

significantly different from the model Y=constant, implying that the fitted model is a non-linear curve or a linear curve with slope, significantly different from zero (OriginLab 2019).

Another extremely important parameter, which is used for estimation of the success of experimental data fitting is the *residual plot analysis* (which is also demonstrated in ORIGIN report). The *residual* is defined as the difference between observed and predicted data by the model Y value (response variable). The residual is a vertical deviation from the line to a data point on the plot. Consequently, points above the line show positive residuals and below the line - negative residuals. If the predicted values are very close to the observed ones the residuals will be small and close to the line. The line with the best fitting data is where the residuals are close to zero (Lock, et al. 2013). The residual plots should be checked to detect *outliers*. Outlier is an extreme observation, which does not accompany to the tendency of the rest data, meaning, that one observation influences extremely on the results. Ideally, the residual plot points should be scattered and do not form patterns. It can be presented as a horizontal band around zero with randomly distributed points without detectable pattern, namely, obvious relation or pattern between the residuals and the predictor should be absent. Thus, the following types of residual plots can indicate inapplicability of an estimated model (Kokoska 2015):

- ✓ Formation of a distinct pattern (curve either mound- or bowl-shaped (parabolic))
- ✓ Nonconstant spread of points. If there is not a uniform horizontal band, or if the spread of the residuals varies outside this band, this suggests that the variance is not constant
- ✓ The residual plot with unusually large (in magnitude) residuals, meaning that one observation is very different from the rest. This can be a signal of incorrect record or entrance of a data. Often, the offending point is excluded, and a new estimated regression line is computed
- ✓ Presence of outliers. If the observation is correct, an outlying residual means that one observation has an unusually large influence on the estimated regression line. This point should be omitted, and a new line is computed

The analysis of literature regarding to the application of release models and the choice of best fitting model shows that most authors choose their model for release based solely on the evaluation of correlation coefficient or r-square statistic (if they are close to 1, the corresponding model is simply chosen as the best one) (Yang, et al. 2007); (Panda, Srivastava and Bahadur 2009); (Hussein, et al. 2010); (Kong, et al. 2010). However, such approach is not totally correct, because there is a chance that despite a high r-square value, residual plot could reveal the presence of patterns or accumulation of residuals close to each other instead of scattering, which is an indication of a biased model. The presence of random (scattered) residuals is a sign of precise and unbiased model. Moreover, the application of non-linear regression model should consequently be carried out by residual plot

analysis (its degree of randomness) and low values of standard errors associated with the estimated parameters. The r square parameter should be reasonably evaluated only for linear regression analysis, but also in context with p-value, because p-value < 0.05 is a sign that the model may be biased (Zellner, Keuzenkamp and McAleer 2001).

2.7 Critical analysis of the state of art

The present PhD thesis is devoted to the preparation of LDH materials with corrosion inhibitors that had already been studied in terms of corrosion protection (Tedim, et al. 2010); (Carneiro, et al. 2015) or microbiological activity (Kuznetsova, et al. 2017); (Martins, et al. 2017), as well as new LDH compositions never studied before including LDH loaded with pH indicators (dyes). In spite of the above-mentioned works showing the applicability of LDH materials for the corresponding application, no data concerning the release mechanisms can be found for these systems. Only a handful of works associated with drug-immobilized LDH materials report the fitting of release models to release profiles (Yang, et al. 2007); (Panda, Srivastava and Bahadur 2009); (Hussein, et al. 2010); (Kong, et al. 2010). Furthermore, these studies tend to rely simply on linear regression analysis, which has some drawbacks associated, as described in the previous section.

In this context, this PhD thesis tries to go beyond the state of art addressing both uptake and release of active compounds used in multi-functional coatings, using both linear and non-linear regression models for fitting of experimental data along with residual plot analysis.

3. EXPERIMENTAL PART

All the reagents were received from Sigma-Aldrich, Alfa Aesar or Riedel-de Haën and used without any modifications.

3.1 Synthesis of LDH precursors by coprecipitation

The LDH precursor was synthesized by coprecipitation methodology, through direct addition of cation salts into a 1.5M $NaNO_3$ or 1.5M Na_2CO_3 solution at constant pH, with simultaneous addition of 2M NaOH under vigorous stirring at room temperature. LDH preparation was carried out under nitrogen atmosphere and all the solutions were prepared using boiled distilled water to avoid contamination with carbonate anions, when nitrate LDH precursor was to be obtained. Afterwards, the prepared slurry was subjected to hydrothermal treatment at 100 ºC for 4 h for crystallization of LDH, centrifuged (Centrifuge Sigma Sartorius 2-16P) and washed two times with boiled distilled water. A small fraction of the LDH slurry precursor was dried at 60 ºC in an oven for further characterization, while the remaining part of the slurry was used for ion-exchange reaction with corrosion inhibitors or dye indicators.

The LDH-nitrate precursor was also synthesized following the coprecipitation reaction in reverse microemulsion suggested by Hu and O'Hare to obtain LDH particles with different morphologies with respect to the conventional coprecipitation method (Hu and O'Hare 2005). First, two solutions were prepared: solution A, which contains the mixture of metal salts, and solution B, which is a mixture of 2.73M $NaNO_3$ and 4M NaOH. The LDHRM precursor was then prepared in a sodium dodecyl sulphate-water-isooctane microemulsion by adding solution A dropwise to the reverse microemulsion under vigorous stirring. Afterwards, solution B was added drop by drop. In the final step the 4M NaOH solution was added to adjust the final pH around 9 (the pH after the reaction was 7). After leaving the mixture under stirring during 1 h at room temperature, it was subsequently heated at 75 ^{0}C in the oven during 24 h. Afterwards, a slurry was obtained after centrifugation and washing steps using boiled distilled water.

The LDHN precursor was synthesized by the same method based on coprecipitation reaction in reverse microemulsion above described, except for the addition of a nonionic triblockcopolymer surfactant during the nucleation step ($H(OC_2H_4)_{11}(OC_3H_6)_{16}(OC_2H_4)_{11}$-OH, called P1940, with average molar mass 1900 $gmol^{-1}$) On the other hand, the LDHC precursor was prepared by coprecipitation reaction in reverse microemulsion, but this time adding the copolymer during the crystallization step. After a first treatment at 75 ^{0}C for 24 h, the copolymer was added, and the thermal

treatment repeated for another 24 h. The final steps of washing were performed similarly to the previous procedures.

Table 5. LDH materials prepared by coprecipitation

LDH designation	pH	Metal salts mixture
Zn(2)Al-NO_3-COP	9	0.5M $Zn(NO_3)_2$/0.25M $Al(NO_3)_3$
Zn(2)Al-NO_3-REV*	9	0.5M $Zn(NO_3)_2$/0.25M $Al(NO_3)_3$
Zn(2)Al-NO_3-REVN*	9	0.5M $Zn(NO_3)_2$/0.25M $Al(NO_3)_3$
Zn(2)Al-NO_3-REVC*	9	0.5M $Zn(NO_3)_2$/0.25M $Al(NO_3)_3$
Mg(3)Al-CO_3-COP	10	0.5M $Mg(NO_3)_2$/0.167M $Al(NO_3)_3$

* these LDH compositions have not been reported in the literature

3.2 Intercalation of active species into LDH by anion-exchange

A 0.1M aqueous solution of active species to be intercalated was prepared using boiled distilled water. Solutions of Glu and FSS were prepared by direct dissolution of the corresponding sodium salt in water, while MBT was dissolved in 0.1M NaOH aqueous solution and in ethanol (when intercalated into LDH precursors obtained by coprecipitation reaction in reverse microemulsion). On the other hand, PhPh and TB were dissolved in ethanol and the resulting solutions (0.1 M) were used for intercalation/immobilization of these pH indicators in anionic form in LDH.

Slurries of LDH precursors (from **Table 5** , except of Mg(3)Al-CO_3-COP) were subsequently immersed in one fraction of the mentioned solution (V=250 mL) and the resulting suspension was held for 24 h under constant stirring. The reaction products after recovery by centrifugation were washed twice with boiled distilled water. The resulting slurries were added to a second portion of 0.1M solutions of active species and the whole procedure was repeated. Afterwards, the washed precipitates were stored in the form of slurry at room temperature in sealed containers, to maintain the water content. A small fraction of LDH slurries with active species were dried at 60 ºC for characterization, as mentioned previously for the LDH precursors.

Table 6. LDH materials prepared by anion-exchange

LDH designation	pH of anion-exchange	Solution with guest anion
Zn(2)Al-CO_3 -AN	10	0.1M Na_2CO_3
Zn(2)Al-Glu -AN	8	0.1M NaGlu

Table 6. LDH materials prepared by anion-exchange (cont.)

LDH designation	pH of anion-exchange	Solution with guest anion
Zn(2)Al-MBT-AN	9	0.1M MBT/NaOH
Zn(2)Al-MBT -REV/AN*	-	0.1M MBT (ethanol)
Zn(2)Al-MBT -REVN/AN*	-	0.1M MBT (ethanol)
Zn(2)Al-MBT -REVC/AN*	-	0.1M MBT (ethanol)
Zn(2)Al-FSS-AN	9	0.1M NaFSS
Zn(2)Al-PhPh -AN	10	0.1M PhPh
Zn(2)Al-TB -AN*	10	0.1M TB

* these LDH compositions have not been reported in the literature

3.3 Preparation of LDH with active species by calcination-rehydration methodology

Commercial synthetic hydrotalcite (SH) obtained from Sigma-Aldrich was used as precursor for preparation of LDH materials with active species by calcination rehydration route. The general formula of SH is $Mg_6Al_2(CO_3)(OH)_{16}\cdot 4H_2O$. **Mg(3)Al-$CO_3$-COP** and **Zn(2)Al-$NO_3$-COP** prepared by coprecipitation were also tested as precursors for comparison purposes. The LDH precursors were calcined at different temperatures (150 ^{0}C and 650 ^{0}C) in alumina crucibles. Afterwards, the calcined LDH materials were immersed into 0.1M solutions of active species for 3 days, at room temperature or 60 ^{0}C, under stirring. MBT was dissolved in 0.1M NaOH aqueous solution or in ethanol (the latter was used in the synthesis of **Mg(3)Al-MBT-SH/CALC150C**). PhPh and TB were dissolved in ethanol. Afterwards, the rehydrated LDH slurries were separated by centrifugation and washed with boiled distilled water twice. Finally, the resulting LDH materials were dried at 60 ^{0}C and were used for characterization and release tests.

Table 7. LDH materials prepared by calcination-rehydration

LDH	pH of rehydration	Solution for rehydration
Mg(3)Al-MBT-SH/CALC650*	9	0.1M MBT/NaOH
Mg(3)Al-MBT-SH/CALC150C*	-	0.1M MBT (ethanol)
Mg(3)Al-MBT-CALC650*	9	0.1M MBT/NaOH
Zn(2)Al-PhPh-CALC150*	10	0.26M PhPh
Mg(3)Al-PhPh-SH/CALC150*	10	0.26M PhPh
Zn(2)Al-TB-CALC150*	10	0.26M TB
Mg(3)Al-TB-SH/CALC150*	10	0.26M TB

* these LDH compositions have not been reported in the literature

3.4. Structural and morphological characterization of LDH

All LDH materials were examined by X-ray diffraction (XRD) using Philips X´Pert difractometer (Ni-filtered Cu Kα radiation, tube power 40 kV; 50 mM; X-celerator detector), Fourier transformed infrared spectroscopy (FTIR) with a FTIR Tensor 27 Bruker Germany, ATR-Golden Gate Specac 128 scans resolution 4 detector DTGS/KBr with the range of wavenumbers 4000-400 cm^{-1}. The morphology and composition of LDH were investigated by scanning electron microscopy (SEM) - Hitachi Su-70 coupled with energy dispersive spectroscopy (EDS).

3.4.1 Textural and thermal properties of LDH

Porosity and specific surface area were measured by Brunauer – Emmett - Teller (BET) analysis, based on gas (nitrogen) adsorption at 77 K, using Micromeritics Gemini 2370 equipment in automatic form mode. From literature data it is known that mesoporosity information can be obtained from the medium and high relative pressure range values. Simultaneous multilayer adsorption and capillary condensation can be described by several methods, but the most common one is "BJH method" (Michot and Villiéras 2006). BJH method is suggested by Barrett, Joyner and Halenda. It is based on emptying of the pores, namely, desorption branch. All mesoporous materials adsorption isotherms contain hysteresis loop and adsorption and desorption branches can be distinguished. Thermal stability of LDH materials were studied by thermal gravimetry (TG) analysis using a Setaram and the Labsys model equipment with heating up to 1000 ^{0}C and ramp temperature 10 ^{0}C per minute. Thermal stability of LDH compositions with TB were not performed due to technical reasons.

3.4.2 Surface (colloidal) properties of LDH

Particle size distribution and zeta potential/electrophoretic mobility measurements were performed by dymanic light scattering measurements (DLS), using a Malvern Zetasizer nanoseries. LDH powders were dispersed in deionized water, ethanol or buffer solution with exact pH values (pH values were previously measured by calibrated pH-meter) and sonicated during 15 minutes before measurements. Each measurement was repeated three times. Buffer solutions (pH 3 - pH 12) were prepared according literature (De Lloyd 2000).

3.5 Adsorption and release experiments

3.5.1 Adsorption isotherms

Adsorption experiments were performed through immersion of a certain mass of LDH materials into solutions of active species with different initial concentrations at room temperature (RT) or 60 ^{0}C (HT) under vigorous stirring (350 rpm) (X. Chen 2015). For determination of adsorption isotherms, the dispersions were stirred at 350 rpm during 2 h. Then, these dispersions were centrifuged and the concentrations of active species in the supernatant were measured by UV-Vis spectrophotometry, using UV-Vis spectrophotometer Spectrascan. Adsorption kinetics was studied in a similar manner; however, the concentrations of active species were measured at determined time scale. The stability of equipment was assessed by validation of background and check of standard solutions absorbance before each set of measurements. The quantitative UV-Vis analysis was based on Bouguer Lambert Beer's law. The analytes were diluted, because in high concentration linearity of the law was no longer applicable (the working range is 15-80% of transmittance or 0.10-0.82 of absorbance). Standard solutions were prepared and measured to obtain calibration curves and the unknown concentration of the sample was then determined (Kenkel 2014).

3.5.2 Release studies

The quantification of active species released from LDH materials was performed in most cases by direct measurements by UV-Vis spectrophotometry, except for gluconate. The quantification of released gluconate was performed following the methodology reported by Alt (Alt 1955), based on the complexation reaction between copper (Cu^{2+}) with gluconate in alkaline medium, with maximum absorbance at λ=660 nm. The detection limit of this method is 1mM, due to the precipitation of cupric ions in alkaline medium. For the concentration range 1mM-10mM (194.15-1941.5 ppm) Beer's law applies. Quantification of released FSS was performed in the bivalent anion form (pH ~ 9).

The loading content of active species in LDH compositions has been estimated by complete dissolution of LDH samples in a 0.1M HNO_3. The resulting solution was then analysed using the above-mentioned methodology (UV-Vis spectrophotometry). After completion of release studies LDH slurries were separated from the solution by centrifugation and dried for subsequent characterization.

The release studies were performed under stirring conditions (350 rpm) at room temperature via immersion of LDH slurries into solutions with different triggers including different sodium chloride concentrations (deionized water medium) and aqueous solutions with different pH values: 3-5; 7; 10-12 (acidic and alkaline solutions were obtained by addition of drops of dilute solutions of 0.05M

HNO_3 and 0.05M NaOH into deionized water, respectively). Buffer solutions were not used to exclude possible anion-exchange reactions with the salts from buffers and to estimate influence of H^+ and HO^- ions on the release process. Additional release investigations in the presence of ethanol were performed for sensing species soluble in ethanolic medium (FSS, PhPh, TB).

All the measurements were done in triplicate. The mass of LDH materials used in these studies was 0.1 g of solid content, except for LDH materials with PhPh and TB, which was 0.01 g due to high values of absorbance associated with the immobilized dyes. At certain times, aliquots were taken and filtered using a 0.45μm filter with a 3 ml syringe. The remaining filtered liquid was returned to the test flasks. For the study of MBT release from **Zn(2)Al-MBT-AN** in 500mM NaCl, comparison tests were also performed, namely with addition of fresh 500mM NaCl (0.1 ml) for conservation of the total volume of suspension. Results of these measurements and choice of final release procedure is described in detail in section 6.

Experiments for evaluation of the activation energy associated with the release of species from LDH were carried out using LDH intercalated with gluconate as a representative system. The release of gluconate was performed at 15 ^{0}C, 35 ^{0}C and 45 ^{0}C under vigorous stirring (350 rpm) to exclude influence of stirring on activation energy of the system.

3.5.3 Data analysis

All the experimental data were assessed using the statistical procedures described below (Norman and Streiner 1998); (Dytham 1999); (Quirk, Quirk and Horton 2015). *Mean* is the arithmetic average of a set of scores. *Standard deviation (S)* demonstrates the closeness of the scores to the mean. Small value of standard deviation confirms that the values are close to the mean. From standard deviation value it is also possible to estimate *standard error (s.e.)*.

$$\bar{X} = \frac{\sum X}{n} \quad (19)$$

n- amount of numbers in a set

$$STDev = S = \sqrt{\frac{\sum(X - \bar{X})}{n - 1}} \quad (20)$$

$$s.e. = S_{\bar{X}} = \frac{S}{\sqrt{n}} \quad (21)$$

There are two hypotheses in statistics, that are called the *null hypothesis* and the *research hypothesis*. The null hypothesis is accepted as true unless we have compelling evidence that it is not true. The research hypothesis is accepted as true; the null hypothesis is rejected. The null hypothesis is accepted, when two sets of data are the same. *P value* is a probability when the tested hypothesis is true. In biology, the probability value is usually 0.05, 5% is a critical level for the rejection of the hypothesis. It is also called *significance level* or *α level*. If estimated P value is higher 0.05, so the null hypothesis is accepted, in opposite case, it is rejected. Or, in other words, if the reference value is lower than the critical value, the null hypothesis is accepted. Otherwise, it is rejected. The mentioned test is called *t*-test and allows comparison of two groups of data.

ANOVA allows testing for the differences between means in presence of three or more groups of data. This ANOVA test is called the *F-test statistic*. ANOVA t-tests show between which pairs of groups the statistical difference is significant. Post-hoc comparisons are applied when one-way ANOVA estimations reject the null hypothesis and support the alternative one. For example, it is possible to apply *Bonferroni correction* for making α level more stringent: it is necessary to count the total amount of comparisons (k) and then 0.05 divide in k.

The t-Test and ANOVA test were calculated in Microsoft Excel program.

In addition, due to the lack of consensus between authors to use a common parameter to track the release as a function of time (concentrations, cumulative masses, percentages), in present PhD thesis the values of fractional uptake (equation **15** presented in Chapter 2) were applied in the release model equations (except for zero order and first order), as well as in the adsorption model kinetics (except of pseudo-first and pseudo-second order adsorption kinetics and Elovich model), where the last timescale point was used as the point of equilibrium (SenGupta 2017).

Analysis of experimental data for the choice of best fitted model was initially performed by linear regression analysis, in the case, when it showed, that the model was biased or the values of standard errors were high, the non-linear regression evaluation was performed for the respective model (Zellner, Keuzenkamp and McAleer 2001); (OriginLab 2019).

4. CHARACTERIZATION OF LDH

4.1 Structural and thermal characterization of prepared LDH materials

4.1.1 Characterization of LDH by XRD

All prepared LDH materials (by methodologies described in experimental part section) were initially characterized by XRD. The XRD pattern gives useful information for determination of a stacking polytype and unit cell parameters. Indexing of powder pattern for rhombohedral polytypes is based on a triple hexagonal unit cell (Evans and Slade 2006).

XRD patterns of pristine LDH samples are presented in **Figure 17** and **Table 8** with appropriate calculated *hkl* indexes for a hexagonal unit cell, using Le-Bail method (FullProf software) and $R\bar{3}m$ space group. **Figure 17** confirms the successful preparation of all LDH materials. The pristine LDH samples were found to be crystalline and single-phase structures. The parameters a_0 and c_0 presented in the first two columns of **Table 8** were calculated from the positions of the corresponding XRD pattern reflections. The values in the remaining columns were estimated by Le-Bail method. Peaks, which are not indexed in the XRD spectra of **Zn(2)Al-NO_3-REV**, **Zn(2)Al-NO_3-REVN** and **Zn(2)Al-NO_3-REVC** are attributed to $NaNO_3$ phase excess, that was used during the synthesis (ICDD 2019). Values of a_0 were found to be very close for all types of pristine LDH materials and are in agreement with the literature data (Evans and Slade 2006).

The parameter a_0 corresponding to pristine LDH-nitrates prepared by coprecipitation reaction in reverse microemulsion (first column of **Table 8**), is slightly out of the range described in the literature as determined by Evans and Slade. However, these authors suggest that the presence of non-LDH phases can influence the value of a_0. Moreover, in some cases the (110) reflection can be weak and broad, overlapping with the adjacent (113) reflection, which limits its estimation (Evans and Slade 2006). However, after refinement, a_0 values were found to be in the range of published data. Values of c_0 for LDH loaded with nitrates and carbonates are also in agreement with the literature (Evans and Slade 2006); (Ghotbi, et al. 2009); (Tedim, et al. 2010).

Hu and O'Hare determined that **Mg(2)-Al-NO_3-REV** (referred in paper as **LDH-RM**) had rhombohedral symmetry polytype, whereas **Mg(2)-Al-NO_3-REVN** (referred in paper as **LDH-N**) possessed hexagonal polytype symmetry. There is a lack of information about **Mg(2)-Al-NO_3-REVC** (referred in paper **LDH-C**) polytype (Hu and O'Hare 2005), though. However, in the case of LDH intercalated with nitrates there is a possibility for polytypes intergrowth. More specifically, $3R_1$ polytype can transform into $2H_1$ due to structural disorders (Radha and Kamath 2012). Thus, the polytypes of synthesized LDH materials determined after Le Bail refinement are in agreement with

aforementioned information. Additionally, for **Zn(2)-Al-NO$_3$-REVC** its symmetry was found to be rhombohedral.

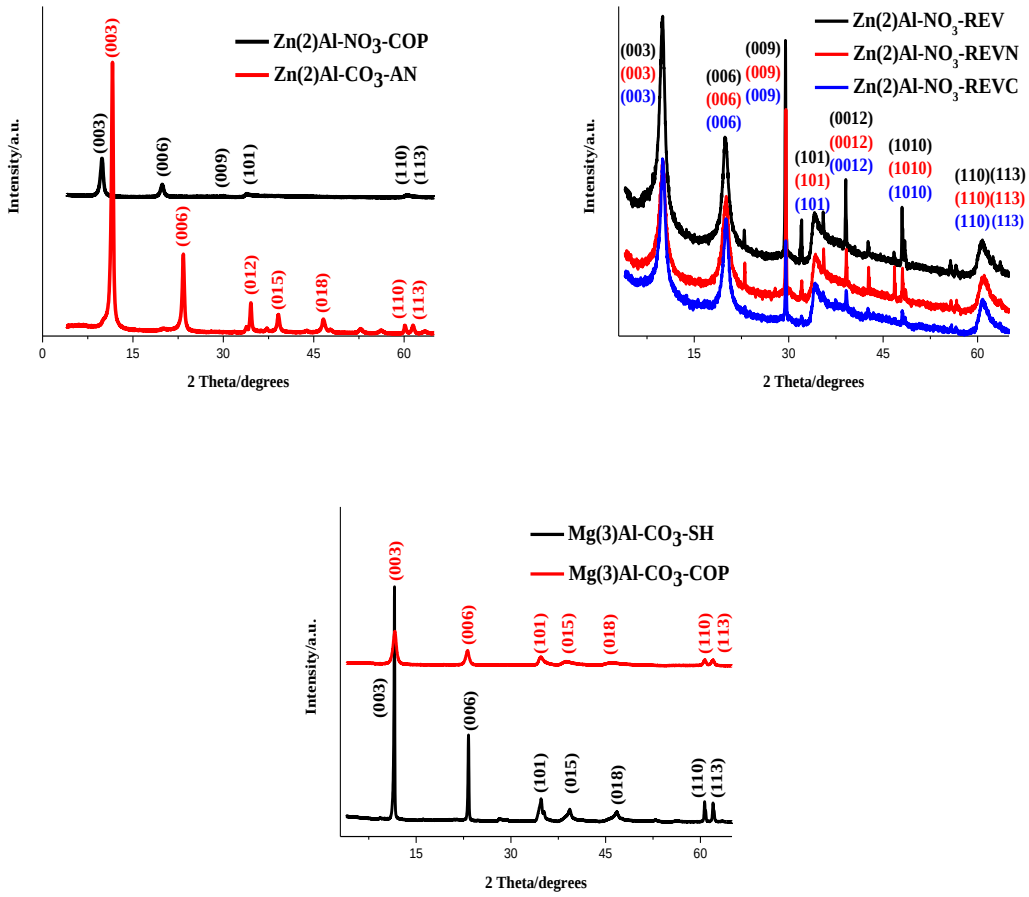

Figure 17. XRD diffractograms of LDH prepared by coprecipitation and anion-exchange (**Zn(2)Al-NO$_3$-COP**, **Zn(2)Al-CO$_3$-AN**, **Mg(3)Al-CO$_3$-COP**), coprecipitation reaction in reverse microemulsion (**Zn(2)Al-NO$_3$-REV**, **Zn(2)Al-NO$_3$-REVN** and **Zn(2)Al-NO$_3$-REVC**) and commercial synthetic hydrotalcite (**Mg(3)Al-CO$_3$-SH**)

Table 8. Main unit cell parameters of pristine LDH materials before and after Le-Bail refinement

LDH	a_0, Å	c_0, Å	a_0 after refinement, Å	c_0 after refinement, Å	c after refinement, Å
Zn(2)Al-NO$_3$-COP	3.06	8.94	3.06	8.97	26.91
Zn(2)Al-CO$_3$-AN	3.07	7.61	3.07	7.64	22.92

Table 8. Main unit cell parameters of pristine LDH materials before and after Le-Bail refinement (cont.)

LDH	a_0, Å	c_0, Å	a_0 after refinement, Å	c_0 after refinement, Å	c after refinement, Å
Mg(3)Al-CO_3-SH	3.05	7.62	3.05	7.69	23.06
Mg(3)Al-CO_3-COP	3.04	7.60	3.06	7.70	23.11
Zn(2)Al-NO_3-REV	3.05	8.82	3.05	9.07	27.20
Zn(2)Al-NO_3-REVN	3.03	8.79	3.10	8.87	26.60
Zn(2)Al-NO_3-REVC	3.04	8.79	3.09	8.84	26.52

Subsequently, some of the LDH compositions above presented were used for immobilization of different active species, as reported in the experimental section: corrosion inhibitors (sodium gluconate and 2-mercaptobenzothiazole) and sensing species (pH indicators phenolphthalein, thymol blue and sodium fluorescein). The XRD diffractograms obtained are described in **Figure 18 - Figure 22**.

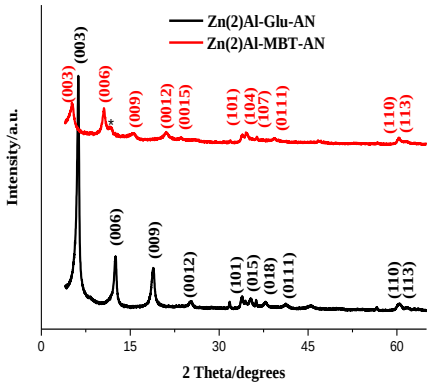

Figure 18. XRD diffractograms of LDH with gluconate (**Zn(2)Al-Glu-AN**) and 2-mercaprtobenzothiazole (**Zn(2)Al-MBT-AN**) prepared by anion-exchange

Figure 18 shows XRD diffractograms corresponding to LDH prepared with corrosion inhibitor sodium gluconate and 2-mercaptobenzothiazolate, obtained from the deprotonation of MBT before the intercalation (MBT^-). In the case of **Zn(2)Al-Glu-AN**, there is a shift of the (003), (006) and (009) reflections towards low angles, which is consistent with an expansion of the interlayer spacing. With respect to **Zn(2)Al-MBT-AN** two LDH phases were detected and are in agreement with

literature data. The main phase corresponds to intercalation of MBT, while the second, marked with an asterisk, corresponds to a LDH phase intercalated with hydroxides, the molar ratio of LDH-OH phase can achieve around 15% (Poznyak, et al. 2009); (Tedim, et al. 2010); (Carneiro, et al. 2015).

The attempt to intercalate MBT by anion-exchange in LDH structures obtained previously by coprecipitation reaction in reverse microemulsion was tried. According to the XRD diffractograms displayed in **Figure 19**, though, the main reflection peaks which can be ascribed to LDH phases seem identical to the LDH precursors. However, additional peaks occurred, which can be due to immobilization of MBT via adsorption in the external surface of the LDH particles. More interestingly, the intercalation of MBT cannot be fully ruled out, as small reflections do occur at low 2 Theta angles, but their intensity is too small to extract information of a possible secondary LDH-phase.

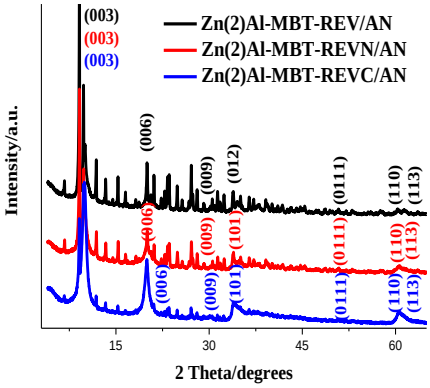

Figure 19. XRD diffractograms of LDH with 2-mercaprobenzothiazole (**Zn(2)Al-MBT-REV/AN, Zn(2)Al-MBT-REVN/AN, Zn(2)Al-MBT-REVC/AN**) prepared by anion-exchange from LDH structures synthesized by coprecipitation reaction in reverse microemulsion

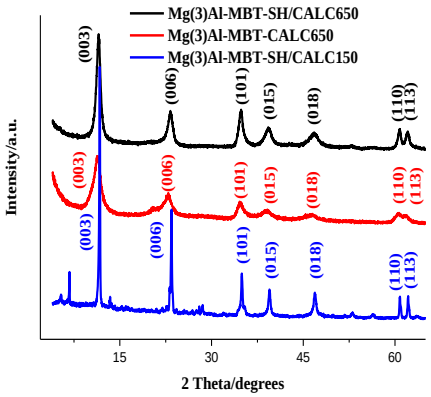

Figure 20. XRD diffractograms of LDH with 2-mercaptobenzothiazole (**Mg(3)Al-MBT-SH/CALC650, Mg(3)Al-MBT-CALC650, Mg(3)Al-MBT-SH/CALC150**) prepared by calcination-rehydration procedure

Figure 20 shows that both **Mg(3)Al-MBT-CALC650** and **Mg(3)Al-MBT-SH/CALC650** prepared by calcination at 650 ^{0}C followed by rehydration in aqueous alkaline MBT solution did not lead to the intercalation of MBT into LDH galleries. Besides, it is worth mentioning that the synthetic hydrotalcite acquired commercially is coated with an organic compound (fatty acid) intended to be used as additives to plastics. Nonetheless, the calcination step at such high temperatures fully removed the organic coating material and both pristine LDH materials exhibited similar XRD patterns, except for the differences in peak intensity. Another attempt to intercalate MBT, consisted of partial calcination of the **Mg(3)Al-CO_3-SH** at 150 ºC and subsequently rehydration in an ethanolic solution with MBT. The resulting diffractogram (**Figure 20**) reveals that the most intense phase corresponds to LDH with a smaller basal spacing than if MBT would have been successfully intercalated. Possibly, a main LDH-OH phase was formed instead.

Figure 21 shows that after performing anion-exchange step to intercalate the anionic form of pH indicators phenolphatlein and thymol blue, the XRD diffractograms obtained are similar to the corresponding parent structure **Zn(2)Al-NO_3-COP**, thereby showing that the attempt for intercalation of these pH indicator molecules was not successful. Moreover, the position of the reflections at low 2 Theta angles seems to have been shifted to higher angles, which is consistent with the intercalation of smaller species such as HO^- or CO_3^{2-} (Zhang and Evans 2012). This may be related to the fact that the pH indicator displays acid-base properties and, knowing that the pH of intercalation for these two species was between 9 and 10, HO^- and CO_3^{2-} resulting from dissolved CO_2 could have been preferentially intercalated. Having failed the anion-exchange route, a calcination-rehydration route was tried. The objective was to explore to use the "memory effect" of LDH when it reconstructs in aqueous environment following a calcination treatment (Newman and Jones 1998) to immobilize these pH indicators. Although expansion of the intergallery was also not

observed using the latter route, new reflections were detected, which may be ascribed to crystallized forms of the molecules on the LDH surface.

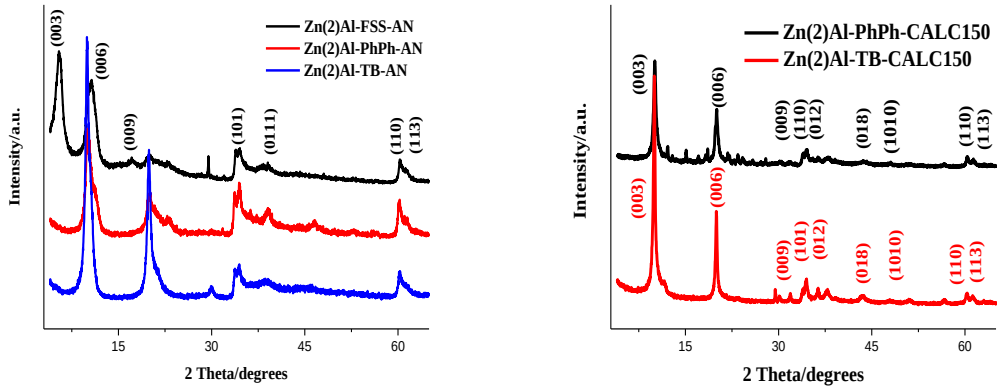

Figure 21. XRD diffractograms of LDH with sensing species prepared by anion-exchange (**Zn(2)Al-FSS-AN**, **Zn(2)Al-PhPh-AN, Zn(2)Al-TB-AN**) and calcination-rehydration procedures (**Zn(2)Al-PhPh-CALC150, Zn(2)Al-TB-CALC150**)

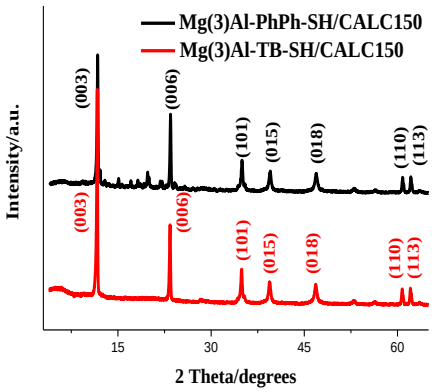

Figure 22. XRD diffractograms of synthetic hydrotalcite with phenolphthalein and thymol blue sensing species (**Mg(3)Al-PhPh-SH/CALC150, Mg(3)Al-TB-SH/CALC150**) prepared by calcination-rehydration procedure

Figure 22 shows the attempt to intercalate pH indicators in **Mg(3)Al-CO_3-SH** by calcination at 150 ^{0}C and further rehydration. Similar to Zn(2)Al LDH samples, no intercalation has occurred, although some small reflections possibly associated with crystallized forms of the indicators are detected (Latterini, et al. 2002).

In **Table 9** the unit cell parameters of all the LDH structures prepared with different species are summarized. The a_0 parameters presented in **Table 9** show that there are no structural changes in the cationic sheets during preparation of LDH materials with the intended anionic guest. High values of c_0 parameter point toward the intercalation of gluconate, fluorescein and 2-mercaptobenzothiazolate (for **Zn(2)Al-MBT-AN**) into the LDH galleries. The values of c_0 closer to carbonate/hydroxide anions (7.50-7.60 Å respectively) (Zhang and Evans 2012) or nitrate (8.80-8.90 Å) (Evans and Slade 2006) in some of the attempted syntheses implies that MBT and pH-indicators like phenolphthalein and thymol blue can be only adsorbed onto the surface of LDH particles in those cases.

Table 9. Main unit cell parameters of LDH materials with corrosion inhibitors and sensing species before and after Le Bail refinement

LDH	a_0, Å	c_0, Å	a_0 after refinement, Å	c_0 after refinement, Å	c after refinement, Å
Zn(2)Al-Glu-AN	3.06	14.17	3.07	14.13	42.38
Zn(2)Al-MBT-AN	3.06	16.95/7.63	3.07	16.82	50.45
Zn(2)Al-MBT-REV/AN	3.01	8.76	3.08	8.88	26.65
Zn(2)Al-MBT-REVN/AN	3.05	8.81	3.07	8.90	26.70
Zn(2)Al-MBT-REVC/AN	3.05	8.88	3.10	8.91	26.74
Zn(2)Al-FSS-AN	3.06	16.03	3.06	15.95	47.86
Zn(2)Al-PhPh-CALC150	3.06	8.75	3.07	8.84	26.52
Zn(2)Al-TB-CALC150	3.06	8.78	3.08	8.87	26.62
Mg(3)Al-MBT-CALC650	3.05	7.73	3.06	7.81	23.42
Mg(3)Al-MBT-SH/CALC650	3.04	7.66	3.05	7.71	23.13
Mg(3)Al-MBT-SH/CALC150	3.04	7.51	3.04	7.60	22.80
Mg(3)Al-PhPh-SH/CALC150	3.04	7.49	3.04	7.59	22.77
Mg(3)Al-TB-SH/CALC150	3.05	7.52	3.05	7.63	22.90

*Unit cell parameters of Zn(2)Al-PhPh-AN and Zn(2)Al-TB-AN from Figure 21 are not presented, because they are not used in the further studies

4.1.2 Characterization of LDH by FTIR

FTIR studies are also useful for structural characterization of the prepared LDH materials, especially for confirmation of corrosion inhibitors or sensing species adsorption onto the LDH surface, when the latter cannot be detected by XRD analysis. Besides, FTIR spectroscopy has been widely applied

for studies of vibration bands change after intercalation process or thermal treatment and estimation of catalytic activity of LDH (Forano, et al. 2006).

Figure 23 depicts the FTIR spectra of different LDH structures which were used as precursors for subsequent immobilization of active species. The assignment of different vibration modes is presented in detail in **Table 10**. The band occurring at 4000-3000 cm^{-1} is assigned to the O-H stretching mode of layered hydroxides and interlayer water molecules, while the band at 1650-1620 cm^{-1} is related to the bending mode of water molecules. Bands occurring at wavenumbers lower than 600 cm^{-1} are ascribed to Metal-O and Metal-OH modes (Rives and Kannan 2000); (Ghotbi, et al. 2009); (Poznyak, et al. 2009). Furthermore, hydrogen bonding interactions established between water molecules, metal hydroxide sheets and interlayer anions can shift the position of vibration modes occurring at 1650-1620 cm^{-1} towards lower values as 1570 cm^{-1}, contributing also to the broadening of the bands. However, Tanaka and co-authors propose that a wide band centred at 1570 cm^{-1} can be specifically ascribed with Metal-OH deformation (Tanaka, et al. 2012).

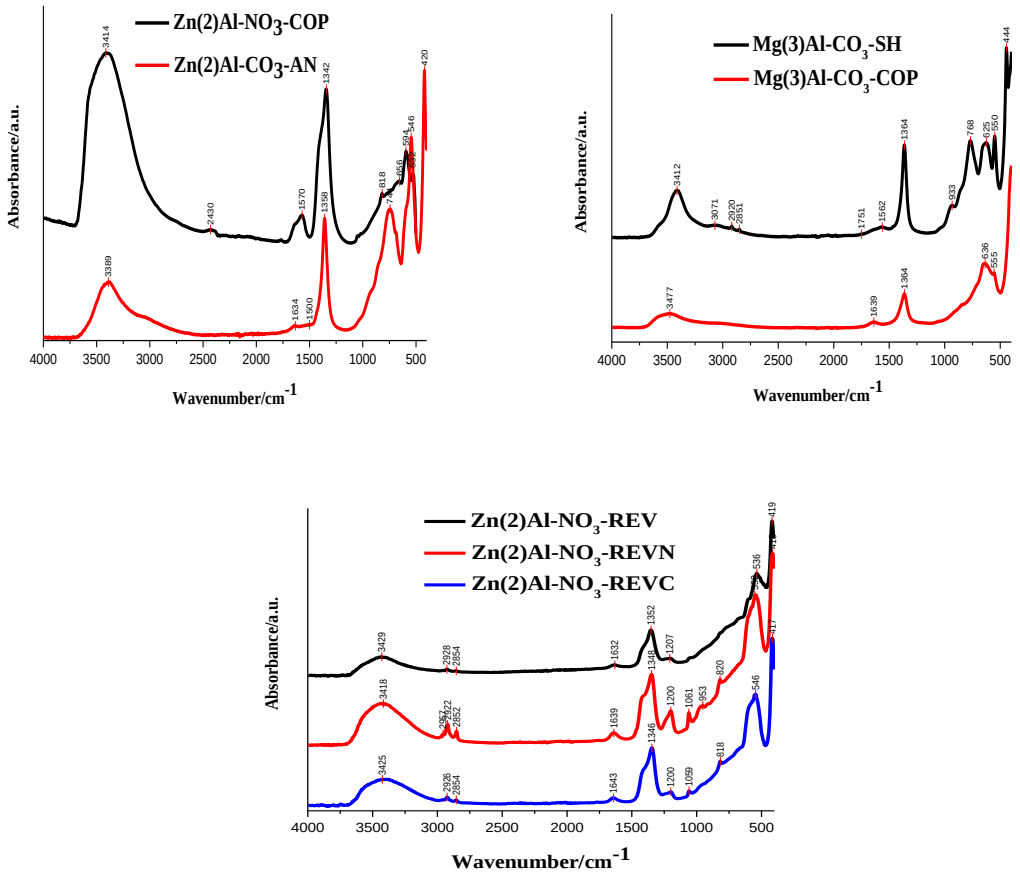

Figure 23. FTIR spectra of LDH prepared by coprecipitation and anion-exchange (**Zn(2)Al-NO_3-COP**, **Zn(2)Al-CO_3-AN**, **Mg(3)Al-CO_3-COP**), coprecipitation reaction in reverse microemulsion (**Zn(2)Al-NO_3-**

REV, **Zn(2)Al-NO_3-REVN** and **Zn(2)Al-NO_3-REVC**) and commercial synthetic hydrotalcite (**Mg(3)Al-CO_3-SH**)

For **Zn(2)Al-NO_3-COP** an intense band occurring at 1342 cm^{-1}, together with bands at 818 and 656 cm^{-1} can be attributed to the presence of nitrates in LDH. Hesse *et al.* proposed that nitrate vibrations occur in two ranges of the spectrum: 1410-1340 cm^{-1} and 860-800 cm^{-1} (Hesse, Meier and Zeeh 1997). On the other hand, Poznyak and co-authors verified the presence of bands ascribed to nitrate anions at comparatively lower wavenumbers, in the range between 1380-1350 cm^{-1} (Poznyak, et al. 2009). Recently, Mahjoubi *et al.* investigated the intercalation of numerous anions into the LDH structure, including nitrates. The authors indicated that as unconstrained NO_3^- has a planar trigonal arrangement of *D3h* symmetry, different vibrational modes can be associated with it: out of plane N-O stretching at 1380 cm^{-1}, out-of-plane deformation at 839 cm^{-1} and antisymmetric deformation mode 670 cm^{-1} (Mahjoubi, et al. 2017).

Worth of mention is that a wide band with the shoulder occurring at 2430 cm^{-1}, along with an additional band at 1767 cm^{-1} can be attributed to the presence of carbonates (Hesse, Meier and Zeeh 1997). Besides, a strong band at 1057 cm^{-1} is attributed to the C-O group of carbonates (Hesse, Meier and Zeeh 1997). As a result, these data confirm the partial intercalation of carbonates during preparation of pristine LDH materials intercalated with nitrates and/or its adsorption on the LDH surface in contact with air. However, absence of a shoulder in 003 peak in the diffractogram of **Zn(2)Al-NO_3-COP** LDH shows, most likely, that carbonates are just adsorbed onto the external surface of LDH particles.

Zn(2)Al-CO_3-AN, **Mg(3)Al-CO_3-SH** and **Mg(3)Al-CO_3-COP** samples reveal similar FTIR spectra with the main vibrations relating to LDH structure discussed before. However, the main intense band associated to carbonate anions is shifted to higher wavenumbers compared to nitrate, namely in the range 1365-1375 cm^{-1} (Rives and Kannan 2000), (Tanaka, et al. 2012).

The LDH structures prepared by coprecipitation reaction in reverse microemulsion show additional bands that can be associated with the presence of solvent, triblock copolymer and surfactant impurities from the synthesis, which is in agreement with XRD diffractograms shown in the previous section. More specifically, bands associated with the isooctane can be found for in **Zn(2)Al-NO_3-REV**, **Zn(2)Al-NO_3-REVN** and **Zn(2)Al-NO_3-REVC** at 3000 cm^{-1} (2854-2928 cm^{-1}), and 1300-680 cm^{-1} (1200 cm^{-1}). Concerning the additional vibrations in the range of 1097-1010 cm^{-1} in **Zn(2)Al-NO_3-REVN** and **Zn(2)Al-NO_3-REVC**, these can be due to the adsorption of triblock copolymer onto LDH surface, together with sodium dodecyl sulphate (SDS) (bands and vibrations

associated with C-H and S=O groups), that was used for preparation of the reverse microemulsion (it is difficult to separate the vibrations of these compounds individually due to their overlapping in this region).

Table 10. Main FTIR peaks observed in pristine LDH spectra

Sample	FTIR main bands			
Zn(2)Al-NO_3-COP; Zn(2)Al-NO_3-REV; Zn(2)Al-NO_3-REVN; Zn(2)Al-NO_3-REVC	Between 4000 cm^{-1} and 3000 cm^{-1} υ(OH)	1643 cm^{-1} δ_{HOH} mode of interlayer water	1342 cm^{-1} υ_2 mode of the NO_3^-	Lower 600 cm^{-1} Metal-O/Metal-OH modes
Mg(3)Al-CO_3-COP; Mg(3)Al-CO_3-SH; Zn(2)Al-CO_3-AN;	Between 4000 cm^{-1} and 3000 cm^{-1} υ(OH)	1643 cm^{-1} δ_{HOH} mode of interlayer water	1365 cm^{-1} υ_2 mode of the CO_3^{2-}	Lower 600 cm^{-1} Metal-O/Metal-OH modes

Figure 24 and **Figure 25,** as well as **Table 11** and **Table 12,** present the FTIR spectra and main vibration modes associated with Zn(2)Al LDH materials intercalated with gluconate and MBT.

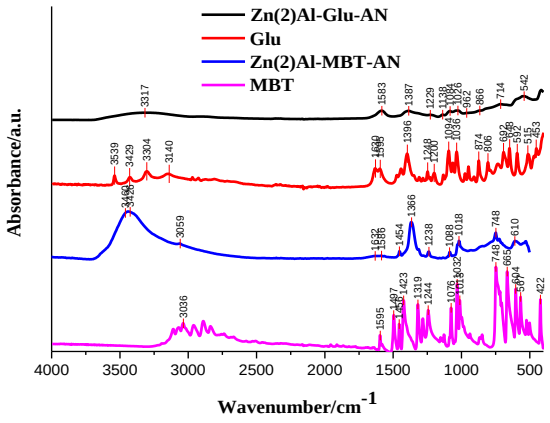

Figure 24. FTIR spectra of LDH with gluconate (**Zn(2)Al-Glu-AN**) and MBT (**Zn(2)Al-MBT-AN**) prepared by anion-exchange and spectra of the corresponding corrosion inhibitors in free form

The FTIR spectrum of **Zn(2)Al-Glu-AN** supports the exchange of nitrate by gluconate, as previously found in section 4.1.1. The C-H stretching mode occurs in the range of 2968-2810 cm^{-1} along with C-O-H vibration mode in the same region 2900-2700 cm^{-1} (Ibrahim, Nada and Kamal 2005); (Ghotbi, et al. 2009). Additionally, bands occurring at 1402 cm^{-1} and at 1634 cm^{-1} are associated with the symmetric and asymmetric stretching vibration of COO^-, respectively (Ghotbi, et al. 2009). Ibrahim *et al.*, noticed slightly different ranges for these vibrations, namely 1557-1559 cm^{-1} for the asymmetric stretching vibration of COO^- and 1412-1410 cm^{-1} for the symmetric stretching vibration of COO^-. The transformation of carboxyl group into carboxylate causes a shift in the carbonyl stretching vibration from 1753 cm^{-1} to 1579 cm^{-1} (Ibrahim, Nada and Kamal 2005). There is a redshift for ν_{sym}(C=O) band, from 1398 cm^{-1} to 1387 cm^{-1}, and ν_{asym}(C=O) band, from 1632 cm^{-1} to 1583 cm^{-1} that can indicate interactions between the carbonyl group of the gluconate and the LDH structure that leads to a decrease in the C=O strength (Ibrahim, Nada and Kamal 2005). This interpretation points toward the intercalation of the gluconate in the LDH galleries.

The existence of bands in the LDH with gluconate spectrum at 1026 cm^{-1} and 1084 cm^{-1} ascribed to the ν(C-O) of the primary and secondary alcohol groups, supports the success of corrosion inhibitor intercalation. Both LDH with gluconate and individual gluconate spectra contains C-H out of plane deformations (865-822 cm^{-1}), whereas C-O/C-O-H stretching out of plane deformations and CH_2 rocking vibrations are attributed to bands at 719 cm^{-1} (Hesse, Meier and Zeeh 1997); (Ibrahim, Nada and Kamal 2005); (Ghotbi, et al. 2009).

Table 11. Main FTIR peaks observed in LDH with gluconate and gluconate in free form

Sample	**FTIR main bands**				
Zn(2)Al-Glu-AN	Between 4000 cm^{-1} and 3000 cm^{-1} υ(OH)	1583 cm^{-1} δ_{HOH} mode of interlayer water/ υ asym (C=O)	1387 cm^{-1} υ_2 mode of the NO_3^-/ υ sym (C=O)	1085 cm^{-1} C-O stretching mode	Lower 600 cm^{-1} Metal-O/Metal-OH modes
Sodium D-gluconate	-	1612 cm^{-1} υ asym (C=O)	1396 cm^{-1} υ sym (C=O)	1093 cm^{-1} C-O stretching mode	-

For LDH materials prepared with MBT (**Figure 24** and **Figure 25**), the vibration modes associated with structural groups of MBT can be found in the following regions: related with rings - 3120-3000 cm^{-1} (C-H stretching vibrations of the phenyl ring), six-ring stretching vibrations (near 1600, 1580, 1490 and 1440 cm^{-1}), the five-ring stretching vibration at 1315 ± 65 cm^{-1} and the C–H out of plane deformation in the region between 1000 and 700 cm^{-1}. C–C stretching modes of benzene are observed in the range of 1578-1220 cm^{-1}. The band at 2600–2550 cm^{-1} is attributed to S–H stretching vibration and C–S stretching vibrations are visible in the region 716-609 cm^{-1}. A band associated with primary aromatic amine with nitrogen directly on the ring is observed at 1319 cm^{-1}. The symmetric and asymmetric C–O–C stretching vibrations produce strong bands at 1076 cm^{-1} and 1261 cm^{-1} respectively (Hesse, Meier and Zeeh 1997); (Li, Tang and Zhang 2009). All these vibrations are visible for **Zn(2)Al-MBT-AN**, **Zn(2)Al-MBT-REV/AN**, **Zn(2)Al-MBT-REVN/AN** and **Zn(2)Al-MBT-REVC/AN** and **Mg(3)Al-MBT-SH/CALC150**. Besides, the FTIR spectra for all the LDH structures prepared by coprecipitation reaction in reverse microemulsion also show bands at 820 cm^{-1}, corresponding to out-of-plane deformation of N-O group, confirming the presence of nitrate anions in the interlayer galleries of LDH samples (along with **Table 9,** Le-Bail refinement data). Furthermore, vibrations attributed previously to copolymer structural groups remain present after the anion-exchange step, being overlapped with vibration modes of MBT in the range between 1400-900 cm^{-1}.

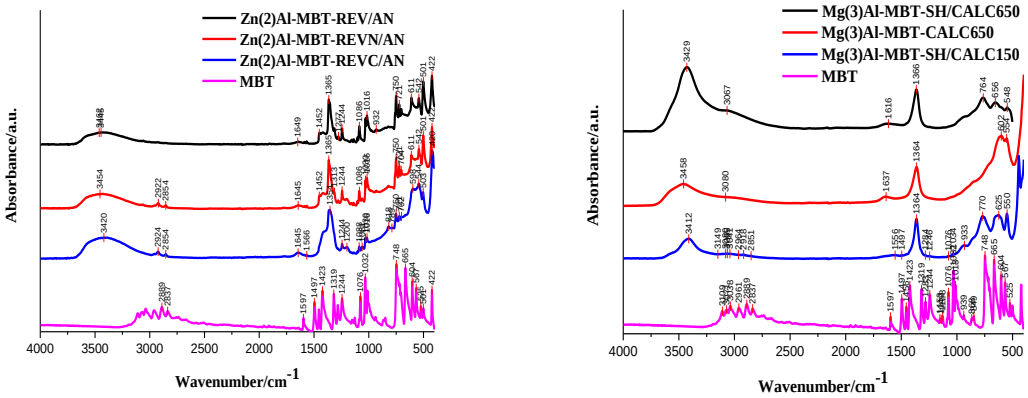

Figure 25. FTIR spectra of LDH with MBT prepared by coprecipitation reaction in reverse microemulsion (**Zn(2)Al-MBT-REV/AN, Zn(2)Al-MBT-REVN/AN, Zn(2)Al-MBT-REVC/AN**), calcination-rehydration method (**Mg(3)Al-MBT-CALC650, Mg(3)Al-MBT-SH/CALC650, Mg(3)Al-MBT-SH/CALC150**) and MBT in free form

In addition, the FTIR spectra of **Mg(3)Al-MBT-SH/CALC650** and **Mg(3)Al-MBT-CALC650** do not show presence of structural groups vibrations that can be ascribed to MBT, which implies that

neither intercalation nor adsorption of MBT in the external surface of LDH has occurred when calcination occurs at high temperatures (650 ºC), which is in agreement with XRD data presented in the previous section (4.1.1), or the amount of MBT onto external surface was not sufficient for detection by FTIR. However, appearance of MBT structural groups vibrations in the spectra of **Mg(3)Al-MBT-SH/CALC150** agrees with obtained XRD diffractogram (**Figure 20**), which indicates MBT adsorption onto external surface of LDH particles after calcination of pristine LDH at 150 ^{0}C.

Table 12. Main FTIR peaks observed in LDH with MBT and MBT in free form

Sample	FTIR main bands				
Zn(2)Al-MBT-AN; Zn(2)Al-MBT-REV/AN; Zn(2)Al-MBT-REVN/AN; Zn(2)Al-MBT-REVC/AN; Mg(3)Al-MBT-SH/CALC650; Mg(3)Al-MBT-SH/CALC150; Mg(3)Al-MBT-CALC650	Between 4000 cm^{-1} and 3000 cm^{-1} ν(OH)/ ν(CH)	1643 cm^{-1} δ_{HOH} mode of interlayer water	1354-1365/1018 cm^{-1} υ_2 mode of the NO_3/CO_3^{2-}/ ring breathing and trigonal bending modes	1084-1076 cm^{-1} sym C–O–C stretching vibration	Lower 600 cm^{-1} Metal-O/Metal-OH modes
MBT	Between 3120 cm^{-1} and 3000 cm^{-1} ν (CH)	2600-2550 cm^{-1} S-H stretching vibration	1395/1011 cm^{-1} ring breathing and trigonal bending modes	1076 cm^{-1} sym C–O–C stretching vibration	609-716 cm^{-1} C-S stretching vibration

In the case of **Zn(2)Al-FSS-AN** (**Figure 26)**, although the XRD presented in the previous section revealed the presence of single-phase LDH, it seems that inorganic anions are presented as well. Bands associated with vibration modes of fluorescein functional groups can be found in three main ranges: 1600-1350 cm^{-1} (aromatic skeletal C-C stretching), 1300-1100 cm^{-1} (C-O stretching) and

900-650 cm^{-1} (aromatic C-H bending vibrations) (Markuszewski and Diehl 1980). Vibrations associated with aromatic rings occur at 1578 cm^{-1} and overlap with vibration modes of interlayer water previously described. Additionally, there is a split of bands occurring at 1360 and 1329 cm^{-1}, which can be an indication of presence of carbonates and incomplete removal of nitrates during the anion-exchange process. The presence of carbonates is further supported by the presence of one band at 1460 cm^{-1}, which was been previously assigned to carbonates (Hesse, Meier and Zeeh 1997).

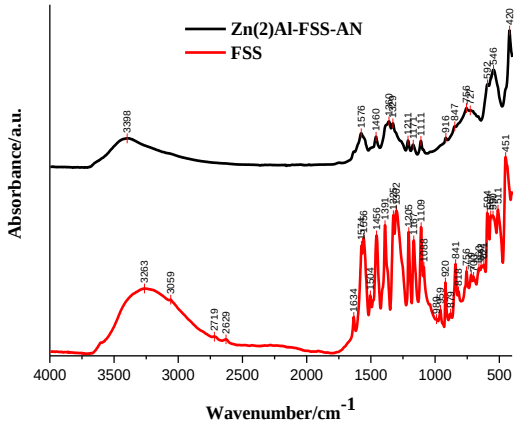

Figure 26. FTIR spectra of **Zn(2)Al-FSS-AN** and FSS in free form

In the case of **Zn(2)Al-PhPh-CALC150** and **Mg(3)Al-PhPh-SH/CALC150** (**Figure 27**), the vibration modes associated with PhPh were detected. In particular, bands associated with vibrations of functional groups of PhPh found around 3000 cm^{-1}, and in the regions between 1500-1000 and 1000-500 cm^{-1} (**Table 13**) confirm the adsorption of PhPh. In the case of TB only a few vibrations associated with this molecule can be detected in the LDH materials. Probably, it is explained by the low content of the dye in the LDH. Besides, in the case of **Zn(2)Al-TB-CALC150** the presence of vibrations at 1346 and 818 cm^{-1} points to the presence of nitrate into the interlayer galleries, which agrees with XRD analysis presented earlier.

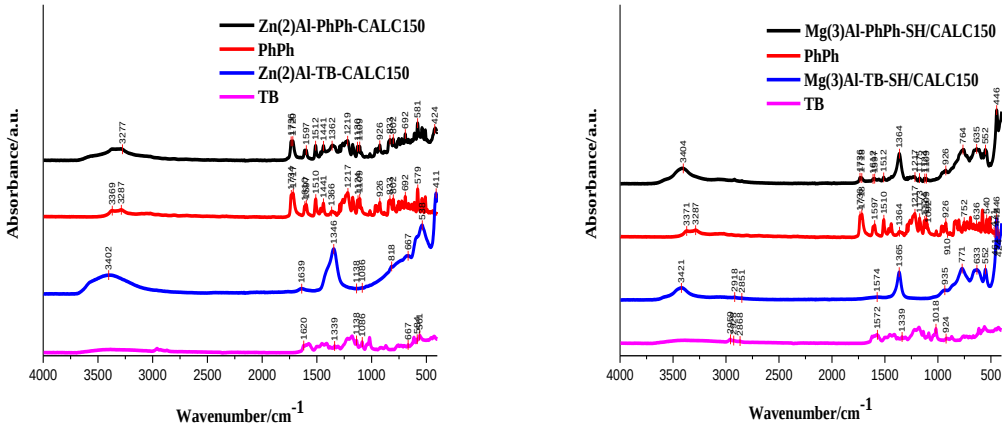

Figure 27. FTIR spectra of LDH with phenolphthalein (**Zn(2)Al-PhPh-CALC150, Mg(3)Al-PhPh-SH/CALC150**) and thymol blue (**Zn(2)Al-TB-CALC150, Mg(3)Al-TB-SH/CALC150**) prepared by calcination-rehydration and respective dyes in free form

Table 13. Main FTIR peaks observed in LDH with dyes (pH indicators) and dyes in free form

Sample	**FTIR main bands**				
Zn(2)Al-FSS-AN; Zn(2)Al-PhPh-CALC150; Zn(2)Al-TB-CALC150; Mg(3)Al-PhPh-SH/CALC150; Mg(3)Al-TB-SH/CALC150;	Between 4000 cm^{-1} and 3000 cm^{-1} υ(OH)	1576 cm^{-1} δ_{HOH} mode of interlayer water/ aromatic skeletal C-C stretching vibration	1360-1346/1329 cm^{-1} υ_2 mode of the NO_3/CO_3^{2-}/ aromatic skeletal C-C stretching vibration	1211-1111 cm^{-1} C–O stretching vibration	Lower 600 cm^{-1} Metal-O/Metal-OH modes/847-727 cm^{-1} aromatic C-H bending vibrations
FSS, PhPh, TB	-	1610-1590 cm^{-1} aromatic skeletal C-C stretching vibration	1460-1370 cm^{-1} aromatic skeletal C-C stretching vibration	1315-1112 cm^{-1} C–O stretching vibration	871-694 cm^{-1} aromatic C-H bending vibrations

Table 14 summarizes the presence of active species in LDH structure based on XRD and FTIR results shown and discussed before. In cases where neither the XRD or FTIR unambiguously revealed the presence of the guest anions (active species), they were detected after complete dissolution of LDH and detection using UV-Vis spectrophotometry.

Table 14. Main structural features of LDH materials with active species

LDH	Intercalation of active species (XRD)	Partial intercalation/adsorption of active species (XRD/FTIR)	Adsorption of active species (UV-Vis)
Zn(2)Al-Glu-AN	+		
Zn(2)Al-FSS-AN	+		
Zn(2)Al-PhPh-CALC150			+
Zn(2)Al-TB-CALC150			+
Zn(2)Al-MBT-AN	+		
Zn(2)Al-MBT-REV/AN		+	
Zn(2)Al-MBT-REVN/AN		+	
Zn(2)Al-MBT-REVC/AN		+	
Mg(3)Al-MBT-SH/CALC650			+
Mg(3)Al-MBT-SH/CALC150		+	
Mg(3)Al-MBT-CALC650			+
Mg(3)Al-PhPh-SH/CALC150			+
Mg(3)Al-TB-SH/CALC150			+

4.1.3 Thermal analysis of LDH by TGA

The evaluation of thermal behaviour of the obtained LDH materials has two main objectives: (i) estimate whether intercalated and immobilized species exhibit an increase in the thermal stability and (ii) for practical applications, to infer if processes associated with coating application and curing processes, practiced at temperatures above room temperature can actually have a detrimental impact in the thermal degradation of LDH structure, active species deactivation or both. In this work thermal stability of prepared LDH materials was estimated by TG analysis. **Figure 28** depicts the thermogram of **Zn(2)Al-CO_3-AN**.

The main regions of weight loss identified in the TG are (**Figure 28**): in the interval between 200-250 ^{0}C there is loss of interlayer water; up to 500 ^{0}C the decomposition of hydroxide layers and respective anions occurs; for temperatures higher than 500 ºC the formation of metal oxides and

spinel structures happens depending on LDH composition. This behaviour is in agreement with literature data (Stanimirova, et al. 2004); (Forano, et al. 2006). More specifically, upon heating of **Zn(2)Al-CO_3-AN**, the loss of 0.5 % of physically adsorbed water starts at 88 ^{0}C followed by loss of 9.5% of interlayer water up to 211 ^{0}C. The largest weight loss (17%) is observed in the interval of temperatures between 211-346 ^{0}C, where interlayer carbonate decomposition and dehydroxylation are observed. Further rise in temperature up to 529 ^{0}C leads to an additional loss of 2 %, which completes the thermal decomposition of LDH. The profiles obtained are in agreement with other works reported in the literature (Yang, et al. 2002), (Mahjoubi, et al. 2017).

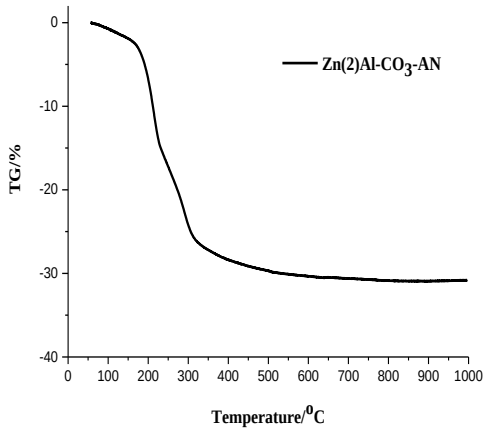

Figure 28. Thermogram of **Zn(2)Al-CO_3-AN** in air

The TG curves obtained for the remaining LDH compositions are depicted in annex (Figures **A1-A3**), and the main results are summarized in **Table 15**. In general, the increase in temperature up to 300 ^{0}C is accompanied by removal of interlayer water and dehydroxylation leading to weight losses in the range of 4-18 % for most LDH samples. The lowest weight loss obtained in this range corresponds to commercial LDH (synthetic hydrotalcite). Much larger weight losses (around 30 %) are observed for LDH samples with nitrate prepared by coprecipitation reaction in reverse microemulsion, which can be associated with additional degradation of organic compounds applied during synthesis, adsorbed onto LDH particles (Patterson, Kortylewicz and Smith 1984); (Ramimoghadam, Hussein and Taufiq-Yap 2012).

Physically adsorbed water is removed from **Mg(3)Al-CO_3-COP** at 105 ^{0}C (3 % of weight loss) with further interlayer water loss at 240 ^{0}C (11 %). Decomposition of hydroxide layers and carbonate anions occurs at 383 ^{0}C (15 % of weight loss) and 458 ^{0}C (8 % of weight loss). Yang and co-authors

determine 22 % weight loss in the interval 220-400 ^{0}C (decomposition of carbonate and dehydroxylation) (Yang, et al. 2002), that is in a good agreement with obtained data for **Mg(3)Al-CO_3-COP** (22 % weight loss for mentioned temperature range). 3 % weight loss is observed in the interval 400-600 ^{0}C (CO_2 removal). During further increase of heating temperature formation of magnesium oxide is observed until 800 ^{0}C with further complete release of aluminium cations and final formation of pure $MgAl_2O_4$ spinel and MgO at temperatures between 900-1000 ^{0}C (Forano, et al. 2006), that corresponds to final 4 % weight loss at 982 ^{0}C. Thus, complete decomposition of **Mg(3)Al-CO_3-COP** is observed at temperature higher 900 ^{0}C, confirming, better thermal stability of MgAl compare to ZnAl LDH (Forano, et al. 2006).

The calcination of **Mg(3)Al-CO_3-SH** up to 180 ^{0}C is accompanied by a gain in weight due to oxidation of organic compounds coating the commercial LDH. The removal of interlayer water detected at 260 ^{0}C corresponds to a 5 % weight loss. Decomposition of hydroxide layers and carbonate anions occurs at 377 ^{0}C (12 % of weight loss) and 458 ^{0}C (12 % of weight loss), respectively. In the interval 400-600 ^{0}C, the weight loss can be also attributed to CO_2 and organic compounds removal (Beyler and Hirschler 2002). Finally, a 2 % weight loss is detected for temperatures higher than 900 ^{0}C.

The thermal degradation behaviour of individual active species was also determined. The thermogram of **MBT** presented in the annex shows the largest weight loss occurring between 257-357 ^{0}C (71 %), with the further weight losses (15 %) occurring for higher temperatures. These results are consistent with data in the literature. Gradwell and McGill determined that decomposition of sulfenamides is observed in the range of 210-220 ^{0}C, with formation of more stable final product-MBT, that starts to degrade at higher temperatures (Gradwell and McGill 1994). Furthermore, according to data of Danish environmental protection agency MBT decomposes at 260 ^{0}C (Nielsen, Østergaard and Larsen 2014).

The thermogram obtained for **FSS** shows several steps of weight loss: a 7 % weight loss is observed when the temperature raises up to 100 ^{0}C, a 10 % weight loss is detected in the temperature range of 100-150 ^{0}C, followed by 14 % up to 520 ^{0}C and further 20 % up to 982 ^{0}C. Studies presented in the literature support these data, in the sense that the majority of weight loss associated with FSS occurs in two main steps: up to 100/150 ^{0}C and 150-500 ^{0}C/600 ºC (Shawky, et al. 2016); (Dere 2019).

In the case of **PhPh** decomposition starts at 260 ^{0}C (1 % weight loss), followed by 22 % weight loss up to 370 ^{0}C, 24 % weight loss upon heating up to 470 ^{0}C and further 12 % when temperature is raised up to 900 ^{0}C. Maia *et al*. studied the thermal degradation of silica nanocapsules with PhPh and observed that their significant thermal degradation starts at 300 ^{0}C with further mass reduction between 350-500 ^{0}C, which can correspond to selective degradation of weak C-N and C-O bonds

with formation of free radicals, accompanied by the reactions of recombination, rearrangement and final degradation at higher temperatures (530-800 ^{0}C) (Ghetiya, et al. 2008); (Maia, et al. 2013).

The thermal decomposition behaviour of **Glu** differs from other active species: there is a weight loss up to 211 ^{0}C due to molecule decomposition (in agreement with sodium gluconate safety data sheet) followed by increase of mass which may occur due to oxidation upon further heating, leading to the formation of intermediate compounds with aldehydes or carboxylic groups.

The analysis of LDH loaded with different active species is not straightforward. This is mainly due to the fact that the decomposition processes associated with LDH can be overlapped with thermal degradation profiles associated with the guest species, as described above, which also impedes the estimation of loading content of active compounds by TG.

In the cases where intercalation has occurred, namely **Zn(2)Al-Glu-AN**, **Zn(2)Al-MBT-AN** and **Zn(2)Al-FSS-AN**, the largest weight loss occurs up to 300 ºC consistent with both degradation of LDH hydroxides and thermal degradation of the intercalated compound. Moreover, larger weight losses are found above these temperatures in LDH with organic guest anions, when compared to the ZnAl precursors. This is consistent with thermal degradation processes described above for the free forms of the guest compounds.

Concerning MgAl LDH materials with MBT immobilized by calcination-rehydration, it can be seen that the TG curve of **Mg(3)Al-MBT-CALC650** is very similar to the TG profile obtained for the corresponding pristine LDH **Mg(3)Al-CO_3-COP**, which can be explained by the presence of a very small amount of MBT, in agreement with the main findings from FTIR and XRD. The adsorption of MBT in synthetic hydrotalcite lead to different results. For the sample **Mg(3)Al-MBT-SH/CALC650**, the degradation profile is consistent with existence of MBT in the sample.

The thermal decomposition of **Mg(3)Al-MBT-SH/CALC150** differs from previous LDH-MBT structures, exhibiting a small weight loss ascribed to physically adsorbed water (0.05 %) and just 1 % of interlayer water loss (170 ^{0}C), followed by 8 % weight loss (250 ^{0}C) due to dehydroxylation of cationic sheets. Such profile is consistent with the hydrophobic nature of synthetic hydrotalcite, which is coated with fatty acids and which was not fully removed upon thermal treatment at 150 ºC. The weight loss observed in the interval between 250-270 ^{0}C can be attributed to the decomposition of the fatty acids. Further increase in temperature leads to additional weight loss which can be due to thermal-related processes associated with MBT as well.

In compositions where the guest species already shows higher thermal stability, such as PhPh, the largest weight losses were detected for temperatures above 500 ºC. This has been found for **Zn(2)Al-PhPh-CALC150** and **Mg(3)Al-PhPh-SH/CALC150**.

Table 15. Results of thermal degradation of studied LDH materials

LDH	Temperature interval 1	Temperature interval 2	Temperature interval 3
Zn(2)Al-NO_3-COP	60-265 ^{0}C: 18 %	265-594 ^{0}C: 18 %	-
Zn(2)Al-Glu-AN	60-256 ^{0}C: 12 %	256-593 ^{0}C: 27 %	593-913 ^{0}C: 6 %
Zn(2)Al-FSS-AN	60-260 ^{0}C: 16 %	260-700 ^{0}C: 16 %	700-985 ^{0}C: 29 %
Zn(2)Al-MBT-AN	60-252 ^{0}C: 13 %	252-614 ^{0}C: 27 %	614-913 ^{0}C: 5 %
Zn(2)Al-PhPh-CALC150	60-264 ^{0}C: 12 %	264-700 ^{0}C: 29 %	700-980 ^{0}C: 23 %
Zn(2)Al-CO_3-AN	60-211 ^{0}C: 10 %	211-529 ^{0}C: 20 %	-
Zn(2)Al-NO_3-REV	60-279 ^{0}C: 29 %	279-557 ^{0}C: 11 %	557-900 ^{0}C: 2 %
Zn(2)Al-NO_3-REVN	60-274 ^{0}C: 30 %	274-602 ^{0}C: 12 %	602-900 ^{0}C: 1 %
Zn(2)Al-NO_3-REVC	60-271 ^{0}C: 30 %	271-602 ^{0}C: 12 %	602-900 ^{0}C: 1 %
Zn(2)Al-MBT-REV/AN	60-274 ^{0}C: 9 %	274-700 ^{0}C: 26 %	700-992 ^{0}C: 10 %
Zn(2)Al-MBT-REVN/AN	60-254 ^{0}C: 12 %	254-700 ^{0}C: 29 %	700-938 ^{0}C: 6 %
Zn(2)Al-MBT-REVC/AN	60-253 ^{0}C: 16 %	253-700 ^{0}C: 24 %	700-994 ^{0}C: 2 %
Mg(3)Al-CO_3-COP	60-240 ^{0}C: 14 %	240-700 ^{0}C: 27 %	700-982 ^{0}C: 3 %
Mg(3)Al-CO_3-SH	60-260 ^{0}C: 4 %	260-600 ^{0}C: 33 %	600-982 ^{0}C: 2 %
Mg(3)Al-MBT-CALC650	60-250 ^{0}C: 14 %	250-670 ^{0}C: 25 %	670-940 ^{0}C: 1 %
Mg(3)Al-MBT-SH/CALC650	60-244 ^{0}C: 12 %	244-700 ^{0}C: 26 %	700-995 ^{0}C: 3 %
Mg(3)Al-MBT-SH/CALC150	60-250 ^{0}C: 9 %	250-700 ^{0}C: 29 %	700-995 ^{0}C: 1 %
Mg(3)Al-PhPh-SH/CALC150	60-270 ^{0}C: 4 %	270-700 ^{0}C: 41 %	700-980 ^{0}C: 6 %

Preliminary conclusions

1. XRD and FTIR results demonstrated the successful preparation of LDH materials by different routes, namely by coprecipitation, coprecipitation reaction in reverse microemulsion, and intercalation/immobilization of active species by anion-exchange and/or calcination-rehydration route. Intercalation of fluorescein, gluconate and 2-mercaptobenzothiazole into ZnAl LDH compositions was confirmed by both structural characterization techniques (XRD and FTIR).
2. Intercalation of PhPh and TB by anion-exchange procedure was not successful. These sensing species were immobilized by calcination-rehydration route. Besides, presence of MBT into the following structures as **Mg(3)Al-MBT-CALC650**, **Mg(3)Al-MBT-SH/CALC650** and TB in **Zn(2)Al-TB-CALC150** and **Mg(3)Al-TB-SH/CALC150** was not evident by results of XRD and FTIR measurements and it was confirmed by dissolution of LDH materials and measurement of MBT and TB absorbance by UV-Vis spectrophotometry (or additionally by change of particles color in the case of TB).

3. Thermal stability of LDH materials depends on cations type present in the metal hydroxide sheets. Namely, MgAl LDHs decompose at higher temperatures compared to ZnAl LDHs.
4. Intercalation/adsorption of corrosion inhibitors and sensing species in LDH materials does not increase their thermal stability, without significant difference if sensing species are the ones intercalated or only adsorbed in the external surface.

4.2 Morphological, porous characterization and colloidal properties of prepared LDH

In the previous section structural and thermal characterization of LDH samples prepared by different synthetic routes was presented. One of the most relevant features of LDH materials for functional coating applications is its anion-exchange ability. Considering that ion-exchange reactions can be function of different factors, from chemical composition to porosity, surface area and colloidal stability in dispersing media (SenGupta 2017), this section is devoted to the evaluation of morphology, porous distribution and agglomeration of prepared LDH particles in various media.

4.2.1 Analysis of morphology of LDH by SEM

Figure 29 depicts SEM images of different pristine LDH materials. All the LDH prepared exhibit a plate-like morphology with tendency for agglomeration (Forano, et al. 2006); (Tedim, et al. 2010), in spite of LDH materials prepared in the lab being more irregular. Contrastingly, the commercial sample (**Mg(3)Al-CO_3-SH**) shows a more regular shape and lower dispersion in particle size. In addition, it can be observed that the ZnAl LDH samples exhibit larger particle size than its MgAl counterparts. Also, it appears that the aspect ratio of ZnAl LDH plates is higher than both **Mg(3)Al-CO_3-SH** and **Mg(3)Al-CO_3-COP**.

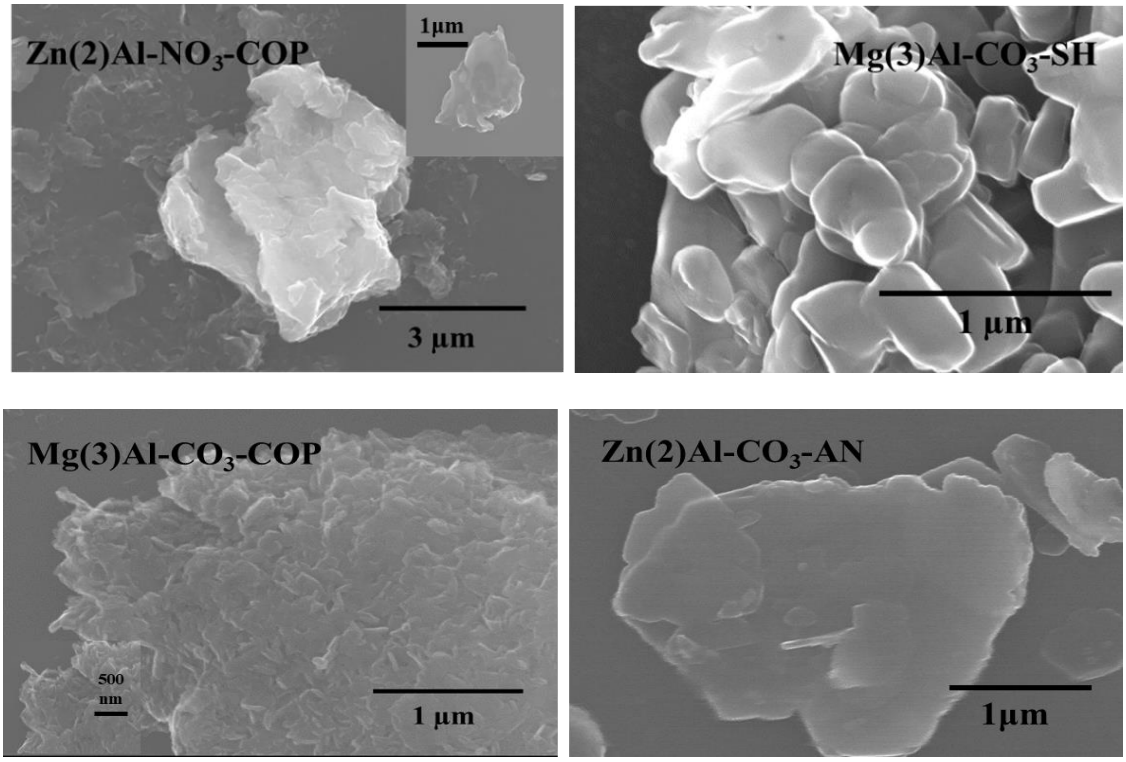

Figure 29. SEM images of different LDH precursors: **Zn(2)Al-NO_3-COP**, **Mg(3)Al-CO_3-SH**, **Mg(3)Al-CO_3-COP** and **Zn(2)Al-CO_3-AN**

Regarding to LDH prepared by coprecipitation reaction in reverse microemulsion (**Figure 30**), **Zn(2)Al-NO_3-REV** reveals some small particles with plate-like morphology, while samples prepared in the presence of triblock copolymer (**Zn(2)Al-NO_3-REVN**, **Zn(2)Al-NO_3-REVC**) show particles with less irregularities, smoother and with concave shape. The morphology of these LDH samples does not match the ones obtained by (Hu and O'Hare 2005). One possible explanation to support these findings is the different chemical composition of LDH in the above referred work (MgAl LDH) and in the present thesis (ZnAl LDH).

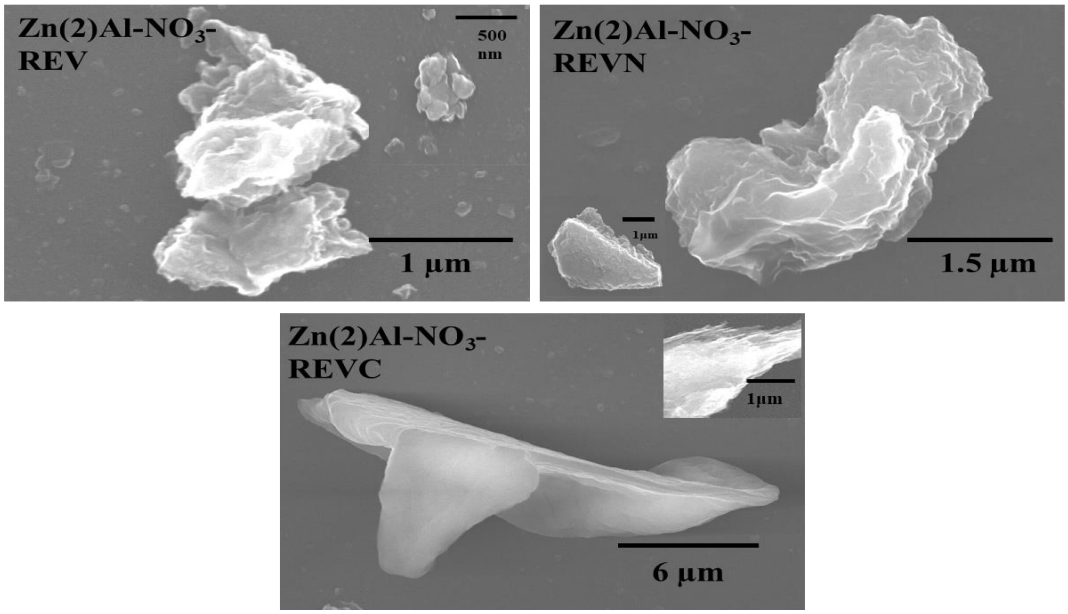

Figure 30. LDH precursors intercalated nitrate prepared by coprecipitation reaction in reverse microemulsion: **Zn(2)Al-NO_3-REV**, **Zn(2)Al-NO_3-REVN** and **Zn(2)Al-NO_3-REVC**

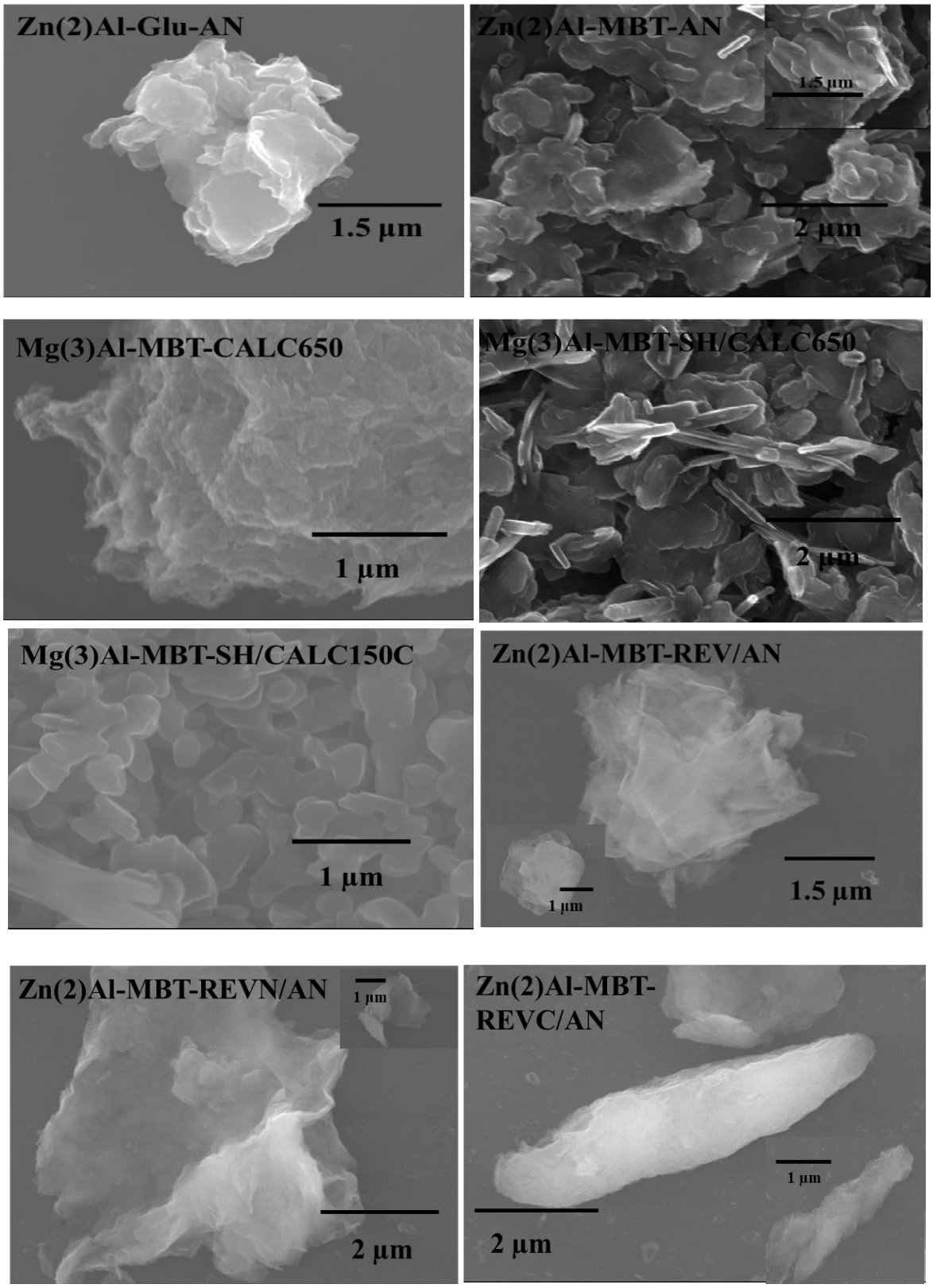

Figure 31. SEM images of LDH containing corrosion inhibitors: **Zn(2)Al-Glu-AN**, **Zn(2)Al-MBT-AN**, **Mg(3)Al-MBT-CALC650**, **Mg(3)Al-MBT-SH/CALC150**, **Mg(3)Al-MBT-SH/CALC650, Zn(2)Al-MBT-REV/AN**, **Zn(2)Al-MBT-REVN/AN** and **Zn(2)Al-MBT-REVC/AN**

In most cases intercalation or adsorption of corrosion inhibitors does not change the morphology of initial particles (**Figure 31**). However, the shape of **Zn(2)Al-MBT-REV/AN**, **Zn(2)Al-MBT-REVN/AN**, seems to differ from the pristine ones. After intercalation of MBT, there is no possibility to distinguish platelets, the shape of the particles is no longer concave and the images of the plates seem more diffuse, which can be related to the particles being less agglomerated. Nonetheless, **Zn(2)Al-MBT-REVC/AN** looks similar to the corresponding nitrate-intercalated LDH, namely smooth, elongated agglomerates.

Figure 32 presents SEM images of LDH samples prepared with sensing species. The intercalation of FSS does not change the platelet-like morphology of pristine particles, along with LDH materials with PhPh and TB anions prepared by calcination rehydration route. However, in the case of **Zn(2)Al-PhPh-CALC150**, smaller regular particles co-exist with the more irregular plates.

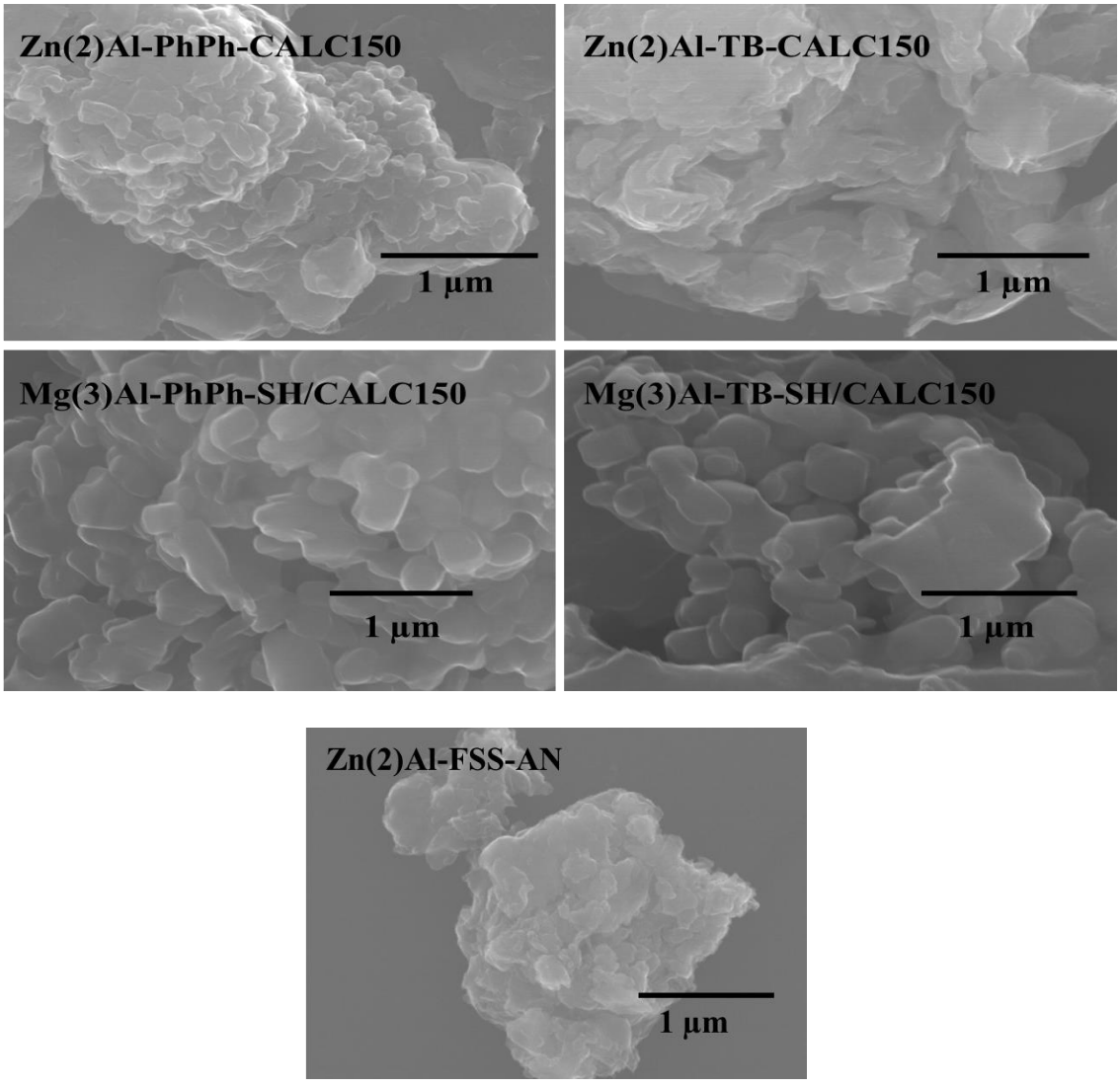

Figure 32. SEM images of LDH containing sensing species: **Zn(2)Al-PhPh-CALC150**, **Zn(2)Al-TB-CALC150**, **Mg(3)Al-PhPh-SH/CALC150**, **Mg(3)Al-TB-SH/CALC150** and **Zn(2)Al-FSS-AN**

4.2.2 Analysis of porosity of LDH

Studies of prepared LDH materials textural properties are shown in detail in the present section (**Table 16**).

Table 16. BET surface area, BJH pore diameters and pore volumes of LDH

LDH	BET surface area, m^2g^{-1}	BJH pore diameter of adsorption branch, Å	BJH pore diameter of desorption branch, Å	BJH pore volume of adsorption branch, cm^3g^{-1}	BJH pore volume of desorption branch, cm^3g^{-1}
Zn(2)Al-NO_3-COP	4	64	60	0.004	0.005
Zn(2)Al-CO_3-AN	46	70	71	0.08	0.08
Mg(3)Al-CO_3-SH	8	91	90	0.01	0.01
Mg(3)Al-CO_3-COP	85	177	178	0.4	0.4
Zn(2)Al-NO_3-REV	319	84	86	0.7	0.7
Zn(2)Al-NO_3-REVN	149	70	74	0.3	0.3
Zn(2)Al-NO_3-REVC	107	101	111	0.3	0.3
Zn(2)Al-Glu-AN	18	40	39	0.02	0.02
Mg(3)Al-MBT-CALC650	84	165	167	0.3	0.4
Zn(2)Al-MBT-AN	28	194	195	0.1	0.1
Zn(2)Al-MBT-AN/REV	24	78	80	0.05	0.05
Zn(2)Al-MBT-AN/REVN	76	76	83	0.1	0.2
Zn(2)Al-MBT-AN/REVC	103	89	102	0.2	0.3
Zn(2)Al-FSS-AN	12	100	95	0.03	0.03
Zn(2)Al-PhPh-CALC150	10	61	59	0.02	0.01
Zn(2)Al-TB-CALC150	12	65	66	0.02	0.02
Mg(3)Al-MBT-SH/CALC650	35	187	191	0.1	0.1
Mg(3)Al-MBT-SH/CALC150	12	88	89	0.03	0.03
Mg(3)Al-PhPh-SH/CALC150	12	83	86	0.03	0.03
Mg(3)Al-TB-SH/CALC150	8	80	76	0.02	0.02

The obtained pore diameter values indicate that LDH materials are mesoporous. Moreover, the values of the measured pore volumes and pore diameters of studied LDH samples in present work agree with data published before for the same type of materials (Hussein, et al. 2012); (Hossein, Nejati and Ghorbani 2014).

Figure 33 presents as an example the pore size distribution of **Zn(2)Al-CO_3-AN** determined from the adsorption and desorption branches of the N_2 isotherms. While the adsorption branch is correlated with equilibrium and can be used for calculation of pore size distribution with information about interior (actual) pore size, the pore distribution estimated from desorption branch is an indication about the pore opening/mouth (Vulic, Reitzmann and Lázár 2012). All synthesized LDH samples studied in the present work show similar behaviour and can be classified as mesoporous materials with presence of hysteresis loop.

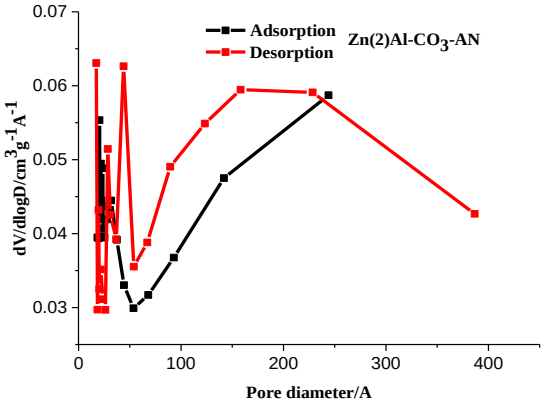

Figure 33. Adsorption and desorption branches of pore size distribution for **Zn(2)Al-CO_3-AN**

Table 17 depicts in a qualitative way the trends verified when intercalation or adsorption of active species was attempted. For all the majority of samples prepared there was an increase in surface area after immobilization of the active species, except for the LDH compositions prepared by coprecipitation reaction in reverse microemulsion. In the latter case, the surface area decreased. Whereas the occlusion of pores due to adsorption of MBT in samples obtained in the reverse microemulsion may explain the decrease in surface area of LDH, the increase in surface area in all the other LDH materials implicitly denotes that they may exhibit a microstructure more accessible after the intercalation step, which is a different behaviour when compared to other mesoporous materials. (Pasqua 2011).

Table 17. Qualitative assessment of textural properties changes after intercalation and/or adsorption of active species into LDH materials, based on data presented previously in **Table 16**.

LDH	BET surface area	BJH pore diameter	BJH pore volume
Zn(2)Al-Glu-AN	↑	↓	↑
Mg(3)Al-MBT-CALC650	=	↓	=
Zn(2)Al-MBT-AN	↑	↑	↑
Zn(2)Al-MBT-REV/AN	↓	↓	↓
Zn(2)Al-MBT-REVN/AN	↓	↑	↓
Zn(2)Al-MBT-REVC/AN	↓	↓	=
Zn(2)Al-FSS-AN	↑	↑	↑
Zn(2)Al-PhPh-CALC150	↑	=	↑
Zn(2)Al-TB-CALC150	↑	=	↑
Mg(3)Al-MBT-SH/CALC650	↑	↑	↑
Mg(3)Al-MBT-SH/CALC150	↑	=	↑
Mg(3)Al-PhPh-SH/CALC150	↑	↓	↑
Mg(3)Al-TB-SH/CALC150	=	↓	↑

As a result, additional studies to determine the textural properties of LDH materials before and after intercalation steps were performed. Besides, supplementary studies were carried out to follow more in detail the effect of calcination-rehydration routes, as well as the effect that simple dispersion in an aqueous media or solvent-based media can have on LDH materials. It is well-known from the literature that depending on the thermal treatment given to LDH, different chemical processes will occur, which will lead to various levels of structural, and consequently, textural changes. For example, calcination at temperature until around 500 ^{0}C is accompanied by degradation of hydroxide layers and intercalating anions, leading to the formation of metal oxides and spinel structures (Stanimirova, et al. 2004); (Forano, et al. 2006). Besides, BET surface area of spinels and mixed metal oxides is higher compared to regular non-calcined LDH (Platero, Arean and Parra 1999).

Table 18, Table 19 and **Table 20** present the textural properties of LDH with different compositions (**Zn(2)Al-NO_3-COP**, **Mg(3)Al-CO_3-COP** and **Mg(3)Al-CO_3-SH**, respectively). In **Table 18**, the textural properties of **Zn(2)Al-NO_3-COP** was determined after exposure to different experimental conditions. The as-obtained LDH materials show a small surface area which increases after dispersion in distilled and deionized water. This result was also observed for **Mg(3)Al-CO_3-COP** (**Table 19)**. This can be explained by the relative solubility of LDH in media with low ionic strength, as shown by Galvão *et al*. (Galvao, et al. 2016). Thus, in distilled/deionized water, it is expected that some small amount of LDH can dissolve, contributing for the exposure of a higher surface.

Table 18. BET surface area and BJH pore diameters and pore volumes of **Zn(2)Al-NO_3-COP** subjected to different treatments

Condition	Surface area, m^2g^{-1}	Pore diameter (ads), Å	Pore diameter (des), Å	Pore volume (ads), cm^3g^{-1}	Pore volume (des), cm^3g^{-1}
As-synthesized	4	64	60	0.004	0.005
Slurry dispersed in CO_2-free DI (20 ºC)	16	147	150	0.06	0.06
Slurry dispersed in DeI water (20 ºC)	123	195	196	0.6	0.6
Calcination (150 ºC)	5	58	55	0.007	0.007
Calcination (650 ºC)	28	51	50	0.04	0.04
Calcination (150 ºC) and rehydration in CO_2-free DI (20 ºC)	4	78	71	0.008	0.008
Calcination (150 ºC) and rehydration in CO_2-free DI (60 ºC)	4	77	81	0.008	0.008
Calcination (150 ºC) and rehydration in DeI (20ºC)	6	72	70	0.01	0.01
Calcination (150 ºC) and rehydration in DeI (60 ºC)	9	65	67	0.01	0.02
Calcination (150 ºC) and rehydration in ethanol (20 ºC)	11	53	52	0.01	0.01
Calcination (150 ºC) and rehydration in ethanol (60 ºC)	7	72	70	0.01	0.01

DI-distilled water; DeI- deionized water

Moreover, the effect of CO_2 in the water has also influence on the surface area of the nitrate-containing samples (**Table 18**). It is well-known in the literature that LDH has a high affinity for carbonates, so in the presence of CO_2 more easily exchangeable species such as NO_3^- will tend to be replaced, both in the interlayer galleries, as well as on the surface. As expected, this effect is less evident for the carbonate-containing samples (**Table 19**).

Another effect that was considered was the application of a thermal treatment at two different temperatures: 150 ºC and 650 ºC. These two conditions were chosen in order to obtain LDH with different structural features: calcination up to 150 ^{0}C leads to the removal of interlayer water and conservation of LDH structure (Forano, et al. 2006), while calcination up to 650 ºC leads to deconstruction of LDH and formation of mixed metal oxides, that exhibit a higher surface area compared to initial LDH (Stanimirova, et al. 2004); (Forano, et al. 2006). Indeed, looking at all the LDH materials studied (**Table 18, Table 19** and **Table 20**), there was an increase in the surface area of LDH as-synthesized after calcination.

Table 19. BET surface area and BJH pore diameters and pore volumes of **Mg(3)Al-CO_3-COP** subjected to different treatments.

Condition	Surface area, m^2g^{-1}	Pore diameter (ads), Å	Pore diameter (des), Å	Pore volume (ads), cm^3g^{-1}	Pore volume (des), cm^3g^{-1}
As-synthesized	85	177	178	0.4	0.4
Slurry dispersed in CO_2-free DI water (20 ºC)	120	191	193	0.6	0.6
Slurry dispersed in DeI water (20 ºC)	113	184	187	0.5	0.5
Calcination (150 ºC)	100	192	196	0.5	0.5
Calcination (650 ºC)	116	171	192	0.5	0.6

DI-distilled water; DeI-deionized water

In addition, the effect of calcination-rehydration was considered for the LDH used for immobilization of the active species in this work, as already mentioned in the previous section: **Zn(2)Al-NO_3-COP** and **Mg(3)Al-CO_3-SH**. The temperatures selected for the calcination step (150 and 650 ºC) above mentioned had as an aim to understand what the optimal thermal treatment to obtain a material was, which, after exposure to a solution with the active species, would be able to intercalate the active species as part of the topotactic reconstruction in solution. After several initial attempts in immobilizing the corrosion inhibitors and pH indicator molecules in samples calcined at 650 ºC, this condition was abandoned, because the XRD of the reconstructed material would only reveal the

presence of LDH with hydroxides intercalated. This can be understood as a follows: when the mixed oxides are added to water to rehydrate, there is an high increase in pH and taking into account that hydroxides are more selective towards LDH than organic molecules the rehydration step was unsuccessful to obtain LDH with immobilized active species. With the lowering of the temperature to 150 ºC the removal of the interlayer water already destabilizes the LDH layers (less hydrogen bonds are available to stabilize the metal hydroxide sheets) and may facilitate the exchange and/or surface immobilization of the organic molecules under study. In the calcination-rehydration step, the influence of two effects were considered: the use of a non-aqueous solvent and temperature to aid on the immobilization of the active species (Forano, et al. 2006).

Table 20. BET surface area and BJH pore diameters and pore volumes of **Mg(3)Al-CO_3-SH** subjected to different treatments

Condition	Surface area, m^2g^{-1}	Pore diameter (ads), Å	Pore diameter (des), Å	Pore volume (ads), cm^3g^{-1}	Pore volume (des), cm^3g^{-1}
As-received	8	91	90	0.01	0.01
Calcination (150 ^{0}C)	10	88	85	0.03	0.03
Calcination (650 ^{0}C)	39	40	41	0.04	0.04
Calcination (150 ^{0}C) and rehydration in CO_2-free DI (20 ºC)	12	100	100	0.03	0.03
Calcination (150 ^{0}C) and rehydration in CO_2-free DI (60 ºC)	14	89	89	0.03	0.03
Calcination (150 ^{0}C) and rehydration in DeI (20 ºC)	13	89	90	0.03	0.03
Calcination (150 ^{0}C) and rehydration in DeI (60 ºC)	11	93	92	0.03	0.03
Calcination (150 ^{0}C) and rehydration in ethanol (20 ºC)	11	105	106	0.03	0.03
Calcination (150 ^{0}C) and rehydration in ethanol (60 ºC)	14	90	89	0.03	0.03

DI-distilled water; DeI-deionized water

In the case of **Zn(2)Al-NO_3-COP**, after calcination, there is a decrease in the surface area in the rehydration step. Nonetheless, although the values of surface area are close to each other, there is an increase in the surface area of calcined-rehydrated LDH in deionized water if the temperature of rehydration is increased from 20 ºC to 60 ºC or if the water is replaced by ethanol (**Table 18**). For **Mg(3)Al-CO_3-SH** the surface area values after rehydration just increased slightly with respect to the calcination at 150 ^{0}C and they remain higher than the initial material in all the conditions tested, which may be explained by the partial removal of the fatty acid present in these commercial LDH materials upon thermal treatment (**Table 20**).

The trend observed in terms of surface area is generally found when comparing pore volume, whilst no clear correlation between surface area and pore diameter was found. Moreover, the hysteresis loop between adsorption and desorption branches is also affected by the immersion step in distilled/deionized water (**Figure 34** and **Figure 35**) as well as calcination (**Figure 36**).

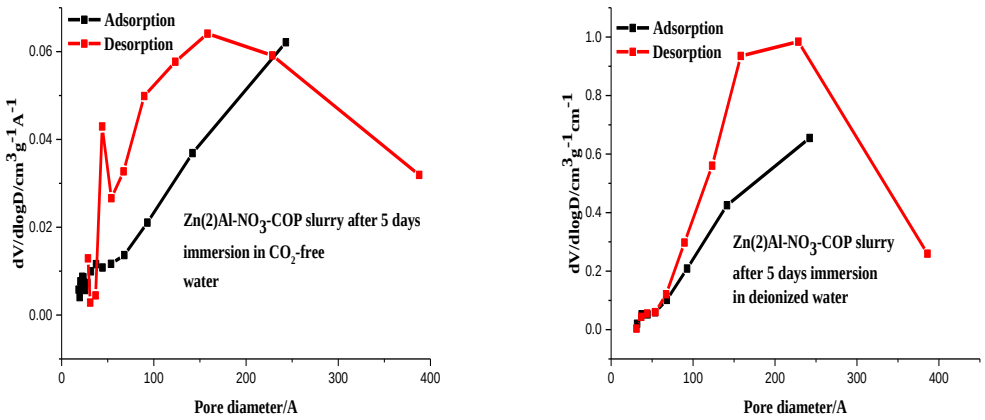

Figure 34. Adsorption and desorption branches of pore size distribution of **Zn(2)Al-NO_3-COP** after immersion in CO_2-free distilled and deionized water

Analysis of data from **Table 16- Table 20** shows that despite similarity of XRD patterns and FTIR spectra of **Mg(3)Al-MBT-CALC650** and **Mg(3)Al-MBT-SH/CALC650**, textural properties of respective LDH materials are different along with their TG thermal decomposition curves, which can affect loading content and arrangement of MBT in aforementioned LDH samples. The latter can have an impact in the release behaviour of corrosion inhibitor.

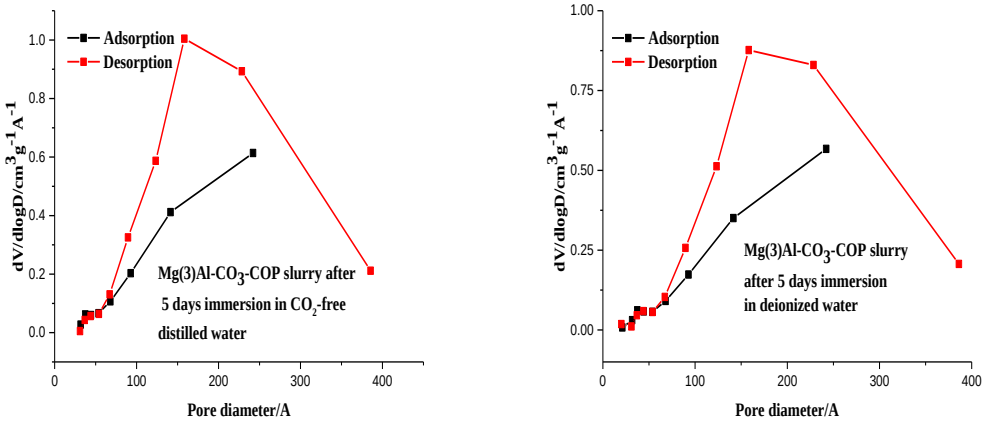

Figure 35. Adsorption and desorption branches of pore size distribution of **Mg(3)Al-CO_3-COP** after immersion in CO_2-free distilled and deionized water

Overall, the textural properties of LDH samples can change depending on the experimental conditions used for the synthesis (regular coprecipitation vs. coprecipitation reaction in reverse microemulsion), ion-exchange step, conditions for calcination and rehydration or just dispersion in a low ionic strength aqueous environment. The analysis of the textural properties gives already a picture of the multitude parameters that can affect LDH. However, it does not show how LDH behaves when dispersed in solution, which constitutes important information to later formulate and propose mechanisms for interaction with species in solution.

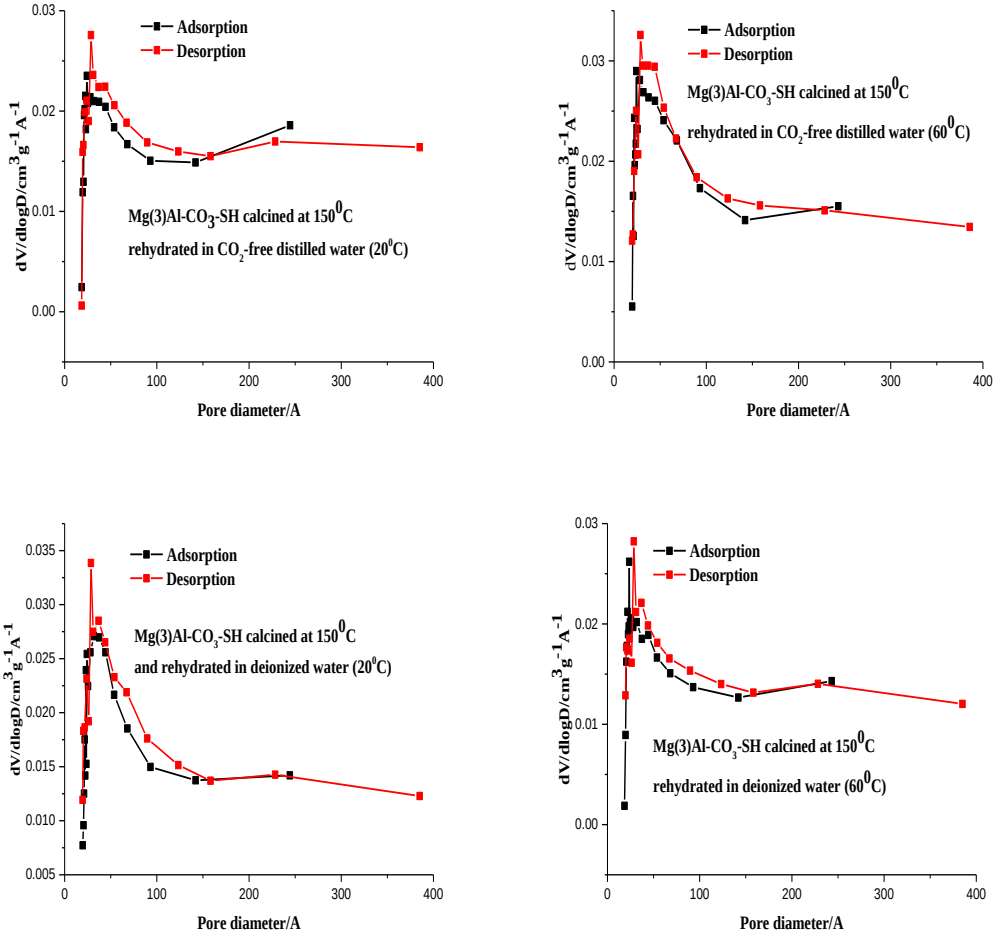

Figure 36. Adsorption and desorption branches of pore size distribution of calcined **Mg(3)Al-CO3-SH** after immersion in CO_2-free distilled and deionized water

The present section is concluded with **Table 21** that presents values of charge density, cross sectional and specific surface areas of prepared LDH materials calculated according to equations **10-12**, described in the introduction. As expected, the theoretical surface area of LDH samples (**Table 21**) is much higher compared to BET values (**Table 16**). This happens, because the internal surfaces of LDH are not accessible (Forano, et al. 2006). As mentioned above, BET surface area values of LDH are usually lower than 100 m^2g^{-1} (Leroux and Besse 2001). However, there is some exceptions: for example, surface area of MgAl LDH with hexacyanoferrate complex is almost 500 m^2g^{-1} (Nijs, de Bock and Vansant 1999). Besides, the surface area tends to decrease during hydrothermal treatment due to crystal growth. Contrastingly, calcination tends to increase of the surface area of LDH particles (Kuhl, et al. 2012). The estimated values of charge density, cross sectional surface in present work agree with literature data (Leroux and Besse 2001); (Forano, et al. 2006).

Table 21. Calculated values of charge density, cross sectional and specific surface areas of prepared LDH materials

LDH	Charge density, chargenm^{-2}	S cross sectional, nm^{2}charge^{-1}	S specific surface area, m^{2}g^{-1}
Zn(2)Al-NO_3-COP	4.07	0.25	821
Zn(2)Al-NO_3-REV	4.09	0.24	818
Zn(2)Al-NO_3-REVN	3.97	0.25	843
Zn(2)Al-NO_3-REVC	3.99	0.25	837
Mg(3)Al-CO_3-COP	3.08	0.32	1139
Zn(2)Al-Glu-AN	4.04	0.25	604
Zn(2)Al-MBT-AN	4.04	0.25	640
Zn(2)Al-MBT-REV/AN	4.04	0.25	640
Zn(2)Al-MBT-REVN/AN	4.04	0.25	640
Zn(2)Al-MBT-REVC/AN	3.97	0.25	652
Mg(3)Al-CO_3-SH	3.10	0.32	1132
Zn(2)Al-CO_3-AN	4.04	0.25	831
Mg(3)Al-MBT-CALC650	3.08	0.32	868
Zn(2)Al-FSS-AN	4.07	0.25	469
Zn(2)Al-PhPh-CALC150	4.04	0.25	483
Zn(2)Al-TB-CALC150	4.02	0.25	392
Mg(3)Al-MBT-SH/CALC650	3.10	0.32	862
Mg(3)Al-MBT-SH/CALC150	3.12	0.32	856
Mg(3)Al-PhPh-SH/CALC150	3.12	0.32	641
Mg(3)Al-TB-SH/CALC150	3.10	0.32	518

4.2.3 Stability of LDH colloidal dispersions

In this section, the stability of LDH dispersions was estimated by measurements of electrophoretic mobility and particle size distribution, obtained from DLS measurements in aqueous media using buffer solutions in the pH range 3-12. LDH samples in solution are polydisperse materials, as expected considering the SEM images presented in section 4.2.1. For this reason, and in order to account for the whole sample of LDH particles, it was decided to present the size of 90 % of sampled particles (D90) instead of the mode of the size distribution.

In order to follow the effect of pH on the surface charge and particle size of LDH, one must bear in mind what can be expected to occur to LDH materials in different conditions. Considering first pH, LDH tends to dissolve at very low (lower than 4) or very high pHs (higher than 12) (Parello, Rojas and Giacomelli 2010); (Jobbágy and Regazzoni 2011); (Zheng, et al. 2013); (Imran, et al. 2016). Thus, LDH tends to be chemically stable in the pH range between 4-12. Within the chemical stability range, the colloidal stability can vary taking into account the charge of the surface, which can then lead to aggregation or agglomeration processes.

Before describing the results obtained, first some points will be considered to aid the interpretation of results:

-D90 values: if larger than 1 micrometer, it is an indication that some level of agglomeration is occurring in solution, since SEM images show individual LDH plate-like materials with sizes with width as large as a several hundreds of nanometers.

-the lack of stability in the dispersions is also reflected upon relatively higher standard errors between replicas measured under the same conditions.

-high magnitude of electrophoretic mobility indicates a larger stability of the dispersion, enhanced by the electrostatic repulsions between particles.

-for the discussion on stability one does not go deeper on the effect of the differences in ionic strength associated with buffer solutions and its possible effect in the compression of the electrical double layer.

Figure 37 presents the variation of electrophoretic mobility as a function of pH for **Zn(2)Al-NO_3-COP**, **Zn(2)Al-NO_3-REV**, **Zn(2)Al-NO_3-REVN** and **Zn(2)Al-NO_3-REVC**. The first point to be considered when looking at the D90 values obtained for all the systems is that there are micrometer-sized agglomerates of LDH in solution. Furthermore, all the LDH materials show a similar behaviour in terms of electrophoretic mobility: at pHs lower than 6-7 the LDH particles are positively charged, while at higher pHs they become negatively charged. This variation in sign of electrophoretic

mobility as a function of increase in pH, is actually observed for all the LDH materials tested and described in this section.

Zn(2)Al-NO$_3$-COP is not very stable near its isoelectric point (pH~6-7) but under more alkaline conditions D90 values are relatively low and stable. This LDH is completely dissolved at pH lower than 5. The sample **Zn(2)Al-NO$_3$-REV** exhibits a low electrophoretic mobility in the range of pH 3-8, lower than **Zn(2)Al-NO$_3$-COP**. As a result, one can see that this low stability has repercussions in the oscillation of D90 values as well as in the dispersion of D90 at each pH (high standard error), particularly for pH values lower than 8.

Contrastingly, the LDH samples prepared in the presence of the nonionic surfactant added in the nucleation and crystallization step (**Zn(2)Al-NO$_3$-REVN** and **Zn(2)Al-NO$_3$-REVC**) revealed an increase in the magnitude of electrophoretic mobility for pH lower than 8 when compared to **Zn(2)Al-NO$_3$-REV**, reflected upon lower dispersion in terms of particle size across the pH range under investigation, most notably for **Zn(2)Al-NO$_3$-REVC**. The nonionic nature of the surfactant seems to have a positive effect in maintaining of D90 values within a smaller range for the latter LDH compared to all others: for this system the D90 particles oscillate around 1 and 3 micrometers in the whole pH range (with low standard errors associated), whereas for the other three LDH samples the values are ranged between 1 and 5 micrometers as a function of pH.

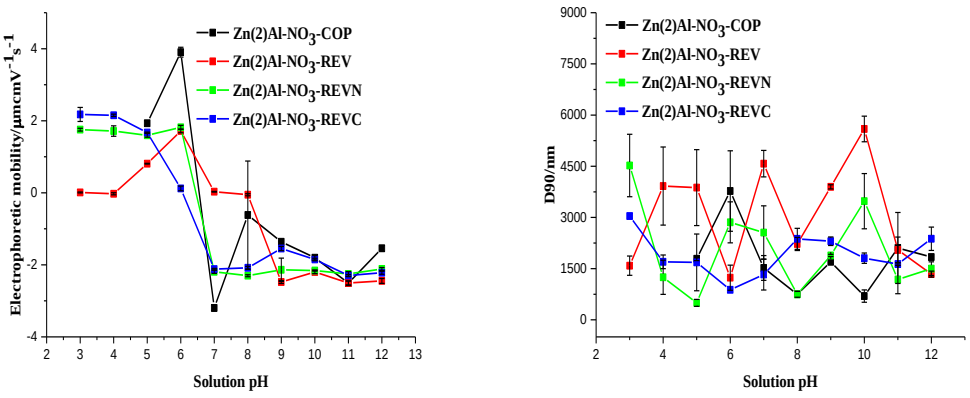

Figure 37. Electrophoretic mobility and D90 of **Zn(2)Al-NO$_3$-COP**, **Zn(2)Al-NO$_3$-REV**, **Zn(2)Al-NO$_3$-REVN** and **Zn(2)Al-NO$_3$-REVC** as a function of pH

Figure 38 shows the variation of electrophoretic mobility and particle size of LDH structures intercalated with carbonates for different pHs. The colloidal properties of as-received **Mg(3)Al-CO$_3$-**

SH were not investigated due to its high hydrophobicity, as a result of the fatty acid coating the particles. The ZnAl LDH shows larger values of electrophoretic mobility when compared to MgAl LDH, which seems to contribute to obtain D90 values with lower standard deviation across the whole pH range for the former material, except for pH 11. However, MgAl LDH samples show smaller D90 values than ZnAl in most of the pH range studied, except for intermediate pH values (7-9), where the electrophoretic mobility of MgAl LDH materials is near zero. Part of the reason for differences in size between MgAl LDHs and ZnAl LDH outside this pH range is that, looking at the SEM images (section 4.2.1) the MgAl LDH materials have smaller individual particles than the ZnAl counterparts. So, assuming that there is higher stability in solution D90 values reflect the size of more stabilized (hence smaller) particles.

In addition, it is interesting to notice that electrophoretic mobility increases with replacement of Mg by Zn (MgAl vs. ZnAl LDH). Therefore, one can argue that the composition of the metal hydroxide sheets (type and ratio of metal cations) has influence on the relative stability of LDH particles. For example, Parello and co-authors stated that there are two steps of LDH dissolution, namely, fast surface-acid-base equilibrium and later slow detachment of cations from the protonated surface sites. Therefore, the value of pH, binding strength of cations to hydroxylated layers and exposed area of the particles play a crucial role in LDH dissolution (Parello, Rojas and Giacomelli 2010). On the other hand, the type of anion intercalated also affects the colloidal properties (c.f. **Zn(2)Al-NO_3-COP** in **Figure 37** and **Zn(2)Al-CO_3-AN** in **Figure 38**): it is expected that the intercalating anions are not found only within the interlayer galleries but also in the outer surface of LDH particles, to compensate the positive charge of hydroxide sheets. From literature it is known that isoelectric point drops for divalent anions at fixed salt concentration (Mg-Al-CO_3 LDH and Mg-Al-NO_3 LDH). Besides, divalent anions tend to decrease particles mobility and can be stronger adsorbed onto LDH surface compared to monovalent anions (Forano, et al. 2006). Moreover, the nature of the anion can have an affect on the solubility and dissolution of LDH samples (Parello, Rojas and Giacomelli 2010); (Zheng, et al. 2013).

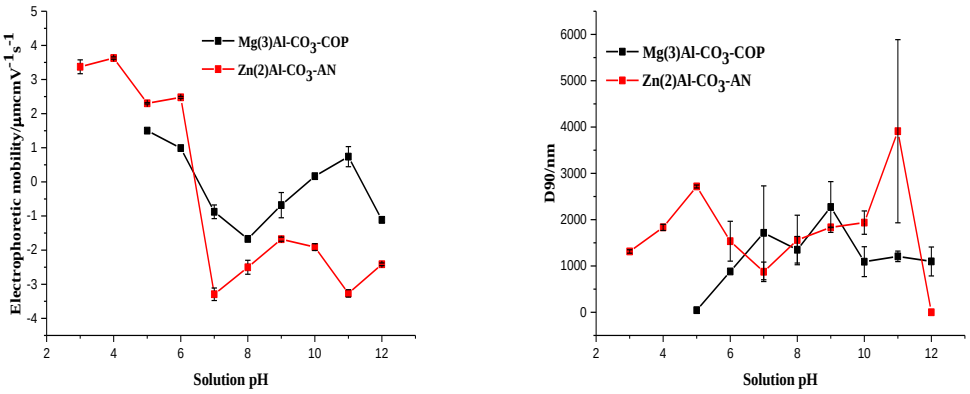

Figure 38. Electrophoretic mobility and D90 values of LDH intercalated with carbonates as a function of pH: **Mg(3)Al-CO_3-COP** and **Zn(2)Al-CO_3-AN**

After intercalation of corrosion inhibitors Glu and MBT (**Figure 39**), ZnAl LDH structures reveal electrophoretic mobility values in the range of nitrate-intercalated LDH samples (**Figure 37**). Furthermore, there is high variability in D90 values as a function of pH, most notably for **Zn(2)Al-MBT-AN**. In the case of **Zn(2)-Al-Glu-AN** larger D90 values are observed for pH around 5-6, where its electrophoretic mobility approaches zero (near the isoelectric point).

For **Zn(2)-Al-MBT-AN**, the electrophoretic mobility is lower than for samples obtained by coprecipitation reaction in reverse microemulsion, especially in alkaline conditions. The system **Zn(2)Al-MBT-REVC/AN**, obtained from the ZnAl LDH materials with the highest stability (**Figure 37**), displays now higher D90 values near the isoelectric point, revealing that the stabilizing nature of the nonionic surfactant is non-longer effective after MBT immobilization at intermediate pH ranges. Nevertheless, stability is still observed in the range of pH 8-12 for this system.

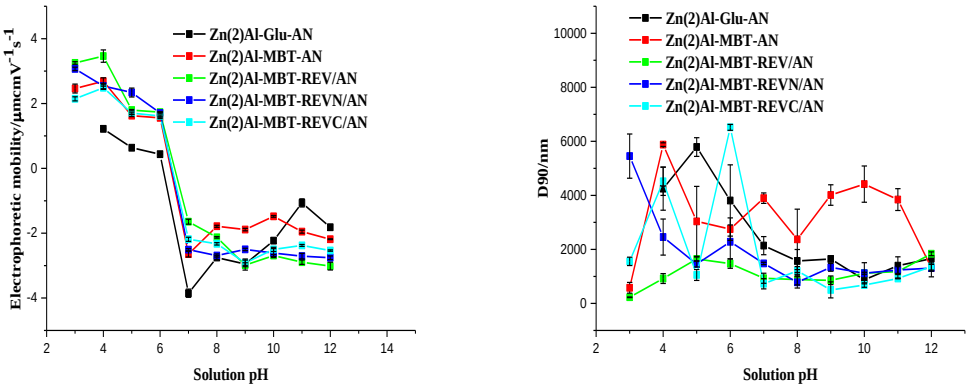

Figure 39. Electrophoretic mobility and D90 values of LDH intercalated with Glu and MBT as a function of pH: **Zn(2)Al-Glu-AN, Zn(2)Al-MBT-AN, Zn(2)Al-MBT-REV/AN, Zn(2)Al-MBT-REVN/AN** and **Zn(2)Al-MBT-REVC/AN**

The immobilization of MBT in MgAl LDH materials treated under different thermal conditions leads to very different results in terms of electrophoretic mobility and particle size (**Figure 40**). Samples calcined at 650 ºC shows higher variation of D90 values across the pH range studied. On the other hand **Mg(3)Al-MBT-SH/CALC150** reveals larger magnitude of electrophoretic mobility under alkaline conditions (pH=7-12) and similar D90 values in this pH range. The larger electrophoretic mobility of **Mg(3)Al-MBT-SH/CALC150**, when compared to samples calcined at 650 ºC, can be due to the combination of adsorbed MBT with fatty acid partially remaining onto LDH surface. In this case, under alkaline conditions, MBT and carboxylate groups deprotonated can contribute for the electrostatic repulsions between particles and to lower D90 values as well.

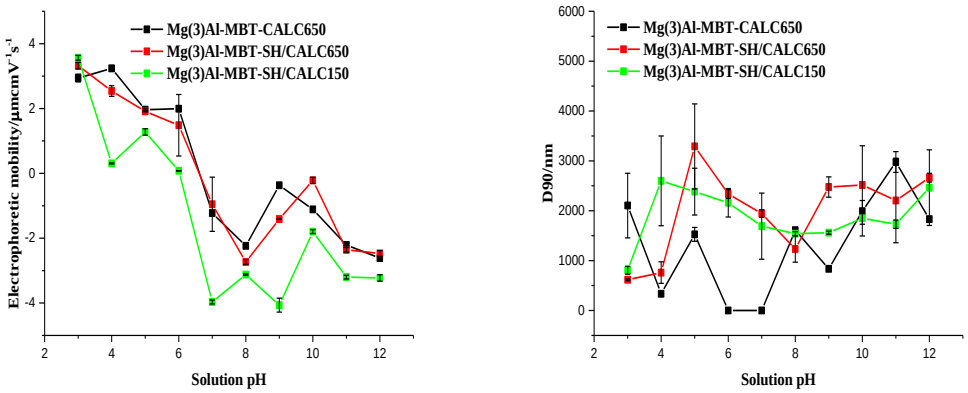

Figure 40. Electrophoretic mobility and D90 values of LDH loaded with MBT as a function of pH: **Mg(3)Al-MBT-CALC650, Mg(3)Al-MBT-SH/CALC650** and **Mg(3)Al-MBT-SH/CALC150**

Figure 41 shows the electrophoretic mobility and D90 values for ZnAl LDH materials with immobilized sensing species: FSS, PhPh and TB. The trend in electrophoretic mobility as a function of pH follows the pattern previously observed for other samples: higher magnitude of electrophoretic mobility is observed under alkaline conditions, which is consistent with the deprotonation of the sensing species under these conditions. However, looking at D90 values, all these samples show a large variation in particle size with pH and large standard error associated with no clear distinction between them. These findings contrast with results obtained for commercial MgAl LDH (SH) treated at 150 ºC (**Figure 42**). In fact, regions of higher stability in alkaline media was found for **Mg(3)Al-PhPh-SH/CALC150** and **Mg(3)Al-TB-SH/CALC150** (**Figure 42**) when compared to ZnAl LDHs (**Figure 37**). Again, the presence of some fatty acid groups may aid on the stabilization of the surface combined with the deprotonation of the sensing species immobilized.

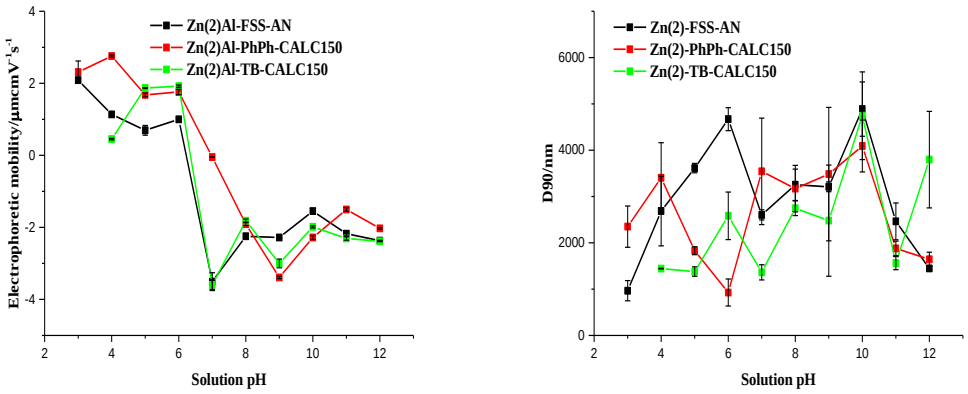

Figure 41. Electrophoretic mobility and D90 values of LDH loaded with dye indicators as a function of pH: **Zn(2)Al-FSS-AN, Zn(2)Al-PhPh-CALC150 and Zn(2)Al-TB-CALC150**

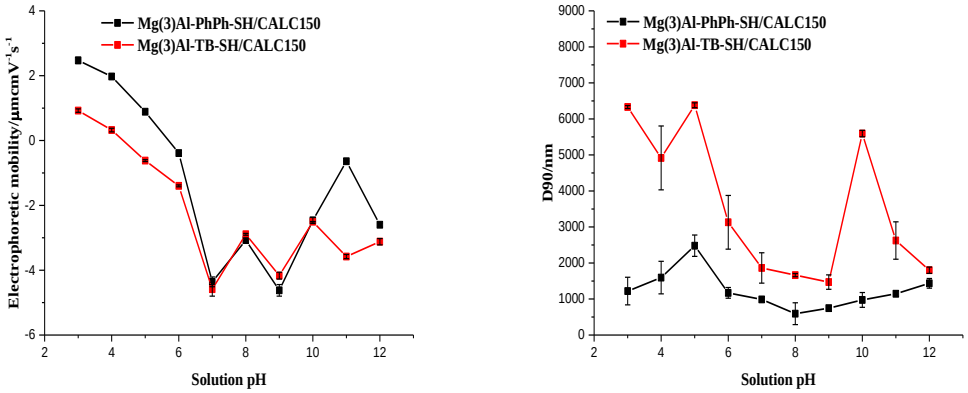

Figure 42. Electrophoretic mobility and D90 values of LDH loaded with dye indicators as a function of pH: **Mg(3)Al-PhPh-SH/CALC150 and Mg(3)Al-TB-SH/CALC150**

Finally, some considerations can be made considering the isoelectric point of different LDH materials, that can be estimated from the electrophoretic mobility graphs presented above (**Figure 37 - Figure 42**). The isoelectric point of **Zn(2)Al-NO_3-COP**, **Zn(2)Al-NO_3-REVN**, **Zn(2)Al-NO_3-REVC, Zn(2)Al-CO_3-AN**, **Mg(3)Al-CO_3-COP** is between 6-7. Upon immobilization of guest anions such as Glu, MBT, FSS and TB in ZnAl LDH precursors obtained by coprecipitation it lowers to 6, becoming lower in SH thermally treated at 150 ºC and with PhPh and TB adsorbed. Therefore, the immobilization of the guest species in LDH samples affects their surface properties and consequently their stability as colloidal dispersions.

Preliminary conclusions

1. The morphology of LDH particles depends on the synthesis method. For most LDH materials prepared the morphology is platelet-like. However, addition of tri-block copolymer during nucleation or crystallization steps of coprecipitation reaction in reverse microemulsion changes the morphology of LDH particles. Samples of MgAl LDH obtained commercially are also different from those prepared with the same composition in the lab. Furthermore, anion-exchange and/or adsorption of corrosion inhibitors or sensing molecules do not alter morphology of most studied LDH, except for **Zn(2)Al-MBT-REV/AN** and **Zn(2)Al-MBT-REVN/AN**.
2. The surface area and pore size volumes were found to depend on the method of synthesis, most notably when comparing conventional routes based on coprecipitation with coprecipitation reaction in reverse microemulsion. The highest BET surface area was observed for nitrate containing-LDH samples prepared by coprecipitation reaction in reverse microemulsion. All the prepared LDH materials are mesoporous.
3. Changes in textural properties were found to be dependent upon exposure of LDH materials to aqueous environment, presence of carbonates for LDH compositions with labile anions and on thermal treatments.
4. The rehydration of calcined samples leads to decrease in surface area compared to the calcined ones. Moreover, the surface area was found to be dependent upon the temperature and nature of the media of rehydration.
5. The stability of LDH dispersions in aqueous conditions depends on their structure and composition. The most stable particles across the whole pH range sampled were stabilized by nonionic surfactant used in the synthesis. For those systems in which immobilization occurred by surface adsorption their stability in alkaline pH conditions can be correlated with electrostatic repulsions of deprotonated forms of the guest molecules.
6. The immobilization of guest species in LDH samples leads to a decrease in the isoelectric point.

5. ADSORPTION STUDIES OF SPECIES ONTO LDH

In previous sections a detailed study of structural, thermal, morphological, textural and colloidal properties rendered a global perspective over the main characteristics of layered double hydroxides prepared by different routes with various species. In this section one aims at studying adsorption of different active species in LDH materials, mimicking and following the process of uptake of active species carried out during the syntheses processes: ion-exchange and rehydration of calcined LDH samples.

The methodology used in the adsorption studies is presented in detail in the Experimental section (Chapter 3). The systems used as adsorbents were calcined powders or slurries of **Zn(2)Al-NO_3-COP**, **Zn(2)Al-CO_3-AN,** **Mg(3)Al-CO_3-SH**, **Mg(3)Al-CO_3-COP** and LDH obtained by coprecipitation reaction in reverse microemulsion (**Zn(2)Al-NO_3-REV**, **Zn(2)Al-NO_3-REVN**, **Zn(2)Al-NO_3-REVC**). Moreover, the adsorption studies were performed under the same conditions of temperature and time used in the synthesis of corresponding LDH materials with immobilized active species, whereas solutions of PhPh, TB and MBT were used as adsorbates. The choice to perform adsorption with these three organic molecules, arises from the differences observed when attempting their intercalation: MBT was found to intercalate in the LDH galleries, while PhPh and TB did not lead to intercalation in most of the cases, although partial replacement could have occurred (not clear from the XRD analysis). Also, depending on the nature of the intercalating anion present in the parent LDH structure, adsorption of molecules on the external surface of LDH seems to occur under certain conditions (section 4.1.1).

The procedure to evaluate adsorption properties is succinctly presented in **Figure 43**: 5 solutions of adsorbate (with different initial concentrations-$\mathbf{C_0}$ and fixed volume **V**) were used for immersion of a certain mass of adsorbent (**m**) at room temperature (20 ^{0}C), or 60 ^{0}C. After 2 h of immersion, equilibrium concentrations ($\mathbf{C_{eq}}$) were estimated by UV-Vis measurements (for studies associated with adsorption kinetics, quantification of adsorbate was done at specific times detailed in the following sections). Afterwards, calculation of adsorbed adsorbate at equilibrium ($\mathbf{q_e}$) from the obtained data were used for estimation of parameters associated with different adsorption isotherm models. For several models, calculation of fractional uptake- **F** was also carried out, which is the amount of adsorbate adsorbed at time t divided by the amount of adsorbate adsorbed at equilibrium. The choice of most appropriate adsorption model was done through comparison of the following parameters: standard error of calculated model constant, residual plot analysis (scattered residuals - indication of precise and unbiased model) for non-linear regression along with Pearson's r, adjusted r square and statistical *p*-value for linear regression analysis. If *p*-value < 0.05 it is a sign, that the model is biased (Zellner, Keuzenkamp and McAleer 2001).

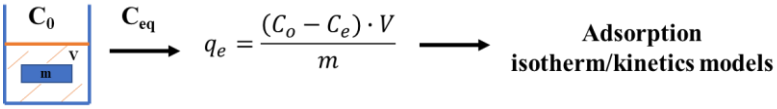

Figure 43. Scheme of evaluation of adsorption properties

In the next sub-sections results concerning adsorption of PhPh, TB and MBT are presented in detail.

5.1 Adsorption studies of PhPh onto LDH

PhPh adsorption studies were specifically targeted for the conditions whereby both XRD and FTIR revealed the presence of PhPh (sections 4.1.1 and 4.1.2). **Figure 44** and **Figure 45** present data collected for **Zn(2)Al-NO_3-COP** and **Mg(3)Al-CO_3-SH** calcined at 150 ^{0}C, which were used as adsorbents, immersed into solutions of PhPh with concentrations ranging 0.25 mM-25.86 mM, at 20 ^{0}C and 60 ^{0}C, for adsorption isotherm experiments. Furthermore, the dependence of PhPh concentration in solution as a function of time (in the presence of aforementioned adsorbents) was carried out at 20 ^{0}C/60 ^{0}C, using the same concentrations range (0.25 mM-25.86 mM) of pH indicator, for adsorption kinetic studies.

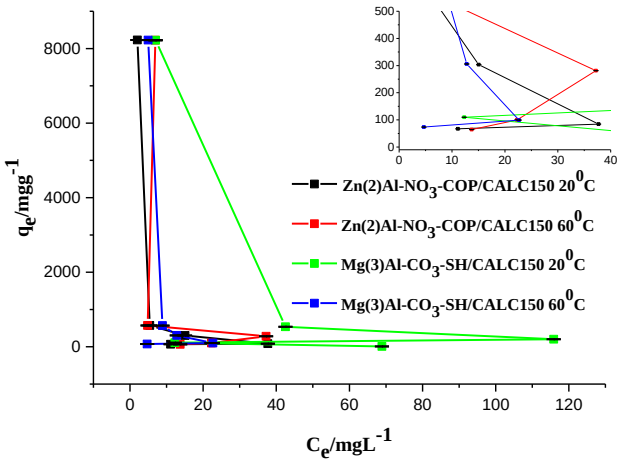

Figure 44. Variation of q_e with C_e corresponding to the adsorption of PhPh at 20 ^{0}C and 60 ^{0}C onto **Zn(2)Al-NO_3-COP** and **Mg(3)Al-CO_3-SH** thermally treated at 150 ^{0}C

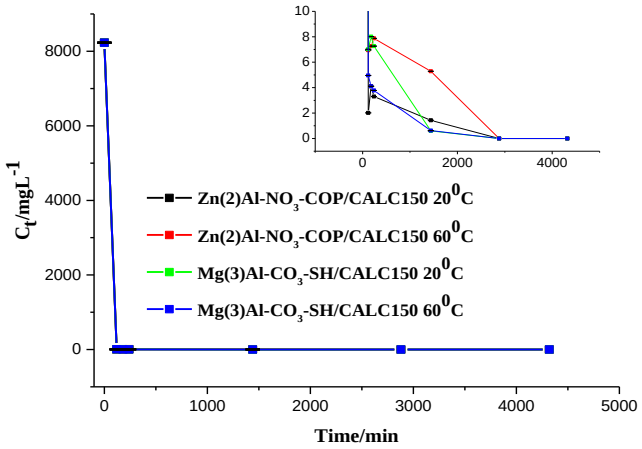

Figure 45. PhPh adsorption at 20 ^{0}C and 60 ^{0}C onto **Zn(2)Al-NO$_3$-COP** and **Mg(3)Al-CO$_3$-SH** thermally treated at 150 ^{0}C with concentration of PhPh 25.86 mM

Figure 44 and **Figure 45** demonstrate, that PhPh adsorption isotherm is of "H" type (Toth 1995), confirming the strong affinity of PhPh for both studied LDH adsorbents. After 24 h the amount of non-adsorbed PhPh is very low and after 48 h the amount of PhPh in solution starts to be lower than detectable limit of UV-Vis spectrophotometer. **Table 22** and **Table 24** show the models that best fit adsorption data for isotherm and kinetics experiments carried out. **Figure 46** and **Figure 47** depict the fitted models and corresponding residual plots.

Table 22. Adsorption isotherm models used to fit adsorption data of PhPh onto LDH

Adsorbent	Exp. conditions	Isotherm model	Adsorption nature associated with the model(s)	Figures of merit
Zn(2)Al-NO$_3$-COP	Calcination at 150 ºC and rehydration in 0.25-25.86 mM PhPh at 20 ºC	Freundlich	Physisorption/ cooperative adsorption	**K$_F$**= 11657.83 mgg^{-1} (Lg)$^{1.53}$ (1.197 - **st.error**); **a**= -1.53 (0.491- **st.error**) **Pearson's r:** -0.87 **Adj. R^2:** 0.68 **p-value**: 0.052

Table 22. Adsorption isotherm models used to fit adsorption data of PhPh onto LDH (cont.)

Adsorbent	Exp. conditions	Isotherm model	Adsorption nature associated with the model(s)	Figures of merit
Zn(2)Al-NO_3-COP (cont.)	Calcination at 150 ºC and rehydration in 0.25-25.86 mM PhPh at 20 ºC	Dubinin Radushkevich	Physisorption/Pore filling mechanism	**K_{DR}**= 11262.73 mol^2J^{-2} (1384.867-**st.error**); **q_m**= 8970.28 mgg^{-1} (229.761- **st.error**)
	Calcination at 150 ºC and rehydration in 0.25-25.86 mM PhPh at 60 ºC	Freundlich	Physisorption/ cooperative adsorption	**K_F**= 9492.47 mgg^{-1} $(Lg)^{1.25}$ (2.974-**st.error**); **a**= -1.25 (1.112-**st.error**) **Pearson's r:** -0.54 **Adj. R^2:** 0.06 **p-value**: 0.344
Mg(3)Al-CO_3-SH	Calcination at 150 ºC and rehydration in 0.25-25.86 mM PhPh at 20 ºC	Freundlich	Physisorption/ cooperative adsorption	**K_F**= 20153.90 mgg^{-1} $(Lg)^{1.28}$ (3.443-**st.error**); **a**= -1.28 (0.958-**st.error**) **Pearson's r:** -0.61 **Adj. R^2:** 0.16 **p-value**: 0.274
	Calcination at 150 ºC and rehydration in 0.25-25.86 mM PhPh at 60 ºC	-		-

pp. 31-33 contain description of used adsorption isotherm models

Due to high values of standard errors it was not possible to determine the mechanism of PhPh adsorption onto **Mg(3)Al-CO_3-SH/CALC150** at 60 ^{0}C.

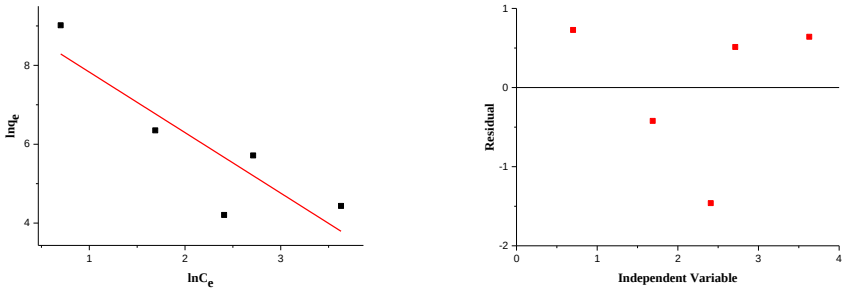

Figure 46. Fitting of data (Freundlich isotherm (linear)) for adsorption of PhPh at 20 ^{0}C onto **Zn(2)Al-NO$_3$-COP** thermally treated at 150 ^{0}C

Dubinin-Radushkevich model allows the estimation of *mean free energy, E per molecule of adsorbate* (for removal of a molecule from its location in the sorption space to the infinity), which can be calculated via the relationship of equation **22** (Dubinin 1960):

$$E = \frac{1}{\sqrt{2K_{DR}}} \qquad \textbf{22}$$

K_{DR} (mol^{2}kJ^{-2})-Dubinin-Radushkevich constant

From all the models tested the better results were given by Freundlich and Dubinin-Radushkevich ones. The calculated energy value of E, using constant of Dubinin-Radushkevich (**Table 22**) is 0.21 kJ mol^{-1} (equation **22)** and it points to the physisorption character of PhPh sorption process (Sparks 2003). The same conclusion can be obtained from the Freundlich model. Moreover, physisorption can be specified as cooperative adsorption (the calculated *a* parameter of Freundlich isotherm model is higher in magnitude than 1)-**Table 22**. Its negative sign shows that concentration of PhPh inversely affects the adsorption capacities. The latter trend is observed for most studied conditions of PhPh adsorption, except for adsorption by calcined **Mg(3)Al-CO$_3$-SH** at 60 ^{0}C due to the impossibility of describing the adsorption behaviour by any of the individual models used (high values of standard errors associated with the estimated constants and pattern formation in the residual plot were found).

The variation of Gibbs energy associated with the adsorption process can be estimated from adsorption isotherm experimental data (equations **23-25**). Besides, due to the fact that PhPh adsorption isotherms data were collected at two different temperatures, it is possible to roughly estimate the values of enthalpy and entropy changes. The mentioned parameters were estimated using the following equations (Song, et al. 2013):

$$lnK_d = \frac{\Delta S}{R} - \frac{\Delta H}{RT} \quad (23)$$

$$\Delta G = \Delta H - T\Delta S \quad (24)$$

$$K_d = \frac{q_e}{C_e} \quad (25)$$

The fitting of adsorption isotherms allows the assessment of the adsorption nature and thermodynamic parameters that are also important for characterization of adsorption process: if the reaction is spontaneous or non-spontaneous, exergonic or endergonic, and exothermic or endothermic. Values presented in **Table 23** reveal that the adsorption of PhPh onto the surface of both adsorbents is a spontaneous, exergonic and exothermic process. Negative value of entropy changes (ΔS) agrees with the nature of adsorption process: when the molecules are adsorbed, their freedom of movement is more restricted. The decrease of the negative value of ΔG with the increase in temperature is an indication that adsorption starts to be less favourable. It is based on the mobility increase of adsorbate molecules or ions with temperature and consequently desorption processes can become more favourable. Saha and Chowdhury made a review of published thermodynamic parameters of heavy metals and dyes adsorption onto various adsorbents. In most cases the values of ΔG are negative (Saha and Chowdhury 2011).

Table 23. Estimation of thermodynamic parameters of PhPh adsorption onto LDH

LDH	ΔG,kJmol^{-1}	ΔH, kJmol^{-1}	ΔS, Jmol^{-1}K^{-1}
Zn(2)Al-NO_3-COP/CALC150	-20.26 (293 K); -15.44 (333 K)	-55.53	-120.40
Mg(3)Al-CO_3-SH/CALC150	-17.21 (293 K); -16.24 (333 K)	-24.31	-24.22

Table 24 and **Figure 47** show the results from the fittings of different kinetic models to the adsorption data of PhPh onto LDH. The kinetics of PhPh adsorption onto the surface of both studied adsorbents is governed by diffusion, that can be distinguished on intraparticle or bulk and surface diffusion, during the monitored time (72 h), at both 20 ºC and 60 ^{0}C. The pseudo-first order model can reflect the physisorption character of adsorption, however, the values of Pearson's r and Adj, r-square are relatively low. During this period, adsorption of 99% of PhPh from solutions occurred, regardless of the adsorption temperature.

Furthermore, detailed analysis of **Table 24** reveals that values of Elovich model constants are oppositely dependent upon the initial PhPh concentration (lower concentration = higher adsorption rate). The latter also agrees with conclusions from adsorption isotherm data: negative value of *a* constant of Freundlich model (**Table 22**) points to an inverse PhPh concentration influence on the adsorption. **Figure 48** shows the dependence of adsorption rate calculated from Elovich model on the initial PhPh concentration used.

Table 24. Kinetic models used to fit adsorption data of PhPh onto calcined **Zn(2)Al-NO_3-COP** and **Mg(3)Al-CO_3-SH**

Adsorbent	Exp. conditions	Kinetics model	Limiting step according to the model(s)	Figures of merit
Zn(2)Al-NO_3-COP	Calcination at 150 ºC and rehydration in 25.86 mM PhPh at 20 ºC	Elovich	Bulk and surface diffusion	**α**= 11.97 $mgg^{-1}min^{-1}$ (3.550- **st.error**); intercept = 8047.00 (6.613- **st.error**);
	Calcination at 150 ºC and rehydration in 25.86 mM PhPh at 60 ºC	Elovich	Bulk and surface diffusion	**α**= 2.23 $mgg^{-1}min^{-1}$ (0.881-**st.error**); intercept = 8212.28 (5.867- **st.error**); **Pearson's r:** 0.78 **Adj. R^2:** 0.52 **p-value**: 0.065
	Calcination at 150 ºC and rehydration in 1.82 mM PhPh at 20 ºC	Elovich	Bulk and surface diffusion	**α**= 17.26 $mgg^{-1}min^{-1}$ (2.125- **st.error**); intercept = 541.95 (3.958- **st.error**);
	Calcination at 150 ºC and rehydration in 1.82 mM PhPh at 60 ºC	Elovich	Bulk and surface diffusion	**α**= 17.62 $mgg^{-1}min^{-1}$ (2.222- **st.error**); intercept = 525.63 (4.139- **st.error**);

Table 24. Kinetic models used to fit adsorption data of PhPh onto calcined **Zn(2)Al-NO_3-COP** and **Mg(3)Al-CO_3-SH** (cont.)

Adsorbent	Exp. conditions	Kinetics model	Limiting step according to the model(s)	Figures of merit
Zn(2)Al-NO_3-COP (cont.)	Calcination at 150 ºC and rehydration in 1 mM PhPh at 20 ºC	Pseudo-first order	One-site occupancy adsorption	**K=** $1.01 \cdot 10^{-5}$ ($5.219 \cdot 10^{-6}$- **st.error)**; **Pearson's r:** 0.70 **Adj. R^2:** 0.14 **p-value**: 0.25
	Calcination at 150 ºC and rehydration in 1 mM PhPh at 60ºC	Elovich	Bulk and surface diffusion	**α**= 71.33 $mgg^{-1}min^{-1}$ (7.092- **st.error**); intercept = 169.03 (13.209- **st.error**);
	Calcination at 150 ºC and rehydration in 0.38 mM PhPh at 20 ºC	Parabolic diffusion	Intraparticle diffusion	**k=** 0.15 $mgg^{-1}min^{-1}$ (0.020- **st.error)**;
	Calcination at 150 ºC and rehydration in 0.38 mM PhPh at 60 ºC	Elovich	Bulk and surface diffusion	**α**= 46.48 $mgg^{-1}min^{-1}$ (4.544- **st.error**); intercept = 25.61 (8.465- **st.error**);
	Calcination at 150 ºC and rehydration in 0.25 mM PhPh at 20 ºC	Pseudo-first order	One-site occupancy adsorption	**K=** $1.05 \cdot 10^{-4}$ min^{-1} ($5.032 \cdot 10^{-5}$- **st.error)**; **Pearson's r:** 0.72 **Adj. R^2:** 0.40 **p-value**: 0.11
	Calcination at 150 ºC and rehydration in 0.25 mM PhPh at 60 ºC	Elovich	Bulk and surface diffusion	**α**= 23.95 $mgg^{-1}min^{-1}$ (5.561- **st.error**); intercept = 28.96 (10.359- **st.error**);
Mg(3)Al-CO_3-SH	Calcination at 150 ºC and rehydration in 25.86 mM PhPh at 20 ºC	Elovich	Bulk and surface diffusion	**α**= 21.78 $mgg^{-1}min^{-1}$ (2.683- **st.error**); intercept = 7988.55 (4.998- **st.error**);

Table 24. Kinetic models used to fit adsorption data of PhPh onto calcined **Zn(2)Al-NO_3-COP** and **Mg(3)Al-CO_3-SH** (cont.)

Adsorbent	Exp. conditions	Kinetics model	Limiting step according to the model(s)	Figures of merit
Mg(3)Al-CO_3-SH (cont.)	Calcination at 150 ºC and rehydration in 25.86 mM PhPh at 60 ºC	Elovich	Bulk and surface diffusion	**α**= 15.05 $mgg^{-1}min^{-1}$ (1.938-**st.error**); intercept = 7846.87 (3.609- **st.error**)
	Calcination at 150 ºC and rehydration in 1.82 mM PhPh at 20 ºC	Elovich	Bulk and surface diffusion	**α**= 45.16 $mgg^{-1}min^{-1}$ (5.266-**st.error**); intercept = 438.99 (9.808- **st.error**);
	Calcination at 150 ºC and rehydration in 1.82 mM PhPh at 60 ºC	Elovich	Bulk and surface diffusion	**α**= 20.94 $mgg^{-1}min^{-1}$ (2.478-**st.error**); intercept = 511.96 (4.615- **st.error**);
	Calcination at 150 ºC and rehydration in 1 mM PhPh at 20 ºC	Pseudo-first order	One-site occupancy adsorption	**K**= $5.56 \cdot 10^{-5}$ min^{-1} ($3.666 \cdot 10^{-5}$- **st.error)**; **Pearson's r:** 0.60 **Adj. R^2:** 0.21 **p-value**: 0.20
	Calcination at 150 ºC and rehydration in 1 mM PhPh at 60 ºC	Elovich	Bulk and surface diffusion	**α**= 23.91 $mgg^{-1}min^{-1}$ (4.118-**st.error**); intercept = 259.61 (7.671- **st.error**);
	Calcination at 150 ºC and rehydration in 0.38 mM PhPh at 20 ºC	Parabolic diffusion	Intraparticle diffusion	**k**= 0.15 $min^{-0.5}$ (0.024- **st.error)**;
	Calcination at 150 ºC and rehydration in 0.38 mM PhPh at 60 ºC	Elovich	Bulk and surface diffusion	**α**= 43.68 $mgg^{-1}min^{-1}$ (3.469-**st.error**); intercept = 27.06 (6.461- **st.error**);

Table 24. Kinetic models used to fit adsorption data of PhPh onto calcined **Zn(2)Al-NO$_3$-COP** and **Mg(3)Al-CO$_3$-SH** (cont.)

Adsorbent	Exp. conditions	Kinetics model	Limiting step according to the model(s)	Figures of merit
Mg(3)Al-CO$_3$-SH (cont.)	Calcination at 150 ºC and rehydration in 0.25 mM PhPh at 20 ºC	Parabolic diffusion	Intraparticle diffusion	**k=** 0.11 min$^{-0.5}$ (0.016- **st.error)**;
	Calcination at 150 ºC and rehydration in 0.25 mM PhPh at 60 ºC	Parabolic diffusion	Intraparticle diffusion	**k=** 0.15 min$^{-0.5}$ (0.019- **st.error)**;

pp.35-36 contain description of used adsorption kinetic models

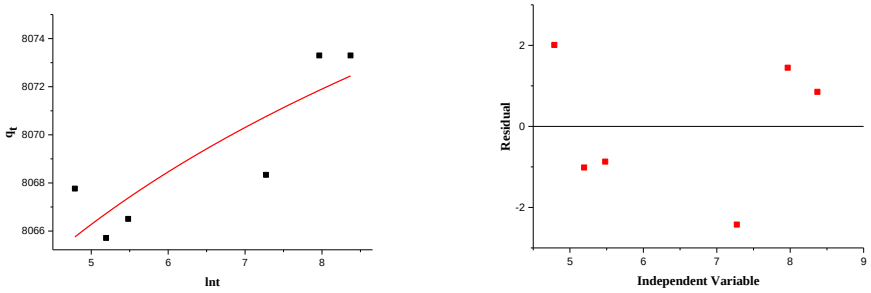

Figure 47. Fitting of PhPh adsorption kinetics (Elovich model (non-linear)) and corresponding residual plot for 25.86 mM solution onto **Zn(2)Al-NO$_3$-COP** thermally treated at 150 ^{0}C

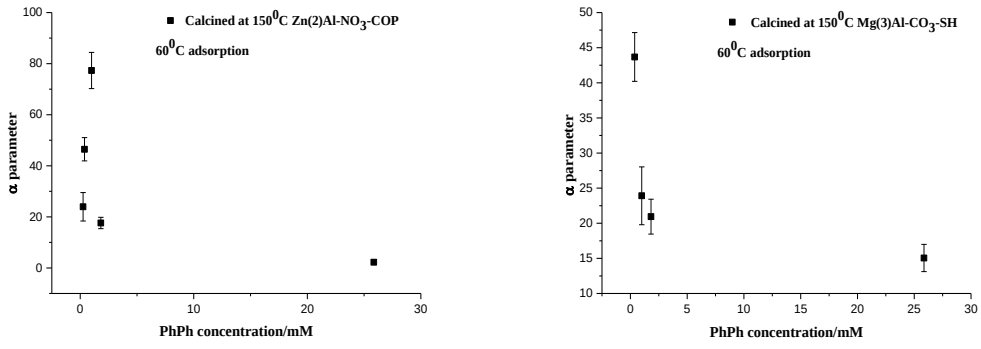

Figure 48. Dependence of adsorption rates calculated from Elovich model on the initial PhPh concentration onto **Zn(2)Al-NO$_3$-COP** and **Mg(3)Al-CO$_3$-SH** thermally treated at 150 ^{0}C

Reaction rates (estimated from the pseudo-first order model) differ for the studied adsorbents, with values higher for calcined **Zn(2)Al-NO$_3$-COP** compared to calcined **Mg(3)Al-CO$_3$-SH** (10^{-4} /10^{-5} vs 10^{-7} /10^{-5} min^{-1}, respectively) –**Table 24**. According to literature data, it is common to find different reaction rates depending on the type of adsorbent. For instance, for studies of potassium adsorption onto different types of soils, rate coefficients can differ in less or higher extent with temperature increase, depending on the soil structure. For potassium adsorption onto kaolinite the rate coefficient at 283 K is 1.321 min^{-1} and at 313 K is 3.784 min^{-1}. However, the values of rate coefficients are much lower for vermiculite, namely 0.049 min^{-1} at 283 K and at 0.069 min^{-1} 313 K (under the same studied conditions) (Sparks 2003).

5.2 Adsorption studies of TB onto LDH

Adsorption experiments with TB were performed in a similar manner as PhPh experiments presented in the previous section. **Figure 49** and **Figure 50** present data using **Zn(2)Al-NO$_3$-COP** and **Mg(3)Al-CO$_3$-SH** calcined at 150 ^{0}C as adsorbents, immersed into solutions of TB with concentrations in the range 0.27 mM - 28.70 mM, at 20 ^{0}C and 60 ^{0}C.

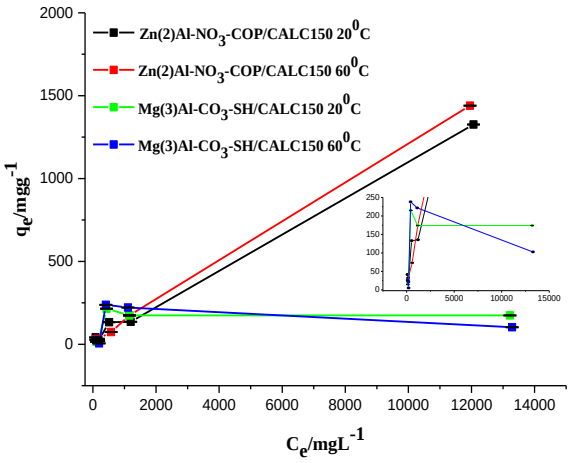

Figure 49. Variation of q_e with C_e corresponding to the adsorption of TB at 20 ^{0}C and 60 ^{0}C onto **Zn(2)Al-NO$_3$-COP** and **Mg(3)Al-CO$_3$-SH** thermally treated at 150 ^{0}C

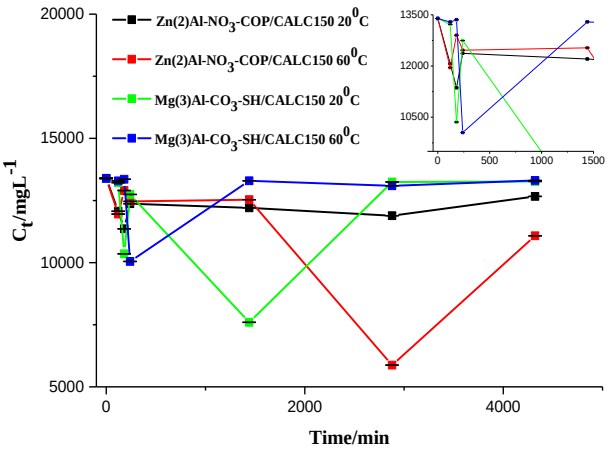

Figure 50. TB adsorption at 20 ^{0}C and 60 ^{0}C onto **Zn(2)Al-NO$_3$-COP** and **Mg(3)Al-CO$_3$-SH** thermally treated at 150 ^{0}C with concentration of TB 28.70 mM

Figure 49 shows that TB adsorption isotherms are closer to "L" with plateau for **Mg(3)Al-CO$_3$-SH/CALC150** and "L" type without plateau for **Zn(2)Al-NO$_3$-COP/CALC150**, implying a progressive saturation of the solid adsorbents with adsorbate molecules (Limousin, et al. 2007). **Figure 50** reveals that there is a strong impact of desorption processes for both types of studied LDH materials. **Table 25** describes the models that best fit the adsorption data collected. **Figure 51** and **Figure 53** show the fitted models and corresponding residual plots.

Table 25. Adsorption isotherm models used to fit adsorption data of TB onto **Zn(2)Al-NO$_3$-COP** and **Mg(3)Al-CO$_3$-SH** LDH

Adsorbent	**Exp. conditions**	**Isotherm model**	**Adsorption nature associated with the model(s)**	**Figures of merit**
Zn(2)Al-NO$_3$-COP	Calcination at 150 ºC and rehydration in 0.27-28.70 mM TB at 20 ºC	Langmuir	Chemisorption	**q_m** = 3048.44 mgg^{-1} **K_L**= 6.10·10^{-5} Lmg^{-1} **R_L**= 0.55 **Pearson's r:** 0.54 **Adj. R^2:** 0.06 **p-value**: 0.347

Table 25. Adsorption isotherm models used to fit adsorption data of TB onto **Zn(2)Al-NO_3-COP** and **Mg(3)Al-CO_3-SH** LDHs (cont.)

Adsorbent	Exp. conditions	Isotherm model	Adsorption nature associated with the model(s)	Figures of merit
Zn(2)Al-NO_3-COP (cont.)	Calcination at 150 ºC and rehydration in 0.27-28.70 mM TB at 60 ºC	Langmuir	Chemisorption	**q_m** = 4126.77mgg^{-1} **K_L**= 4.36·10^{-5} Lmg^{-1} **R_L**= 0.63 **Pearson's r:** 0.61 **Adj. R^2:** 0.17 **p-value**: 0.27
		Dubinin-Radushkevich	Chemisorption/ Pore filling mechanism	**q_m**= 219.20 mgg^{-1}; **K_{DR}**= 0.00312 mol^{2}J^{-2} (0.0021- **st.error**); **Pearson's r:** 0.65 **Adj. R^2:** 0.24 **p-value**: 0.24
Mg(3)Al-CO_3-SH	Calcination at 150 ºC and rehydration in 0.27-28.70 mM TB at 20 ºC	Temkin	Chemisorption	**A_T** = 0.23 Lg^{-1} (0.032- **st.error)** **b**= 9.47 (2.880- **st.error)**
	Calcination at 150 ºC and rehydration in 0.27-28.70 mM TB at 60 ºC	-	-	-

pp. 31-33 contain description of used adsorption isotherm models

Due to high values of standard errors it was not possible to determine the mechanism of TB adsorption onto **Mg(3)Al-CO_3-SH/CALC150** at 60 ^{0}C.

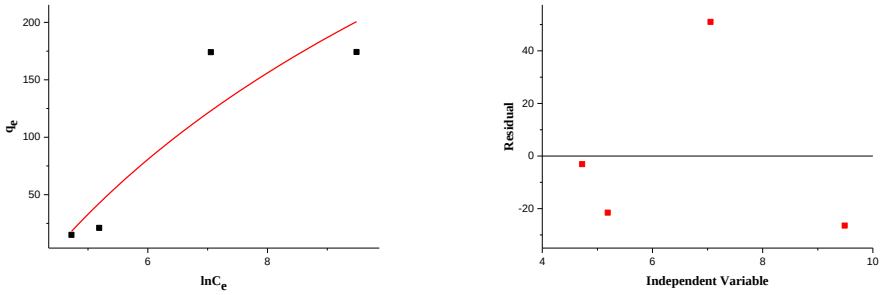

Figure 51. Fitting of data (Temkin isotherm (non-linear)) for adsorption of TB at 20 ^{0}C onto **Mg(3)Al-CO$_3$-SH** thermally treated at 150 ºC

Table 25 demonstrates that the nature of adsorption of TB is chemisorption with formation a monolayer. Using the Langmuir isotherm model, the maximum monolayer capacity is higher for adsorption of TB at 60 ^{0}C onto **Zn(2)Al-NO$_3$-COP/CALC150** compared to the same system at 20 ^{0}C (4127 mgg^{-1} *vs.* 3048 mgg^{-1}). The R_L parameter in both cases confirms that chemisorption process is favourable (values are lower than 1). Besides, Dubinin-Radushkevich model was successfully applied for fitting of TB adsorption experimental data at 60 ºC, revealing that the energy value for removal of a molecule from its location corresponds to 400 kJ mol^{-1}, calculated from equation **22** (Chapter 2). This order of magnitude implies that a strong interaction between adsorbate and adsorbent is established, supporting the chemical nature of the adsorption process. According to some authors this can correspond to grafting of the anion onto the hydroxylated sheets, through exchange of hydroxyl group of the sheet by the oxygen of anionic group (Elkhattabi, et al. 2016).

However, the adsorption of TB on the surface of **Mg(3)Al-CO$_3$-SH/CALC150** particles is different (**Table 25**). Experimental data obtained at 20 ºC was successfully fitted using Temkin adsorption isotherm, which is based on a chemisorption mechanism (Ismadji, Soetaredjo and Ayucitra 2015). Besides, the parameters of Temkin isotherm model allow the evaluation of interaction of ions in solution (A_T) and adsorbent-adsorbate interaction (RT/b), as well. In this case, the latter parameter value is equal to 257.23, which is a sign of strong interaction between adsorbent surface and adsorbate molecules. A_T is lower than 1 and is in agreement with the literature data for other systems such as adsorption of phosphate anions onto cellulose membranes (Nechifor, et al. 2015). Nonetheless, the BET surface area of **Mg(3)Al-CO$_3$-SH/CALC150** is 2 times higher than calcined **Zn(2)Al-NO$_3$-COP/CALC150** (10 vs 5 m^{2}g^{-1}, section 4.2.2) and the pore size distribution shows strong hysteresis loop, which indirectly points out for the possibility of multilayer adsorption, as well.

From literature it is known that chemisorption can be observed in solutions even at room temperature. Chemisorption can proceed together with physisorption, depending on adsorbate and adsorbent structure (Kipling 1965). For example, hydrogen bonds are considered by some authors as physisorption and by others as chemisorption, because their formation energy lies in between (4-30 $kJmol^{-1}$) (Ballantine Jr., et al. 1997); (Sims, Harmer and Quinton 2019). However, chemisorption initially can change the surface of adsorbent and afterwards, physical adsorption of species from solution can take place onto the chemisorbed layer. In the latter case preferential physical adsorption is observed as second layer on the first chemisorbed one. Thus, the final isotherm can be envisaged as the sum of two isotherms: dependent and independent from solution concentration (Kipling 1965).

The thermodynamic parameters calculated according to equations **23-25** are depicted in **Table 26** and show that adsorption of TB onto both LDH adsorbents is not spontaneous and endothermic. The positive values of variation of Gibbs energy is an indication of presence of energy barrier (which is in agreement with high mean free energy evaluated from Dubinin-Radushkevich model, namely 400 $kJmol^{-1}$, as was discussed before). The decrease of ΔG values with increase of temperature shows that the increase in temperature stimulates the adsorption process. The latter can be explained by the chemisorption nature of the adsorption process. The endothermic character of the process is a sign of chemical reaction between adsorptive and the layer surface of adsorbent along with positive values of entropy change. According to the literature, the surface of the adsorbent can be classified as energetically homogeneous or heterogenous, based on its energetic state. Furthermore, the heterogeneous surface can be presented as uniformly or exponentially non-homogeneous. The system's entropy (ΔS_θ) is determined as sum of adsorbed compound entropy (ΔS_a) and adsorbent's entropy (ΔS_s). It is possible to assume that ΔS_θ does not change with surface coverage increase, when variation in the adsorbed compound entropy ($\Delta S_a < 0$) is the only effect taken into account: adsorbed molecules are fixed onto the adsorbent surface and possess few degrees of freedom. In the case of chemisorption, breaking of bonds with different strength occurs along with variation of surface structure and the variation of adsorbent's entropy ($\Delta S_s > 0$), with high impact to the total entropy of the system. Thus, the total entropy of the system can be positive or negative, depending on the predominating effect of ΔS_a or ΔS_s. However, when adsorption occurs onto uniformly non-homogeneous surface the system's entropy (ΔS_θ) varies with surface coverage (in this case the adsorbent's active centres are distributed linearly based on their enthalpy of adsorption) (Radeva, Valcheva and Veleva 2009). For example, Saha and Chowdhury showed, that adsorption of Cr(VI) on the surface of chitosan is endergonic at 323 and 333 K, with positive values of entropy change (Saha and Chowdhury 2011).

Table 26. Estimation of thermodynamic parameters of TB adsorption onto LDH

LDH	ΔG, kJmol^{-1}	ΔH, kJmol^{-1}	ΔS, Jmol^{-1}K^{-1}
Zn(2)Al-NO_3-COP/CALC150	5.38 (293 K); 4.77 (333 K)	9.82	15.16
Mg(3)Al-CO_3-SH/CALC150	10.55 (293 K); 4.71 (333 K)	53.25	145.76

Data from **Table 27** confirms the adsorption mechanisms suggested above. The increase of maximum monolayer capacity of calcined **Zn(2)Al-NO_3-COP/CALC150** particles with temperature growth can be associated with chemisorption mechanism of TB adsorption. On the other hand, the increase of surface area with temperature (recall the discussion of textural properties of LDH materials- section 4.2.2) can justify the percentage of fixed TB molecules by chemisorption. A very small difference with temperature increase in the values of adsorbed TB for **Mg(3)Al-CO_3-SH/CALC150** is an indication of a physisorption (multilayer) mechanism co-presence with monolayer chemisorption (Dabrowski 2001); (Davis and Dykstra 2012).

Table 27. Average values of adsorbed TB onto the LDH adsorbent

LDH	Average TB adsorbed RT, %	Average TB adsorbed HT, %
Zn(2)Al-NO_3-COP/CALC150	11.4	17.0
Mg(3)Al-CO_3-SH/CALC150	13.2	14.0

Table 28 depicts the values of parameters of best fitted kinetic models for both adsorbents, only for some of the TB solutions tested, at 20 ^{0}C and 60 ^{0}C. The kinetics of TB adsorption is governed by intraparticle diffusion as a rate-limiting step for both studied adsorbents and temperatures (**Table 28**). Thus, it is based on the initial external mass transfer with continuous diffusion into pores (Cooney 1999); (Ismadji, Soetaredjo and Ayucitra 2015). However, for many concentrations it was not possible to determine the best fitted model due to the high standard errors associated. Even for the models presented in **Table 28** the magnitude of scattering of residuals relative to the zero line **(Figure 53**) can mean that several processes have an impact on the adsorption of TB, thereby complicating the description of the adsorption process. As referred previously, (recall **Figure 50**) there is influence of desorption process, especially for long timescales for both studied adsorbents. **Figure 49** and **Figure 52** show that **Zn(2)Al-NO_3-COP/CALC150** reveals better affinity to TB and its adsorbed amount is much higher during first 2 hours compared to **Mg(3)Al-CO_3-SH/CALC150**. The latter adsorbent slowly saturates with the dye during the first 3-4 hours depending on

temperature. However, in the case of **Zn(2)Al-NO$_3$-COP/CALC150**, desorption processes seem to occur during the first hours of immersion. Thus, despite the chemisorption character of adsorption according to the adsorption isotherm model fitted, there is indication of physisorption ongoing on the chemisorbed TB monolayer as well. As a result, the co-existence of chemisorption and physisorption can be a reason for difficulties in fitting the adsorption kinetic data using one single model.

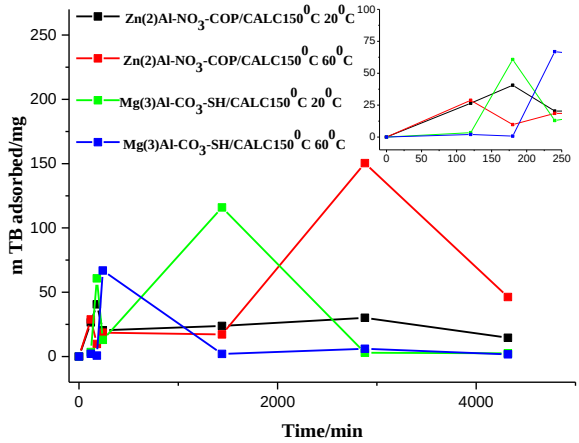

Figure 52. Dependence of adsorbed TB mass on time (concentration of TB of 28.70 mM)

Table 28. Kinetic models used to fit adsorption data of TB onto **Zn(2)Al-NO$_3$-COP** and **Mg(3)Al-CO$_3$-SH** thermally treated at 150 ºC

Adsorbent	**Exp. conditions**	**Kinetics model**	**Limiting step according to the model**	**Figures of merit**
Zn(2)Al-NO$_3$-COP	Calcination at 150 ^{0}C and rehydration in 28.70 mM TB at 20 ^{0}C	Parabolic diffusion	Intraparticle diffusion	**k** = 0.23 min$^{-0.5}$ (0.065-**st.error**);

Table 28. Kinetic models used to fit adsorption data of TB onto **Zn(2)Al-NO$_3$-COP** and **Mg(3)Al-CO$_3$-SH** thermally treated at 150 ^{o}C (cont.)

Adsorbent	Exp. conditions	Kinetics model	Limiting step according to the model	Figures of merit
Zn(2)Al-NO$_3$-COP (cont.)	Calcination at 150 ^{0}C and rehydration in 0.27 mM TB at 20 ^{0}C	Parabolic diffusion	Intraparticle diffusion	**k** = 0.15 min-$^{0.5}$ (0.038-**st.error**);
Mg(3)Al-CO$_3$-SH	Calcination at 150 ^{0}C and rehydration in 0.27 mM TB at 20 ^{0}C	Parabolic diffusion	Intraparticle diffusion	**k** = 0.15 min-$^{0.5}$ (0.038-**st.error**);
	Calcination at 150 ^{0}C and rehydration in 1.39 mM TB at 60 ^{0}C	Parabolic diffusion	Intraparticle diffusion	**k**= 0.20 min-$^{0.5}$ (0.048-**st.error**);

pp.35-36 contain description of used adsorption kinetic models

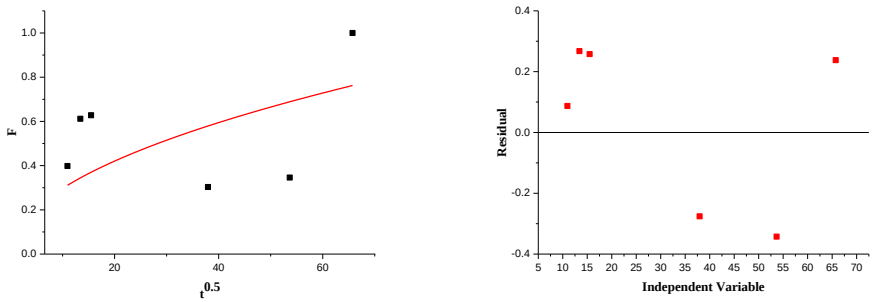

Figure 53. Fitting of TB adsorption kinetics (Parabolic diffusion model (non-linear)) and corresponding residual plot for 2.85 mM solution at 20 ^{0}C onto **Zn(2)Al-NO$_3$-COP** thermally treated at 150 ^{o}C

5.3 Adsorption studies of MBT onto LDH

This section is devoted to adsorption studies of MBT. MBT solution used in this study was prepared as an initial aqueous solution (in this case MBT was dissolved in an equimolar solution of NaOH). Other solutions of MBT were prepared by dissolution of MBT in ethanol. The following adsorbents were studied: **Mg(3)Al-CO$_3$-SH**, which is a commercially available type of LDH and **Mg(3)Al-CO$_3$-COP** with identical chemical composition but obtained in the lab. The aim of this comparison is to understand if the presence of organic impurities in **Mg(3)Al-CO$_3$-SH** can influence MBT immobilization by calcination-rehydration route. Furthermore, nitrate-containing LDH materials prepared by coprecipitation reaction in reverse microemulsion (**Zn(2)Al-NO$_3$-REV**, **Zn(2)Al-NO$_3$-**

REVN, **Zn(2)Al-NO_3-REVC**), **Zn(2)Al-NO_3-COP** and **Zn(2)Al-CO_3-AN** aqueous slurries were also studied to get insights on the possible influence of external surface adsorption when intercalated species are present as well (which will be discussed in more detail in chapter 6).

5.3.1 Adsorption of aqueous MBT by LDH

5.3.1.1 Adsorption of MBT in Mg(3)-Al-CO_3 LDH

MBT adsorption experiments were performed in a similar manner as presented before for PhPh and TB. **Figure 54** and **Figure 55** present data obtained using **Mg(3)Al-CO_3-SH** LDH calcined at 150 ^{0}C and 650 ^{0}C as adsorbents, immersed into MBT solutions with concentrations in the range 0.39 mM - 23.59 mM for adsorption isotherm experiments and kinetic studies at 20 ^{0}C and 60 ^{0}C.

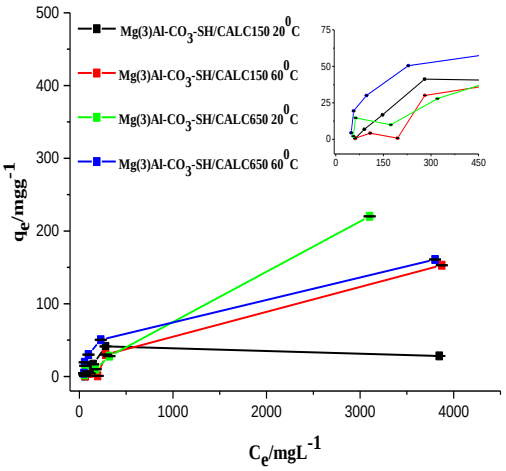

Figure 54. Variation of q_e with C_e corresponding to the adsorption of MBT at 20 ^{0}C and 60 ^{0}C onto **Mg(3)Al-CO_3-SH**, thermally treated at 150 ^{0}C and 650 ^{0}C

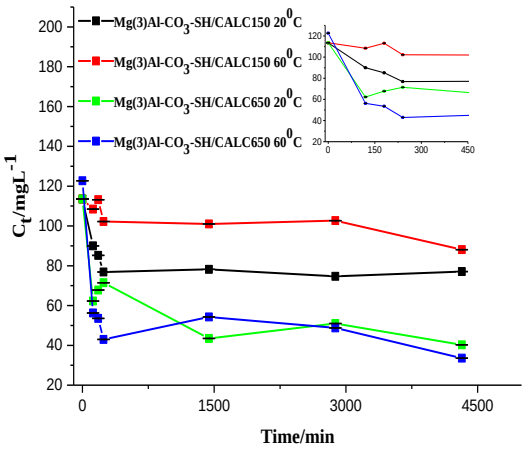

Figure 55. MBT adsorption at 20 ^{0}C and 60 ^{0}C onto **Mg(3)Al-CO$_3$-SH** thermally treated at 150 ^{0}C and 650 ^{0}C with concentration of MBT 0.68 mM

Figure 54 shows a "L" adsorption isotherm with a plateau for MBT adsorbed onto **Mg(3)Al-CO$_3$-SH** previously calcined at 150 ^{0}C (for studies performed at 20 ^{0}C), corresponding to a continuous saturation of adsorbent with this corrosion inhibitor, while for the rest of tested adsorbents and conditions the isotherm corresponds the "L" without plateau. In addition, there is a domination of adsorption process over desorption for monitored time (**Figure 55**).

Table 29 summarizes the selected models for adsorption isotherms. These findings show that aqueous MBT can be adsorbed onto **Mg(3)Al-CO$_3$-SH** after calcination (either at 150 ^{0}C or 650 ^{0}C) and it is governed by a chemisorption mechanism at both 20 ºC and 60 ºC (**Figure 56**). **Table 30** presents thermodynamic parameters calculated from equations **23 - 25**.

The maximum monolayer capacity is higher for **Mg(3)Al-CO$_3$-SH** calcined at 650 ^{0}C compared to the same LDH calcined at 150 ^{0}C (108.57 vs 36.75 mgg^{-1}). **Table 20** (section 4.2.2) confirms that the increase in the calcination temperature leads to growth in BET surface area (10 *vs.* 39 m^{2}g^{-1}). Furthermore, evaluation of adsorbent-adsorbate interactions by Temkin isotherm model gives *RT/b* values 232.65 and 295.38 for SH calcined at 150 ^{0}C/60 ^{0}C and 650 ^{0}C/20^{0}C, respectively, and the values of free energy per molecules estimated from Dubinin-Radushkevich model constant parameter are 536.06 and 604.12 kJmol^{-1} for these adsorbents. Consequently, the adsorption of aqueous MBT onto **Mg(3)Al-CO$_3$-SH** is governed by a chemisorption mechanism, independently of the temperature of calcination and temperature at which the adsorption process occurred.

Table 29. Adsorption isotherm models used to fit adsorption data of MBT onto LDH **Mg(3)Al-CO_3-SH** adsorbent

Adsorbent	**Exp. conditions**	**Isotherm model**	**Adsorption nature associated with the model(s)**	**Figures of merit**
Mg(3)Al-CO_3-SH	Calcination at 150 ºC and rehydration in 0.38-23.59 mM MBT at 20 ºC	Langmuir	Chemisorption	**q_m** = 36.75 mgg^{-1} **K_L**= 0.78 Lmg^{-1} **R_L**= $3.23 \cdot 10^{-3}$ **Pearson's r:** 0.74 **Adj. R^2:** 0.4 **p-value**: 0.15
	Calcination at 150 ºC and rehydration in 0.38-23.59 mM MBT at 60 ºC	Temkin	Chemisorption	**A_T** = 0.22 Lg^{-1} (0.014- **st.error)** **b**= 11.90 (2.662- **st.error)**
		Dubinin-Radushkevich	Chemisorption/ Pore filling mechanism	**q_m**= 18.73 mgg^{-1}; **K_{DR}**=0.00174 mol^2J^{-2} (0.00125-**st.error**); **Pearson's r:** 0.62 **Adj. R^2:** 0.19 **p-value**: 0.26
	Calcination at 650 ºC and rehydration in 0.38-23.59 mM MBT at 20 ºC	Temkin	Chemisorption	**A_T** = 0.23 Lg^{-1} (0.023- **st.error)** **b**= 8.25 (2.574- **st.error)**
		Dubinin-Radushkevich	Chemisorption/ Pore filling mechanism	**q_m**= 49.40 mgg^{-1}; **K_{DR}**=0.00137mol^2J^{-2} ($7.349 \cdot 10^{-4}$-**st.error**); **Pearson's r:** 0.73 **Adj. R^2:** 0.38 **p-value**: 0.16

Table 29. Adsorption isotherm models used to fit adsorption data of MBT onto LDH **Mg(3)Al-CO_3-SH** adsorbent (cont.)

Adsorbent	Exp. conditions	Isotherm model	Adsorption nature associated with the model(s)	Figures of merit
Mg(3)Al-CO_3-SH (cont.)	Calcination at 650 ºC and rehydration in 0.38-23.59 mM MBT at 60 ºC	Langmuir	Chemisorption	**q_m**=108.57mgg^{-1} (51.956- st.error) **K_L**= 0.0036 Lmg^{-1} **R_L**= 0.059 **Pearson's r:** 0.74 **Adj. R^2:** 0.4 **p-value**: 0.15

pp. 31-33 contain description of used adsorption isotherm models

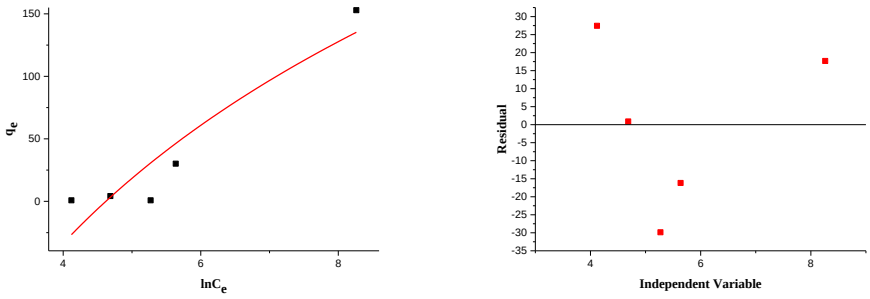

Figure 56. Fitting of data (Temkin model (non-linear)) for adsorption of MBT at 60 ^{0}C onto **Mg(3)Al-CO_3-SH** thermally treated at 150 ^{0}C

In addition, the estimated thermodynamic parameters presented in **Table 30** reveal that adsorption of aqueous MBT solutions by both **Mg(3)Al-CO_3-SH/CALC150** and **Mg(3)Al-CO_3-SH/CALC650** is an endergonic reaction (which is consistent with the chemisorption nature of the process). The increase of temperature favours the adsorption onto **Mg(3)Al-CO_3-SH/CALC150** (decrease of positive ΔG), whereas an opposite behaviour is observed **Mg(3)Al-CO_3-SH/CALC650**. Moreover, adsorption of aqueous MBT is an exothermic reaction for **Mg(3)Al-CO_3-SH/CALC650** and endothermic reaction for **Mg(3)Al-CO_3-SH/CALC150**. From literature, it is known that physisorption is an intrinsic exothermic process. However, chemisorption may also be an endothermic reaction (De Boer 1957). The symmetric signs of entropy change values depending on the adsorbent type can indicate different impacts of ΔS_a or ΔS_s in the total entropy change.

Table 30. Thermodynamic parameters of aqueous MBT adsorption onto calcined **Mg(3)Al-CO_3-SH**

LDH	ΔG, kJmol^{-1}	ΔH, kJmol^{-1}	ΔS, Jmol^{-1}K^{-1}
Mg(3)Al-CO_3-SH/CALC150	11.97 (293 K); 8.95 (333 K)	34.07	75.44
Mg(3)Al-CO_3-SH/CALC650	6.44 (293 K); 8.76 (333 K)	-10.51	-57.88

The kinetics of adsorption of MBT in **Mg(3)Al-CO_3-SH** is governed by intraparticle diffusion (**Table 31** and **Figure 57**). The decrease of adsorbed MBT at 60 ^{0}C onto **Mg(3)Al-CO_3-SH/CALC150** can be attributed to possible interactions of MBT and organic impurities of commercial LDH or co-presence of physisorption processes (**Table 31** and **Table 32**). The latter possibility cannot be excluded on the chemisorbed layer, as discussed in the previous sections for TB. **Table 31** includes only values of parabolic diffusion constant for the most concentrated solution. The constants estimated by this model using MBT solutions in the range of 0.39 mM - 23.59 mM are: $k_{average}$= 0.16±0.007 min$^{-0.5}$ for **Mg(3)Al-CO_3-SH/CALC150** at 20 ^{0}C and $k_{average}$= 0.14±0.02 min$^{-0.5}$ for **Mg(3)Al-CO_3-SH/CALC150** at 60 ^{0}C; $k_{average}$=0.12±0.04 min$^{-0.5}$ for **Mg(3)Al-CO_3-SH/CALC650** at 20 ^{0}C and $k_{average}$= 0.14±0.04 min$^{-0.5}$ for **Mg(3)Al-CO_3-SH/CALC650** at 60 ^{0}C.

Table 31. Kinetic models used to fit adsorption data of MBT onto LDH **Mg(3)Al-CO_3-SH** adsorbent

Adsorbent	Exp. conditions	Kinetics model	Limiting step according to the model(s)	Figures of merit
Mg(3)Al-CO_3-SH	Calcination at 150 ºC and rehydration in 23.59 mM MBT at 20 ºC	Parabolic diffusion	Intraparticle diffusion	**k** = 0.17 min$^{-0.5}$ (0.044-**st.error**);

Table 31. Kinetic models used to fit adsorption data of MBT onto LDH **Mg(3)Al-CO_3-SH** adsorbent (cont.)

Adsorbent	Exp. conditions	Kinetics model	Limiting step according to the model(s)	Figures of merit
Mg(3)Al-CO_3-SH (cont.)	Calcination at 150 ºC and rehydration in 23.59 mM MBT at 60 ºC	Parabolic diffusion	Intraparticle diffusion	**k** = 0.14 $min^{-0.5}$ (0.058-**st.error**);
	Calcination at 650 ºC and rehydration in 23.59 mM MBT at 20 ºC	Parabolic diffusion	Intraparticle diffusion	**k** = 0.09 $min^{-0.5}$ (0.032-**st.error**);
	Calcination at 650 ºC and rehydration in 23.59 mM MBT at 60 ºC	Parabolic diffusion	Intraparticle diffusion	**k** = 0.18 $min^{-0.5}$ (0.040-**st.error**);

pp. 35-36 contain description of used adsorption kinetic models

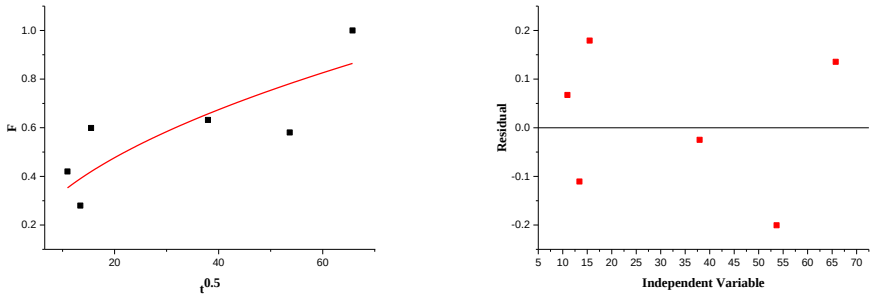

Figure 57. Fitting of MBT adsorption kinetics (Parabolic diffusion model (non-linear)) and corresponding residual plot for 0.68 mM MBT adsorption at 60 ^{0}C onto **Mg(3)Al-CO_3-SH** thermally treated at 150^{0}C

Table 32. Average values of adsorbed aqueous MBT onto **Mg(3)Al-CO_3-SH** adsorbent

LDH	Average MBT adsorbed RT, %	Average MBT adsorbed HT, %
Mg(3)Al-CO_3-SH/CALC150	21.6	14.0
Mg(3)Al-CO_3-SH/CALC650	31.2	38.4

Identical studies were performed using **Mg(3)Al-CO_3-COP** obtained in the lab, after performing thermal treatments similar to those carried out for SH: calcination at 150 ºC and 650 ºC.

Figure 58 and **Figure 59** depict data obtained for adsorption of MBT in **Mg(3)Al-CO_3-COP** LDH, using MBT solutions concentrations in the range 0.47 mM - 24.07 mM, for determination of adsorption isotherms and adsorption kinetics at 20 ^{0}C. The corresponding results, namely selection of adsorption isotherm and kinetic model of adsorption are presented in **Table 33 - Table 35** and **Figure 60 - Figure 61**.

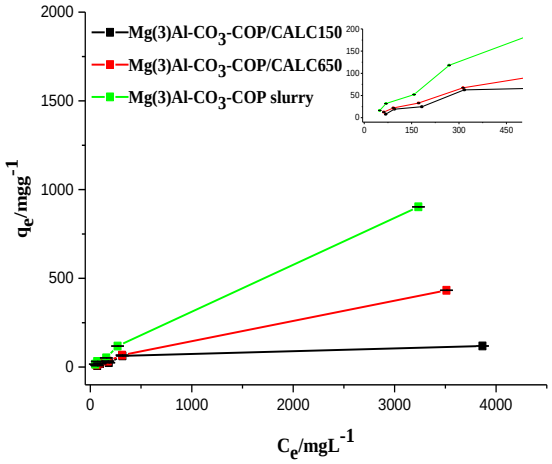

Figure 58. Variation of q_e with C_e corresponding to the adsorption of MBT at 20 ^{0}C onto **Mg(3)Al-CO_3-COP** thermally treated at 150 ^{0}C, 650 ^{0}C and in aqueous slurry form

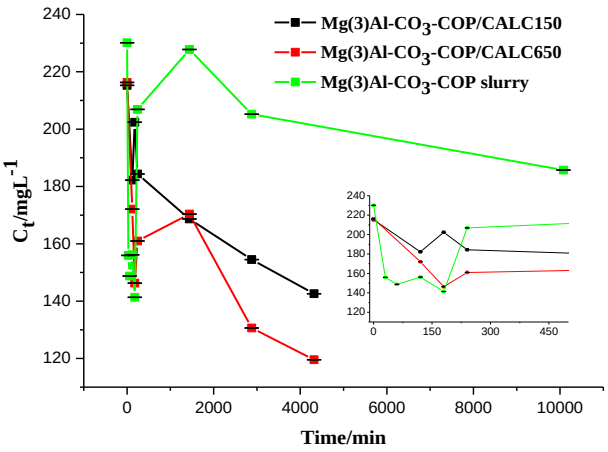

Figure 59. MBT adsorption at 20 ^{0}C onto **Mg(3)Al-CO_3-COP** thermally treated at 150 ^{0}C, 650 ^{0}C and in aqueous slurry with concentration of MBT 1.29 mM

Figure 58 presents a "L"-shaped curve for MBT adsorption isotherm onto calcined **Mg(3)Al-CO_3-COP** LDH and slurry of LDH without thermal treatment, which is an indication of continuous saturation of MBT onto the studied adsorbent (Limousin, et al. 2007). Looking at MBT concentration in solution as a function of time (**Figure 59**), adsorption is the dominating process throughout the timescale studied for calcined LDH samples. Nevertheless, in the case of LDH slurry, there seems to occur desorption process after 24 h, followed again by further adsorption.

Table 33. Adsorption isotherm models used to fit adsorption data of MBT onto LDH **Mg(3)Al-CO_3-COP**

Adsorbent	**Exp. conditions**	**Isotherm model**	**Adsorption nature associated with the model(s)**	**Figures of merit**
Mg(3)Al-CO_3-COP	Calcination at 150 ºC and rehydration in 0.47-24.07 mM MBT at 20 ºC	Langmuir	Chemisorption	**q_m** = 100.98mgg^{-1} **K_L**= 0.00253Lmg^{-1} **R_L**= 0.090 **Pearson's r:** 0.61 **Adj. R^2:** 0.16 **p-value**: 0.17
		Temkin	Chemisorption	**A_T** = 0.24 Lg^{-1} (0.009-**st.error)** **b**= 14.05 (1.525-**st.error)**
	Calcination at 650 ºC and rehydration in 0.47-24.07 mM MBT at 20 ºC	Dubinin-Radushkevich	Chemisorption/ Pore filling mechanism	**q_m**= 108.85 mgg^{-1}; **K_{DR}**=0.00163mol^{2}J^{-2} (8.00·10^{-4}-**st.error**); **Pearson's r:** 0.76 **Adj. R^2:** 0.44 **p-value**: 0.13

Table 33. Adsorption isotherm models used to fit adsorption data of MBT onto LDH **Mg(3)Al-CO_3-COP** (cont.)

Adsorbent	Exp. conditions	Isotherm model	Adsorption nature associated with the model(s)	Figures of merit
Mg(3)Al-CO_3-COP (cont.)	Slurry immersion in 0.38-23.59 mM MBT at 20 ºC	Langmuir	Chemisorption	**q_m**=3251.51mgg^{-1} (51.956- st.error) **K_L**= 0.00030Lmg^{-1} **R_L**= 0.42 **Pearson's r:** 0.72 **Adj. R^2:** 0.37 **p-value**: 0.17
		Dubinin-Radushkevich	Chemisorption/ Pore filling mechanism	q_m= 194.42 mgg^{-1}; K_{DR}=0.00115mol^{2}J^{-2} (5.458·10^{-4}- st.error); Pearson's r: 0.77 Adj. R^2: 0.46 p-value: 0.13

pp. 31-33 contain description of used adsorption isotherm models

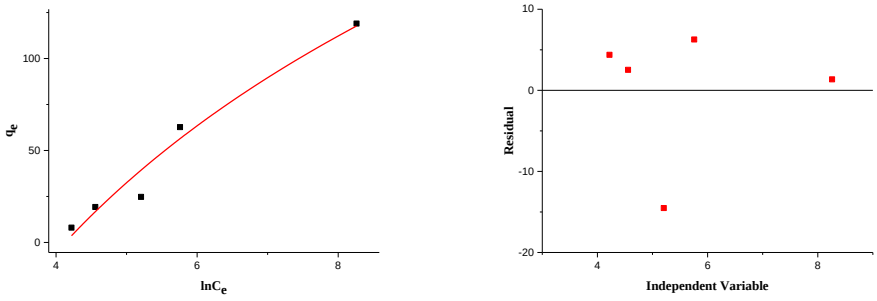

Figure 60. Fitting of data (Temkin model (non-linear)) for adsorption of MBT at 20 ^{0}C onto **Mg(3)Al-CO_3-COP** thermally treated at 150 ^{0}C

Table 33 shows that aqueous MBT is adsorbed onto calcined and slurry form of **Mg(3)Al-CO_3-COP** according to a chemisorption mechanism. Besides, the maximum monolayer capacity of **Mg(3)Al-CO_3-COP/CALC650** and aqueous slurry **Mg(3)Al-CO_3-COP** is higher compared to the **Mg(3)Al-CO_3-SH/CALC150**. This can be associated with differences in the surface area of **Mg(3)Al-CO_3-COP** in either calcined or slurry forms, which are higher when compared to **Mg(3)Al-CO_3-SH**

(**Table 19** and **Table 20,** section 4.2.2). Additionally, *RT/b* parameter estimated from Temkin model is equal to 173.40, which is a sign of strong interaction between aqueous MBT and LDH adsorbent calcined at 150 ^{0}C. On the other hand, the values of free energy removal per molecule estimated from Dubinin-Radushkevich model constant parameter are 553.85 and 659.38 kJmol^{-1} for **Mg(3)Al-CO$_3$-COP/CALC650** and slurry form of **Mg(3)Al-CO$_3$-COP**, respectively, supporting existence of a chemisorption type of interaction between MBT and these LDH materials.

Furthermore, adsorption of aqueous MBT by **Mg(3)Al-CO$_3$-COP/CALC150, Mg(3)Al-CO$_3$-COP/CALC650** and **Mg(3)Al-CO$_3$-COP** (slurry) is an endergonic reaction (in agreement with the chemisorption nature determined before) (**Table 34**). The decrease of ΔG reveals the easiness of aqueous MBT adsorption with increase of calcination temperature. The values of ΔH and ΔS could not be evaluated due to measurements had been carried out at 20 ºC, only.

Table 34. Thermodynamic parameters of aqueous MBT adsorption onto **Mg(3)Al-CO$_3$-COP**

LDH	ΔG,kJmol^{-1}	ΔH, kJmol^{-1}	ΔS, Jmol^{-1}K^{-1}
Mg(3)Al-CO$_3$-COP/CALC150	8.48 (293 K)	-	-
Mg(3)Al-CO$_3$-COP/CALC650	5.10 (293 K)	-	-
Mg(3)Al-CO$_3$-COP slurry	3.11 (293 K)	-	-

Intraparticle diffusion of aqueous MBT into **Mg(3)Al-CO$_3$-COP** is a rate-limiting step under all studied conditions (**Figure 61** and **Table 35**). **Table 35** includes only values of parabolic diffusion constant for the most concentrated solution. The constants estimated in the range of concentrations 0.47 mM - 24.07 mM are: $k_{average}$= 0.13±0.02 min^{-1} for **Mg(3)Al-CO$_3$-COP/CALC150** at 20 ^{0}C and $k_{average}$= 0.14±0.02 min^{-1} for **Mg(3)Al-CO$_3$-COP/CALC650** at 20 ^{0}C; $k_{average}$= 0.15±0.02 min^{-1} for **Mg(3)Al-CO$_3$-COP/slurry** at 20 ^{0}C. The values of adsorbed MBT (**Table 36**) are close and correlate with BET surface area of **Mg(3)Al-CO$_3$-COP** particles (**Table 19**, section 4.2.2).

Table 35. Kinetic models used to fit adsorption data of MBT onto LDH **Mg(3)Al-CO_3-COP**

Adsorbent	Exp. conditions	Kinetics model	Limiting step according to the model(s)	Figures of merit
Mg(3)Al-CO_3-COP	Calcination at 150 ºC and rehydration in 24.07 mM MBT at 20 ºC	Parabolic diffusion	Intraparticle diffusion	**k** = 0.17 $min^{-0.5}$ (0.062-**st.error**);
	Calcination at 650 ºC and rehydration in 24.44 mM MBT at 20 ºC	Parabolic diffusion	Intraparticle diffusion	**k** = 0.16 $min^{-0.5}$ (0.051-**st.error**);
	Slurry immersion in 26.71 mM MBT at 20 ºC	Parabolic diffusion	Intraparticle diffusion	**k** = 0.15 $min^{-0.5}$ (0.029-**st.error**);

pp. 35-36 contain description of used adsorption kinetic models

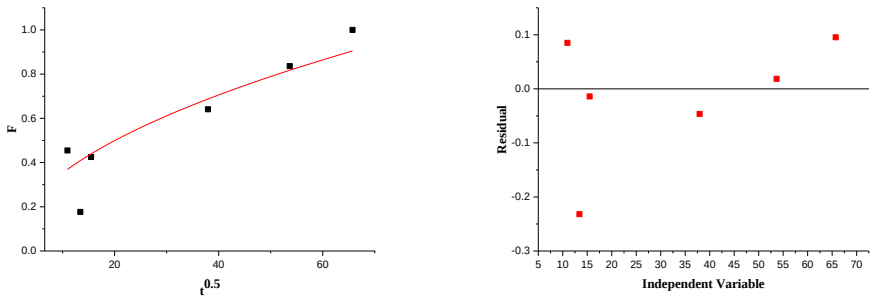

Figure 61. Fitting of MBT adsorption kinetics (Parabolic diffusion model (non-linear)) and corresponding residual plot for 1.29 mM solution at 20 ^{0}C onto **Mg(3)Al-CO_3-COP** thermally treated at 150 ^{0}C

Table 36. Average values of adsorbed aqueous MBT onto the **Mg(3)Al-CO_3** adsorbent

LDH	Average MBT adsorbed RT, %
Mg(3)Al-CO_3-COP/CALC150	23.4
Mg(3)Al-CO_3-COP/CALC650	27.2
Mg(3)Al-CO_3-COP slurry	22.2

*adsorption experiments were not performed at 60 ^{0}C, because synthesis of Mg(3)Al-MBT-CALC 650 was done at room temperature

XRD diffractograms and FTIR spectra do not reveal differences between **Mg(3)Al-CO_3-COP** and **Mg(3)Al-CO_3-SH** (section 4.1.1 and 4.1.2), though the textural and thermal degradation properties of the mentioned LDH being different. Analysis of **Table 29**-**Table 36** show that along with the same main adsorption nature (chemisorption), the adsorption kinetic constants estimated using the parabolic diffusion model also look similar (**Table 37**). **Table 37** presents the most representative parameters of each type of MgAl LDH samples (obtained in lab by coprecipitation vs acquired commercially).

Table 37. Comparative table with several parameters of **Mg(3)Al-CO_3-SH** and **Mg(3)Al-CO_3-COP** thermally treated at 150 ^{0}C and 650 ^{0}C

LDH	BET surface area,m^2g^{-1}	k_{av} of parabolic diffusion model	Average MBT adsorbed RT, %	ΔG, $kJmol^{-1}$
Mg(3)Al-CO_3-SH/CALC150	10	0.16	22	11.97
Mg(3)Al-CO_3-COP/CALC150	100	0.13	23	8.48
Mg(3)Al-CO_3-SH/CALC650	39	0.12	31	6.44
Mg(3)Al-CO_3-COP/CALC650	116	0.14	27	5.10

Figure 62 and **Figure 63** show the influence of adsorption/desorption process for the highest and lowest MBT concentrations used in the range, namely 24.07 mM and 0.47 mM, during 72 h. In the highest studied MBT concentration (24.07 mM) a strong influence of desorption is observed after 1000 min for both studied adsorbents calcined at 150 ^{0}C (desorption is more significant for **Mg(3)Al-CO_3-COP/CALC150**). Nonetheless, for the lowest MBT concentration tested (0.47mM) the impact of desorption is less significant. For samples calcined at 650 ^{o}C higher adsorption extent is observed for both adsorbents. However, the influence of desorption in this case is also more significant for both studied concentrations and occurs in two steps. In 24.07 mM aqueous solution of MBT the detected difference in concentrations is around 3.76 mM and 5.18 mM on the first and second desorption steps, respectively, for **Mg(3)Al-CO_3-SH** thermally treated at 650 ^{0}C. For **Mg(3)Al-CO_3-COP** thermally treated at 650 ^{0}C the difference is even higher: 0.98 mM and 8.74 mM for the first and second desorption steps, respectively. Such behaviour can be explained by differences in textural properties of the studied adsorbents, that allow different amounts of MBT to be initially chemisorbed into the surface and later physisorbed as multilayers.

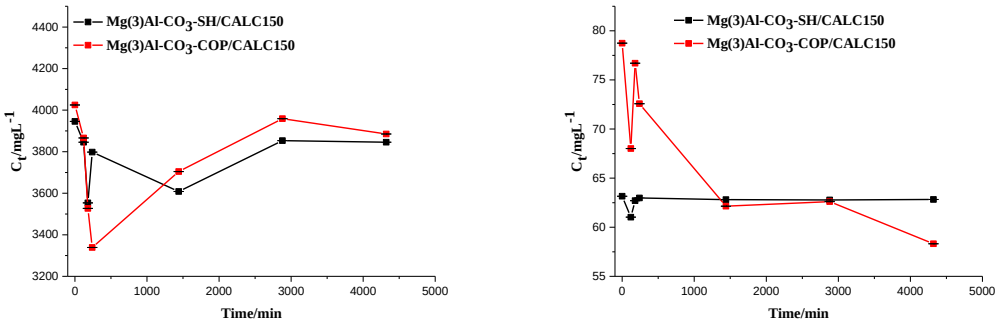

Figure 62. Variation of MBT concentration (using solutions with initial concentration of 24.07 mM and 0.47 mM) with time in the presence of **Mg(3)Al-CO_3-SH** and **Mg(3)Al-CO_3-COP** (both thermally treated at 150 ^{0}C), at 20 ^{0}C

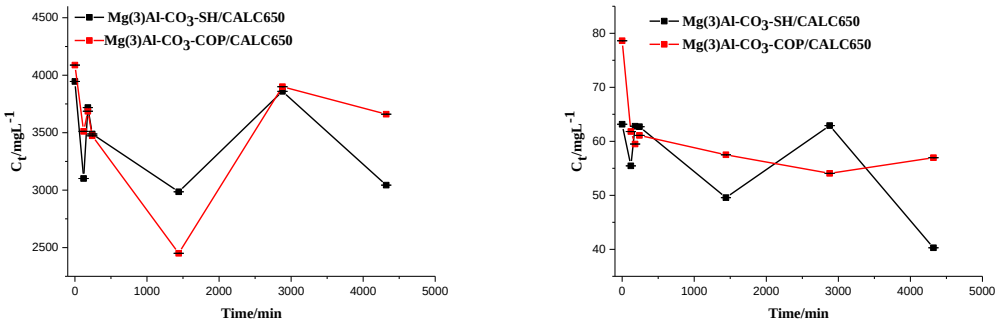

Figure 63. Variation of MBT concentration (using solutions with initial concentration of 24.07 mM and 0.47 mM) as a function of time in the presence of **Mg(3)Al-CO_3-SH** and **Mg(3)Al-CO_3-COP** (both thermally treated at 650 ^{0}C), at 20 ^{0}C

5.3.1.2 Adsorption of MBT in Zn(2)-Al-X (X=NO_3^-, CO_3^{2-}) LDH

The adsorption studies of MBT from aqueous solution onto the slurries of **Zn(2)Al-NO_3-COP** and **Zn(2)Al-CO_3-AN,** as well as for nitrate-containing LDH materials prepared by coprecipitation reaction in reverse microemulsion (**Zn(2)Al-NO_3-REV**, **Zn(2)Al-NO_3-REVN**, **Zn(2)Al-NO_3-REVC**), are presented below.

Figure 64 and **Figure 65** show the experimental data obtained for adsorption of MBT onto Zn(2)-Al-X (X=NO_3^-, CO_3^{2-}) LDH samples, from aqueous MBT solutions with concentrations in the range 0.23 mM - 25.15 mM, for adsorption isotherm studies and the variation of MBT concentration as a function of time using a solution with initial concentration of 25.15 mM.

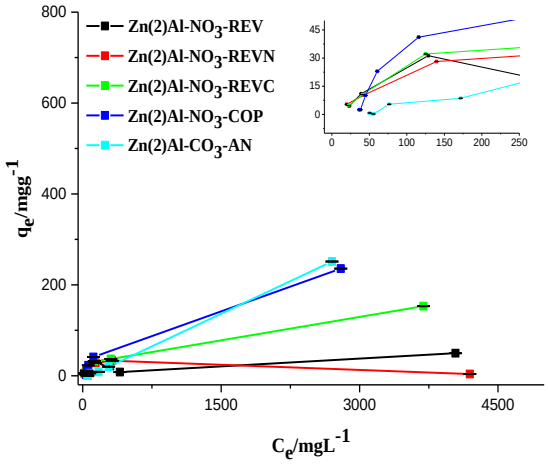

Figure 64. Variation of q_e with C_e corresponding to the adsorption of MBT at 20/23 ^{0}C onto **Zn(2)-Al-X** (X=NO_3^-, CO_3^{2-})

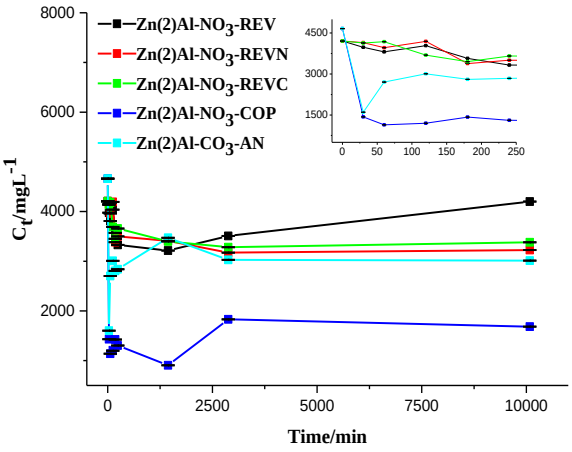

Figure 65. MBT adsorption at 20/23 ^{0}C onto **Zn(2)-Al-X** (X=NO_3^-, CO_3^{2-}) for a MBT with concentration 25.15 mM

Figure 64 presents an "L"-shaped curve with plateau for MBT adsorption isotherm onto **Zn(2)-Al-NO_3-REV**, **Zn(2)-Al-NO_3-REVN**. Isotherm of "L" shape without plateau was observed for **Zn(2)-Al-NO_3-REVC** and **Zn(2)-Al-NO_3-COP** and **Zn(2)-Al-CO_3-AN** LDH materials, consistent with saturation of MBT adsorbate onto these adsorbents (Limousin, et al. 2007). Similarly to the findings obtained for MgAl LDH samples, MBT adsorption in ZnAl LDH materials seems to be followed by

desorption processes, especially for **Zn(2)Al-NO_3-REV**, **Zn(2)Al-NO_3-COP** and **Zn(2)Al-CO_3-AN** (**Figure 65**).

Aqueous MBT solutions are adsorbed mainly by chemisorption mechanism onto the particles of LDH with nitrate prepared by coprecipitation reaction in reverse microemulsion (**Table 38**). The value of *RT/b* parameter is 38.88 for **Zn(2)Al-NO_3-REV**, which is lower compared to other LDH sorbents presented, though high enough to be classified as a process of chemisorption nature. In the case of **Zn(2)Al-NO_3-REVN** the experimental data was fitted using the Flory-Huggins model (**Figure 66**) with the isotherm exponent equal to 14 – which corresponds to the number of solute molecules on the adsorbent surface (Ismadji, Soetaredjo and Ayucitra 2015). Besides, the Flory-Huggins constant (K_{FH}) can be used for estimation of ΔG of sorption process ($\Delta G = -RT\ln K_{FH}$) (Latif, et al. 2018). The value of calculated ΔG is 32.81 kJ mol^{-1}. As a result, adsorption of MBT is not spontaneous and it is difficult to distinguish the nature of adsorption process: it is within the border between chemi- and physisorption (Humpola, et al. 2013). MBT adsorption onto **Zn(2)Al-NO_3-REVC** is governed by chemisorption (Langmuir isotherm model).

The fitting of experimental data using **Zn(2)Al-NO_3-COP** slurry as a sorbent was not successful. The standard error values were higher compared to the calculated parameters. However, aqueous MBT molecules are adsorbed by physisorption mechanism on the surface of **Zn(2)Al-CO_3-AN** LDH particles.

Table 38. Adsorption isotherm studies of aqueous MBT onto adsorbents **Zn(2)-Al-X** (X=NO_3^-, CO_3^{2-})

Adsorbent	Exp. conditions	Isotherm model	Adsorption nature associated with the model(s)	Figures of merit
Zn(2)Al-NO_3-REV	Powder immersed in 0.23-25.15 mM MBT at 23 ºC	Langmuir	Chemisorption	**q_m** = 56.53 mgg^{-1} **K_L**= 0.018 Lmg^{-1} **R_L**= 0.013 **Pearson's r:** 0.87 **Adj. R^2:** 0.68 **p-value**: 0.054
		Temkin	Chemisorption	**A_T** = 0.36 Lg^{-1} (0.115- **st.error)** **b**= 63.30 (31.210- **st.error)**
Zn(2)Al-NO_3-REVN	Powder immersed in 0.23-25.15 mM MBT at 23 ºC	Flory-Huggins	Surface coverage between adsorbate and adsorbent	**n**= -13.81 (0.952- **st.error**); **K_{FH}**=$1.62 \cdot 10^{-6}$ Lmg^{-1} ($9.621 \cdot 10^{-7}$ - **st.error**);
Zn(2)Al-NO_3-REVC	Powder immersed in 0.23-25.15 mM MBT at 23 ºC	Langmuir	Chemisorption	**q_m**=143.78 mgg^{-1} (38.880- st.error) **K_L**= 0.0019 Lmg^{-1} **R_L**= 0.11 **Pearson's r:** 0.85 **Adj. R^2:** 0.62 **p-value**: 0.072
Zn(2)Al-NO_3-COP	Slurry immersed in 0.23-25.15 mM MBT at 20 ºC	-	-	-
Zn(2)Al-CO_3-AN	Slurry immersed in 0.23-25.15 mM MBT at 20 ºC	Freundlich	Physisorption/ cooperative adsorption	**K_F**= 0.03 mgg^{-1} $(Lmg)^{-1.16}$ (0.0079- **st.error**); **a**= 1.16 (0.039-**st. error**);

pp. 31-33 contain description of used adsorption isotherm models

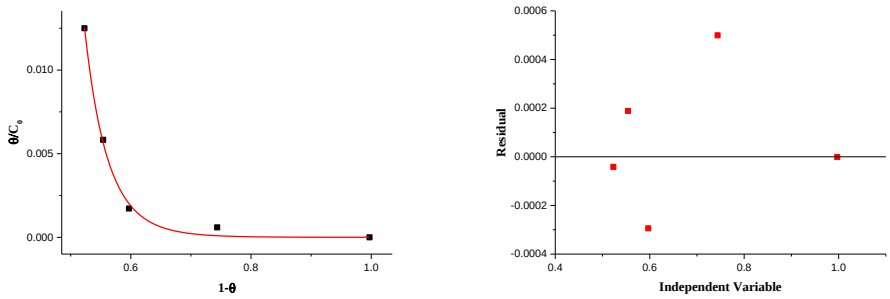

Figure 66. Fitting of data (Flory-Huggins model (non-linear)) of MBT adsorption at 23 ^{0}C onto **Zn(2)Al-NO$_3$-REVN**

The chemisorption nature of aqueous MBT solution onto LDH with nitrate and carbonate is additionally confirmed by the positive values of ΔG through presence of energy barrier (the adsorption is endergonic) (**Table 39**). The positive value of Gibbs energy change is an indication of chemisorption, however, desorption impact (**Figure 65**) can be explained by possibility of MBT to be physisorbed on the chemisorbed first layer, as discussed in previous sections**.** The values of ΔH and ΔS could not be evaluated as the measurements were performed at room temperature only.

Table 39. Thermodynamic parameters of aqueous MBT adsorption onto **Zn(2)-Al-X** (X=NO_3^-, CO_3^{2-}) adsorbents

LDH	ΔG,kJmol^{-1}	ΔH, kJmol^{-1}	ΔS, Jmol^{-1}K^{-1}
Zn(2)Al-NO$_3$-REV	10.83 (296 K);	-	-
Zn(2)Al-NO$_3$-REVN	17.32 (296 K);	-	-
Zn(2)Al-NO$_3$-REVC	7.83 (296 K);	-	-
Zn(2)Al-NO$_3$-COP	6.03 (293 K);	-	-
Zn(2)Al-CO$_3$-AN	5.79 (293 K);	-	-

Table 40 and **Figure 67** reveal that MBT adsorption kinetics is governed by intraparticle or bulk and surface diffusion as rate limiting step for all investigated examples of adsorbents. Average constants values of parabolic diffusion model are equal $k_{average}$= 0.11±0.01, 0.12±0.005, 0.12±0.02 and 0.16±0.04 min$^{-0.5}$ for the following LDH materials: **Zn(2)Al-NO$_3$-REVN**, **Zn(2)Al-NO$_3$-REVC, Zn(2)Al-NO$_3$-COP** and **Zn(2)Al-CO$_3$-AN**, respectively for studied concentrations range 0.23 mM-25.15 mM.

Table 40. Kinetic models used to fit adsorption data of MBT onto adsorbents **Zn(2)-Al-X** (X=NO_3^-, CO_3^{2-}) adsorbents

Adsorbent	Exp. conditions	Kinetics model	Limiting step according to the model(s)	Figures of merit
Zn(2)Al-NO_3-REV	Powder immersion in 25.15 mM MBT at 23 ºC	-	-	-
	Powder immersion in 2.57 mM MBT at 23 ºC	Elovich	Bulk and surface diffusion	**α** = 54.67 $mgg^{-1}min^{-1}$ (16.441-**st.error**); intercept= -66.33 (28.903-**st.error**);
	Powder immersion in 1.40 mM MBT at 23 ºC	Parabolic diffusion	Intraparticle diffusion	**k** = 0.12 $min^{-0.5}$ (0.008-**st.error**);
	Powder immersion in 0.46 mM MBT at 23 ºC	Elovich	Bulk and surface diffusion	**α** = 11.46 $mgg^{-1}min^{-1}$ (0.906-**st.error**); **intercept**= -7.70 (1.593-**st.error**);
	Powder immersion in 0.23 mM MBT at 23 ºC	Elovich	Bulk and surface diffusion	**α** = 12.81 $mgg^{-1}min^{-1}$ (1.468-**st.error**); intercept= -9.73 (2.580-**st.error**);
Zn(2)Al-NO_3-REVN	Powder immersion in 25.15 mM MBT at 23 ºC	Parabolic diffusion	Intraparticle diffusion	**k**= 0.12 $min^{-0.5}$ (0.016-**st.error**);
	Powder immersion in 0.46 mM MBT at 23 ºC	Elovich	Bulk and surface diffusion	**α** = 10.98 $mgg^{-1}min^{-1}$ (1.108-**st.error**); intercept= -7.25 (1.948-**st.error**);
	Powder immersion in 0.23 mM MBT at 23 ºC	Elovich	Bulk and surface diffusion	**α** = 6.25 $mgg^{-1}min^{-1}$ (0.774-**st.error**); intercept= -4.474 (1.361-**st.error**);

Table 40. Kinetic models used to fit adsorption data of MBT onto adsorbents **Zn(2)-Al-X** (X=NO_3^-, CO_3^{2-}) (cont.)

Adsorbent	Exp. conditions	Kinetics model	Limiting step according to the model(s)	Figures of merit
Zn(2)Al-NO_3-REVC	Powder immersion in 25.15 mM MBT at 23 ºC	Parabolic diffusion	Intraparticle diffusion	**k** = 0.13 $min^{-0.5}$ (0.017-**st.error**);
	Powder immersion in 0.46 mM MBT at 23 ºC	Elovich	Bulk and surface diffusion	**α** = 10.15 $mgg^{-1}min^{-1}$ (1.026-**st.error**); intercept= -5.94 (1.803-**st.error**);
Zn(2)Al-NO_3-COP	Slurry immersion in 27.87 mM MBT at 20 ºC	-	-	-
	Slurry immersion in 2.62 mM MBT at 20 ºC	Elovich	Bulk and surface diffusion	**α** = 9.21 $mgg^{-1}min^{-1}$ (1.504-**st.error**); intercept= 29.97(2.644-**st.error**);
	Slurry immersion in 1.42 mM MBT at 20ºC	Elovich	Bulk and surface diffusion	**α** = 8.09 $mgg^{-1}min^{-1}$ (1.428-**st.error**); intercept= 7.67 (2.511-**st.error**);
	Slurry immersion in 0.71 mM MBT at 20ºC	Parabolic diffusion	Intraparticle diffusion	**k** = 0.13 $min^{-0.5}$ (0.014-**st.error**);
Zn(2)Al-CO_3-AN	Slurry immersion in 27.87 mM MBT at 20ºC	Parabolic diffusion	Intraparticle diffusion	**k** = 0.15 $min^{-0.5}$ (0.029-**st.error**);

pp.35-36 contain description of used adsorption kinetic models

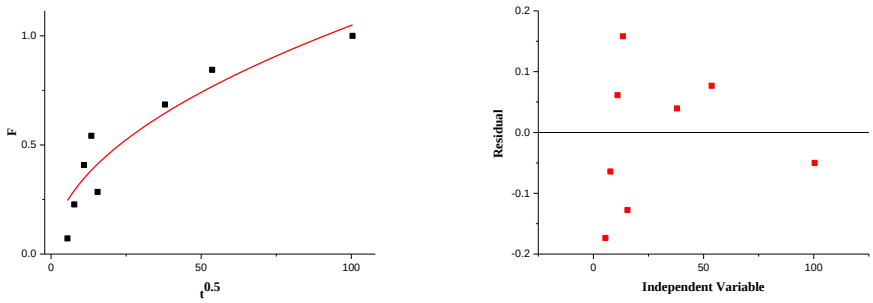

Figure 67. Fitting of MBT adsorption kinetics (Parabolic diffusion model (non-linear)) and corresponding residual plot for 2.57 mM solution at 23 ^{0}C onto **Zn(2)Al-NO$_3$-REVN**

In addition, the highest value of adsorbed MBT is observed for **Zn(2)Al-NO$_3$-COP** LDH particles prepared by coprecipitation (more than 60 %). For all the other adsorbents the MBT present is similar and around 40 wt % (**Table 41**). The additional amount of MBT into **Zn(2)Al-NO$_3$-COP** can be due to its immobilization on both external surface (adsorption) as well as in the interlayer galleries (by ion-exchange reaction). As **Zn(2)Al-NO$_3$-COP** LDH was used as pristine LDH for preparation of **Zn(2)Al-MBT-AN**, where MBT was intercalated into the LDH galleries as well, this may be a reason why classical adsorption isotherm models did not successfully fit the experimental data.

Table 41. Average values of adsorbed aqueous MBT onto **Zn(2)-Al-X** (X=NO_3^-, CO_3^{2-}) adsorbents

LDH	Average MBT adsorbed RT, %
Zn(2)Al-NO$_3$-REV	37.4
Zn(2)Al-NO$_3$-REVN	39.2
Zn(2)Al-NO$_3$-REVC	38.0
Zn(2)Al-NO$_3$-COP	62.2
Zn(2)Al-CO$_3$-AN	41.8

5.3.2 Adsorption of MBT in LDH using ethanolic medium

The reason for performing the studies presented in this section is based on the difference of calcination-rehydration synthesis results, namely those obtained for **Mg(3)Al-MBT-SH/CALC650** and those obtained for **Mg(3)Al-MBT-SH/CALC150** (the former LDH was prepared using aqueous alkaline MBT for rehydration step and the latter was obtained using neutral form of MBT in ethanolic solution). If in the case of **Mg(3)Al-MBT-SH/CALC650** neither XRD nor FTIR measurements confirmed presence of MBT in the galleries, the structural characterization of **Mg(3)Al-MBT-**

SH/CALC150 revealed the possibility of partial intercalation of MBT into the galleries. Thus, the present studies are called to find out if those structural differences are due to the change of calcination temperature and/or due to the form of MBT used in rehydration step. It is important to stress that in aqueous medium there are MBT tautomeric forms equilibrium dependent upon pH (**Figure 11**, Chapter 2). Probably, this can also have an impact in the differences observed. Besides, ethanolic solutions of MBT were used for anion-exchange reaction when LDH materials with nitrates were prepared by coprecipitation reaction in reverse microemulsion. This decision was based on the adsorption of organic compounds in the pristine LDH samples during synthesis as discussed before (sections 4.1.1 and 4.1.2) and better compatibility of these LDH particles with ethanolic medium than aqueous one.

Figure 68 - **Figure 71** show data obtained for **Mg(3)Al-CO_3-SH** calcined at 150/650 ^{0}C and **Zn(2)-Al-X** (X=NO_3^-) LDH used as adsorbents in adsorption studies of MBT, from ethanolic MBT solutions with concentrations in the range of 0.11 mM - 17 mM. The dependence of MBT concentration in solution as a function of time was monitored in the presence of adsorbents at 20 ^{0}C and 60 ^{0}C.

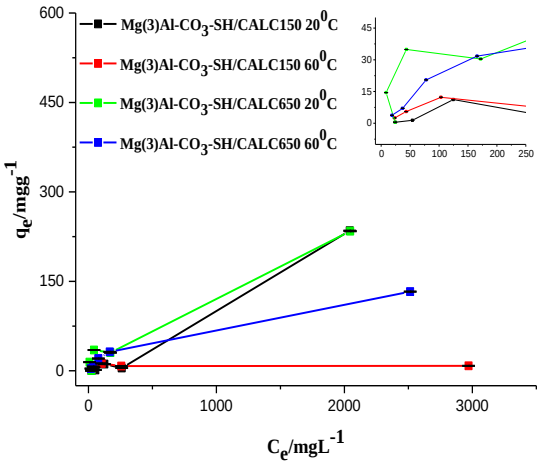

Figure 68. Variation of q_e with C_e corresponding to the adsorption of ethanolic MBT at 20 ^{0}C and 60 ^{0}C onto **Mg(3)Al-CO_3-SH** thermally treated at 150 ^{0}C and 650 ^{0}C

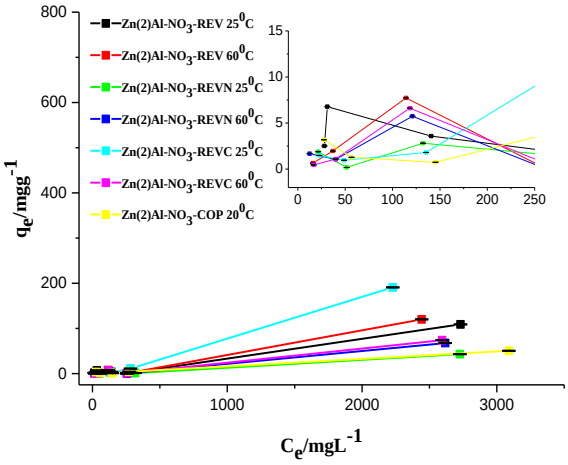

Figure 69. Variation of q_e with C_e corresponding to the adsorption of ethanolic MBT at 20/25 ^{0}C and 60 ^{0}C onto **Zn(2)Al- X** (X=NO_3^-)

Figure 68 and **Figure 69** present "L" curve type of MBT adsorption isotherm, which points to a continuous saturation of MBT adsorbate onto studied adsorbent's surface (Limousin, et al. 2007). Besides, there seems to exist influence of desorption processes for long timescales (**Figure 70** and **Figure 71**).

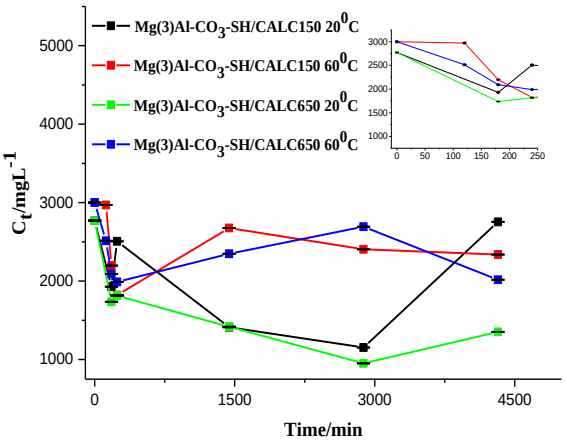

Figure 70. MBT (ethanolic) adsorption at 20 ^{0}C and 60 ^{0}C onto **Mg(3)Al-CO_3-SH**, thermally treated at 150 ^{0}C and 650 ^{0}C, with concentration of MBT 17 mM

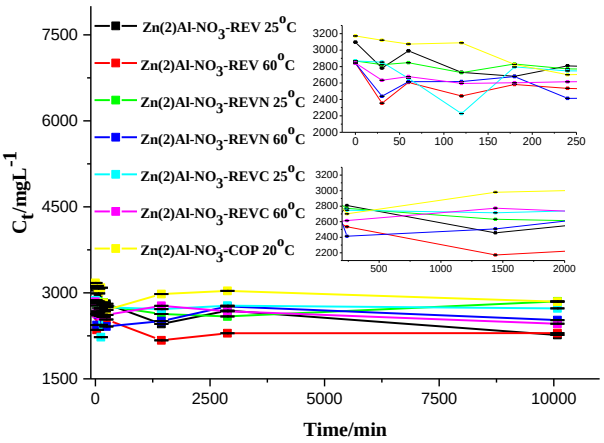

Figure 71. MBT (ethanolic) adsorption at 20/25 ^{0}C and 60 ^{0}C onto **Zn(2)Al- X** (X=NO_3^-), with concentration of MBT 17 mM

Table 42 shows that standard errors associated with the parameters calculated using different adsorption isotherm models are high. This can point out to the co-existence of physisorption and chemisorption processes.

The Freundlich isotherm was found to be the best model to fit the MBT adsorption onto calcined **Mg(3)Al-CO_3-SH**, along with **Zn(2)Al-NO_3-REVN** and **Zn(2)Al-NO_3-REVC**. On the other hand, the Temkin isotherm model points towards chemisorption of ethanolic MBT onto **Zn(2)Al-NO_3-REV** at 20 ^{0}C. Moreover, the fitted *RT/b* parameter is equal to 101.52 for **Zn(2)Al-NO_3-REV** (at 20 ^{o}C), thereby indicating the strong adsorbate-adsorbent interaction. Besides, the latter is also confirmed by estimated of ΔG from Flory-Huggins model, which is equal to 22.88 kJmol^{-1}, with 9 molecules in the surface of **Zn(2)Al-NO_3-REV**, which again indicates the chemisorption nature of adsorption. For the same LDH at 60 ^{0}C ΔG is 29.03 kJmol^{-1}, with 22 molecules in the surface of LDH.

Adsorption of MBT onto **Zn(2)Al-NO_3-REVN** was successfully fitted by Flory-Huggins model (**Figure 72**). The estimated ΔG is 22.81 kJmol^{-1} at 20 ^{0}C and 28.38 kJmol^{-1} at 60 ^{0}C, with the corresponding number of molecules in the surface being 17 and 18, supporting the chemisorption character of the process. However, Freundlich isotherm also can fit these isotherm data, which can be rationalised as discussed before: co-presence of chemi- and physisorption processes. Adsorption is best fitted by Freundlich isotherm model onto **Zn(2)Al-NO_3-REVC**, pointing on physisorption nature of the process. Adsorption of ethanolic MBT onto **Zn(2)Al-NO_3-COP** slurry was also fitted

by Flory-Huggins model, giving a ΔG equal to 22.43 $kJmol^{-1}$ with 23 molecules number onto adsorbent surface. Thus, there is a high possibility of co-existence of chemisorption and physisorption during adsorption of ethanolic MBT onto the studied adsorbents.

Table 42. Adsorption isotherm studies of ethanolic MBT onto adsorbents calcined **Mg(3)Al-CO_3-SH** and **Zn(2)-Al- X (X=NO_3^-)** at 20 ^{0}C and 60 ^{0}C

Adsorbent	**Exp. conditions**	**Isotherm model**	**Adsorption nature associated with the model(s)**	**Figures of merit**
Mg(3)Al-CO_3-SH	Calcined at 150 ^{0}C rehydrated in 0.29-16.57 mM MBT at 20 ºC	-	-	-
	Calcined at 150 ^{0}C rehydrated in 0.29-16.57 mM MBT at 60 ºC	Freundlich	Physisorption	**K_F** = 2.61mgg^{-1} $(Lmg^{-1})^{-0.18}$ **a**= 0.18 (0.150- **st.error)** **Pearson's r:** 0.57 **Adj. R^2:** 0.10 **p-value**: 0.314
	Calcined at 650 ^{0}C rehydrated in 0.29-16.57 mM MBT at 20 ºC	Freundlich	Physisorption	**K_F** = 1.05 mgg^{-1} $(Lmg^{-1})^{-0.71}$ (0.947- **st.error)** **a**= 0.71 (0.120- **st.error)**
	Calcined at 650 ^{0}C rehydrated in 0.29-16.57 mM MBT at 60 ºC	Freundlich	Physisorption	**K_F** = 1.52 mgg^{-1} $(Lmg^{-1})^{-0.57}$ (0.457- **st.error)** **a**= 0.57 (0.039- **st.error)**
Zn(2)Al-NO_3-REV	Powder immersed in 0.29-16.57 mM MBT at 25 ºC	Temkin	Chemisorption	**A_T** = 0.27 Lg^{-1} (0.054 **st.error)** **b**= 23.99 (11.88- **st.error)**

Table 42. Adsorption isotherm studies of ethanolic MBT onto adsorbents calcined **Mg(3)Al-CO_3-SH** and **Zn(2)-Al- X (X=NO_3^-)** at 20 ^{0}C and 60 ^{0}C (cont.)

Adsorbent	Exp. conditions	Isotherm model	Adsorption nature associated with the model(s)	Figures of merit
Zn(2)Al-NO_3-REV (cont.)	Powder immersed in 0.29-16.57 mM MBT at 25 ºC	Flory-Huggins	Surface coverage between adsorbate and adsorbent	**n**= -9.49 (4.103-**st.error**); **K_{FH}**= $8.33\cdot10^{-5}$ Lmg^{-1}; **Pearson's r:** -0.80 **Adj. R^2:** 0.52 **p-value**: 0.103
	Powder immersed in 0.29-16.57 mM MBT at 60 ºC	Flory-Huggins	Surface coverage between adsorbate and adsorbent	**n**= -21.90 (15.557-**st.error**); **K_{FH}**= $2.80\cdot10^{-5}$ Lmg^{-1}; **Pearson's r:** -0.63 **Adj. R^2:** 0.20 **p-value**: 0.254
Zn(2)Al-NO_3-REVN	Powder immersed in 0.29-16.57 mM MBT at 25 ºC	Freundlich	Physisorption	**K_F** = 0.04 mgg^{-1} $(Lmg^{-1})^{-0.80}$ **a**= 0.80 (0.480-**st.error)** **Pearson's r:** 0.75 **Adj. R^2:** 0.41 **p-value**: 0.146
		Flory-Huggins	Surface coverage between adsorbate and adsorbent	**n**= -17.41 (2.039-**st.error**); **K_{FH}**= $9.44\cdot10^{-5}$ Lmg^{-1} ($4.861\cdot10^{-5}$ -**st.error**);
	Powder immersed in 0.29-16.57 mM MBT at 60 ºC	Flory-Huggins	Surface coverage between adsorbate and adsorbent	**n**= -17.89 (6.695-**st.error**); **K_{FH}**= $3.53\cdot10^{-5}$ Lmg^{-1} **Pearson's r:** -0.84 **Adj. R^2:** 0.60 **p-value**: 0.076

Table 42. Adsorption isotherm studies of ethanolic MBT onto adsorbents calcined **Mg(3)Al-CO_3-SH** and **Zn(2)-Al- X (X=NO_3^-)** at 20 ^{0}C and 60 ^{0}C (cont.)

Adsorbent	Exp. conditions	Isotherm model	Adsorption nature associated with the model(s)	Figures of merit
Zn(2)Al-NO_3-REVC (cont.)	Powder immersed in 0.29-16.57 mM MBT at 25 ºC	Freundlich	Physisorption	**K_F** = 0.003 mgg^{-1} (Lmg^{-1})$^{-1.42}$ (0.0015- **st.error)** **a**= 1.42 (0.056- **st.error)**
	Powder immersed in 0.29-16.57 mM MBT at 60 ºC	Freundlich	Physisorption	**K_F** = 0.03 mgg^{-1} (Lmg^{-1})$^{-0.92}$ **a**= 0.92 (0.304- **st.error)**
Zn(2)Al-NO_3-COP	Slurry immersed in 0.29-16.57 mM MBT at 20 ºC	Flory-Huggins	Surface coverage between adsorbate and adsorbent	**n**= -23.03 (4.364- **st.error**); **K_{FH}**= 1.10·10^{-4} Lmg^{-1} (7.712·10^{-5}- **st.error**);

pp. 31-33 contain description of used adsorption isotherm models

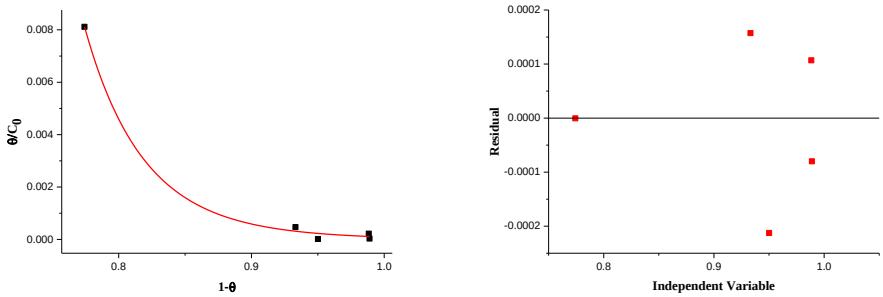

Figure 72. Fitting of data (Flory-Huggins model (non-linear)) for adsorption of MBT (ethanolic) at 25 ^{0}C onto **Zn(2)Al-NO_3-REVN**

The kinetics of adsorption is based on intraparticle diffusion or bulk/surface diffusion, regardless of the adsorbent type (**Table 43** and **Figure 73)**. The rate limiting step for studied adsorbents is again based on intraparticle diffusion. The average constant values of parabolic diffusion models between 5 studied concentrations in the concentrations range 0.11 mM - 17 mM are: $k_{average}$= 0.16±0.02 and 0.15±0.06 min$^{-0.5}$ for **Mg(3)Al-CO_3-SH/CALC150** at 20 ^{0}C and 60 ^{0}C, respectively; $k_{average}$= 0.17±0.03 and 0.13±0.02 min$^{-0.5}$ for **Mg(3)Al-CO_3-SH/CALC650** at 20 ^{0}C and 60 ^{0}C, respectively;

$k_{average}$= 0.10±0.03 and 0.14±0.03 $min^{-0.5}$ for **Zn(2)Al-NO_3-REV** at 20 ^{0}C and 60 ^{0}C, respectively; $k_{average}$= 0.11±0.06 and 0.14±0.04 $min^{-0.5}$ for **Zn(2)Al-NO_3-REVN** at 20 ^{0}C and 60 ^{0}C, respectively; $k_{average}$= 0.09±0.02 and 0.10±0.006 $min^{-0.5}$ for **Zn(2)Al-NO_3-REVC** at 20 ^{0}C and 60 ^{0}C, respectively; and $k_{average}$= 0.10±0.01 for **Zn(2)Al-NO_3-COP**.

Table 43. Kinetic models used to fit adsorption data of ethanolic MBT onto LDH calcined **Mg(3)Al-CO_3-SH** and **Zn(2)-Al-NO_3**

Adsorbent	Exp. conditions	Kinetics model	Limiting step according to the model(s)	Figures of merit
Mg(3)Al-CO_3-SH	Calcined 150 ^{0}C rehydrated in 16.57 mM MBT at 20 ºC	Parabolic diffusion	Intraparticle diffusion	**k** = 0.16 $min^{-0.5}$ (0.012-**st.error**);
	Calcined 150 ^{0}C rehydrated in 17.94 mM MBT at 60 ºC	Parabolic diffusion	Intraparticle diffusion	**k** = 0.12 $min^{-0.5}$ (0.030-**st.error**);
	Calcined 650 ^{0}C rehydrated in 16.57 mM MBT at 20 ºC	Pseudo-first order	Occupation of one-site of adsorbent	**K** = $1.07 \cdot 10^{-4}$ min^{-1} ($5.308 \cdot 10^{-5}$-**st.error**); **Pearson's r:** 0.76 **Adj. R^2:** 0.44 **p-value**: 0.137
		Parabolic diffusion	Intraparticle diffusion	**k** = 0.16 $min^{-0.5}$ (0.011-**st.error**);
	Calcined 650 ^{0}C rehydrated in 17.94 mM MBT at 60 ºC	Parabolic diffusion	Intraparticle diffusion	**k** = 0.17 $min^{-0.5}$ (0.028-**st.error**);
	Calcined 650 ^{0}C rehydrated in 0.19 mM MBT at 60 ºC	Pseudo-first order	Occupation of one-site of adsorbent	**K** = $3.78 \cdot 10^{-4}$ min^{-1} ($2.202 \cdot 10^{-4}$-**st.error**); **Pearson's r:** 0.65 **Adj. R^2:** 0.28 **p-value**: 0.161

Table 43. Kinetic models used to fit adsorption data of ethanolic MBT onto LDH calcined **Mg(3)Al-CO_3-SH** and **Zn(2)-Al-NO_3** (cont.)

Adsorbent	Exp. conditions	Kinetics model	Limiting step according to the model(s)	Figures of merit
Zn(2)Al-NO_3-REV	Powder immersion in 18.51 mM MBT at 25 ºC	Parabolic diffusion	Intraparticle diffusion	**k** = 0.10 $min^{-0.5}$ (0.009-**st.error**);
	Powder immersion in 17.00 mM MBT at 60 ºC	Parabolic diffusion	Intraparticle diffusion	**k** = 0.15 $min^{-0.5}$ (0.025-**st.error**);
Zn(2)Al-NO_3-REVN	Powder immersion in 17.15 mM MBT at 25 ºC	Parabolic diffusion	Intraparticle diffusion	**k** = 0.22 $min^{-0.5}$ (0.125-**st.error**);
	Powder immersion in 17.00 mM MBT at 60 ºC	Parabolic diffusion	Intraparticle diffusion	**k** = 0.11 $min^{-0.5}$ (0.029-**st.error**);
Zn(2)Al-NO_3-REVC	Powder immersion in 17.15 mM MBT at 25 ºC	Parabolic diffusion	Intraparticle diffusion	**k** = 0.11 $min^{-0.5}$ (0.017-**st.error**);
	Powder immersion in 17.00 mM MBT at 60 ºC	Parabolic diffusion	Intraparticle diffusion	**k** = 0.10 $min^{-0.5}$ (0.020-**st.error**);
	Powder immersion in 0.11 mM MBT at 60 ºC	Elovich	Bulk and surface diffusion	**α** = 2.58 $mgg^{-1}min^{-1}$ (0.375-**st.error**); intercept= -3.28 (0.671-**st.error**)
Zn(2)Al-NO_3-COP	Slurry immersion in 18.97 mM MBT at 20 ºC	Parabolic diffusion	Intraparticle diffusion	**k** = 0.09 $min^{-0.5}$ (0.007-**st.error**);
	Slurry immersion in 0.35 mM MBT at 20 ºC	Elovich	Bulk and surface diffusion	**α** = 12.72 $mgg^{-1}min^{-1}$ (3.16-**st.error**); intercept= -16.52 (5.557-**st.error**)

pp. 35-36 contain description of used adsorption kinetic models

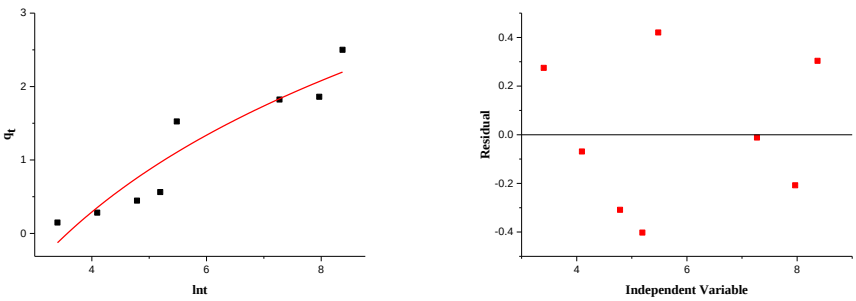

Figure 73. Fitting of MBT adsorption kinetics (Elovich model (non-linear)) and corresponding residual plot for 0.11 mM MBT (ethanolic) solution at 60 ^{0}Conto **Zn(2)Al-NO_3-REVC**

Table 44 presents the estimated thermodynamic parameters for adsorption of MBT from ethanolic solution onto LDH materials. This process is not spontaneous. The presence of energetical barrier is indication of chemisorption process co-presence with physisorption, as discussed before. ΔG value is higher for ethanolic MBT solution adsorption onto **Zn(2)Al-NO_3-COP** slurry compared to adsorption of MBT from an aqueous solution (**Table 39**). However, neither XRD nor FTIR measurements confirmed presence of ethanolic MBT adsorbed or intercalated in **Zn(2)Al-NO_3-COP** (probably, due to its low content). The reason for this low content of MBT can be due to the insufficient amount of anionic MBT molecules necessary to foster the anion-exchange reaction.

MBT in ethanolic solutions is better adsorbed by calcined **Mg(3)Al-CO_3-SH** compared to aqueous MBT in its anionic form. Moreover, the temperature dependence of adsorbed MBT from ethanolic solutions points to physisorption. The latter fact correlates with XRD, FTIR and TG results of **Mg(3)Al-MBT-SH/CALC150** (**Figure 20**, **Figure 25** and **A3** in Annex), whereby MBT presence into external surface was suggested in previous chapters.

The adsorption of ethanolic MBT is exothermic for the following adsorbents: **Mg(3)Al-CO_3-SH/CALC150**, **Mg(3)Al-CO_3-SH/CALC650** and **Zn(2)Al-NO_3-REVC**. For the remaining LDH samples MBT adsorption is endothermic process. Furthermore, the total entropy changes observed in **Table 44** are consistent with averaged MBT adsorbed amounts presented in **Table 45**: negative ΔS values are observed for all LDH sorbents, except **Zn(2)Al-NO_3-REVN** (domination of desorption with increase in temperature due to physisorption nature of the process). Furthermore, the positive total ΔS for **Zn(2)Al-NO_3-REVN** particles is an indication of high impact of chemisorption (Radeva, Valcheva and Veleva 2009).

Table 44. Thermodynamic parameters of ethanolic MBT adsorption onto LDH

LDH	ΔG,kJmol^{-1}	ΔH, kJmol^{-1}	ΔS, Jmol^{-1}K^{-1}
Mg(3)Al-CO_3-SH-CALC150	5.27 (293 K); 16.25 (333 K)	-75.19	-274.60
Mg(3)Al-CO_3-SH-CALC650	5.28 (293 K); 8.14 (333 K)	-15.68	-71.53
Zn(2)Al-NO_3-REV	7.85 (298 K); 8.34 (333 K)	4.22	-12.38
Zn(2)Al-NO_3-REVN	10.29 (298 K); 10.12 (333 K)	11.67	4.64
Zn(2)Al-NO_3-REVC	6.09 (298 K); 9.85 (333 K)	-25.95	-107.51
Zn(2)Al-NO_3-COP	10.02 (293 K)	-	-

Table 45. Average values of adsorbed ethanolic MBT onto LDH adsorbents

LDH	Average MBT adsorbed RT, %	Average MBT adsorbed HT, %
Mg(3)Al-CO_3-SH-CALC150	47.4	27.8
Mg(3)Al-CO_3-SH-CALC650	65.8	44.8
Zn(2)Al-NO_3-REV	18.6	14.6
Zn(2)Al-NO_3-REVN	8.6	13.0
Zn(2)Al-NO_3-REVC	13.4	10.8
Zn(2)Al-NO_3-COP	10.2	-

Thus, neutral MBT dissolved into ethanol can be adsorbed in higher extent by calcined **Mg(3)Al-CO_3-SH** compared to the aqueous, anionic form of MBT. For **Zn(2)-Al-NO_3-COP**, the neutral ethanolic form of MBT can be only adsorbed without anion-exchange reaction. Overall, the obtained results suggest different extent of physi- and chemisorption processes depending on type of solvent and type of adsorbent, as well as the speciation of MBT within each medium.

Preliminary conclusions

1. Adsorption of active species onto LDH particles depends on adsorbent type, adsorption temperature and solution medium (aqueous or ethanolic, in the case of MBT).
2. Only several adsorption processes can be determined as physisorption as dominating mechanism (adsorption of PhPh onto thermally treated **Zn(2)Al-NO_3-COP** and **Mg(3)Al-CO_3-SH)**. For the other sorbents there is a combination of both physisorption and chemisorption. The possibility of such behavior is described in literature (Kipling 1965); (Sims, Harmer and Quinton 2019).
3. Intraparticle diffusion or bulk/surface diffusion are a rate-limiting step of adsorption kinetics for all studied adsorbent-adsorbate systems, regardless of the studied molecules being immobilized onto the surface of LDH or also intercalated into the galleries. The latter allows to suggest that the initially the mass transfer of active species occurs into the external surface of LDH with further intraparticle pore diffusion (Cooney 1999); (Ismadji, Soetaredjo and Ayucitra 2015) and further movement to the interlayer galleries of LDH.

6. RELEASE OF ACTIVE SPECIES FROM LDH

In the previous chapter the interaction between active species (including corrosion inhibitor MBT and pH indicator molecules PhPh and TB) was discussed in terms of adsorption isotherms and kinetics of adsorption, aiding in the understanding of structural (section 4.1), textural and colloidal properties (section 4.2) of the LDH samples prepared.

The present chapter is devoted to investigation of release of active species from synthesized LDH materials. The results presented in this chapter intend to provide additional information on what happens after the synthesis (i.e. after immobilization): the release of active species under different conditions. There are several papers in the literature claiming the controlled release ability of LDH (Yang, et al. 2007); (Panda, Srivastava and Bahadur 2009); (Kong, et al. 2010), including by the author of the present thesis (Kuznetsova, et al. 2017). This ability in delivering an active compound under certain triggering conditions has contributed into a large extent for the development of the area of self-responsive, multi-functional coatings (Zheludkevich, et al. 2010), although its investigation has been more focused on simple presentation of release profiles and study of the effect rendered by the immobilized active species: corrosion detection (Maia, et al. 2013) or corrosion inhibition (Carneiro, et al. 2015). Therefore, the results presented in this section aim at enlightening the dynamics and extent of release of different active compounds from LDH.

Experimentally, the release profiles can be obtained via two main methods: taking aliquots and replacing the same volume of release medium for conservation of the total volume of the system (Liu, et al. 2006); (Estrada, Daniel-da-Silva and Trindade 2013) or without addition of the removed volume of release medium and further recalculation of the released concentration with changed volume (Singh, et al. 2010); (Donato, et al. 2012). Comparison of data obtained by both methods was carried out using as representative example the release of MBT from **Zn(2)Al-MBT-AN** in a 500mM NaCl aqueous solution.

Comparing with conventional release studies of capsules in solution, changes in the media composition when studying ion-exchangers can have a different effect in the way the species can be released. For example, when one refers to a mesoporous inorganic material which releases a compound simply by diffusion, changes in the ionic strength or pH will eventually affect the release depending on the solubility of the compound (Maia, et al. 2013); (Sousa, Maia, et al. 2015). However, with LDH the analysis can be more complicated: LDH with intercalated anions (as in the case of **Zn(2)Al-MBT-AN**) can release a compound by anion-exchange with anions present in the surrounding media, and the equilibrium constant for that release is not only dependent on the concentration of the anion in solution (in the present case chlorides or MBT) but the concentration of the same species within LDH (Sparks 2003). Therefore, one may assume that when replacing the

aliquot with fresh solution it can have the effect of decreasing the amount of released MBT, thus displacing the equilibrium in the direction of the exchange with chlorides (more MBT would have been detected). However, that is not what is experimentally observed **(Figure 74**).

MBT is particularly an interesting system: under neutral pH conditions MBT (which is in anionic form) tends to protonate, leading to an increase of HO^- in solution, which can further enhance release of additional MBT because, in addition to chlorides, hydroxides can also intercalate into LDH. Thus, the effect in the reduction of MBT imposed by the removal of aliquot and dilution of MBT in the releasing medium seems to have a lower impact than the raise in pH when the release medium is not replaced. Measurements of pH during the release studies showed that after addition of LDH into the NaCl solution the pH increased from 6.79 (initial NaCl solution) up to 8.95, remaining in the range 8.00-8.92 during 24 h, decreasing down to 7.07-7.70 after one week of measurements. Taking into account these differences, the release studies performed and presented subsequently, were carried out based on the "non-replacement of volumes" approach.

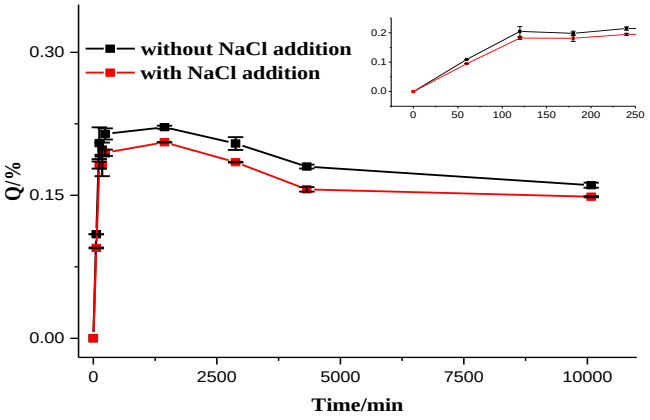

Figure 74. MBT release profiles from **Zn(2)Al-MBT-AN** with and without addition of fresh 500 mM NaCl solutions to replace the removal of aliquots (error bars correspond to standard errors between 3 measurements)

Another aspect worth of notice is that after an initial release of MBT its concentration in solution tends to decrease with evolution of immersion time, when it would be expected that it would be kept constant, if not increased.

The first factor that could lead to this surprising effect is of instrumental nature, assuming lack of stability in the measurements of the solutions in the UV-Vis spectrophotometer. In order to guarantee that this was not the case, every time the spectrophotometer was used, in addition to the validation

of background, standard solutions were checked to confirm identical values of absorbance for the same concentration of MBT. Then, excluding the instrumental factor, only intrinsic properties of LDH within the release media would explain the release profile obtained. The adsorption of released MBT from interlayer galleries in LDH external surface could explain why after a fast release of MBT (both externally adsorbed and intercalated), with evolution of time this concentration decreases. In subsequent sections the combination of desorption with adsorption models will be used to better fit the release profiles, whenever applicable. Further experiments will be shown to support the combined effect of release by ion-exchange/desorption from the external surface area with adsorption of released MBT for longer timescales.

Second, for the ion-exchange reaction, the rate-limiting step can be based on film diffusion or/and particle diffusion. Thus, strong mixing or agitation allows reduction of film diffusion influence (diffusion of adsorptive through imperfectly mixed film (layer) around the particle). However, other types of mass transport and particle diffusion are not affected by mixing (Sparks 2003). As mentioned in experimental part section, all release studies were performed under vigorous stirring (350 rpm), therefore, the effect of film diffusion is expected to be low under these circumstances.

In the next sections, the release data will be presented according to the nature of immobilization in LDH: release of active species intercalated/adsorbed into LDH with formation of single-phase materials (Glu/FSS); release of active species that are only adsorbed onto LDH surface (PhPh/TB/MBT) and release of active species that are intercalated with formation of double LDH phases (Zn(2)Al-MBT-AN).

6.1 Gluconate release studies from LDH

Results presented in section 4.1.1 and 4.1.2 confirmed that **Zn(2)Al-Glu-AN** is a single-phase material with corrosion inhibitor intercalated into LDH galleries. **Table 46** shows gluconate loading content and the anion-exchange capacity of the obtained LDH.

Table 46. Gluconate loading content and theoretical AEC of **Zn(2)Al-Glu-AN**

LDH	Glu loading content, %wt	AEC theoretical, $cmolkg^{-1}$
Zn(2)Al-Glu-AN	45	202.63

AEC is calculated using equation **12**

The study of release of gluconate from LDH was performed under different conditions, namely using three different concentrations of NaCl solution and under three different pH conditions for 48 hours

of immersion (**Figure 75** and **Figure 76**). These conditions were selected due to the relevance of concentration of aggressive species and pH for the occurrence of corrosion processes (Zheludkevich, Salvado and Ferreira 2005). **Figure 75** and **Figure 76** present the fractional uptake *F* (equation **15**, Chapter 2), that was calculated as the ratio between amount of gluconate released at time *t* and amount of gluconate released at equilibrium time (the last timescale point) (Sparks 2003), which in the present studies is the 2880 min (48 h) point.

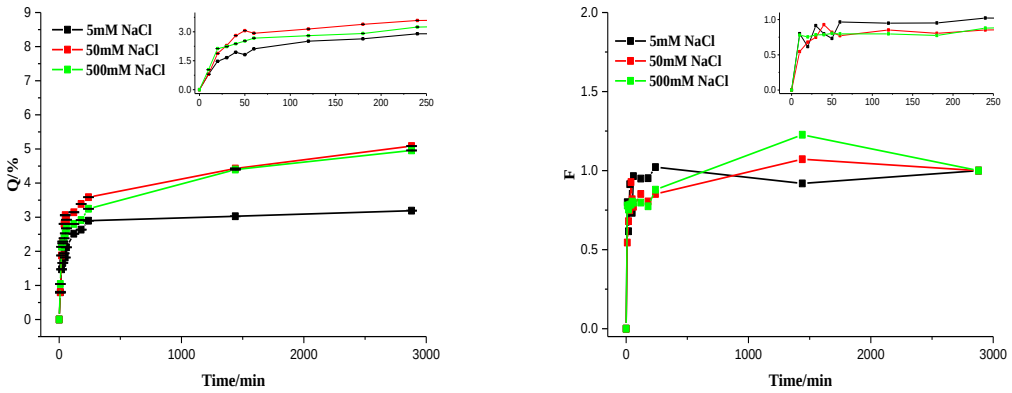

Figure 75. Glu release profiles and fraction of released Glu from **Zn(2)Al-Glu-AN** with different NaCl triggers (error bars are standard errors between 3 measurements; Q-cumulative release % and F-fractional uptake)

Moreover, the qualitative analysis of the release profile in **Figure 75** reveals that the amount of gluconate released in this case tends to increase during the first 24 hours immersion, where a maximal concentration is detected. Up to 24 h, there is a clear effect of NaCl concentration in the amount of gluconate released: the largest amount of gluconate release occurs at 50/500 mM NaCl, which is consistent with an ion-exchange equilibrium (Sparks 2003). However, for longer immersion times, the amount of gluconate released increases for the most diluted NaCl solutions and decreases for 50/500 mM NaCl. Therefore, for the most concentrated solution it may be that the amount of gluconate released after 24 h overcomes a threshold concentration above which competitive adsorption of gluconate on LDH may occur.

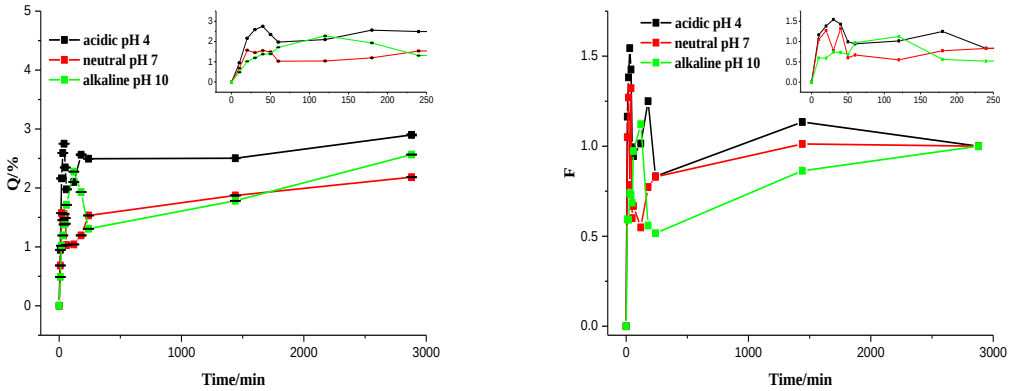

Figure 76. Glu release profiles and fraction of released Glu from **Zn(2)Al-Glu-AN** with different pH triggers (error bars are standard errors between 3 measurements; Q-cumulative release % and F-fractional uptake)

In the case of LDH exposed to solutions with different pHs (**Figure 76**), the mechanism upon which LDH release of gluconate may be different. Under acidic pHs (pH below 4-4.5 (Zheng, et al. 2013)) LDH dissolves and the release of gluconate occurs mostly as a result of LDH dissolution. Contrastingly, under alkaline conditions HO^-, an anion with strong propensity to intercalate within LDH, can trigger the exchange by anion-exchange. Under neutral conditions the extent of release by anion exchange should be limited, except for some amount released by exchange due to CO_2(aq) that can speciate into CO_3^{2-}(aq) or gluconate which can desorb if partially adsorbed in the external surface of LDH in the end of the synthesis. However, even in the last case a very small dissolution of LDH cannot be excluded (Galvao, et al. 2016).

The study of LDH under different conditions of pH is not straightforward, though. On one hand, as referred in the beginning of this chapter, if LDH materials are studied using pH buffer solutions to maintain pH constant over the monitoring time, the anions from the salts in the buffer solution will exchange so that the species are released by ion exchange with the buffer and not due to pH, only. On the other hand, the dissolution of LDH under acidic conditions or capture of hydroxides in alkaline conditions cause a buffer effect induced by the LDH and after some time the solution pH is no longer in initial acidic or alkaline conditions, subsequently affecting the release for longer immersion times (Seida, Nakano and Nakamura 2001); (Forano, et al. 2006). Indeed, a buffering pH effect introduced by the LDH was found during the release of Glu (**Figure 77**).

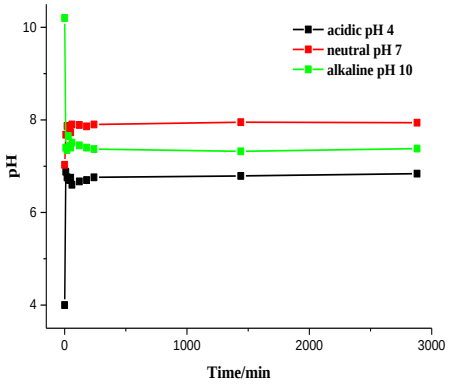

Figure 77. Buffering effect of **Zn(2)Al-Glu-AN** during release studies under different pH triggers

The amount of Glu released for **Zn(2)Al-Glu-AN** depending on the triggers described above is depicted in **Table 47** and supports the discussion above presented: under the conditions tested, a larger amount of Glu is released for larger NaCl concentrations, which is consistent with an anion-exchange triggered release. On the other hand, LDH releases more Glu under acidic conditions, probably due to the dissolution of LDH. The smallest release of Glu was observed in deionized water (neutral pH), whereas a comparatively higher release of Glu was found under the influence of an initial alkaline pH, which can be explained by additional anion-exchange reaction with HO^-.

Table 47. Amount of Glu released from **Zn(2)Al-Glu-AN** under influence of various triggers

Trigger	Average gluconate released amount from loading content, % wt
5 mM NaCl	22
50 mM NaCl	30
500 mM NaCl	28
Acidic pH 4	23
Neutral pH 7	14
Alkaline pH 10	16

Looking at the release profiles obtained one finds that there is a fast increase of release gluconate (within the first 4 hours of immersion) followed by a decrease of gluconate in solution, ending with a small increase in Glu released. The interpretation of such behaviour is not trivial. However, as described in Chapter 5, adsorption of organic species from solution onto LDH can occur, even if

intercalation within the interlayer galleries does not occur and one can expect that when intercalation may occur, adsorption in the external surface layers of LDH is also possible. Therefore, we propose the division of the release profile into these following stages:

-Stage I: release of Glu by ion-exchange reaction from the interlayer galleries + possible desorption of Glu in the external galleries (although LDH materials have been washed extensively after preparation and Glu is a soluble species in water).

-Stage II: decrease of Glu in solution as a result of adsorption of Glu in the external LDH metal hydroxide sheets, triggered by an 'excessive amount' of Glu released by ion-exchange, which shifted the adsorption-desorption equilibrium toward adsorption.

-Stage III: further release of Glu from interlayer galleries as effective concentration of Glu in solution was decreased.

Therefore, fitting of models to the release and uptake of Glu was carried out in the following way (**Figure 78**): data corresponding to stages I and III were fitted using release models. Whenever possible (because in some conditions only 1 or 2 points were available) adsorption models presented in Chapter 5 were used to fit data corresponding to stage II.

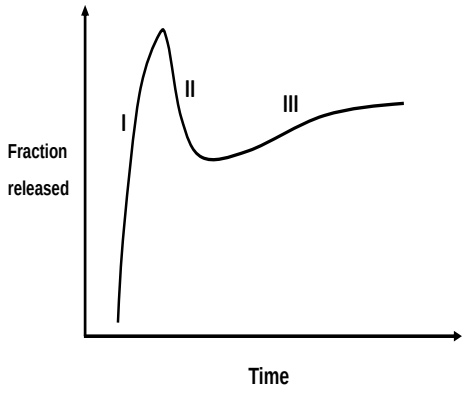

Figure 78. Schematic representation of release profile corresponding to Glu

Data corresponding to the release of Glu was fitted using different possible models that could explain the release of species from LDH, including: zero order, first order, pseudo-second order, Higuchi, Power function, Kopcha, Bhaskar and Elovich models (**Table 4**). The best fitted models of gluconate release from LDH are presented in **Table 48** and **Figure 79.**

For short immersion times and in the presence of 5 and 50 mM NaCl, the model fitted to stage I was Higuchi's, while for 500 mM NaCl the Power function model gave better fitting results. In stage III the release of Glu was fitted by the zero order reaction (5 mM NaCl), Power function's (50 mM) and Higuchi's (500 mM NaCl). Concerning the release as a function of pH, one can see that except for release under alkaline conditions (initial pH 10) in which Higuchi's model is also fitted to stage I as for the NaCl trigger, in acidic and neutral conditions the model which best fit the initial release is first order (release in pH 4) and zero order (release under neutral conditions). Recall that under acidic and neutral conditions (especially low ionic strength media (Galvao, Neves, et al. 2016) dissolution of LDH is expected to occur).

Table 48. Models used to fit gluconate release profiles from **Zn(2)-Al-Glu-AN**

LDH	**Exp. Conditions/time of fitting**	**Kinetics model**	**Limiting step according to the model(s)**	**Figures of merit**
Zn(2)Al-Glu-AN	Immersion in 5 mM NaCl at 25 ºC/0_30 min	Higuchi	Diffusion	**K_H** = 0.37 $min^{-0.5}$ (0.036-**st.error**);
	Immersion in 5 mM NaCl at 25 ºC/60_240 min	Zero order	-	**K** = 0.36 $mgL^{-1}min^{-1}$ (0.085-**st.error**); **Pearson's r:** 0.95 **Adj. R^2:** 0.85 **p-value**: 0.50
	Immersion in 50 mM NaCl at 25 ºC/0_40 min	Higuchi	Diffusion	**K_H** = 0.33 $min^{-0.5}$ (0.012-**st.error**);
	Immersion in 50 mM NaCl at 25 ºC/120_1440 min	Power function	Diffusion	**a** = 0.47 $min^{-0.11}$ (0.068-**st.error**); **k**= 0.11 (0.024-**st.error**)
	Immersion in 500 mM NaCl at 25 ºC/0_50 min	Power function	Diffusion	**a** = 0.73 $min^{-0.02}$ (0.042-**st.error**); **k**= 0.02 (0.017-**st.error**)

Table 48. Models used to fit gluconate release profiles from **Zn(2)-Al-Glu-AN** (cont.)

LDH	Exp. Conditions/time of fitting	Kinetics model	Limiting step according to the model(s)	Figures of merit
Zn(2)Al-Glu-AN (cont.)	Immersion in 500 mM NaCl at 25 ºC/120_1440 min	Higuchi	Diffusion	**K_H** = 0.21 $min^{-0.5}$ (0.009-**st.error**);
	Immersion in deionized water with initial pH 4 at 25 ºC/0_30 min	First order	-	**K** = 0.02 min^{-1} (0.002-**st.error**); **Pearson's r:** 0.99 **Adj. R^2:** 0.98 **p-value**: 0.059
		Higuchi	Diffusion	**K_H** = 0.66 $min^{-0.5}$ (0.002-**st.error**);
	Immersion in deionized water with initial pH 4 at 25 ºC/120_1440 min	Higuchi	Diffusion	**K_H** = 0.23 $min^{-0.5}$ (0.037-**st.error**);
	Immersion in deionized water at 25 ºC/0_40 min	Zero order	-	**K** = 4.14 $mgL^{-1}min^{-1}$ (2.047-**st.error**); **Pearson's r:** 0.76 **Adj. R^2:** 0.44 **p-value**: 0.136
		Higuchi	Diffusion	**K_H** = 0.50 $min^{-0.5}$ (0.054-**st.error**);
	Immersion in deionized water at 25ºC/180_2880 min	Zero order	-	**K_H** = 0.03 $mgL^{-1}min^{-1}$ (0.009-**st.error**); **Pearson's r:** 0.92 **Adj. R^2:** 0.77 **p-value**: 0.08
		Power function	Diffusion	**a** = 0.49 $min^{-0.09}$ (0.069-**st.error**); **k=** 0.09 (0.021-**st.error**)

Table 48. Models used to fit gluconate release profiles from **Zn(2)-Al-Glu-AN** (cont.)

LDH	Exp. Conditions/time of fitting	Kinetics model	Limiting step according to the model(s)	Figures of merit
Zn(2)Al-Glu-AN (cont.)	Immersion in deionized water with initial pH 10 at 25 ºC/0_120 min	Higuchi	Diffusion	K_H = 0.31 $min^{-0.5}$ (0.012-**st.error**);

pp.40-42 contain description of used release kinetic models

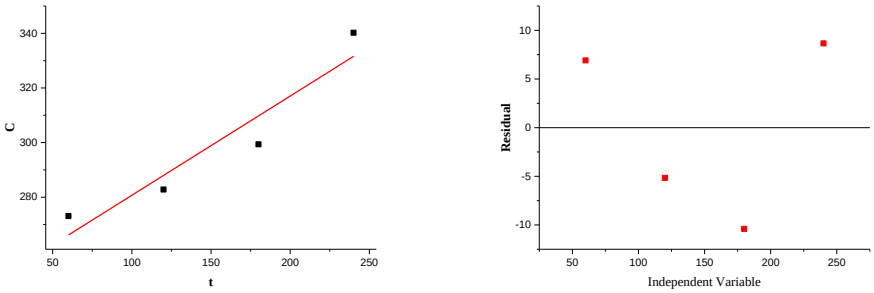

Figure 79. Fitting of data (zero order model (linear)) of Glu release from **Zn(2)Al-Glu-AN** during immersion in 5mM NaCl

The fitting of data for stage II (adsorption step) was carried out only for the release of Glu under acidic conditions, as this is the only situation in which sufficient data points existed to fit adsorption models. The results depicted in **Table 49**, show that two models could be fitted to this branch of the release profile curve: pseudo-first order and parabolic diffusion. Pseudo-first order model indicates the possibility of Glu physisorption onto LDH surface, however, parabolic diffusion model determines that intraparticle diffusion is the rate-limiting step for adsorption of this corrosion inhibitor.

Table 49. Kinetic models used to fit gluconate adsorption profiles from **Zn(2)-Al-Glu-AN**

LDH	Exp. Conditions/time of fitting	Kinetics model	Limiting step according to the model(s)	Figures of merit
Zn(2)Al-Glu-AN	Immersion in deionized water with initial pH 4 at 25 ºC/40_60 min	Pseudo-first order	-	**K** = 0.006 min^{-1} (0.0030-**st.error**); **Pearson's r:** 0.91 **Adj. R^2:** 0.64 **p-value**: 0.278
		Parabolic diffusion	Intraparticle diffusion	**k** = 0.37 $min^{-0.5}$ (0.006-**st.error**);

pp. 35-36 contain description of used adsorption kinetic models

In order to understand the structural changes which accompanied the release of Glu under different triggering conditions, XRD and FTIR of LDH materials after release studies were performed (**Figure 80** and **Figure 81**).

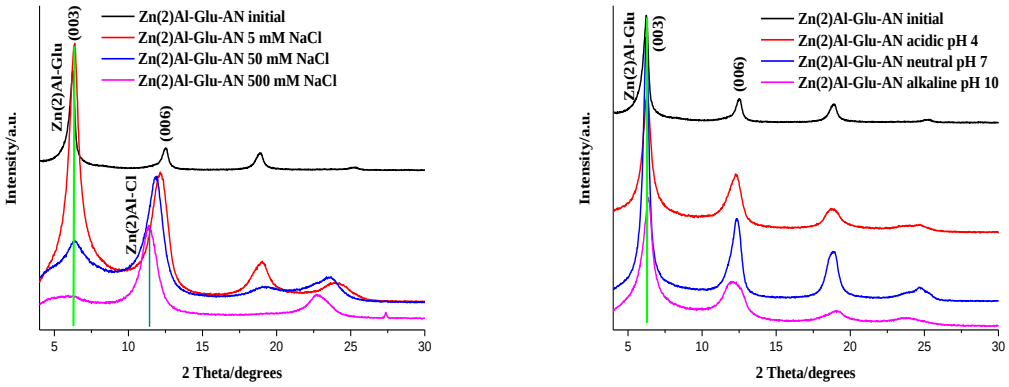

Figure 80. XRD patterns of **Zn(2)Al-Glu-AN** after release studies

Figure 80 reveals that in the presence of chlorides anion exchange occurs and chlorides replace Glu in the interlayer galleries. Most notably, after immersion in 500 mM NaCl the peak at lower 2 Theta angles almost disappear and next peak position shifts to higher 2 Theta angle position (0.75-0.76 nm). Additionally, anion-exchange of gluconate by chlorides is confirmed by EDS measurements (Figure **A4** Annex), through appearance of Cl peak in LDH structure after release studies in 500mM NaCl solution.

The above described interlayer distance can be associated with different types of anions like hydroxides, carbonates and chlorides: 7.5 Å-carbonates/hydroxides; 7.7 Å -chlorides (Zhang and Evans 2012). In the case of XRD patterns of LDH materials after release in different pH values media, one cannot detect large structural changes with respect to the initial LDH, which can be explained by the small amount of gluconate released and correspondingly small structural changes. Under acidic conditions, if the initial release (stage I) is mainly due to dissolution of LDH, the remaining fraction of LDH which does not dissolve may still keep the initial LDH-Glu structure, while under neutral conditions anion-exchange is also not expected to occur into a large extent. However, under alkaline conditions, the peak ascribed to (006) of LDH-Glu becomes asymmetric, which can be due to overlapping of the (003) reflection of carbonates and hydroxides at 2 Theta 11.50 with the (006) reflection of LDH-Glu. Such result can support the exchange of HO^- under alkaline conditions.

The FTIR spectra presented in **Figure 81** indicate that after immersion in sodium chloride solutions the band associated with interlayer water is shifted from 1583 cm^{-1} in synthesized **Zn(2)Al-Glu-AN** to 1593-1608 cm^{-1} in LDH after release in NaCl and pH triggers, together with the shift in vibration from 1387 to 1362 cm^{-1} (except for the release in deionized water). The latter can be attributed to symmetric deformation vibrations of C-H groups of Glu (Hesse, Meier and Zeeh 1997). Thus, the changes in vibrations associated with both Glu and interlayer water are an indication that the environment within the interlayers changed in the presence of chlorides. Also, the presence of carbonates with vibrations associated typically occurring at 1450 and 880 cm^{-1} (Huang and Wang 2009) can be inferred by the vibration occurring at 860 cm^{-1}. This result is not surprising at all as the release studies are performing under normal atmospheric conditions, in which contamination with carbonates can occur. Anyhow, vibrations that were previously associated with gluconate are still presented in the structure after release, which is also in agreement with the release profiles and XRD patterns, supporting a partial exchange of gluconates.

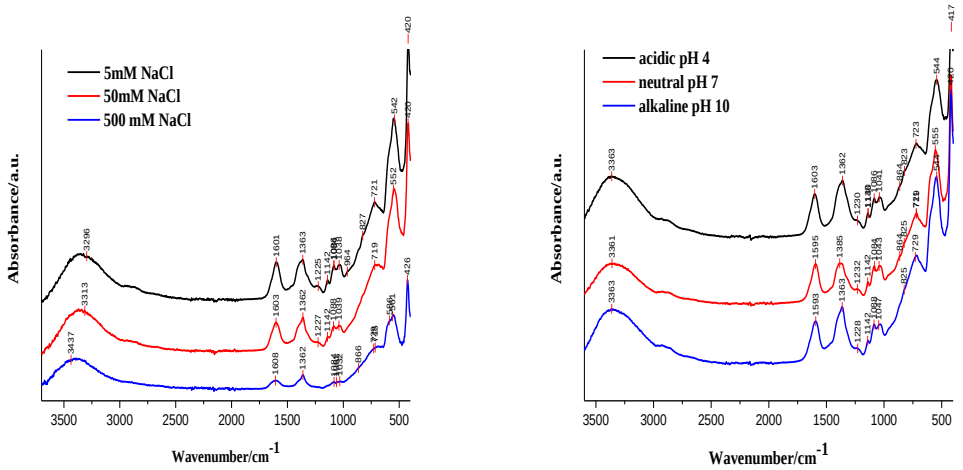

Figure 81. FTIR measurements of **Zn(2)Al-Glu-AN** after release studies

6.1.1 Adsorption of Gluconate in LDH

Coming back to the issue related with interpretation of release data in stage II and the possibility of adsorption, additional experiments were carried out to follow the uptake of Glu from solution under conditions in which anion-exchange are not expected to occur. To evaluate this possibility, the solution resulting from the release of Glu from **Zn(2)Al-Glu-AN** in 5 mM NaCl, was separated from the LDH material and subsequently used to prepare dispersions of **Zn(2)Al-NO_3-COP** and **Zn(2)Al-CO_3-AN**.

The fitting of obtained experimental data shows that adsorption of gluconate anions onto **Zn(2)Al-NO_3-COP** particles is governed by intraparticle diffusion (Parabolic diffusion model with k equal to 0.16 $min^{-0.5}$ and 0.018 standard error). The same model was successfully applied for adsorption kinetics on the surface of **Zn(2)Al-CO_3-AN** particles (k= 0.13 $min^{-0.5}$ and 0.015 standard error) along with pseudo-first order ($K=1.77\cdot10^{-4}$ min^{-1} and $9.601\cdot10^{-5}$ standard error), which is a sign of physisorption nature of the process (**Figure 82**) (Selim 2015). Analysis of LDH powders after adsorption experiments by FTIR does not show presence of gluconate vibrations, possibly because of insufficient content of Glu in the material (its initial concentration in solution was found to be only 2 mM).

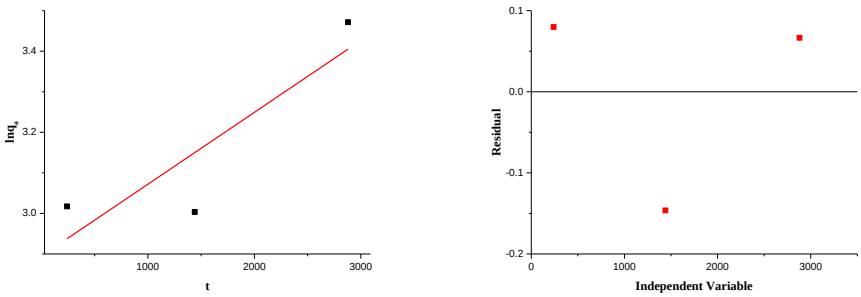

Figure 82. Fitting of data (pseudo-first order model (linear)) of 2 mM Glu adsorption at 20 ^{0}C onto **Zn(2)Al-CO_3-AN**

These results support the interpretation of decrease in Glu in stage II of the release profile as being associated with adsorption of Glu. However, it must be stressed that this simple interpretation of release-adsorption-release sort of behaviour associated with LDH can occur not as consecutive but as coupled processes in which the interpretation of results may become significantly more complicated.

6.1.2 Release of Glu from LDH as a function of temperature

Earlier in section 6.1, the fitting of the release data revealed that the rate-limiting step is associated with diffusion (determined by Higuchi or Power function models), regardless of the triggers, although in some cases zero order and first order models could also be fitted (**Table 48**). For additional confirmation of this possibility, the release of Glu in 5mM NaCl was performed at three different temperatures (15 ^{0}C, 35 ^{0}C and 45 ^{0}C, **Figure 83**), to evaluate the activation energy given by *Arrhenius equation* (equation **26**):

$$k_r = A \cdot e^{-\frac{\Delta E^*}{R \cdot T}} \qquad \textbf{26}$$

Where ΔE^* or E_a is known as *energy activation of chemical reaction* and A is *Arrhenius pre-exponential factor*. The Arrhenius pre-exponential factor has the same dimensions as the rate constant and is associated with the frequency of collisions between reactant molecules. For determination of energy of activation of reaction, it is necessary to measure the rate constant of the reaction at different temperatures. The slope of the plot lnk_r *vs1/T* gives the value $\Delta E^*/ R$ (Marangoni

2017). The kinetic models fitted and the corresponding rate constants are presented in **Table 50** and **Table 51.**

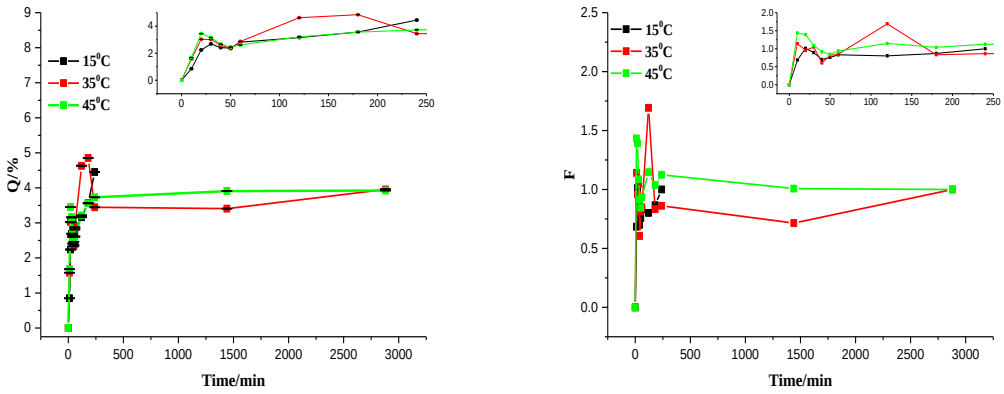

Figure 83. Glu release profiles and fraction of released Glu from **Zn(2)Al-Glu-AN** in 5mM NaCl trigger at different temperatures (error bars are standard errors between 3 measurements; Q-cumulative release % and F-fractional uptake).

Table 50. Kinetic models used to fit gluconate release profiles from **Zn(2)-Al-Glu-AN** at different temperatures

LDH	**Exp. Conditions/time of fitting**	**Kinetics model**	**Limiting step according to the model(s)**	**Figures of merit**
Zn(2)Al-Glu-AN	Immersion in 5 mM NaCl at 15 ºC/0_20 min	Higuchi	Diffusion	$\mathbf{K_H}$ = 0.44 $min^{-0.5}$ (0.033-**st.error**);
	Immersion in 5 mM NaCl at 15 ºC/60_240 min	Higuchi	Diffusion	$\mathbf{K_H}$ = 0.25 $min^{-0.5}$ (0.012-**st.error**);

Table 50. Kinetic models used to fit gluconate release profiles from **Zn(2)-Al-Glu-AN** at different temperatures (cont.)

LDH	Exp. Conditions/time of fitting	Kinetics model	Limiting step according to the model(s)	Figures of merit
Zn(2)Al-Glu-AN (cont.)	Immersion in 5 mM NaCl at 35 ºC/0_30 min	Higuchi	Diffusion	K_H = 0.50 $min^{-0.5}$ (0.047-**st.error**);
	Immersion in 5 mM NaCl at 35 ºC/50_120 min	Higuchi	Diffusion	K_H = 0.40 $min^{-0.5}$ (0.072-**st.error**);
	Immersion in 5 mM NaCl at 45 ºC/0_20 min	Higuchi	Diffusion	K_H = 0.72 $min^{-0.5}$ (0.052-**st.error**);
	Immersion in 5 mM NaCl at 45 ºC/60_240 min	Higuchi	Diffusion	K_H = 0.31 $min^{-0.5}$ (0.017-**st.error**);

pp. 40-42 contain description of used release kinetic models

Table 51. Kinetic models used to fit gluconate adsorption profiles from **Zn(2)-Al-Glu-AN** at different temperatures

LDH	Exp. Conditions/time of fitting	Kinetics model	Limiting step according to the model(s)	Figures of merit
Zn(2)Al-Glu-AN	Immersion in 5 mM NaCl at 15 ºC/30_50 min	Power function	Intraparticle diffusion	**a** = 0.82 $min^{-0.07}$ (0.199-**st.error**); **k=** 0.07 (0.066-**st.error**);

Table 51. Kinetic models used to fit gluconate adsorption profiles from **Zn(2)-Al-Glu-AN** at different temperatures (cont.)

LDH	Exp. Conditions/time of fitting	Kinetics model	Limiting step according to the model(s)	Figures of merit
Zn(2)Al-Glu-AN (cont.)	Immersion in 5 mM NaCl at 35 ºC/180_1440 min	Pseudo-first order	One site occupancy adsorption	**K** = $5.05 \cdot 10^{-5}$ min^{-1} ($1.219 \cdot 10^{-5}$-**st.error**); **Pearson's r:** 0.97 **Adj. R^2:** 0.89 **p-value**: 0.151
		Power function	Intraparticle diffusion	**a** = 0.92 $min^{-0.03}$ (0.056-**st.error**); **k=** 0.03 (0.01-**st.error**);
	Immersion in 5 mM NaCl at 45 ºC/30_50 min	Pseudo-first order	One site occupancy adsorption	**K** = 0.005 min^{-1} (0.001-**st.error**); **Pearson's r:** 0.97 **Adj. R^2:** 0.87 **p-value**: 0.164

pp.35-36 contain description of used adsorption kinetic models

The release of Glu in stages I and III was fitted using Higuchi model, whereas in stage II experimental data was fitted using adsorption models which confirm intraparticle diffusion as a rate-limiting step (Power function), along with pseudo-first order kinetics (Freundlich) kinetics (indication of physisorption) for higher temperatures.

The values obtained from Higuchi model for stage I were used in the Arrhenius equation (equation **26**).The activation energy obtained was 11.21 $kJmol^{-1}$ if data corresponding to three temperatures presented in this section are used (288, 308 and 318 K) and 13.26 $kJmol^{-1}$ if data obtained at room temperature and presented in **Table 50** is used as well (288, 298, 308 and 318 K), respectively (**Figure 84**). The order of magnitude of these activation energies is consistent with diffusion as limiting step (Sparks 2003); (SenGupta 2017).

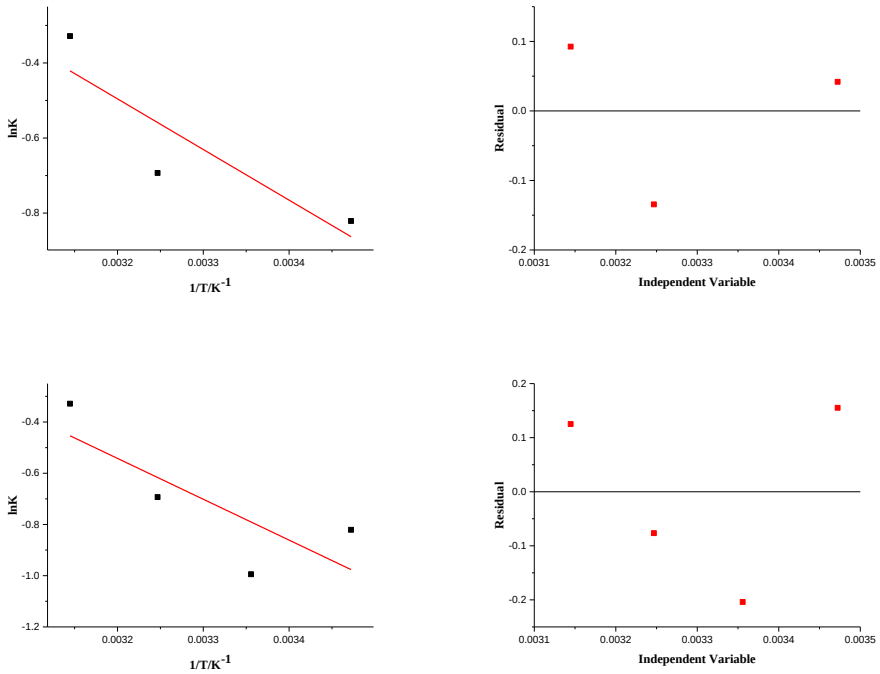

Figure 84. Evaluation of activation energy by Arrhenius equation, using three temperatures (288, 308 and 318 K) and four temperatures (288, 298, 398 and 318 K), K values were calculated from Higuchi model

Another aspect which was considered was whether variation in the average particle size could have an effect on the decrease of available surface area for subsequent adsorption after the initial release evidenced in **Figure 75** and **Figure 76**. **Figure 85** shows that higher amount of gluconate is released in presence of anions (chloride, hydroxide or nitrate) compared to deionized water, but the amount of adsorbed material decreases with increase in ionic strength of the medium (increase of sodium chloride concentration), thereby suggesting that the increase in particle size (D90) leads to a lowering of the surface area available to adsorption.

Under acidic conditions LDH dissolves more extensively than in neutral conditions, meaning that a larger amount of Glu is released in solution. The lower amount of adsorbed Glu in LDH under acidic conditions vs. in neutral pH conditions may be explained by decrease in the mass of available LDH to adsorb Glu due to dissolution in the former case. At high pH agglomeration occurs and adsorption of smaller amounts of gluconate may take place.

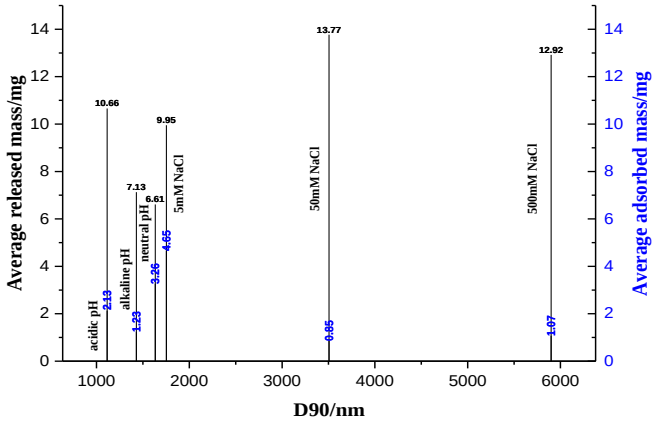

Figure 85. Dependence of gluconate released and adsorbed amounts from **Zn(2)Al-Glu-AN** particles diameter (D90) using different triggers at 25 ^{0}C

To summarize, under the conditions tested, one can see that the release mechanisms associated with ion-exchange in the presence of chlorides (NaCl) and hydroxides (pH 10), show the presence of new phases associated with the replacement of Glu with the corresponding anions (XRD). In these conditions Higuchi and Power function models fitted data in stage I of the release. Under acidic and neutral conditions different kinetics of release were observed: first order and zero order models were used to fit to the experimental data and XRD do not show appearance of new LDH phases, which may imply a different release process such as partial dissolution.

6.2 Fluorescein release studies from LDH

Results of section 4.1.1 and 4.1.2 showed that **Zn(2)Al-FSS-AN** is a single-phase material with sensing species intercalated into LDH galleries. **Table 52** presents FSS loading content and anion-exchange capacity of the resulting LDH.

Table 52. Fluorescein loading content and theoretical AEC of **Zn(2)Al-FSS-AN**

LDH	FSS loading content, %wt	AEC theoretical, cmolkg^{-1}
Zn(2)Al-FSS-AN	11	158.56

AEC is calculated using equation **12**

Investigation of FSS release from LDH was performed using the following types of triggers: 50 mM NaCl, acidic (pH 4), neutral (deionized water) - pH 7, alkaline (pH 11) and ethanol, due to the high

solubility of FSS in ethanol. The latter trigger can be relevant for other applications of LDH materials in multi-functional coatings such as food packaging. Furthermore, it may also bring some information concerning the stability of these materials for solvent-based protective coatings.

Similar to **Zn(2)Al-Glu-AN**, **Zn(2)Al-FSS-AN** LDH also reveals a buffering pH, with the solution pH being around 8.00 in the end of all the release experiments performed. The largest amount of FSS released was found to occur in the presence of ethanol, followed by an initial alkaline pH. On the other hand, the lowest values correspond to release in deionized water and using initial acidic conditions (**Table 53, Figure 86** and **Figure 87**).

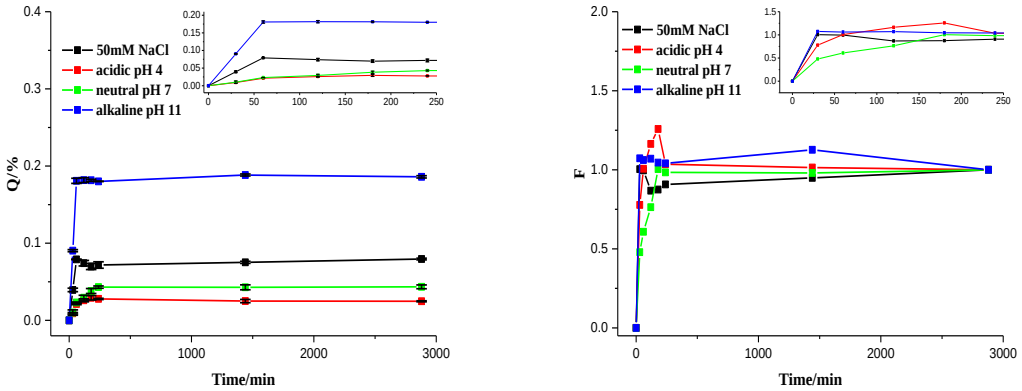

Figure 86. FSS release profiles and fraction of released FSS from **Zn(2)Al-FSS-AN** with aqueous triggers (error bars are standard errors between 3 measurements; Q-cumulative release % and F-fractional uptake)

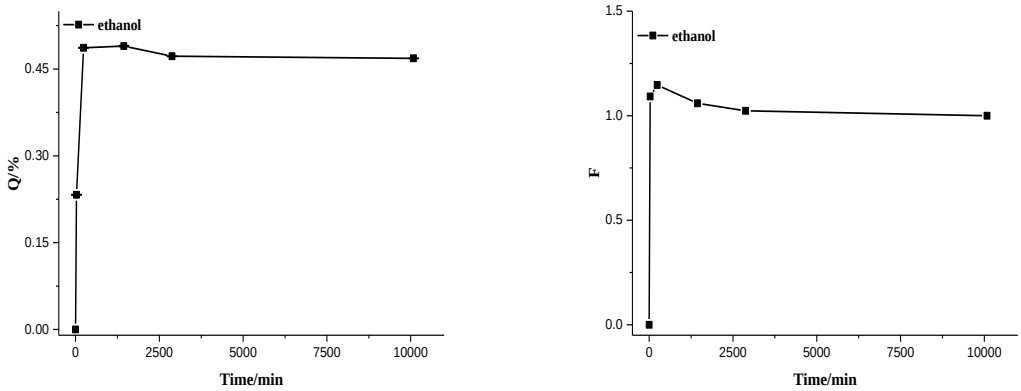

Figure 87. FSS release profiles and fraction of released FSS from **Zn(2)Al-FSS-AN** with ethanol trigger (error bars are standard errors between 3 measurements; Q-cumulative release % and F-fractional uptake)

Table 53. Amount of FSS released under influence of various triggers

Trigger	**Average FSS released amount from loading content, % wt**
50 mM NaCl	6
Acidic pH 4	2
Neutral pH 7	3
Alkaline pH 11	14
Ethanol	11

According to data presented in **Table 54** and **Figure 88** the release mechanism associated with FSS is based on diffusion processes, similarly to Glu (Higuchi, Power function, Elovich models). Moreover, fitting of adsorption part could only be performed for the initial acidic pH 4 and for release studies in ethanol (**Table 55** and **Figure 89**). The rate limiting step during adsorption is also diffusion dependent. Besides, pseudo-first order (Freundlich) kinetics is consistent with the physisorption nature of the process.

Table 54. Kinetic models used to fit fluorescein release profiles from **Zn(2)-Al-FSS-AN** under different triggers

LDH	Exp. Conditions/time of fitting	Kinetics model	Limiting step according to the model(s)	Figures of merit
Zn(2)Al-FSS-AN	Immersion in 50 mM NaCl at 25 ºC/0_60 min	Higuchi	Diffusion	**K_H** = 0.39 $min^{-0.5}$ (0.025-**st.error**);
	Immersion in 50 mM NaCl at 25 ºC/120_2880 min	Power function	Diffusion	**a** = 0.71 $min^{-0.04}$ (0.023-**st.error**); **k** = 0.04 (0.0051-**st.error**)
	Immersion in deionized water with initial pH 4 at 25 ºC/0_180 min	Elovich	Bulk and surface diffusion	**a** = 1.12 min^{-1} (0.034-**st.error**); **b**= -0.59 (0.051-**st.error**)
		First order	-	**K** = 0.003 min^{-1} ($8.614 \cdot 10^{-4}$-**st.error**); **Pearson's r:** 0.93 **Adj. R^2:** 0.80 **p-value**: 0.071
	Immersion in deionized water at 25 ºC/0_180 min	Power function	Diffusion	**a** = 0.11 $min^{-0.42}$ (0.029-**st.error**); **k=** 0.42 (0.057-**st.error**)
		Elovich	Bulk and surface diffusion	**a** = 1.15 min^{-1} (0.263-**st.error**); **b**= -0.97 (0.387-**st.error**)
	Immersion in deionized water at 25 ºC/240_2880 min	First order	-	**K** = 0.003 min^{-1} ($8.614 \cdot 10^{-4}$-**st.error**); **Pearson's r:**0.93 **Adj. R^2:** 0.73 **p-value**: 0.240

Table 54. Kinetic models used to fit fluorescein release profiles from **Zn(2)-Al-FSS-AN** under different triggers (cont.)

LDH	Exp. Conditions/time of fitting	Kinetics model	Limiting step according to the model(s)	Figures of merit
Zn(2)Al-FSS-AN (cont.)	Immersion in deionized water with initial pH 11 at 25 ºC/60_1440 min	Power function	Diffusion	**a** = 0.96 $min^{-0.02}$ (0.055-**st.error**); **k=** 0.02 (0.010-**st.error**)
	Immersion in ethanol at 25 ºC/0_1440 min	Higuchi	Diffusion	K_H = 0.34 $min^{-0.5}$ (0.054-**st.error**);

pp. 40-42 contain description of used release kinetic models

Table 55. Adsorption kinetic models used to fit fluorescein release profiles from **Zn(2)-Al-FSS-AN** under different triggers

LDH	Exp. Conditions/time of fitting	Kinetics model	Limiting step according to the model(s)	Figures of merit
Zn(2)Al-FSS-AN	Immersion in deionized water with initial pH 4 at 25 ºC/240_2880 min	Pseudo-first order	One site occupancy adsorption	**K** = $2.58 \cdot 10^{-7}$ min^{-1} ($4.231 \cdot 10^{-8}$-**st.error**); **Pearson's r:** 0.99 **Adj. R^2:** 0.95 **p-value**: 0.1
		Power function	Intraparticle diffusion	**a** = 1.00 $min^{-0.0003}$ ($2.608 \cdot 10^{-4}$-**st.error**); **k=** $2.66 \cdot 10^{-4}$ ($3.741 \cdot 10^{-5}$-**st.error**);

Table 55. Adsorption kinetic models used to fit fluorescein release profiles from **Zn(2)-Al-FSS-AN** under different triggers (cont.)

LDH	Exp. Conditions/time of fitting	Kinetics model	Limiting step according to the model(s)	Figures of merit
Zn(2)Al-FSS-AN (cont.)	Immersion in ethanol at 25 ºC/1440_10080 min	Pseudo-first order	One site occupancy adsorption	**K** = $6.83 \cdot 10^{-7}$ min^{-1} ($3.631 \cdot 10^{-7}$-**st.error**); **Pearson's r:** 0.88 **Adj. R^2:** 0.56 **p-value**: 0.311
		Elovich	Bulk and surface diffusion	**α=** 2.86 min^{-1} (0.741-**st.error**); **intercept=** 92.84 (1.554 -**st.error**)

pp. 35-36 contains description of used adsorption kinetic models

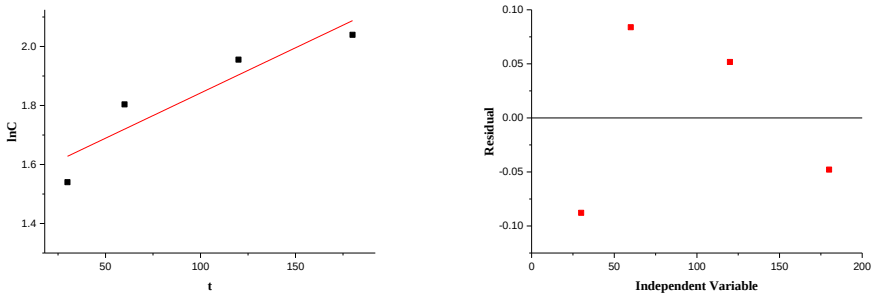

Figure 88. Fitting of data (first order model (linear)) of FSS release from **Zn(2)Al-FSS-AN** during immersion in deionized water with initial pH 4

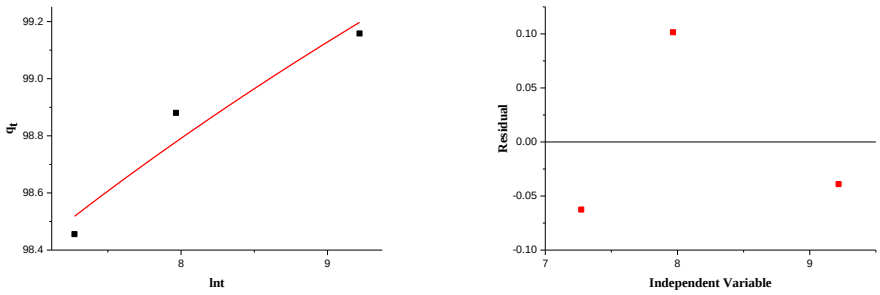

Figure 89. Fitting of data (Elovich model (non-linear)) of FSS adsorption at 20 ^{0}C onto **Zn(2)Al-FSS-AN** during immersion in ethanol

Analysis of LDH with FSS powders after release does not show significant structural changes (**Figure 90**). The reflections occurring at low 2 Theta angles after release corresponds to the values determined initially for **Zn(2)Al-FSS-AN** material **(Table 9).** Besides, the presence of FSS in this LDH after release is additionally confirmed by vibrations associated with this dye (Hesse, Meier and Zeeh 1997). At this point is important to make a partial discussion of the results presented so far.

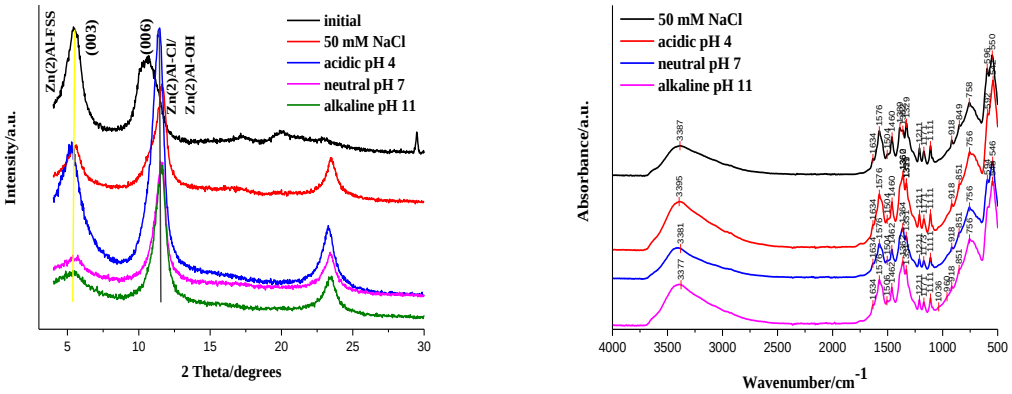

Figure 90. XRD and FTIR results of **Zn(2)Al-FSS-AN** after release studies

For the triggers which were also tested for LDH materials with Glu, namely 50 mM NaCl, pH 4, pH 7 and pH 11 a very small amount of FSS was released (lower than 10 % for all the conditions except pH 11). Under these conditions little to no effect in the XRD would be expected, particularly because the appearance of low intensity LDH-Cl or LDH-OH reflections would be masked by the higher intensity reflections associated with LDH-FSS. However, there is consistency in terms of kinetic models of release fitted for LDH-FSS and LDH-Glu. The reduced extent of release of FSS compared

to Glu can be related to changes in solubility, charge density and additional stability imparted to LDH structure by FSS, which can be reflected on a lower extent of exchange with chlorides and hydroxides. Also, the small effect of acidic conditions on the release of FSS by dissolution may be due to increase stability of this structure magnified with the ability to act as pH buffer on its own, as several acid-base equilibria is associated with FSS.

Figure 91 shows that LDH-FSS particles are very unstable in aqueous medium (neutral pH in the Figure) and in ethanol (for the latter solvent it was not possible even to make a repeated measurement of particle size distribution). Relatively lower agglomeration is observed in 50 mM NaCl, initial alkaline and acidic conditions. Thus, it is possible to say that after release of FSS under different pH triggers the particles diameter decreases (less tendency to agglomeration). The same trend as found for Glu is observed: lower agglomeration of particles leads to a higher extent of adsorption in aqueous medium due to higher surface available (ANOVA estimations show that there is a statistical difference between initial pH of release and LDH particles diameter). Moreover, initial **Zn(2)Al-FSS-AN** particles are negatively charged in aqueous (zeta-potential-5.04±0.085mV) and after release the charge of particles becomes less negative (zeta-potential is -4.79.±0.161; -0.68.±0.065; -2.74.±0.418; -2.16.±0.208 mV for respective triggers: 50mM NaCl; initial acidic pH 4; neutral pH and initial alkaline pH 11). The negative charge of **Zn(2)Al-FSS-AN** is consistent with partial adsorption of this dye onto the external surface of LDH, which is also consistent with the thermal decomposition of compound (Figure **A1** Annex). The change of particles charge after release studies is consistent with release of FSS from external LDH surfaces.

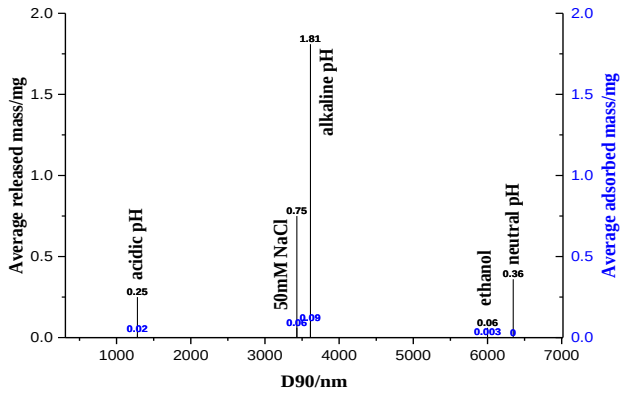

Figure 91. Dependence of FSS released and adsorbed amounts from LDH particles diameter (D90) using different triggers

*initial mass of LDH for release studies in ethanol trigger was 100 times smaller, than for aqueous triggers (0.005 g vs 0.5 g.)

The mechanism of FSS release can be described as controlled by diffusion under the studied conditions, depending on the level of LDH agglomeration, solubility of FSS and presence of anionic species in the respective medium to promote the anion-exchange reaction. For example, the largest amount of FSS released occurred in aqueous medium with initial pH 11, corresponding to ca. 45 mgL^{-1}, which is very close to limit of FSS solubility in water according to literature (50 mgL^{-1}) (Dehn 1917). For the other triggers under aqueous conditions, the largest amount of FSS released is in the range 7-20 mgL^{-1}. In addition, the presence of anionic species increases the extent of release of sensing species due to anion-exchange reaction with Cl^-, HO^-/CO_3^{2-}. Moreover, the decrease of negative charge of **Zn(2)Al-FSS-AN** after release of FSS, along with models of release based on bulk and surface diffusion as rate-limiting steps, point toward diffusion of FSS from external surfaces and further diffusion and exchange of FSS from the interlayer with anions presenting in the medium (although the extent of ion-exchange from interlayer galleries is not enough to see structural changes in the XRD).

6.3 Phenolphthalein release studies from LDH

The release of PhPh from two types of LDH materials prepared by calcination-rehydration procedure, namely **Zn(2)Al-PhPh-CALC150** and **Mg(3)Al-PhPh-SH/CALC150** was studied. Previously (Chapter 4), it was found that this pH indicator was only adsorbed onto the surface of LDH without intercalation in LDH interlayer galleries. **Table 56** shows the loading content of PhPh. Such high values of adsorbed dye can be explained by the multilayer physical adsorption, which was fitted by Freundlich model (section 5.1).

Figure 92 depicts the release profiles of PhPh from ZnAl LDHs and **Table 57** shows the amount of PhPh released under the surveyed conditions. Under different aqueous conditions, less than 10 % of the total PhPh is released, whereas in ethanol PhPh release rises up to more than 50 % of the total loading content. These differences can be explained by the low solubility of PhPh in water. Solubility data available in the literature indicate that solubility of PhPh in water is 400 mgL^{-1} (Yalkowsky and He 2003), whereas in ethanol it is solubility of PhPh is $83 \cdot 10^3$ mgL^{-1} (O'Neil 2001).

Table 56. PhPh loading content and theoretical AEC of prepared LDH

LDH	PhPh loading content, %wt	AEC theoretical, cmolkg^{-1}
Zn(2)Al-PhPh-CALC150	71	162.16
Mg(3)Al-PhPh-SH/CALC150	76	166.30

AEC is calculated using equation **12**

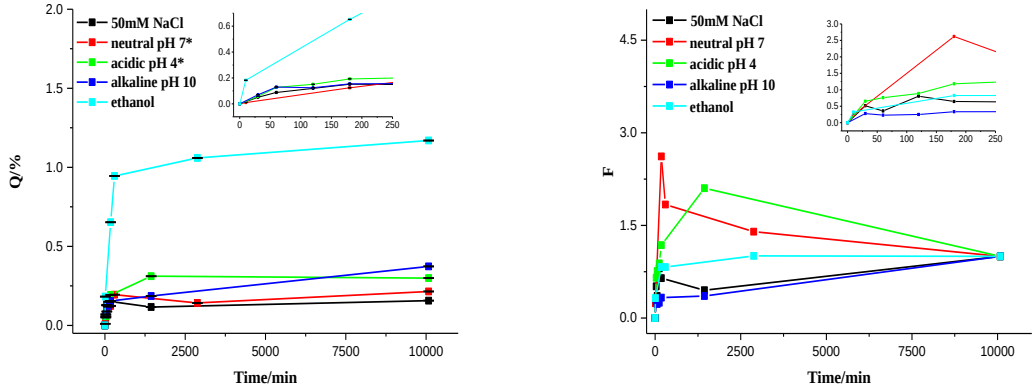

Figure 92. PhPh release profiles and fraction of released PhPh from **Zn(2)Al-PhPh-CALC150** with different triggers (error bars are standard errors between 3 measurements; Q-cumulative release % and F-fractional uptake)

* a strong decrease of PhPh concentration observed under influence of triggers marked with asterisks

Table 57. Amount of PhPh released from **Zn(2)Al-PhPh-CALC150** under influence of different triggers

Trigger	Average PhPh released amount from loading content, % wt
50 mM NaCl	4
Acidic pH 4	6
Neutral pH 7	7
Alkaline pH 10	6
Ethanol	54

The release profiles of PhPh from **Zn(2)Al-PhPh-CALC150** were successfully fitted using Higuchi and Power function models (whereby diffusion is a rate-limiting step)- **Figure 93** and **Table 58**. The highest Higuchi constant is determined in deionized water trigger during first 180 min of release. The highest Power function constant is determined in ethanol trigger for 1-week measurements of

release. However, and contrary to the previously presented systems LDH-Glu and LDH-FSS, in the present case after an increase of PhPh there is a monotonic decrease of PhPh under neutral and acidic conditions. Therefore, and considering that the release PhPh is on the limit of its solubility in water, it is possible that PhPh may precipitate as a result of increase in ionic strength of the media due to partial dissolution of LDH or some salting out effect due to combination of the metal cations with PhPh into some insoluble form. During dropping of PhPh reagent in aqueous neutral or acidic solutions appearance of white turbidity can take place due to low solubility of PhPh in water and its precipitation (ChemicalBook 2017). The level of PhPh released concentrations under aqueous triggers is in the range of 76-195 mgL^{-1} (lower than PhPh limit of solubility in pure water). For this reason, we will only discuss the release of PhPh and attribute the subsequent decrease in PhPh concentration to the precipitation of PhPh.

Table 58. Kinetic models used to fit phenolphtalein release profiles from **Zn(2)-Al-PhPh-CALC150** under different triggers

LDH	Exp. Conditions/time of fitting	Kinetics model	Limiting step according to the model(s)	Figures of merit
Zn(2)Al-PhPh-CALC150	Immersion in 50 mM NaCl at 25 ºC/0_120 min	Higuchi	Diffusion	$\mathbf{K_H}$ = 0.20 $min^{-0.5}$ (0.029-**st.error**);
	Immersion in deionized water with initial pH 4 at 25 ºC/0_1440 min	Power function	Diffusion	**a** = 0.22 $min^{-0.31}$ (0.025-**st.error**); **k=** 0.31 (0.019-**st.error**)
	Immersion in deionized water at 25 ºC/0_180 min	Higuchi	Diffusion	$\mathbf{K_H}$ = 0.60 $min^{-0.5}$ (0.161-**st.error**);
	Immersion in deionized water with initial pH 10 at 25 ºC/60_10080 min	Higuchi	Diffusion	$\mathbf{K_H}$ = 0.09 $min^{-0.5}$ (0.0073-**st.error**);
	Immersion in ethanol at 25 ºC/0_10080 min	Power function	Diffusion	**a** = 0.39 $min^{-0.11}$ (0.116-**st.error**); **k=** 0.11 (0.039-**st.error**)

pp. 40-42 contain description of used release kinetic models

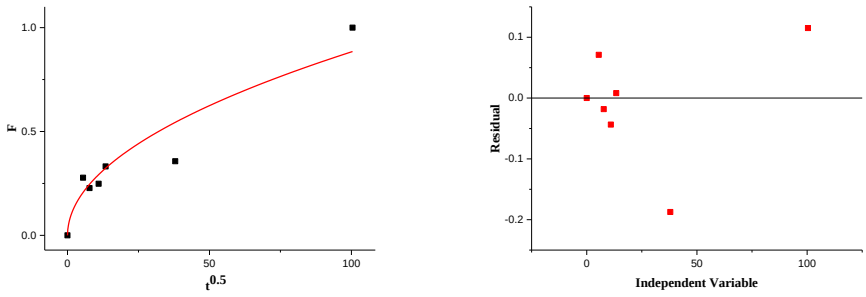

Figure 93. Fitting of data (Higuchi model (non-linear)) of PhPh release from **Zn(2)-Al-PhPh-CALC150** during immersion in deionized water with initial pH 10

Figure 94 demonstrates, that the lowest D90 values were obtained for **Zn(2)Al-PhPh-CALC150** particles dispersed into aqueous and ethanolic medium. Note that under these conditions PhPh release was the highest, (**Table 57**). Nonetheless, limitations in PhPh solubility in different media must be accountable for the large difference in terms of released PhPh in water vs. ethanol, in spite of a minor variation in D90 values.

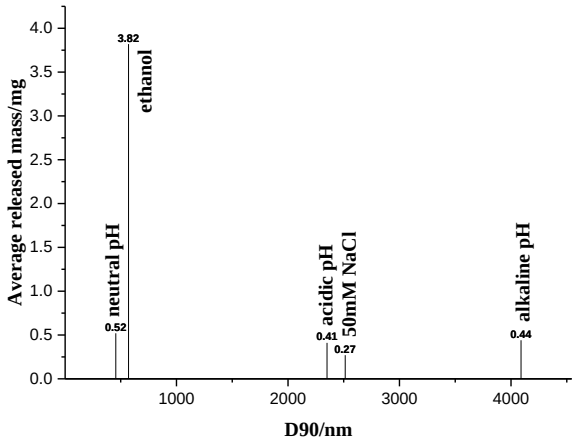

Figure 94. Dependence of PhPh released amounts using different triggers from **Zn(2)Al-PhPh-CALC150** particles diameter (D90)

The release profiles and PhPh loading content in **Mg(3)Al-PhPh-SH/CALC150** are presented below (**Figure 95** and **Table 59**). Similar to the ZnAl LDH, there is a high release of PhPh from MgAl LDHs in ethanol, when compared to other conditions in aqueous media, which is consistent with differences in solubility of PhPh in these two media. Moreover, the decrease in PhPh as a function of time was rationalized as being due to its solubility limitations and some sort of salting out effect triggered by increase in ionic strength due to partial LDH dissolution.

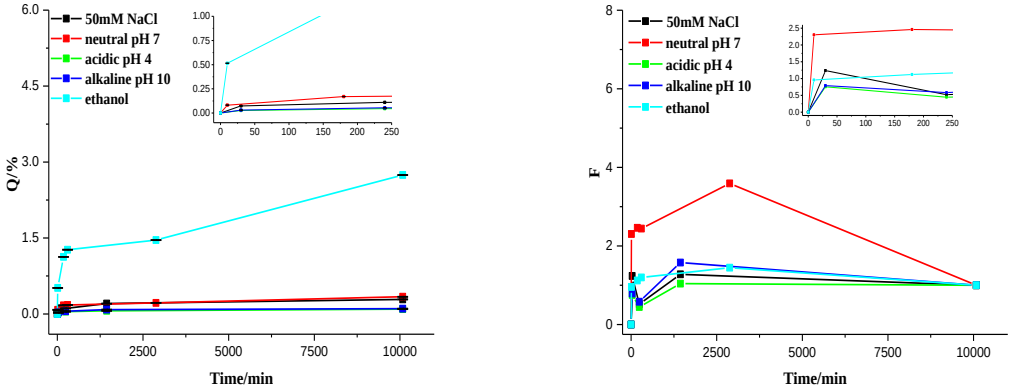

Figure 95. PhPh release profiles and fraction of released PhPh from **Mg(3)Al-PhPh-SH/CALC150** with different triggers (error bars are standard errors between 3 measurements; Q-cumulative release % and F-fractional uptake)

Table 59. Amount of PhPh released from **Mg(3)Al-PhPh-SH/CALC150** under influence of various triggers

Trigger	Average PhPh released amount from loading content, % wt
50 mM NaCl	1
Acidic pH 4	2
Neutral pH 7	3
Alkaline pH 10	2
Ethanol	74

The results of fitting of release data are presented in **Table 60**. The PhPh release profiles were successfully fitted by Higuchi, Power function, Elovich and first order models, revealing that PhPh release is limited mainly by diffusion. The values of Higuchi constants are very close for the following triggers 50mM NaCl, deionized water with initial pH 4 and pH 10. However, the Power

function constant is much higher for release in deionized water than in ethanol during the first 2880 min.

Table 60. Release kinetic models used to fit phenolphtalein release profiles from **Mg(3)-Al-PhPh-SH/CALC150** under different triggers

LDH	Exp. Conditions/time of fitting	Kinetics model	Limiting step according to the model(s)	Figures of merit
Mg(3)-Al-PhPh-SH/CALC150	Immersion in 50 mM NaCl at 25 ºC/0_1440 min	Higuchi	Diffusion	K_H = 0.22 $min^{-0.5}$ (0.061-**st.error**);
	Immersion in deionized water with initial pH 4 at 25 ºC/0_1440 min	Higuchi	Diffusion	K_H = 0.17 $min^{-0.5}$ (0.032-**st.error**);
	Immersion in deionized water at 25º C/0_2880 min	Power function	Diffusion	**a** = 1.79 $min^{-0.07}$ (0.180-**st.error**); **k=** 0.07 (0.033-**st.error**)
	Immersion in deionized water with initial pH 10 at 25 ºC/0_1440 min	Higuchi	Diffusion	K_H = 0.24 $min^{-0.5}$ (0.033-**st.error**);
		First order	-	**K** = $6.27 \cdot 10^{-4}$ min^{-1} ($2.804 \cdot 10^{-4}$-**st.error**); **Pearson's r:** 0.91 **Adjacent r^2:** 0.67 **p-value:** 0.268
	Immersion in ethanol at 25 ºC/0_2880 min	Power function	Diffusion	**a** = 0.78 $min^{-0.08}$ (0.037-**st.error**); **k=** 0.08 (0.008-**st.error**)
		First order	-	**K** = $1.17 \cdot 10^{-4}$ min^{-1} ($4.544 \cdot 10^{-5}$-**st.error**); **Pearson's r:** 0.88 **Adjacent r^2:** 0.65 **p-value:** 0.24

pp.40-42 contains description of used release kinetic models

The release of PhPh from ZnAl and MgAl LDHs thermally treated at 150 ºC, is consistent with a diffusion-controlled process. Moreover, the extent of release of PhPh is very much controlled by its solubility in different media, and processes such as increase in ionic strength can also play a role (e.g. salting out effect) on the decrease of PhPh detected in solution for long immersion times.

6.4 Thymol blue release studies from LDH

The release of TB from **Zn(2)Al-TB-CALC150** and **Mg(3)Al-TB-SH/CALC150**, is presented in this section. These LDH materials were found not to have TB intercalated in the LDH galleries (Chapter 4). Furthermore, the adsorption studies presented in section 5.2 revealed mixture of chemisorption with physisorption of **Zn(2)Al-NO_3-CALC150** and **Mg(3)Al-CO_3-SH/CALC150**. The values of loading content presented in **Table 61**, seem to support the adsorption findings, as only 1 wt % of TB is present in ZnAl and 8 % in MgAl LDH samples.

Table 61. TB loading content and theoretical AEC of prepared LDH

LDH	TB loading content, %wt	AEC theoretical, $cmolkg^{-1}$
Zn(2)Al-TB-CALC150	1	130.73
Mg(3)Al-TB-SH/CALC150	8	133.40

AEC is calculated using equation **12**

Figure 96 shows the release profiles of TB from **Zn(2)Al-TB-CALC150** under different conditions and **Table 62 -** the amount of TB released. The largest release of TB was found in ethanol and the smallest in deionized water. Data for solubility of TB in water could not be found, though its solubility in ethanol is relatively high ($10 \cdot 10^3$ mgL^{-1}) (Merck 2019). Assuming a chemisorption mechanism for adsorption of TB in ZnAl LDH, the higher extent of release of TB in ethanol observed can be explained by some TB which remained after the synthesis (as physisorbed multilayer-section 5.2). Moreover, differences in release of TB as a function of extreme pH values, may be ascribed to dissolution of LDH under low pHs or conversion of ZnAl hydroxides into oxides at high pHs (ZnO nanoparticles can be synthesized according to literature under alkaline conditions pH 8-12.5, (Amin, et al. 2011)) combined with higher solubility of TB under alkaline conditions (ChemicalBook 2017). Moreover, studies by Galvão and colleagues revealed that dissolution of cationic sheets occurs even during LDH washing with deionized water (Galvao, et al. 2016), which can explain the release of TB under neutral conditions (although only 2 % of the 1 wt % in loading content was detected).

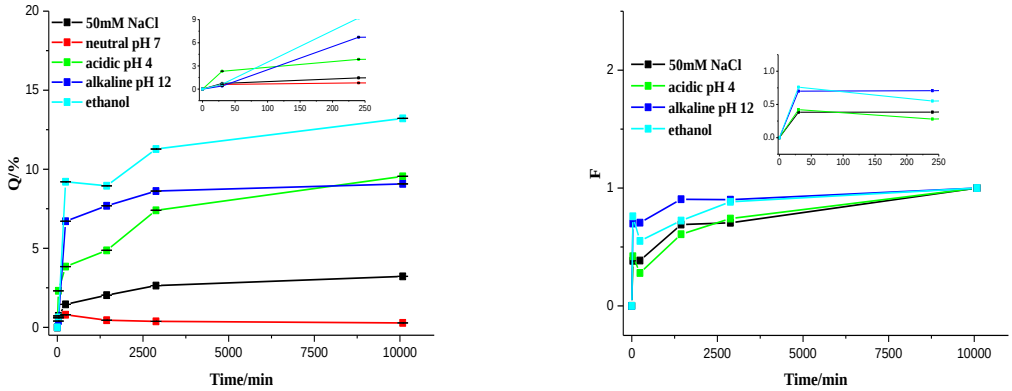

Figure 96. TB release profiles and fraction of released TB from **Zn(2)Al-TB-CALC150** with different triggers (error bars are standard errors between 3 measurements; Q-cumulative release % and F-fractional uptake)

Table 62. Amount of TB released from **Zn(2)Al-TB-CALC150** under influence of various triggers

Trigger	**Average TB released amount from loading content, % wt**
50 mM NaCl	7
Acidic pH 4	20
Neutral pH 7	2
Alkaline pH 12	24
Ethanol	32

The release profiles of TB from **Zn(2)Al-TB-CALC150** were successfully fitted by the following kinetic models: Higuchi and Power function models, whereby diffusion is the rate-limiting step (**Table 63** and **Figure 97**). The values of constants determined by the same model are similar regardless of trigger considered.

Table 63. Kinetic models used to fit thymol blue release profiles from **Zn(2)Al-TB-CALC150** under different triggers

LDH	Exp. Conditions/time of fitting	Kinetics model	Limiting step according to the model(s)	Figures of merit
Zn(2)Al-TB-CALC150	Immersion in 50 mM NaCl at 25 ºC/0_10080 min	Higuchi	Diffusion	$\mathbf{K_H}$ = 0.10 $min^{-0.5}$ (0.005-**st.error**);
	Immersion in deionized water with initial pH 4 at 25 ºC/0_10080 min	Higuchi	Diffusion	$\mathbf{K_H}$ = 0.10 $min^{-0.5}$ (0.006-**st.error**);
		First order	-	**K** = $9.72 \cdot 10^{-5}$ min^{-1} ($4.019 \cdot 10^{-5}$-**st.error**); **Pearson's r:** 0.81 **Adj. R^2:** 0.55 **p-value**: 0.094
	Immersion in deionized water at 25 ºC/0_30 min	-	-	-
	Immersion in deionized water with initial pH 12 at 25 ºC/0_10080 min	Power function	Diffusion	**a** = 0.53 $min^{-0.07}$ (0.051-**st.error**); **k=** 0.07 (0.013-**st.error**)
		First order	-	**K** = $3.17 \cdot 10^{-5}$ min^{-1} ($1.427 \cdot 10^{-5}$-**st.error**); **Pearson's r:** 0.79 **Adj. R^2:** 0.50 **p-value**: 0.113
	Immersion in ethanol at 25 ºC/0_10080 min	Higuchi	Diffusion	$\mathbf{K_H}$ = 0.12 $min^{-0.5}$ (0.016-**st.error**);
		First order	-	**K** = $4.27 \cdot 10^{-5}$ min^{-1} ($1.931 \cdot 10^{-5}$-**st.error**); **Pearson's r:** 0.79 **Adj. R^2:** 0.49 **p-value**: 0.114

pp. 40-42 contain description of used release kinetic models

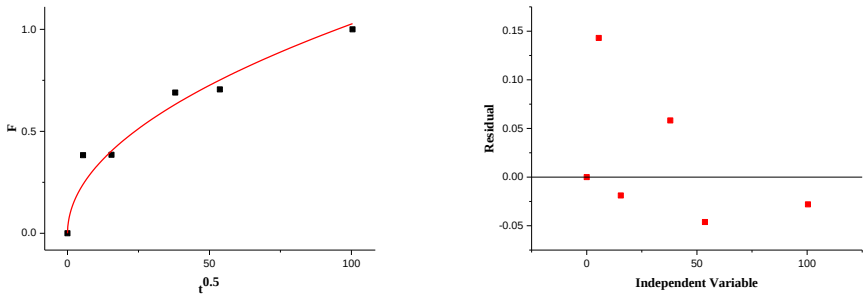

Figure 97. Fitting data (Higuchi model (non-linear)) of TB release from **Zn(2)Al-TB-CALC150** during immersion in 50 mM NaCl

The release profiles for TB from **Mg(3)Al-TB-SH/CALC150** and the amount of TB released under different triggers is presented in **Figure 98** and **Table 64**. Considering that TB is both chemi- and physisorbed, it is no surprise that larger amounts of TB were released for this pH indicator under tested conditions compared to **Zn(2)Al-TB-CALC150**. However, for MgAl LDH samples the system seems less responsive to release under acidic medium than the ZnAl. This difference in solubility may be due to changes in the LDH composition and to the presence of some groups from the fatty acids covering the SH LDH, as referred in previous chapters.

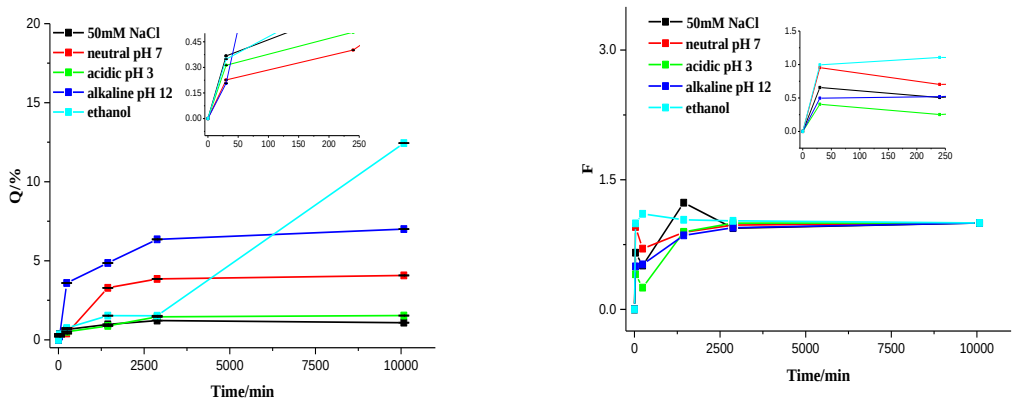

Figure 98. TB release profiles and fraction of released TB from **Mg(3)Al-TB-SH/CALC150** with different triggers (error bars are standard errors between 3 measurements; Q-cumulative release % and F-fractional uptake)

Table 64. Amount of TB released from **Mg(3)Al-TB-SH/CALC150** under influence of various triggers

Trigger	Average TB released amount from loading content, % wt
50 mM NaCl	3
Acidic pH 3	3
Neutral pH 7	11
Alkaline pH 12	16
Ethanol	36

Table 65. Kinetic models used to fit thymol blue release profiles from **Mg(3)Al-TB-SH/CALC150** under different triggers

LDH	Exp. Conditions/time of fitting	Kinetics model	Limiting step according to the model(s)	Figures of merit
Mg(3)Al-TB-SH/CALC150	Immersion in 50 mM NaCl at 25 ºC/0_1440 min	Higuchi	Diffusion	**K_H** = 0.19 $min^{-0.5}$ (0.025-**st.error**);
		First order	-	**K** = $5.49 \cdot 10^{-4}$ min^{-1} ($2.472 \cdot 10^{-4}$-**st.error**); **Pearson's r:** 0.91 **Adj. R^2:** 0.66 **p-value**: 0.269
	Immersion in deionized water with initial pH 3 at 25 ºC/0_10080 min	Higuchi	Diffusion	**K_H** = 0.12 $min^{-0.5}$ (0.012-**st.error**);
		First order	-	**K** = $9.72 \cdot 10^{-5}$ min^{-1} ($6.844 \cdot 10^{-5}$-**st.error**); **Pearson's r:** 0.62 **Adj. R^2:** 0.18 **p-value**: 0.263

Table 65. Kinetic models used to fit thymol blue release profiles from **Mg(3)Al-TB-SH/CALC150** under different triggers (cont.)

LDH	Exp. Conditions/time of fitting	Kinetics model	Limiting step according to the model(s)	Figures of merit
Mg(3)Al-TB-SH/CALC150 (cont.)	Immersion in deionized water at 25 ºC/0_10080 min	Higuchi	Diffusion	**K_H** = 0.13 $min^{-0.5}$ (0.023-**st.error**);
		First order	-	**K** = $2.08 \cdot 10^{-5}$ min^{-1} ($1.681 \cdot 10^{-5}$-**st.error**); **Pearson's r:** 0.58 **Adj. R^2:** 0.12 **p-value**: 0.304
	Immersion in deionized water with initial pH 12 at 25 ºC/0_10080 min	Higuchi	Diffusion	**K_H** = 0.12 $min^{-0.5}$ (0.010-**st.error**);
		First order	-	**K** = $6.12 \cdot 10^{-5}$ min^{-1} ($3.281 \cdot 10^{-5}$-**st.error**); **Pearson's r:** 0.73 **Adj. R^2:** 0.58 **p-value**: 0.159
	Immersion in ethanol at 25 ºC/0_240 min	Higuchi	Diffusion	**K_H** = 0.32 $min^{-0.5}$ (0.045-**st.error**);

pp. 40-42 contain description of used release kinetic models

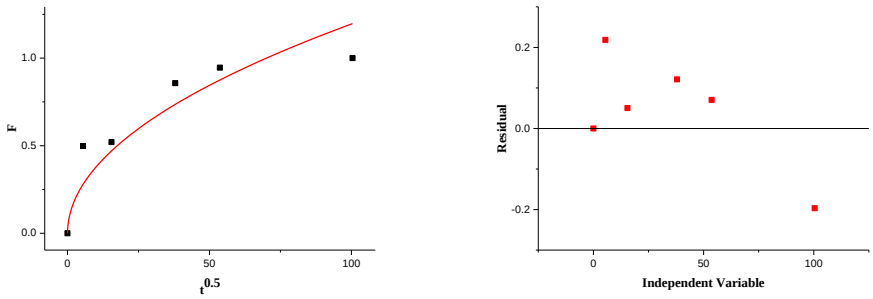

Figure 99. Fitting data (Higuchi model (non-linear)) of TB release from **Mg(3)Al-TB-SH/CALC150** during immersion in deionized water with initial pH 12

The release of TB from **Mg(3)Al-TB-SH/CALC150** is described by the Higuchi model, confirming, that diffusion is a rate-limiting step. Besides, it was possible to evaluate reaction rates under influence of the following triggers (**Table 65** and **Figure 99)**: 50mM NaCl, initial acidic pH 3 and neutral pH 7. The highest reaction rate is observed for TB release in presence of 50mM NaCl: $5.49 \cdot 10^{-4}$ min^{-1}, which corresponds to LDH with lowest D90 values (**Figure 100**). For the other triggers, the reaction is ten times slower (**Table 65**). Another aspect worth of mention is that under acidic conditions high agglomeration occurs, which may be related with protonation of fatty acid groups remaining on the surface of SH after thermal treatment at 150 ºC (electrophoretic mobility of particles at this pH is 0.92 $\mu m cm V^{-1} s^{-1}$- **Figure 42**). The largest value of Higuchi constant is observed for TB release in ethanol during first 240 min.

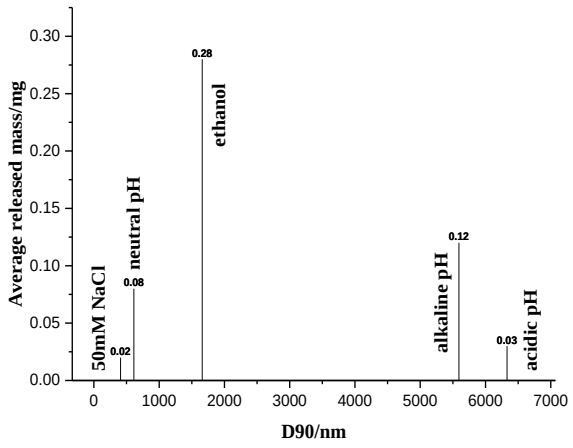

Figure 100. Dependence of TB released amounts using different triggers from **Mg(3)Al-TB-SH/CALC150** particles diameter (D90)

Summarizing this section, ZnAl and MgAl LDH used to immobilize TB gives rise to different loadings and extent of release of TB. This is consistent with the kind of adsorption mechanism governing the adsorption of TB in the external layers of LDH, as well as with effects of surface composition (presence of fatty acids in SH structure). This effect on the surface of LDH is also well seen comparing D90 and electrophoretic mobility of these two types of LDH presented in section 4.

6.5 MBT release studies from LDH

Chemical speciation of MBT (**Figure 11**) in aqueous solution can play a significant role on its release from LDH. Another aspect to be considered is if the compound degrades as a function of time, which can make the interpretation of the release profiles difficult, not to mention that the presence of Na^+ from (NaOH or NaCl) can additionally induce transformation of MBT^- into MBTNa.

Regarding to the speciation of MBT, theoretical computational data predicted that different MBT species have different wavelengths of maximum absorbance (**Table 66**) (Galvao, et al. 2016). Besides, additional experimental data not only proved the simulations correct as it was found that in the pH range lower than 7 the predominant MBT form is thione, while for pH higher than 7 anionic MBT form (MBT^-) starts to be prevalent (Galvao, et al. 2016).

Table 66. Theoretical wavelengths of MBT species in UV-Vis spectra

MBT species	Wavelength of peaks, nm (theoretical method for calculation)
MBT thiol	228 (EOM-CCSD); 220/268 (TD-B3LYP); 207/243 (TD-M06-2X)
MBT thione	203/291 (EOM-CCSD); 222/303 (TD-B3LYP); 215/293 (TD-M06-2X)
MBT^-	207/278 (EOM-CCSD); 233/308 (TD-B3LYP); 216/289 (TD-M06-2X)
MBTNa	206/277 (EOM-CCSD); 228/305 (TD-B3LYP); 221/287 (TD-M06-2X)
$MBTH^+$	191/242 (EOM-CCSD); 219/290 (TD-B3LYP); 200/270 (TD-M06-2X)

In respect to the degradation of MBT, according to literature data, MBT degrades upon UV irradiation (Serdechnova, et al. 2014). In order to verify if degradation of MBT could be an issue for the present work, additional laboratory studies were performed for MBT in solution, in the

presence/absence of environmental light and at 20 ºC and 35 ºC (data not shown). The results obtained revealed that under the conditions found daily in the lab MBT did not degrade as a function of time, although there is an equilibrium between two forms of MBT species: MBTNa and MBT^- (Figure **A5** Annex).

6.5.1 MBT release from Mg(3)Al-MBT-CALC650

In Chapter 4, MBT was found to be loaded in **Mg(3)Al-MBT-CALC650**, though not intercalated in the interlayer galleries. Moreover, in Chapter 5 the adsorption of MBT was proposed to occur according to a chemisorption mechanism with possibility of multilayer physisorption. **Table 67** reveals MBT loading and **Figure 101** the release profiles of MBT from this LDH system.

The release of MBT seems to be very fast, achieving the final concentration in the first minutes of release (NaCl solutions). Under different pH conditions it seems that the peak of MBT release occurs later (after 24 h) and then the values decrease slightly, tending to the value obtained for the solution with initial pH 7. These results may be due to the pH variation associated with pH buffering effect with LDH and variation of solubility of MBT as a function of pH. Data available in the literature shows that MBT solubility in water is 120 mgL^{-1} at 24 ^0C, 900 mgL^{-1} in water with pH 9 and 51 mgL^{-1} in water with pH 5. The level of released MBT is in the range of 65-75 mgL^{-1}, depending on the studied triggers, which is slightly lower than MBT solubility in pure water and much lower than MBT solubility at pH 9.

In fact, variations in the solution pH were noticed during release studies. The position of the second MBT absorbance peak associated with anionic form of MBT (UV-Vis spectra not shown), mean that for the whole timescale the anionic form of MBT was predominating for all the studied conditions, except for the initial pH 10. In the latter case, during the first hour of immersion the predominating form was sodium MBT (MBTNa) with domination of MBT^- species for the remaining monitored time (though the pH kept at 10.00 until the end of the study). In NaCl solutions the solution pH was 9 during all the monitored time and when the solution with initial pH 4 was used, it immediately increased to 9 as well (consistent with dissolution of MgAl LDH), remaining in this value until the end of the measurements. Under initial neutral conditions, the solution pH 7 increased up to 9. In the case of all the solutions showing more alkaline conditions than with guest species reported before, this may be due to an effect associated with partial protonation of MBT^- released in solution which acts as a base, raising the solution pH.

Table 67. MBT loading content and theoretical AEC of **Mg(3)Al-MBT-CALC650**

LDH	MBT loading content, %wt	AEC theoretical, cmolkg^{-1}
Mg(3)Al-MBT-CALC650	3	222.1

AEC is calculated using equation **12**

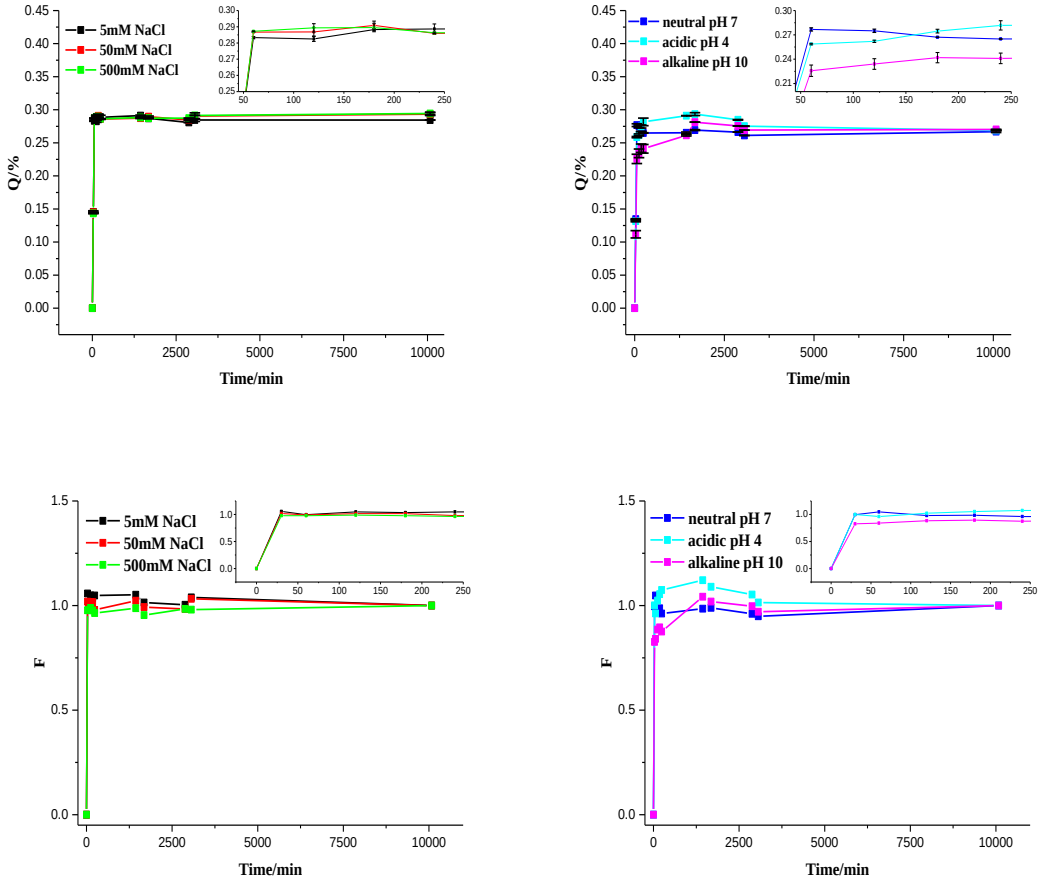

Figure 101. MBT release profiles and fraction of released MBT from **Mg(3)Al-MBT-CALC650** with different triggers (error bars are standard errors between 3 measurements; Q-cumulative release % , F-fractional uptake)

Table 68 presents the amounts of MBT released under the influence of different triggers. The results show that the majority of MBT adsorbed is released under the tested conditions. Taking into account the chemisorption nature of the MBT adsorption discussed in Chapter 5, the release of MBT can be due to partial dissolution of LDH even under neutral conditions, as discussed before, and also due to ion-exchange reaction occurring between MBT adsorbed in the outer surface of LDH with anions present in solution. The latter possibility is addressed in more detail in the following sections.

Table 68. Amount of MBT released from **Mg(3)Al-MBT-CALC650** under influence of various triggers

Trigger	Average MBT released amount from loading content, % wt
5 mM NaCl	95
50 mM NaCl	95
500 mM NaCl	95
Acidic pH 4	92
Neutral pH 7	89
Alkaline pH 10	82

Table 69 shows that the release of MBT for the initial times of immersion was successfully fitted by Higuchi, Power function and Elovich models in aqueous medium and first order in 500 mM NaCl. Thus, diffusion is a rate-limiting step of MBT release (**Table 69**).

Table 69. Kinetic models used to fit MBT release profiles from **Mg(3)Al-MBT-CALC650** under different triggers

LDH	Exp. Conditions/time of fitting	Kinetics model	Limiting step according to the model(s)	Figures of merit
Mg(3)Al-MBT/CALC650	Immersion in 500 mM NaCl at 25 ºC/0_60 min	First order	-	**K** = $1.05 \cdot 10^{-5}$ min^{-1} ($6.982 \cdot 10^{-6}$-**st.error**); **Pearson's r:** 0.60 **Adj. R^2:** 0.20 **p-value**: 0.207
	Immersion in deionized water with initial pH 4 at 25 ºC/0_1440 min	Power function	Diffusion	**a** = 0.86 $min^{-0,04}$ (0.038-**st.error**); **k**= 0.04 (0.0080-**st.error**)
	Immersion in deionized water at 25 ºC/0_60 min	Higuchi	Diffusion	K_H = 0.40 $min^{-0.5}$ (0.017-**st.error**);

Table 69. Kinetic models used to fit MBT release profiles from **Mg(3)Al-MBT-CALC650** under different triggers (cont.)

LDH	Exp. Conditions/time of fitting	Kinetics model	Limiting step according to the model(s)	Figures of merit
Mg(3)Al-MBT/CALC650 (cont.)	Immersion in deionized water with initial pH 10 at 25 ºC/60_1440 min	Elovich	Bulk and surface diffusion	**a** = 0.27 min^{-1} (0.062-**st.error**); **b**= 0.47 (0.10-**st.error**)

pp. 40-42 contain description of used release kinetic models

Figure 102 shows, that structure of LDH after release of MBT in deionized water is similar to the pristine material (Chapter 4). Nonetheless, after release studies in NaCl solution, reflections ascribed to NaCl crystals can be found as well (Openlab 2018).

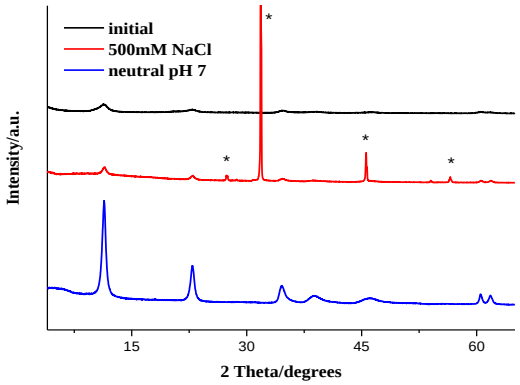

Figure 102. XRD diffractogram of **Mg(3)Al-MBT/CALC650** after release in 500 mM NaCl solution and neutral pH (deionized water)

* NaCl crystals reflections

6.5.2 MBT release from Mg(3)Al-MBT-SH/CALC650

The release profiles of MBT for **Mg(3)Al-MBT-SH/CALC650** are presented in **Figure 103** and the loading content in **Table 70**.

Table 70. MBT loading content and theoretical AEC of **Mg(3)Al-MBT-SH/CALC650**

LDH	MBT loading content, %wt	AEC theoretical, $cmolkg^{-1}$
Mg(3)Al-MBT-SH/CALC650	14	222.1

AEC is calculated using equation **12**

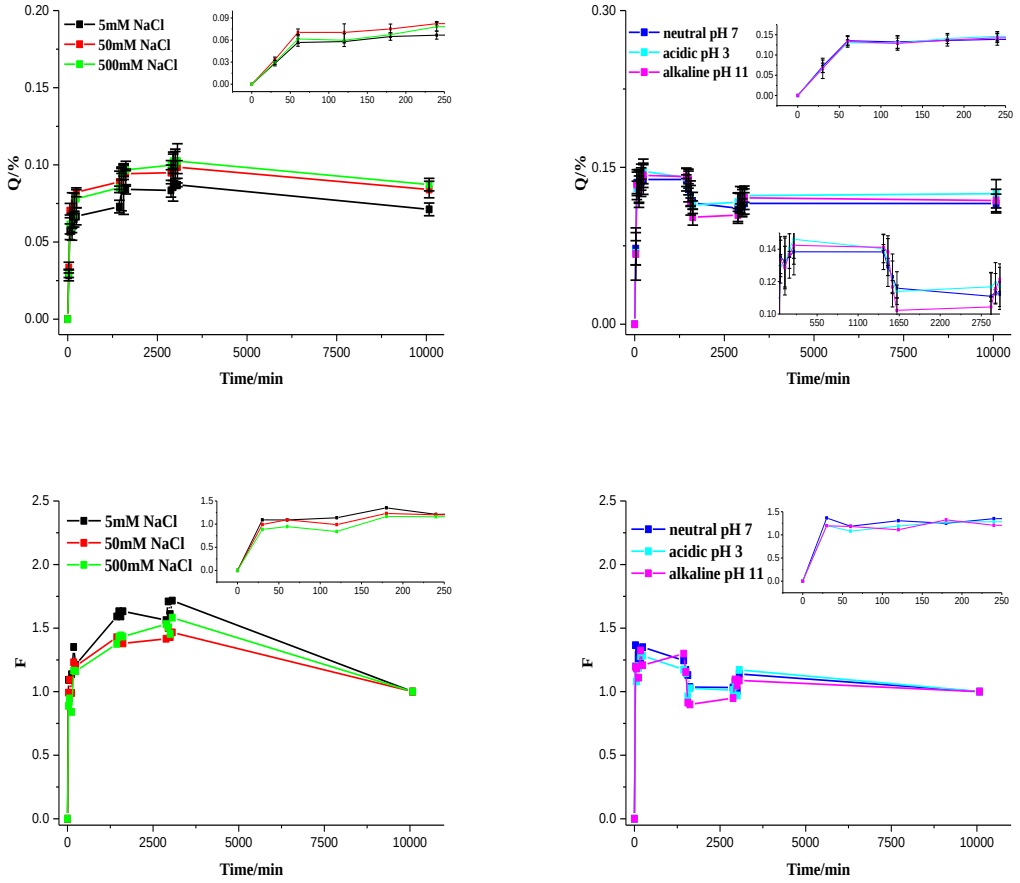

Figure 103. MBT release profiles and fraction of released MBT from **Mg(3)Al-MBT-SH/CALC650** with different triggers (error bars are standard errors between 3 measurements; Q-cumulative release % , F-fractional uptake)

In Chapter 4, structural analysis revealed that MBT was not intercalated, while in Chapter 5 the adsorption of MBT was fitted according to a chemisorption mechanism with possibility of multilayer physisorption. The chemisorption mechanism, typically concerned with primary bonds of covalent type, may actually not be the most accurate interpretation of the interaction between MBT and the LDH surface. This is supported by the fact that the release of MBT increases with increase of NaCl concentration as if an ion-exchange reaction would be occurring (**Table 71**). In fact, the order of

magnitude of electrostatic (ionic) interactions and hydrogen bonding that stabilize the intercalation of guest species within LDH are similar in magnitude to covalent bonds and can also be established externally between the adsorbed anion and the positively charged metal hydroxide sheets. In this way, the data presented in this section, supports the assumption of MBT ion exchange with chlorides from the external surface of LDH, as well. The data from the previous section regarding to **Mg(3)Al-MBT-CALC650** did not reveal this trend, because of the loading content of MBT in that sample (3 wt %), the release of MBT was more or less constant in the presence of 5, 50 and 500 mM NaCl. On the other hand, the differentiated release of MBT as a function of pH can be explained by the solubility of LDH in acidic and neutral conditions and anion exchange with hydroxides under alkaline conditions. The position of the second MBT absorbance peak in the UV-Vis spectra (data not shown) reveal that for the whole timescale the anionic form of MBT is predominating under all the studied conditions. In presence of NaCl the pH of all solutions was 9 - 10 during all the monitored time. For the solution with initial pH 3, it became more alkaline (pH 9) for the whole timescale and for the solution with initial pH 7, the pH increased up to 9-10, decreasing later to 8.00 between 48 h-1 week period. Furthermore, for the solution with initial pH 11, pH decreased down to 10.00 and later to 9.00 for the remaining monitored time.

Table 71. Amount of MBT released from **Mg(3)Al-MBT-SH/CALC650** under influence of various triggers

Trigger	Average MBT released amount from loading content, % wt
5 mM NaCl	49
50 mM NaCl	58
500 mM NaCl	57
Acidic pH 3	84
Neutral pH 7	41
Alkaline pH 11	83

After peaking its release, MBT detected in solution tends to decrease as a function of time, monotonically in the presence of NaCl and with some “bumps” under different pH triggering conditions. Taking into account that MBT can speciate into less soluble forms (neutral MBT, NaMBT) and possibly precipitate, we avoid interpreting the decrease of MBT in solution as a result of adsorption on LDH surfaces as both processes cannot be separated. Therefore, the kinetics of release discussed below will only refer to the initial part of the release curve. This part of the release curve was successfully fitted by Higuchi, Power function and Elovich models in aqueous conditions.

Thus, diffusion is a rate-limiting step of MBT release (**Table 72**). Higuchi constants obtained for release in 5 mM NaCl and deionized water triggers are similar. The Power function model constants increase in the following way: 500mM NaCl<50mM NaCl<deionized water with initial pH 3.

Table 72. Kinetic models used to fit MBT release profiles from **Mg(3)Al-MBT-SH/CALC650** under different triggers

LDH	Exp. Conditions/time of fitting	Kinetics model	Limiting step according to the model(s)	Figures of merit
Mg(3)Al-MBT-SH/CALC650	Immersion in 5 mM NaCl at 25 ºC/0_1500 min	Higuchi	Diffusion	$\mathbf{K_H}$ = 0.30 $min^{-0.5}$ (0.022-**st.error**);
	Immersion in 50 mM NaCl at 25 ºC/0_1440 min	Power function	Diffusion	**a** = 0.71 $min^{-0.1}$ (0.082-**st.error**); **k=** 0.10 (0.021-**st.error**)
	Immersion in 500 mM NaCl at 25 ºC/0_2880 min	Power function	Diffusion	**a** = 0.55 $min^{-0.13}$ (0.052-**st.error**); **k=** 0.13 (0.014-**st.error**)
	Immersion in deionized water with initial pH 3 at 25 ºC/0_240 min	Power function	Diffusion	**a** = 0.94 $min^{-0.05}$ (0.160-**st.error**); **k=** 0.05 (0.036-**st.error**)
		First order	-	**K** = $6.20 \cdot 10^{-4}$ min^{-1} ($3.079 \cdot 10^{-4}$-**st.error**); **Pearson's r:** 0.76 **Adj. R^2:** 0.43 **p-value**: 0.178
	Immersion in deionized water at 25 ºC/0_240 min	Higuchi	Diffusion	$\mathbf{K_H}$ = 0.39 $min^{-0.5}$ (0.033-**st.error**);
	Immersion in deionized water with initial pH 11 at 25 ºC/0_1440 min	Elovich	Bulk and surface diffusion	**a** = 0.16 min^{-1} (0.130-**st.error**); **b**= 0.96 (0.208-**st.error**)

pp. 40-42 contain description of used release kinetic models

The hypothesis of anion-exchangeable nature of MBT release in presence of NaCl is supported by EDS measurements of LDH samples before and after release in presence of 500 mM NaCl (Figure **A6** Annex). This figure shows growth of Cl signal and decrease of S content into LDH after release, thereby suggesting MBT release through anion-exchange reaction.

6.5.3 MBT release from Mg(3)Al-MBT-SH/CALC150

The loading content of MBT in **Mg(3)Al-MBT-SH/CALC150** is presented in **Table 73** and the release profiles obtained for MBT are depicted in **Figure 104**. Before discussing the release studies presented below, it must be recalled that previous studies regarding to structural characterization and textural properties, particle size and electrophoretic mobility (Chapter 4) of this sample suggested a different behavior when compared to the calcined samples at 650 ºC. This difference in behavior was associated with presence of the fatty acid covering the commercial LDH which was not fully removed from the LDH surface as opposed to the samples calcined at higher temperatures, presented in the previous section.

Table 73. MBT loading content and theoretical AEC of **Mg(3)Al-MBT-SH/CALC150**

LDH	MBT loading content, %wt	AEC theoretical, $cmolkg^{-1}$
Mg(3)Al-MBT-SH/CALC150	11	222.10

AEC is calculated using equation **12**

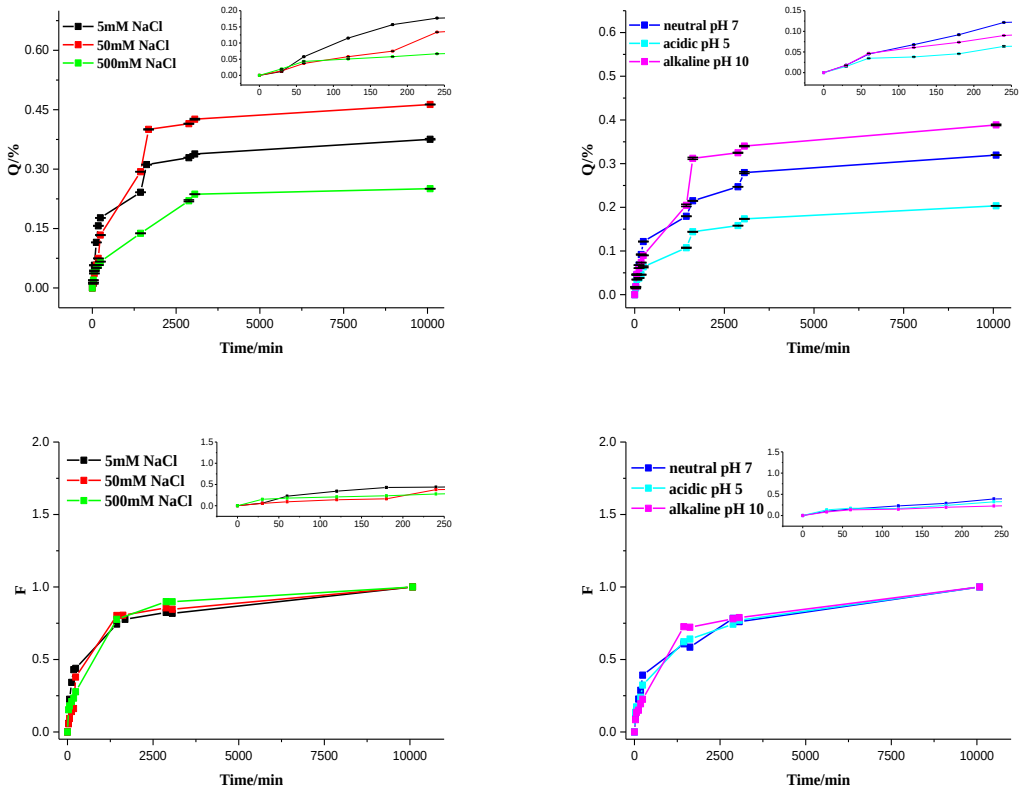

Figure 104. MBT release profiles and fraction of released MBT from **Mg(3)Al-MBT-SH/CALC150** with different triggers (error bars are standard errors between 3 measurements; Q-cumulative release % , F-fractional uptake)

The loading content of MBT obtained for **Mg(3)Al-MBT-SH/CALC150** is lower than for **Mg(3)Al-MBT-SH/CALC650**, which may be due to differences in surface area between the samples. Higher calcination temperatures lead to increase in surface area. Furthermore, the variation of pH during the measurements carried out in solution show a different trend as compared to other LDH. First, it was found that the dispersion of **Mg(3)Al-MBT-SH/CALC150** in aqueous media was more difficult, underlining the hydrophobic character of the material. Second, the pH measured in solution was not as high as for the other calcined samples. In presence of NaCl the pH of all solutions was around 8. More important, changing the initial conditions towards lower pH did not lead to a subsequent rise in pH as a consequence of an expected LDH buffering effect. Finally, under alkaline conditions the initial pH was kept at 10 and in deionized water the pH measured was 8. The fact that the LDH did not dissolve under acidic conditions may imply that the fatty acids are still present in the LDH surface limiting its dissolution. For this reason, the amount of released MBT becomes the lowest among the initial pH conditions tested. On the other hand, the highest release of MBT was found in 5 and 50

mM NaCl, again supporting an ion-exchange reaction from MBT chemisorbed on the LDH surface. For the highest NaCl, though, the release was lower when compared to more dilute solutions. At this stage it is not clear what may be the reason for this result.

Table 74. Amount of MBT released from **Mg(3)Al-MBT-SH/CALC150** under influence of various triggers

Trigger	Average MBT released amount from loading content, % wt
5 mM NaCl	35
50 mM NaCl	34
500 mM NaCl	20
Acidic pH 5	15
Neutral pH 7	24
Alkaline pH 10	27

The release of MBT from this LDH was fitted by the Elovich model (**Table 75** and **Figure 105**). These results support a release controlled by diffusion. The values of *a* parameter estimated by the model is lower than 1 min^{-1} for the following triggers: 5 mM NaCl, initial acidic pH 5 and neutral pH (deionized water). For the other triggers the values of *a* are slightly higher than 1 min^{-1}.

Table 75. Kinetic models used to fit MBT release profiles from **Mg(3)Al-MBT-SH/CALC150** under different triggers

LDH	Exp. Conditions/time of fitting	Kinetics model	Limiting step according to the model(s)	Figures of merit
Mg(3)Al-MBT-SH/CALC150	Immersion in 5 mM NaCl at 25 ºC/0_10080 min	Elovich	Bulk and surface diffusion	**a** = 0.93 min^{-1} (0.024-**st.error**); **b**= -1.10 (0.042-**st.error**)
	Immersion in 50mM NaCl at 25 ºC/0_10080 min	Elovich	Bulk and surface diffusion	**a** = 1.11 min^{-1} (0.109-**st.error**); **b**= -1.48 (0.198-**st.error**)

Table 75. Kinetic models used to fit MBT release profiles from **Mg(3)Al-MBT-SH/CALC150** under different triggers (cont.)

LDH	Exp. Conditions/time of fitting	Kinetics model	Limiting step according to the model(s)	Figures of merit
Mg(3)Al-MBT-SH/CALC150 (cont.)	Immersion in 500mM NaCl at 25 ºC/0_10080 min	Elovich	Bulk and surface diffusion	**a** = 1.02 min^{-1} (0.132-**st.error**); **b**= -1.28 (0.237-**st.error**)
	Immersion in deionized water with pH 5 at 25 ºC/0_10080 min	Elovich	Bulk and surface diffusion	**a** = 0.90 min^{-1} (0.101-**st.error**); **b**= -1.12 (0.184-**st.error**)
	Immersion in deionized water at 25 ºC/0_240 min	Elovich	Bulk and surface diffusion	**a** = 0.89 min^{-1} (0.082-**st.error**); **b**= -1.11 (0.149-**st.error**)
	Immersion in deionized water with initial pH 10 at 25 ºC/0_1440 min	Elovich	Bulk and surface diffusion	**a** = 1.01 min^{-1} (0.114-**st.error**); **b**= -1.34 (0.207-**st.error**)

pp. 40-42 contain description of used release kinetic models

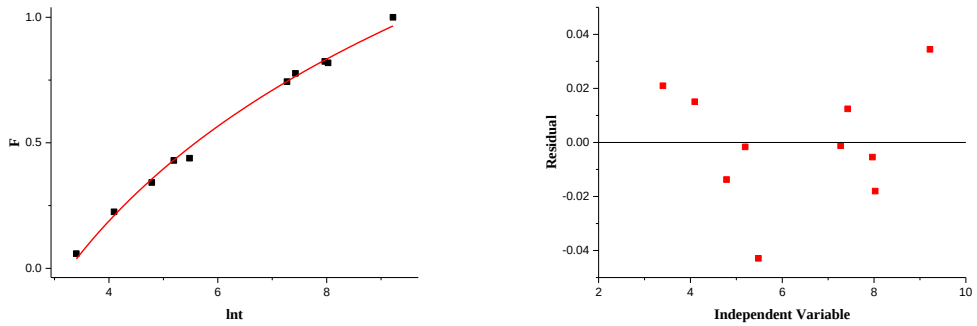

Figure 105. Fitting of data (Elovich model (non-linear)) of MBT release from **Mg(3)Al-MBT-SH/CALC150** during immersion in 5mM NaCl

6.5.4 MBT release from Zn(2)Al-MBT (precursors prepared by coprecipitation reaction in reverse microemulsion)

The loading content of MBT in **Zn(2)Al-MBT-REV/AN** was found to be 3 wt % (**Table 76**). In this case MBT was found to be mainly adsorbed in LDH external surface (Chapter 5) and the model of adsorption governed by chemisorption. The release profiles presented in **Figure 106** show that only a minor fraction of MBT adsorbed is released, with the largest amount being in NaCl solution (6 % of total loading content)- **Table 77**. Furthermore, the pH of all the solutions, regardless of the initial pH was found to be 6 throughout the monitored time. These findings imply that some level of anion-exchange has occurred between the external mixed-metal hydroxide sheets or that MBT is released when partial dissolution of LDH occurs. Similar findings was obtained for **Zn(2)Al-MBT-REVN/AN** (**Table 78** and **Table 79**, **Figure 107**) and for **Zn(2)Al-MBT-REVC/AN** (**Table 80** and **Table 81, Figure 108**).

Table 76. MBT loading content and theoretical AEC of **Zn(2)Al-MBT-REV/AN**

LDH	MBT loading content, %wt	AEC theoretical, $cmolkg^{-1}$
Zn(2)Al-MBT-REV/AN	3	214.77

AEC is calculated using equation **12**

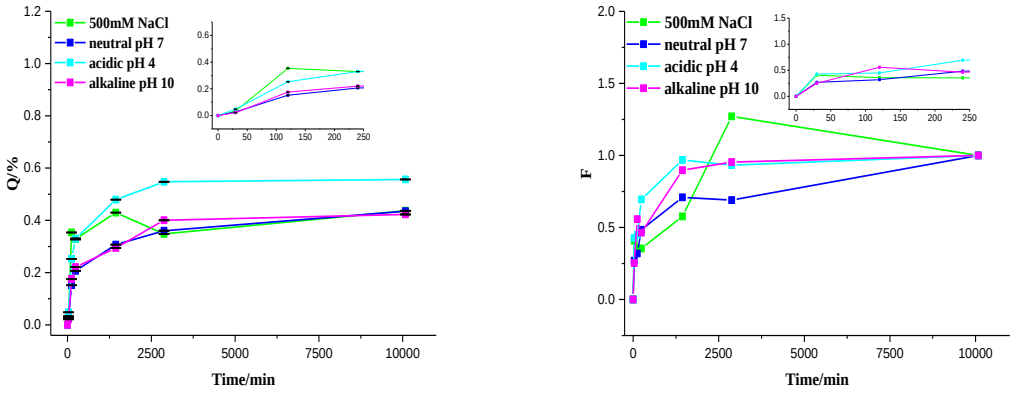

Figure 106. MBT release profiles and fraction of released MBT from **Zn(2)Al-MBT-REV/AN** with different triggers (error bars are standard errors between 3 measurements; Q-cumulative release % , F-fractional uptake)

Table 77. Amount of MBT released from **Zn(2)Al-MBT-REV/AN** under influence of various triggers

Trigger	Average MBT released amount from loading content, % wt
500mM NaCl	6
Acidic pH 4	4
Neutral pH 7	3
Alkaline pH 10	3

Table 78. MBT loading content and theoretical AEC of **Zn(2)Al-MBT-REVN/AN**

LDH	MBT loading content, %wt	AEC theoretical, $cmolkg^{-1}$
Zn(2)Al-MBT-REVN/AN	4	214.77

AEC is calculated using equation **12**

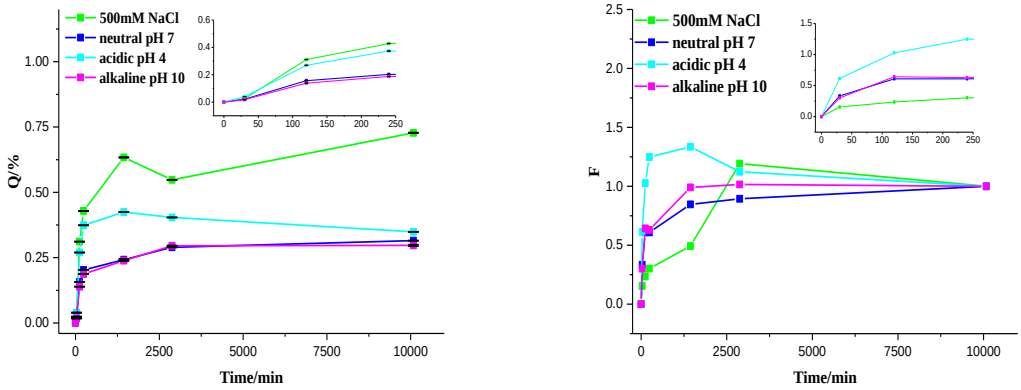

Figure 107. MBT release profiles and fraction of released MBT from **Zn(2)Al-MBT-REVN/AN** with different triggers (error bars are standard errors between 3 measurements; Q-cumulative release % , F-fractional uptake)

Table 79. Amount of MBT released from **Zn(2)Al-MBT-REVN/AN** under influence of various triggers

Trigger	Average MBT released amount from loading content, % wt
500mM NaCl	9
Acidic pH 4	3
Neutral pH 7	2

Table 79. Amount of MBT released from **Zn(2)Al-MBT-REVN/AN** under influence of various triggers (cont.)

Trigger	Average MBT released amount from loading content, % wt
Alkaline pH 10	2

Table 80. MBT loading content and theoretical AEC of **Zn(2)Al-MBT-REVC/AN**

LDH	MBT loading content, %wt	AEC theoretical, $cmolkg^{-1}$
Zn(2)Al-MBT-REVC/AN	5	214.77

AEC is calculated using equation **12**

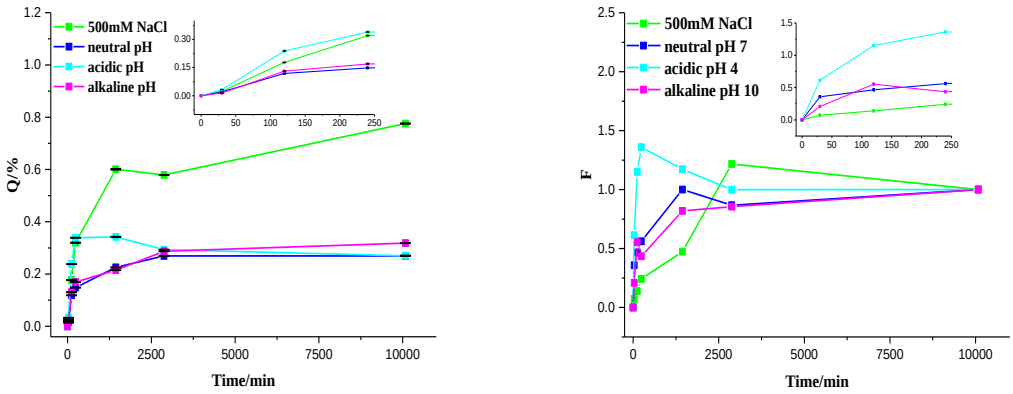

Figure 108. MBT release profiles and fraction of released MBT from **Zn(2)Al-MBT-REVC/AN** with different triggers (error bars are standard errors between 3 measurements; Q-cumulative release % , F-fractional uptake)

Table 81. Amount of MBT released from **Zn(2)Al-MBT-REVC/AN** under influence of various triggers

Trigger	Average MBT released amount from loading content, % wt
500mM NaCl	9
Acidic pH 4	3
Neutral pH 7	2
Alkaline pH 10	2

The initial part of the release curve was successfully fitted by Higuchi and Elovich models (**Table 82** and **Figure 109**), Power function and Elovich models (**Table 83** and **Figure 110**) and Higuchi and Elovich models (**Table 84** and **Figure 111**). Thus, diffusion is a rate-limiting step for MBT release for all the three LDH samples, when precursors were prepared by coprecipitation reaction in reverse microemulsion.

The decrease of MBT concentration for longer times of immersion, namely under NaCl and initial acidic conditions, can be due to the relatively low solubility of species formed with MBT: recall that MBT is within a complex chemical equilibrium (section 6.5) and that when MBT^- is released in solution it may speciate being also in equilibrium with less soluble form MBTH. Other species such as MBTNa and precipitates of MBT with zinc can also be formed (Neves, et al. 2019). Furthermore, the possibility of anion-exchange reaction with chlorides is also supported by SEM-EDS measurements of LDH samples before and after release in presence of 500 mM NaCl (Figures **A7-A9** Annex).

Table 82. Kinetic models used to fit MBT release profiles from **Zn(2)Al-MBT-REV/AN** under different triggers

LDH	**Exp. Conditions/time of fitting**	**Kinetics model**	**Limiting step according to the model(s)**	**Figures of merit**
Zn(2)Al-MBT-REV/AN	Immersion in 500 mM NaCl at 25 ºC/0_2880 min	Higuchi	Diffusion	K_H = 0.13 $min^{-0.5}$ (0.018-**st.error**);
	Immersion in deionized water with initial pH 4 at 25 ºC/0_10080 min	Elovich	Bulk and surface diffusion	**a** = 0.67 min^{-1} (0.113-**st.error**); **b**= -0.46 (0.206-**st.error**)
	Immersion in deionized water at 25 ºC/0_10080 min	Elovich	Bulk and surface diffusion	**a** = 0.70 min^{-1} (0.123-**st.error**); **b**= -0.68 (0.224-**st.error**)
	Immersion in deionized water with initial pH 10 at 25 ºC/0_10080 min	Elovich	Bulk and surface diffusion	**a** = 0.80 min^{-1} (0.107-**st.error**); **b**= -0.75 (0.196-**st.error**)

pp. 40-42 contain description of used release kinetic models

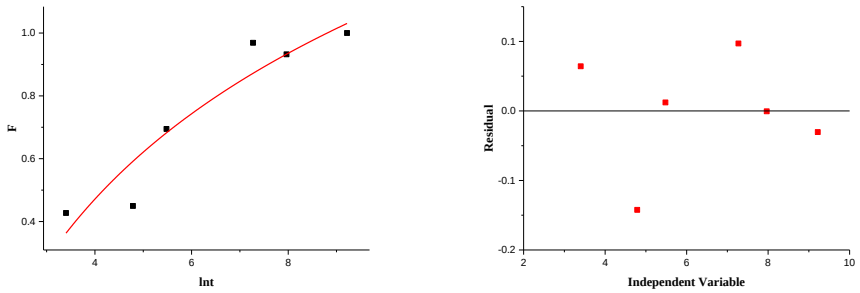

Figure 109. Fitting of data (Elovich model (non-linear)) of MBT release from **Zn(2)Al-MBT-REV/AN** during immersion in deionized water with initial pH 4

Table 83. Kinetic models used to fit MBT release profiles from **Zn(2)Al-MBT-REVN/AN** under different triggers

LDH	**Exp. Conditions/time of fitting**	**Kinetics model**	**Limiting step according to the model(s)**	**Figures of merit**
Zn(2)Al-MBT-REVN/AN	Immersion in 500 mM NaCl at 25 ºC/0_2880 min	Elovich	Bulk and surface diffusion	**a** = 0.98 min^{-1} (0.426-**st.error**); **b**= -1.21 (0.739-**st.error**)
	Immersion in deionized water with initial pH 4 at 25 ºC/0_1440 min	Elovich	Bulk and surface diffusion	**a** = 0.98 min^{-1} (0.193-**st.error**); **b**= -0.54 (0.317-**st.error**)
	Immersion in deionized water at 25 ºC/0_10080 min	Elovich	Bulk and surface diffusion	**a** = 0.66 min^{-1} (0.039-**st.error**); **b**= -0.47 (0.071-**st.error**)
	Immersion in deionized water with initial pH 10 at 25 ºC/0_10080 min	Elovich	Bulk and surface diffusion	**a** = 0.76 min^{-1} (0.093-**st.error**); **b**= -0.60 (0.170-**st.error**)

pp. 40-42 contain description of used release kinetic models

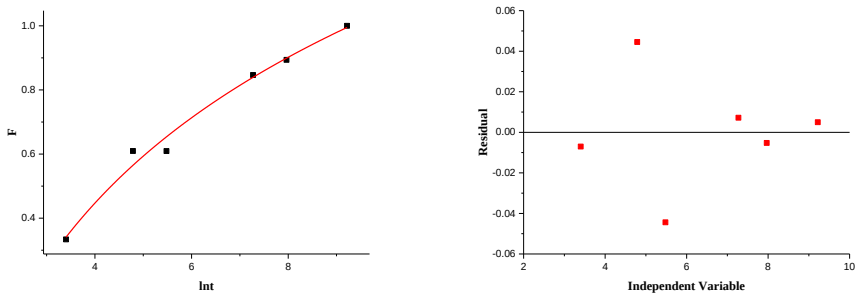

Figure 110. Fitting of data (Elovich model (non-linear)) of MBT release from **Zn(2)Al-MBT-REVN/AN** during immersion in deionized water

Table 84. Release kinetic models used to fit MBT release profiles from **Zn(2)Al-MBT-REVC/AN** under different triggers

LDH	**Exp. Conditions/time of fitting**	**Kinetics model**	**Limiting step according to the model(s)**	**Figures of merit**
Zn(2)Al-MBT-REVC/AN	Immersion in 500 mM NaCl at 25 ºC/0_2880 min	Elovich	Bulk and surface diffusion	**a** = 1.11 min^{-1} (0.460-**st.error**); **b**= -1.47 (0.800-**st.error**)
	Immersion in deionized water with initial pH 4 at 25 ºC/0_1440 min	Higuchi	Diffusion	$\mathbf{K_H}$ = 0.26 $min^{-0.5}$ (0.037-**st.error**);
	Immersion in deionized water at 25 ºC/0_10080 min	Elovich	Bulk and surface diffusion	**a** = 0.72 min^{-1} (0.125-**st.error**); **b**= -0.59 (0.228-**st.error**)
	Immersion in deionized water with initial pH 10 at 25 ºC/0_10080 min	Elovich	Bulk and surface diffusion	**a** = 0.78 min^{-1} (0.101-**st.error**); **b**= -0.76 (0.184-**st.error**)

pp. 40-42 contain description of release kinetic models

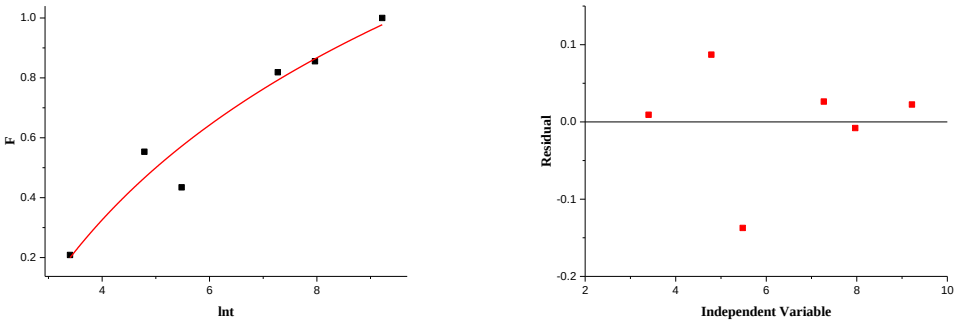

Figure 111. Fitting of data (Elovich model (non-linear)) of MBT release from **Zn(2)Al-MBT-REVC/AN** during immersion in deionized water with initial pH 10

6.5.5 MBT release from Zn(2)Al-MBT-AN

Zn(2)Al-MBT-AN, from all the MBT-containing samples studied so far, is the one that XRD analysis in Chapter 4 has shown successful intercalation of MBT. However, this is not a single-phase material, as LDH-OH was found as a secondary phase. Another aspect to be noticed is that MBT loading content often varies, so LDH samples obtained in different batches in the present study, revealed a loading content between 27 and 38 wt % (**Figure 18** and **Table 85**). Moreover, based on previous studies with MBT adsorbed in the surface of LDH (in MgAl and ZnAl) suggest that the externally adsorbed MBT may also be released by ion-exchange. **Figure 112** and **Table 85** demonstrate that MBT is more extensively released in presence of NaCl, responding to the increasing NaCl concentration. This is an important factor which has contributed for the positive outcome of many works related to the application of these materials in protective coatings against corrosion (Tedim, et al. 2010); (Carneiro, et al. 2015).

Regarding to MBT speciation and pH monitoring during the release studies, the position of the second MBT absorbance peak shows that for the whole monitored time the anionic form of MBT is predominating under all studied conditions. More specifically, in the presence of NaCl, the solution pH remained between 7-8. For the initial acidic conditions (pH 4), the pH increased up to 6-7, remaining in this range until the end of the release experiments. Under initial neutral conditions pH increased up to 8 right in the beginning, lowering to the range 6-7. For the initial conditions of pH 10, its pH lowered down to 6-8.

Table 85. MBT loading content and theoretical AEC of **Zn(2)Al-MBT-AN**

LDH	MBT loading content, %wt	AEC theoretical, $cmolkg^{-1}$
Zn(2)Al-MBT-AN	38/27	214.77

AEC is calculated using equation **12**

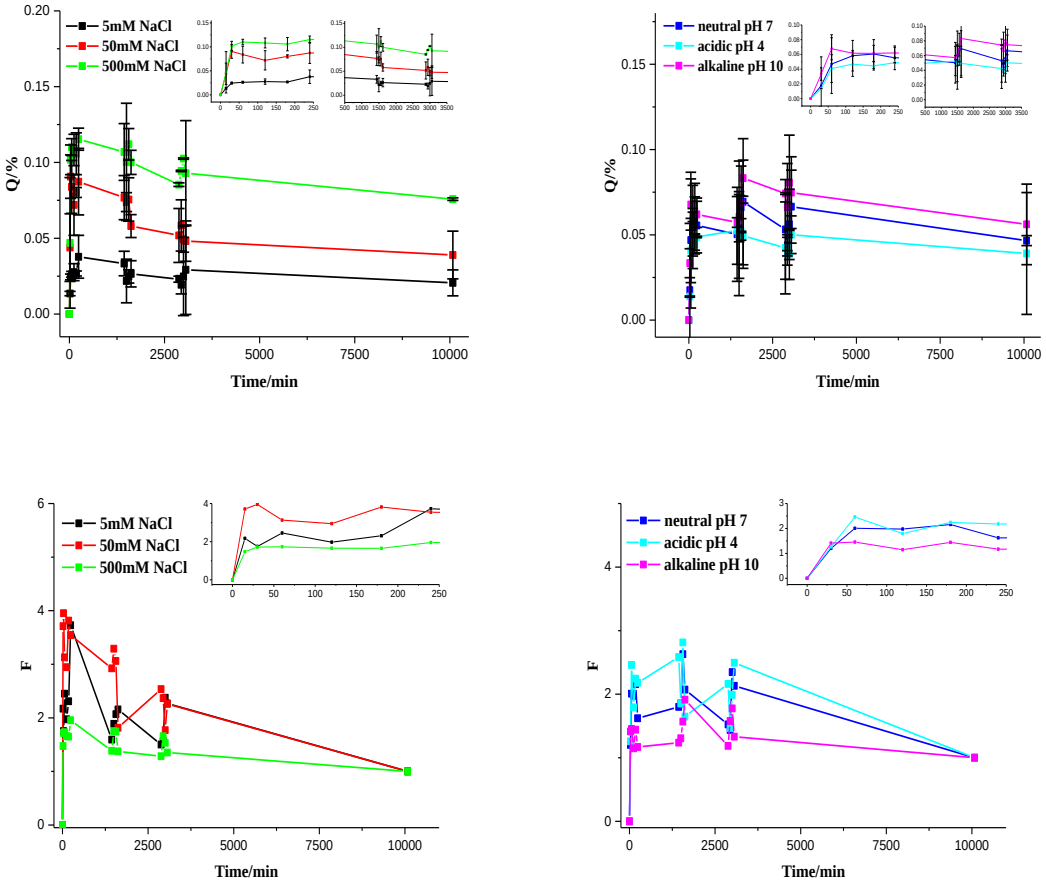

Figure 112. MBT release profiles and fraction of released MBT from **Zn(2)Al-MBT-AN** with different triggers (error bars are standard errors between 3 measurements; Q-cumulative release % ; F-fractional uptake)

Another aspect worth to be mentioned is that the release in MBT does not follow the monotonic shape presented earlier for samples with MBT adsorbed in the external surface of LDH only. There is some sort of fluctuation after an initial peak in the release for short immersion times. The nature of this variation in MBT needs to be discussed considering different factors:

-the release/adsorption/release, as described for LDH-Glu in section 6.1, may also occur in this system because MBT is also intercalated, so the ion-exchange reaction of intercalated species can render a similar trend.

-the decrease in MBT concentration in solution, observed for all the samples in which MBT was not intercalated, may result from the complex equilibria established between different MBT forms (with different solubilities associated), together with possible precipitation of MBT with zinc from partially dissolved LDH.

-the decrease in MBT concentration in solution is not seen in the absence of LDH, which means that the LDH structure has to play some part in this reduction of MBT concentration (Figure **A5** Annex).

Based on the above assumptions, one cannot rule out the effect of adsorption/precipitation of MBT after initial release triggered by anion exchange (NaCl, initial alkaline conditions) or partial dissolution of LDH. With the decrease of MBT concentration in solution LDH has the ability to release more MBT, hence giving rise to the fluctuations observed as a function of the monitored time. However, for simplicity of data analysis, the fitting of experimental data with release models will be restricted the initial part of the release curve, as described below.

Table 86. Amount of MBT released from **Zn(2)Al-MBT-AN** under influence of various triggers

Trigger	Average MBT released amount from loading content, % wt
5 mM NaCl	17
50 mM NaCl	44
500 mM NaCl	66
Acidic pH 4	15
Neutral pH 7	18
Alkaline pH 10	22

The initial part of the release profile was successfully fitted by Higuchi, Elovich models, supporting that diffusion is a rate-limiting step for MBT release and first order kinetics (**Table 87** and **Figure 113**).The lowest Higuchi constant is determined in water with initial pH 4 and pH 10 triggers, slightly increasing in deionized water, achieving the highest values in NaCl (5 mM and 50 mM).

Table 87. Kinetic models used to fit MBT release profiles from **Zn(2)Al-MBT-AN** under different triggers

LDH	Exp. Conditions/time of fitting	Kinetics model	Limiting step according to the model(s)	Figures of merit
Zn(2)Al-MBT-AN	Immersion in 5 mM NaCl at 25 ºC/0_240 min	Higuchi	Diffusion	**K_H** = 0.79 $min^{-0.5}$ (0.068-**st.error**);
		First order	-	**K** = 0.002 min^{-1} ($9.790 \cdot 10^{-4}$-**st.error**); **Pearson's r:** 0.74 **Adj. R^2:** 0.44 **p-value**: 0.091
	Immersion in 50mM NaCl at 25 ºC/0_180 min	Higuchi	Diffusion	**K_H** = 1.18 $min^{-0.5}$ (0.148-**st.error**);
	Immersion in 500mM NaCl at 25 ºC/0_240 min	Power function	Diffusion	**a** = 1.32 $min^{-0.06}$ (0.189-**st.error**); **k**= 0.06 (0.032-**st.error**)
	Immersion in deionized water with initial pH 4 at 25 ºC/0_1560 min	Higuchi	Diffusion	**K_H** = 0.46 $min^{-0.5}$ (0.043-**st.error**);
	Immersion in deionized water at 25 ºC/0_180 min	Higuchi	Diffusion	**K_H** = 0.61 $min^{-0.5}$ (0.032-**st.error**);
		First order	-	**K** = 0.003 min^{-1} (0.0019-**st.error**); **Pearson's r:** 0.75 **Adj. R^2:** 0.35 **p-value**: 0.248
	Immersion in deionized water with initial pH 10 at 25 ºC/0_180 min	Higuchi	Diffusion	**K_H** = 0.43 $min^{-0.5}$ (0.046-**st.error**);

pp.40-42 contain description of used release kinetic models

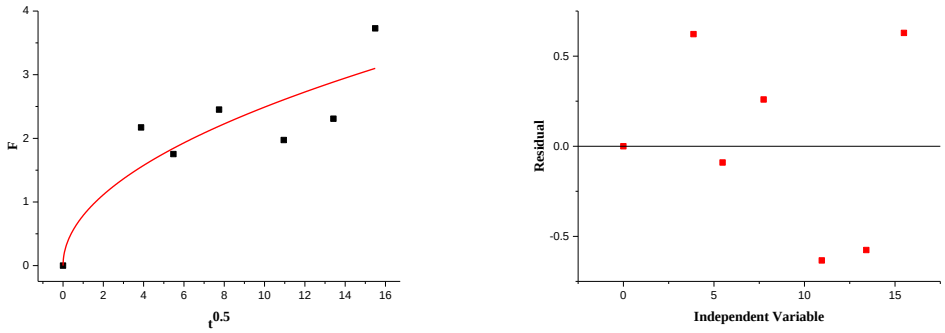

Figure 113. Fitting of data (Higuchi model (non-linear)) of MBT release from **Zn(2)Al-MBT-AN** during immersion in 5mM NaCl

Moreover, the anion-exchange nature of MBT release in the presence of NaCl is supported by SEM-EDS measurements of LDH samples before and after release in presence of 500 mM NaCl (Figure **A10** Annex). This Figure shows growth of Cl and decrease of S and N content into LDH after release, that can indicate MBT release through anion-exchange reaction. Besides, decrease of Zn content may indicate partial dissolution of LDH under these conditions.

Preliminary conclusions

1. The release of both gluconate (Glu) and fluorescein (FSS) intercalated into LDH with formation of single-phased material is governed by diffusion. However, the reaction rates are different. Gluconate is released faster (reaction rate of first order models 10^{-3}- 10^{-2} min^{-1} order of magnitude and of FSS release are 10^{-5}- 10^{-3} min^{-1}). The magnitude of these rate constants agrees with published data based on drugs release from various LDH, that equal to 10^{-5}-10^{-2} (Yang, et al. 2007); (Hussein, et al. 2010).
2. Analysis of the release profiles of either **Zn(2)Al-Glu-AN** or **Zn(2)Al-FSS-AN** allows detection of adsorption processes overlapped with release. Besides, the adsorption impact is stronger for LDH-Glu particles. The adsorption process is rate-limited by diffusion and can be determined as physisorption in nature.
3. Estimation of activation energy of release process for **Zn(2)Al-Glu-AN** using 5 mM NaCl trigger at three different temperatures confirms the diffusion-based mechanism of the release process.
4. Conservation of LDH structure is observed for both LDH with Glu and FSS systems after release process. The release of active species can be described by diffusion from external surfaces and

simultaneous anion-exchange from interlayer galleries with ions available in the media (chloride, carbonate, hydroxide or nitrate).

5. The release of PhPh is governed by diffusion (desorption) for both ZnAl and MgAl-containing LDH materials. The lowest released values are observed in aqueous medium and largest in ethanol due to significant differences of PhPh solubility between these two media.
6. Lower amounts of PhPh released under influence of NaCl, initial acidic and alkaline pH (containing anion-exchangeable anions) compared to just deionized water is an indication of absence of ion-exchange process, which is consistent with physisorption nature of PhPh adsorption in LDH.
7. The values of released TB are very low under aqueous conditions, because of its low solubility in pure water, which increases in alkaline and ethanolic media. Taking into account chemisorption nature of TB adsorption onto LDH the release of dye occurs by diffusion due to partial dissolution of LDH in acidic, alkaline and even neutral pH and by ion-exchange of the TB from external LDH surface.
8. The release of MBT is dependent on the synthesis procedure and corresponding structure of the LDH precursors. When MBT is chemisorbed onto LDH external surface, the release of corrosion inhibitor can be based on ion-exchange and the limiting step is associated with diffusion (**Mg(3)Al-MBT-CALC650**; **Mg(3)Al-MBT-SH/CALC650**; **Mg(3)Al-MBT-SH/CALC150; Zn(2)Al-MBT-REV/AN**; **Zn(2)Al-MBT-REVN/AN**; **Zn(2)Al-MBT-REVC/AN**). In **Zn(2)Al-MBT-AN** MBT is not only intercalated into the galleries but also chemisorbed onto external surface of the LDH particles.

7. BRIEF DISCUSSION OF THE MAIN RESULTS

The results presented in a systematic way in the previous chapters show that a large number of LDH compositions was prepared and characterized. Furthermore, the detail of analysis given to each system under different conditions can cause some loss of information by not considering a wide overview of the results obtained. **Table 88** contains a summary of the main results obtained for the different LDH materials.

As mentioned in Chapter 2, most works published in the literature relies simply on the application of LDH materials and only some of them attempted to fit models to the release of drugs from LDH. From the results presented in Chapter 4, LDH can indeed be prepared by different methods although only in a handful set of cases intercalation of active species in the interlayer galleries occur. What is equally relevant is that although in some cases adsorption of the guest molecules has occurred in the external surface, in the majority of the adsorption studies carried out classical models associated with chemisorption fitted better the adsorption results in comparison to physisorption, with the latter being observed only for adsorption of PhPh in both MgAl and ZnAl LDH (Chapter 5). At the same time, this chemisorption nature found in some systems (e.g. with TB and MBT) is consistent with strong interaction of the active molecules with the external LDH surface and can be rationalized as a strong interaction of electrostatic nature, as it is expected to occur in materials where release takes place by ion-exchange. In other words, although not intercalated, the LDH compositions had the ability to release the active species in response to the presence of anions in solution (chlorides, hydroxides, carbonates,…) in a similar was as it is expected to occur when the compounds are actually intercalated between the LDH hydroxide layers (Chapter 6). This is an outcome which has not been referred in the literature, although implicitly observed: quite often LDH compositions where incorporation of inhibitors was attempted do not show any successful intercalation of the compounds in the LDH, although still showing corrosion inhibition associated with the material. Another aspect worth of mention is that the release of compounds from LDH quite often becomes complicated by the characteristics of its structure. In Chapter 4, we could see that changes in the surface area can occur upon immersion in water under different conditions, or that thermal treatment may induce additional changes as well. This contrasts often with a more “inert” nature of materials such as silicas, in which its structural and textural properties are rather constant. Furthermore, the “living” characteristics associated with LDH materials can be seen in its propensity to dissolve or react under extreme pH conditions which, coupled with changes in the surface properties, induce higher or lower effects of agglomeration and/or aggregation, therefore playing some effect on the release and adsorption of active species.

Concerning a more detailed analysis of the release data, in most of the cases the release of species from LDH is governed by diffusion-related processes (although in some conditions where dissolution may occur other models can be adjusted as well). This is in agreement with what is expected in terms of ion-exchangers and particularly what has already been considered for other type of materials, in which the ion-exchange reaction itself is faster than other steps associated with the mobility of the species (Chapter 2).

Finally, looking at all the LDH compositions prepared, except for those in which physisorption governs the immobilization of the active species (e.g. PhPh) LDH were found to present different extents of release depending on the solution media, which also underlines the applicability of these materials for coatings where corrosion phenomena play a key role.

Table 88. Summary of results based on LDH with active species

LDH	Active specie loading content, %; type of immobilization	Mechanism of adsorption	wt of active specie released, %		Release kinetics rate-limiting step	Mechanism of active specie release
Zn(2)Al-Glu-AN	45 wt % Intercalation + adsorption on external LDH surface	Not investigated (Chapter 5). Adsorption processes as part of the release consistent with physisorption (Chapter 6)	5mM NaCl	22	Data fitted with models based on diffusion. Release at 5 mM NaCl and deionized water (pH 7) is additionally fitted by the zero order model. For acidic pH first order model is fitted. (Chapter 6)	Three stages of release: release-adsorption-release. Release may occur due to ion-exchange and partial LDH dissolution, depending on the triggering conditions.
			50mM NaCl	30		
			500mM NaCl	28		
			pH 4	23		
			pH 7	14		
			pH 10	16		
Zn(2)Al-FSS-AN	11 wt % Intercalation + adsorption on external LDH surface	Not investigated	50mM NaCl	6	Data fitted with models based on diffusion (bulk and surface). Release data in acidic pH and deionized water (pH 7) are additionally fitted by first order model. (Chapter 6)	Release may occur due to ion-exchange and partial LDH dissolution, depending on the triggering conditions. Restrictions to the extent of release associated with low solubility of FSS.
			pH 4	2		
			pH 7	3		
			pH 11	14		
			ethanol	11		
Zn(2)Al-PhPh-CALC150	71 wt % Adsorption on external LDH surface	Physisorption (Chapter 5)	50mM NaCl	4	Data fitted with models based on diffusion. (Chapter 6)	Desorption of PhPh is controlled mainly by PhPh solubility in different media.
			pH 4	6		
			pH 7	7		
			pH 11	6		
			ethanol	54		

Table 88. Summary of results based on LDH with active species (cont.)

LDH	Active specie loading content, %; type of immobilization	Mechanism of adsorption	wt of active specie released, %		Release kinetics rate-limiting step	Mechanism of active specie release
Mg(3)Al-PhPh-SH/CALC150	76 wt % Adsorption on external LDH surface	Physisorption (Chapter 5)	50mM NaCl	1	Data fitted with models based on diffusion. Release data in alkaline pH and ethanol are additionally fitted by first order model. (Chapter 6)	Desorption of PhPh is controlled mainly by PhPh solubility in different media.
			pH 4	2		
			pH 7	3		
			pH 11	2		
			ethanol	74		
Zn(2)Al-TB-CALC150	1 wt % Adsorption onto external LDH surface	Chemisorption (Chapter 5)	50mM NaCl	7	Data fitted with models based on diffusion. Release data in acidic pH, alkaline pH and in ethanol are additionally fitted by first order model. (Chapter 6)	The nature of the adsorption process may imply some level of ion-exchange. Partial dissolution of LDH under acidic and alkaline conditions may also occur. Extent of release is limited by TB solubility.
			pH 4	20		
			pH 7	2		
			pH 11	24		
			ethanol	32		
Mg(3)Al-TB-SH/CALC150	8 wt % Adsorption onto external LDH surface	Chemisorption (Chapter 5)	50mM NaCl	3	Data fitted with models based on diffusion. Release data in 50mM NaCl, acidic pH, deionized water (pH 7) and alkaline pH are additionally fitted by first order model. (Chapter 6)	The nature of the adsorption process may imply some level of ion-exchange. Partial dissolution of LDH may also occur. Extent of release is limited by TB solubility.
			pH 4	3		
			pH 7	11		
			pH 11	16		
			ethanol	36		

Table 88. Summary of results based on LDH with active species (cont.)

LDH	Active specie loading content, %; type of immobilization	Mechanism of adsorption	wt of active specie released, %		Release kinetics rate-limiting step	Mechanism of active specie release
Mg(3)Al-MBT-CALC650	3 wt % Adsorption onto external LDH surface	Chemisorption (Chapter 5)	5mM NaCl	95	Data fitted with models based on diffusion (bulk and surface). Release data in 500mM NaCl is additionally fitted by first order model. (Chapter 6)	The nature of the adsorption process may imply ion-exchange of MBT with anions in solution. Partial dissolution of LDH may also occur. Presence of MBT (aq) tautomeric forms, that are pH dependent.
			50mM NaCl	95		
			500mM NaCl	95		
			pH 4	92		
			pH 7	89		
			pH 11	82		
Mg(3)Al-MBT-SH/CALC650	14 wt % Adsorption onto external LDH surface	Chemisorption (Chapter 5)	5mM NaCl	49	Data fitted with models based on diffusion (bulk and surface). Release in initial acidic pH is additionally fitted by first order model. (Chapter 6)	The nature of the adsorption process may imply some extent of ion-exchange of MBT with anions in solution. Partial dissolution of LDH under acidic conditions may also occur. Presence of MBT (aq) tautomeric forms, that are pH dependent. Precipitation of MBT may occur.
			50mM NaCl	58		
			500mM NaCl	57		
			pH 3	84		
			pH 7	41		
			pH 11	83		

Table 88. Summary of results based on LDH with active species (cont.)

LDH	Active specie loading content, %; type of immobilization	Mechanism of adsorption	wt of active specie released, %		Release kinetics rate-limiting step	Mechanism of active specie release
Mg(3)Al-MBT-SH/CALC150	11 wt % Adsorption onto external LDH surface	Physisorption (Chapter 5)	5mM NaCl	35	Data fitted with models based on diffusion (bulk and surface). (Chapter 6)	The nature of the adsorption process may imply some extent of ion-exchange of MBT with anions in solution. Partial dissolution of LDH under acidic and alkaline conditions may also occur. Presence of MBT (aq) tautomeric forms, that are pH dependable. Precipitation of MBT may occur.
			50mM NaCl	34		
			500mM NaCl	20		
			pH 5	15		
			pH 7	24		
			pH 10	27		
Zn(2)Al-MBT-REV/AN	3 wt % Adsorption onto external LDH surface	Chemisorption (Chapter 5)	500mM NaCl	6	Data fitted with models based on diffusion (bulk and surface). (Chapter 6)	The nature of the adsorption process may imply ion-exchange of MBT with anions in solution. Presence of MBT (aq) tautomeric forms, that are pH dependable.
			pH 4	4		
			pH 7	3		
			pH 10	3		
Zn(2)Al-MBT-REVN/AN	4 wt % Adsorption onto external LDH surface	Physisorption (Chapter 5)	500mM NaCl	9	Data fitted with models based on diffusion (bulk and surface). (Chapter 6)	The nature of the adsorption process may imply ion-exchange of MBT with anions in solution. Presence of MBT (aq) tautomeric forms, that are pH dependent.
			pH 4	3		
			pH 7	2		
			pH 10	2		

Table 88. Summary of results based on LDH with active species (cont.)

LDH	Active specie loading content, %; type of immobilization	Mechanism of adsorption	wt of active specie released, %		Release kinetics rate-limiting step	Mechanism of active specie release
Zn(2)Al-MBT-REVC/AN	5 wt % Adsorption onto external LDH surface	Physisorption (Chapter 5)	500mM NaCl	9	Data fitted with models based on diffusion (bulk and surface). (Chapter 6)	The nature of the adsorption process may imply ion-exchange of MBT with anions in solution. Presence of MBT (aq) tautomeric forms, that are pH dependent.
			pH 4	3		
			pH 7	2		
			pH 10	2		
Zn(2)Al-MBT-AN	27-38 wt % Intercalation + adsorption on external LDH surface (two LDH phases present)	Not determined	5mM NaCl	17	Data fitted with models based on diffusion. Release data in 5 mM NaCl and deionized water are additionally fitted by first order model.	Release may occur due to ion-exchange and partial LDH dissolution, depending on the triggering conditions. Presence of MBT (aq) tautomeric forms, that are pH dependent. Precipitation of MBT can occur.
			50mM NaCl	44		
			500mM NaCl	66		
			pH 4	15		
			pH 7	18		
			pH 10	22		

8. CONCLUSIONS AND FURTHER ACTIVITIES

Twenty LDH compositions (pristine and containing corrosion inhibitors and sensing species) were investigated in the frame of the present PhD work. They were prepared using a variety of methodologies like coprecipitation, coprecipitation reaction in reverse microemulsion, intercalation or/and immobilization of active species through anion-exchange and calcination-rehydration approach. Some studied active compounds like gluconate and fluorescein were intercalated into LDH galleries with formation of single-phase material. Others, like phenolphthalein and thymol blue dyes were immobilized into external surface of LDH by adsorption without intercalation into LDH galleries. Besides, MBT corrosion inhibitor was intercalated into structure by anion-exchange reaction with formation of two LDH phases into the final material. The main one with MBT and second one with hydroxides. However, other synthesis routes allowed immobilization of MBT through adsorption onto external surfaces, that gives opportunity to evaluate change of MBT release behaviour under influence of specific triggers.

Parameters relevant for coating technology such as particle size distribution, colloidal and thermal stability, textural properties and anion-exchange capacity were evaluated for all studied systems. Thermal stability of LDH materials is dependent upon their structure. The morphology of the prepared LDH is platelet-like, except for LDH synthesized by coprecipitation reaction in reverse microemulsion (with addition of tri-block copolymer during nucleation and crystallization step). The textural properties of LDH materials, including surface area and pore size distribution depend upon the synthesis route, especially when comparing conventional methods (coprecipitation) and coprecipitation reaction in reverse microemulsion. The latter route allows preparation of LDH with very high BET surface area. The pore size distribution showed that all prepared LDH are mesoporous materials. Moreover, there is a dependence of the prepared LDH textural properties on the environment during immersion or rehydration followed by calcination, along with thermal treatments. In addition, the structure and composition of LDH was found to play a role on their stability in solution. The colloidal stability of the surveyed materials was determined in buffer solutions, within the pH range pH 3-12. The highest stability in this pH range was observed for LDH samples stabilized by nonionic surfactant during synthesis (**Zn(2)Al-NO_3-REVN** and **Zn(2)Al-NO_3-REVC**), whereas for other LDH compositions the increase in stability under alkaline conditions can be associated with electrostatic repulsions of deprotonated forms of the guest molecules immobilized on the LDH surface (e.g. PhPh and TB).

Adsorption and release studies performed in the frame of this work revealed that the release of surface adsorbed compounds can occur by ion-exchange (similarly to what occurs when compounds are intercalated in the LDH galleries) and in most cases the release is controlled by diffusion-related

processes. A diffusion-based mechanism was confirmed by evaluation of activation energy for **Zn(2)Al-Glu-AN**. Additionally, different processes can impede the interpretation of release profiles, including agglomeration of LDH, dissolution, solubility (especially when molecules are just physisorbed, such as PhPh) and precipitation of released compounds, particularly for long timescales. In some cases, fluctuation on the release profiles was rationalized as release followed by adsorption of the released compounds in the external surface of LDH. In spite of these complicating factors, the release studies performed under different conditions confirmed that most LDH compositions are responsive to pH and NaCl.

LDH materials with dyes like FSS, PhPh and TB are attractive candidates for preparation of sensing coatings for corrosion detection. The release of dyes occurs in a very low extent in aqueous medium, though in higher extent in the presence of ethanol. However, washing procedures using ethanol may be implemented to reduce spontaneous leaching of these pH indicators under conditions of coating preparation. Regarding to LDH loaded with corrosion inhibitors, although **Zn(2)Al-MBT-AN** has already been tested, other compositions with MBT and Glu show promising features to be considered as anti-corrosion additives.

As future activities associated with this work two lines are suggested. Experimentally, additional corrosion tests may be attempted to fully investigate the corrosion inhibition efficiency as well as corrosion detection functionality associated with the LDH materials. Part of this work is already being implemented in the frame of ongoing projects in SECOP group. In parallel, computational activities supported by Density Functional Theory and Molecular Dynamics will be carried out in collaboration with a computational research group to further unveil the mechanisms of adsorption and release, and compare the kinetic parameters obtained experimentally with simulated ones. In other words, this work may constitute the “library data” of experiments necessary to validate models capable of predicting the uptake and release of active species from LDH. This information, together with further studies performed on modified coatings can ultimately help to predict and design LDH materials and alter the coating properties in order to adjust the release of compounds to render a more effective condition-specific protection to the underlying metallic substrate.

Bibliography

Abellán, G., E. Coronado, C. Martí-Gastaldo, E. Pinilla-Cienfuegos, and A. Ribera. 2010. "Hexagonal nanosheets from the exfoliation of Ni2+-Fe3+ LDHs: a route towards layered multifunctional materials." *Journal of Materials Chemistry* 7451-7455 .

Adachi-Pagano, M., C. Forano, and J.-P. Besse. 2003. "Synthesis of Al-rich hydrotalcite-like compounds by using the urea hydrolysis reaction—control of size and morphology ." *Journal of Materials Chemistry* 1988-1993 .

Adamson, A.W. 1990. *Physical Chemistry of Surfaces.* Wiley.

Alt, L.L. 1955. "Spectrophotometric Determination of Gluconic Acid and Its Salts ." *Analytical Chemistry* 749-751.

Amin, G., M.H. Asif, A. Zainelabdin, S. Zaman, O. Nur, and M. Willander. 2011. "Influence of pH, Precursor Concentration, Growth Time, and Temperature on the Morphology of ZnO Nanostructures Grown by the Hydrothermal Method." *1D Nanomaterials.*

Antizar-Ladislao, B. 2008. "Environmental levels, toxicity and human exposure to tributyltin (TBT)-contaminated marine environment. A review." *Environment International* 292-308.

Atkins, P., and J. de Paula. 2010. *Physical Chemistry, Ninth Edition.* Oxford University Press.

Badawi, A.M., M.A. Hegazy, A.A. El-Sawy, H.M. Ahmed, and W.M. Kamel. 2010. "Novel quaternary ammonium hydroxide cationic surfactants as corrosion inhibitors for carbon steel and as biocides for sulfate reducing bacteria (SRB)." *Materials Chemistry and Physics* 458-465.

Balderas-Hernández, P., R. Vargas, A. Rojas-Hernández, M.T. Ramírez-Silva, and M. Galván. 2007. "Dimerization of thymol blue in solution: Theoretical evidence." *Talanta* 1061–1067.

Ball, D. W. 2015. *Physical Chemistry, Second Edition.* Cengage Learning.

Ballantine Jr., D.S.., S.J. Martin, A.J. Ricco, G.C. Frye, H. Wohltjen, R.M. White, and E.T. Zellers. 1997. *Acoustic wave sensors. Theory, Design, and Physico-Chemical Applications.* Imprint Academic Press.

Bardal, E. 2004. *Corrosion and Protection.* Springer.

Benito, P., F.M. Labajos, and V. Rives. 2009. "Microwaves and layered double hydroxides: A smooth understanding." *Pure and Applied Chemistry* 1459–1471.

Bergaya, F., and G. Lagaly. 2006. "General introduction: clay, clay minerals and clay science." In *Handbook of clay science*, by F. Bergaya, B.K.G. Theng and G. Lagaly, 1-18. Elsevier.

Beyler, C.L., and M.M. Hirschler. 2002. "Thermal Decomposition of Polymers." In *SFPE Handbook of Fire Protection Engineering 2*, by M. Hurley, 111-131. Springer.

Brown, E.N, S.R White, and N.R Sottos. 2005. "Retardationand repair of fatigue cracks in a microcapsule tough-ened epoxy composite- Part II: In situ self-healing." *Composites Science and Technology* 2474-2480.

Buchheit, R. G., S. Chrisanti, and S. Mahajanam. 2004. "Corrosion inhibiting and sensing ion exchange pigments for organic coatings." *Electrochemical Society Proceedings* 376-385.

Buchheit, R.G., H. Guan, S. Mahajanam, and F. Wong. 2003. “Active corrosion protection and corrosion sensing in chromate-free organic coatings.” *Progress in Organic Coatings* 174-182.

Büchler, M., T. Watari, and W.H. Smyrl. 2000. “Investigation of the initiation of localized corrosion on aluminum alloys by using fluorescence microscopy.” *Corrosion Science* 1661-1668.

Calle, L.M., P.E. Hintze, W. Li, and J.W. Buhrow. 2010. “Smart Coatings for Autonomous Corrosion Detection and Control.” *AIAA SPACE 2010 Conference & Exposition.* Anaheim, California: Aerospace Research Central. 1-11.

Carneiro, J., A.F. Caetano, A. Kuznetsova, F. Maia, A.N. Salak, J. Tedim, N. Scharnagl, M.L. Zheludkevich, and M.G.S. Ferreira. 2015. “Polyelectrolyte-modified layered double hydroxide nanocontainers as vehicles for combined inhibitors.” *RCS Advances* 39916–39929 .

Chandrasekaran, A.R., C.Y. Jia, C.S. Theng, Muniandy T., Muralidharan S., and S.A. Dhanaraj. 2011. “Invitro studies and evaluation of metformin marketed tablets-Malaysia.” *Journal of Applied Pharmaceutical Science* 214-217.

Chang, Z., D. Evans, X. Duan, P. Boutinaud, M. de Roy, and C. Forano. 2006. “Preparation and characterization of rare earth-containing layered double hydroxides.” *Journal of Physics and Chemistry of Solids* 1054–1057.

ChemicalBook. 2017. https://www.chemicalbook.com/ProductChemicalPropertiesCB4141228_EN.htm.

Chen, S.-C., H. Nakamura, and Z. Tamura. 1979. “Supplimental studies on relationship between structure and spectrum of fluorescein.” *Chemical and Pharmaceutical Bulletin* 475-479.

Chen, X. 2015. “Modeling of Experimental Adsorption Isotherm Data.” *Information* 14-22 .

Cho, S.H, H.M Andersson, S.R White, N.R Sottos, and P.V. Braun. 2006. “Polydimethylsiloxane-Based Self-Healing Materials.” *Advanced Materials* 997-1000.

Cicek, V., and B. Al-Numan. 2011. *Corrosion Chemistry.* Scrivener/Wiley.

Clause, O., M. Gazzano, F. Trifiro, A. Vaccari, and L. Zatorski. 1991. “Preparation and thermal reactivity of nickel/chromium and nickel/aluminium hydrotalcite-type precursors.” *Applied Catalysis* 217-236.

Cooney, D.O. 1999. *Adsorption Design for Wastewater Treatment.* Lewis Publishers.

Costantino, U., F. Marmottini, M. Nocchetti, and R. Vivani. 1998. “New Synthetic Routes to Hydrotalcite-Like Compounds—Characterization and Properties of the Obtained Materials.” *European Journal of Inorganic Chemistry* 1439-1446.

Crespo, I., C. Barriga, V. Rives, and M.A. Ulibarri. 1997. “Intercalation of iron hexacyano complexes in Zn, Al-hydrotalcite.” *Solid State Ionics* 729–735.

Cruz, A.S., J. Flores, R. Guerra, C. Felipe, and E. Lima. 2018. “Organic biocides hosted in layered double hydroxides: enhancing antimicrobial activity.” *Open Chemistry* 163-169.

Dabrowski, A. 2001. “Adsorption-from theory to practice.” *Advances in Colloid and Interface Science* 135-224.

Dash, S., P. N. Murthy, L. Nath, and P. Chowdhury. 2010. “Kinetic modelling on drug release from controlled drug delivery systems.” *Acta Poloniae Pharmaceutica* 217-223.

Davis, W.M., and C. E. Dykstra. 2012. *Physical Chemistry. A modern introduction, Second Edition.* CRC Press is an imprint of Taylor & Francis Group.

Dawodu, F.A., G.K. Akpomie, and I.C. Ogbu. 2012. “Application of Kinetic Rate Equations on the Removal of Copper(II) Ions by Adsorption Unto “Aloji” Kaolinite Clay Mineral.” *International Journal of Multidisciplinary Sciences and Engineering* 21-26.

De Boer, J.H. 1957. “50 Endothermic Chemisorption and Catalysis.” *Advances in Catalysis* 472-480.

De Lloyd, D. 2000. *delloyd2000.* http://delloyd.50megs.com/moreinfo/buffers2.html.

Dehn, W.M. 1917. “Comparative solubilities in water, in pyridine and in aqueous pyridine .” *Journal of American Chemical Society* 1399-1404.

del Hoyo, C. 2007. “Layered double hydroxides and human health: An overview.” *Applied Clay Science* 103-121.

Delmas, C., and Y. Borthomieu. 1993. “Chimie Douce Reactions: A New Route to Obtain Well Crystallized Layer Double Hydroxides.” *Solid State Chemistry* 345-352.

Dere, A. 2019. “Kinetics of Fluorescein Sodium Salt /Polystyrene (FFS/PS) Composites by TG Technique .” *European Journal of Science and Technology* 460-465.

Donato, L., G. Barbaro, E. Drioli, and C. Algieri. 2012. “Controlled Release of Tramadol from Mixed Matrix Membranes.” *Journal of Membrane and Separation Technology* 137-144.

Dubinin, M.M. 1960. “The potential theory of adsorption of gases and vapors for adsorbents with energetically non-uniform surface.” *Chemical Reviews* 235–266 .

Dytham, C. 1999. *Choosing and Using Statistics: A biologist’s guide.* Blackwell Science Ltd.

Elkhattabi, E., M. Lakraimi, M. Berraho, A. Legrouri, R. Hammal, M. Badreddine, and L. El Gaini. 2016. “Study of the properties of intercalation and grafting of phosphonate ions in layered double hydroxides .” *Journal of Materials and Environmental Science* 790-798.

Estrada, A.C., A. L. Daniel-da-Silva, and T. Trindade. 2013. “Photothermally enhanced drug release by k-carrageenan hydrogels reinforced with multi-walled carbon nanotubes.” *RSC Advances* 10828-10836.

Evans, D.G., and R.C.T. Slade. 2006. “Structural aspects of layered double hydroxides.” *Structure and Bonding* 1-87.

Feng, L., and Z. Chen. 2007. “2-Mercaptobenzothiazole benzoates as highly sensitive fluorescent enhancement chemosensors for transition metal ions.” *Sensors and Actuators B: Chemical* 665-668.

Forano, C., T. Hibino, F. Leroux, and C. Taviot-Guého. 2006. “Layered Double Hydroxides.” In *Handbook of Clay Science*, by F. Bergaya, B.K.G. Theng and G. Lagaly, 1021-1096. Elsevier.

Fu, Y., and W.J. Kao. 2010. “Drug Release Kinetics and Transport Mechanisms of Nondegradable and Degradable Polymeric Delivery Systems.” *Expert Opinion on Drug Delivery* 429–444.

Galvao, T.L.P., A. Kuznetsova, J.R.B. Gomes, M.L. Zheludkevich, J. Tedim, and M.G.S. Ferreira. 2016. “A computational UV–Vis spectroscopic study of the chemical speciation of 2-mercaptobenzothiazole corrosion inhibitor in aqueous solution.” *Theoretical Chemistry Accounts* 78.

Galvao, T.L.P., C.S. Neves, A.P.F. Caetano, F. Maia, D. Mata, E. Malheiro, M.J. Ferreira, et al. 2016. “Control of crystallite and particle size in the synthesis of layered double hydroxides: Macromolecular insights and a complementary modeling tool.” *Journal of Colloid and Interface Science* 86-94.

Galvão, T.L.P., I. Sousa, M. Wilhelm, Carneiro. J., J. Oprsal, H. Kukackova, V. Spacek, et al. 2018. “Improving the functionality and performance of AA2024 corrosion sensing coatings with nanocontainers.” *Chemical Engineering Journal* 526-538.

Ghetiya, R.M., D.S. Kundariya, P.H. Parsania, and V.A. Patel. 2008. “Synthesis and characterization of cardo bisbenzoxazines and their thermal polymerization.” *Polymer-Plastics Technology and Engineering* 836-841.

Ghosh, S.K. 2006. *Functional Coatings: by Polymer Microencapsulation.* Wiley-VCH Verlag GmbH & Co. KGaA .

Ghotbi, M.Y., M.Z. bin Hussein, A.H. Yahaya, and M.Z.A. Rahman. 2009. “LDH-intercalated d-gluconate: Generation of a new food additive-inorganic nanohybrid compound.” *Journal of Physics and Chemistry of Solids* 948-954.

Gimbert, F., N.M. Crini, F. Renault, P.M. Badot, and G. Crini. 2008. “Adsorption isotherm models for dye removal by cationized starch-based material in a single component system: Error analysis.” *Journal of Hazardous Materials* 34-46.

Gradwell, M.H.S., and W.J. McGill. 1994. “The thermal decomposition of sulfenamide accelerators.” *Applied Polymer Science* 169-176.

Gursky, J.A., S.D. Blough, C. Luna, C. Gomez, A.N. Luevano, and E.A. Gardner. 2006. “Particle-Particle Interactions between Layered Double Hydroxide Nanoparticles.” *Journal of American Chemical Society* 8376-8377 .

Hakeem, M., S. Rajendran, and A.P. Pascal Regis. 2014. “Calcium gluconate as a corrosion inhibitor for aluminium.” *Journal of Engineering, Computers and Applied Sciences* 1-11.

Hall, K. R., L. C. Eagleton, A. Acrivos, and T. Vermeulen. 1966. “Pore and solid-diffusion kinetics in fixed-bed adsorption under constant-pattern conditions.” *Industrial &. Engineering Chemistry Fundamentals* 212-222.

Han, K.S., L. Guerlou-Demourgues, and C. Delmas. 1996. “A new metavanadate inserted layered double hydroxide prepared by ‘chimie douce’.” *Solid State Ionics* 227-238.

Hang, T.T.X., T.A. Truc, N.T. Duong, P.G. Vu, and T. Hoang. 2012. “Preparation and characterization of nanocontainers of corrosion inhibitor based on layered double hydroxides.” *Applied Clay Science* 18-25.

He, J., M. Wei, B. Li, Y. Kang, D.G. Evans, and X. Duan. 2006. “Preparation of Layered Double Hydroxides.” *Structure and Bonding* 89-119.

Hesse, M., H. Meier, and B. Zeeh. 1997. *Spectroscopic methods in organic chemistry.* Georg Thieme.

Ho, Y.-S. 2004. “Citation review of Lagergren kinetic rate equation on adsorption reactions.” *Scientometrics* 171-177 .

Hofmeister, W., and H. Von Platen. 1992. “Crystal Chemistry and Atomic Order in Brucite-related Double-layer Structures.” *Crystallography Reviews* 3-26.

Hossein, A.-Z., K. Nejati, and E. Ghorbani. 2014. “Synthesis, Characterization and Application of Zn-Al Layered Double Hydroxide as a Nano-Sorbent for the Removal of Direct Red 16 From Industrial Wastewater Effluents.” *Chemical Engineering Communications* 1349-1359.

Hu, G., and D. O'Hare. 2005. “Unique Layered Double Hydroxide Morphologies Using Reverse Microemulsion Synthesis.” *American Chemical Society* 17808-17813.

Huang, N.H., and J.Q. Wang. 2009. “A new route to prepare nanocomposites based on polyvinylchloride and MgAl layered double hydroxide intercalated with laurylether phosphate.” *Polymer Letters* 595-604.

Hudson, M.J., S. Carlino, and D.C. Apperley. 1995. “Thermal conversion of a layered (Mg/Al) double hydroxide to the oxide.” *Journal of Material Chemistry* 323-329.

Hughes, A, S Furman, T Harvey, Hardin S, P Corrigan, F Scholes, T Muster, P White, and H. Fischer. 2007. “Self-healing coating for corrosion protection.” *Proceedings of the First International Conference on Self Healing Materials* 1-6.

Humpola, P.D., H.S. Odetti, A.E. Fertitta, and J.L. Vicente. 2013. “Thermodynamic analysis of adsorption models of phenol in liquid phase on different activated carbons.” *Journal of the Chilean Chemical Society* 1541-1544.

Hussein, M. Z., Mohamad J. A., A.H. Yahaya, and Z. Zainal. 2010. “Inorganic-based phytohormone delivery vector of 2-chloroethylphosphonate nanohybrid: a new stimulating compound with controlled release property to increase latex production.” *Journal of Experimental Nanoscience* 310-318.

Hussein, S.H, A. Ali, M. Al-Qubaisi, M.Z. Hussein, M. Ismail, Z. Zainal, and M.N. Hakim. 2012. “Comparative study of Mg/Al- and Zn/Al-layered double hydroxide-perindopril erbumine nanocomposites for inhibition of angiotensin-converting enzyme.” *International Journal of Nanomedicine* 4251–4262.

Ibrahim, M., A. Nada, and D.E. Kamal. 2005. “Density functional theory and FTIR spectroscopic study of carboxyl group.” *Indian Journal of Pure and Applied Physics* 911-917.

ICDD. 2019. *Powder Diffraction FileTM (PDF®) Search.* http://www.icdd.com/pdfsearch/.

Imanieh, I., and A. Afshar. 2019. “Corrosion protection of aluminum by smart coatings containing layered double hydroxide (LDH) nanocontainers.” *Journal of Materials Research and Technology* 3004-3023.

Imran, A., S. López-Rayo, J. Magid, and H.C.B. Hansen. 2016. “Dissolution kinetics of pyroaurite-type layered double hydroxide doped with Zn: Perspectives for pH controlled micronutrient release.” *Applied Clay Science* 56-63.

Ismadji, S., F.E. Soetaredjo, and A. Ayucitra. 2015. *Clay Materials for environmental remediation.* Springer Cham.

Jlassi, K., A. B. Radwan, K. K. Sadasivuni, M. Mrlik, A.M. Abdullah, M. M. Chehimi, and I. Krupa. 2018. “Anti-corrosive and oil sensitive coatings based on epoxy/polyaniline/magnetite-clay composites through diazonium interfacial chemistry.” *Scientific Reports* 13369.

Jobbágy, M., and A.E. Regazzoni. 2011. “Dissolution of nano-size Mg–Al–Cl hydrotalcite in aqueous media.” *Applied Clay Science* 366-369.

Kenkel, J. 2014. *Analytical Chemistry for Technicians, 4th Edition.* CRC Press, Taylor and Francis Group.

Khan, A.I., and D. O'Hare. 2002. “Intercalation chemistry of layered double hydroxides: recent developments and applications .” *Journal of Materials Chemistry* 3191-3198.

Khramov, A.N, N.N Voevodin, V.N Balbyshev, and R.A. Mantz. 2005. “Sol–gel-derived corrosion-protective coatings with controllable release of incorporated organic corrosion inhibitors.” *Thin Solid Films* 191-196.

Kipling, J.J. 1965. *Adsorption from solutions of non-electrolytes.* Academic Press.

Kokoska, S. 2015. *Introductory Statistics a Problem-Solving Approach. Second edition.* W. H. Freeman and Company.

Kong, X., L. Jin, M. Wei, and Duan X. 2010. “Antioxidant drugs intercalated into layered double hydroxide: Structure and in vitro release.” *Applied Clay Science* 324-329.

Kuhl, S., M. Friedrich, M. Armbruster, and M. Behrens. 2012. “Cu,Zn,Al layered double hydroxides as precursors for copper catalysts in methanol steam reforming – pH-controlled synthesis by microemulsion technique.” *Materials Chemistry* 9632-9638.

Kumar, K.V. 2006. “Linear and non-linear regression analysis for the sorption kinetics of methylene blue.” *Journal of Hazardous Materials* 1538–1544 .

Kunimoto, K.-K., H. Sugiura, T. Kato, H. Senda, A. Kuwae, and K. Hanai. 2001. “Molecular structure and vibrational spectra of.” *Spectrochimica Acta Part A* 265-271.

Kuznetsova, A., P.M. Domingues, T. Silva, A. Almeida, M.L. Zheludkevich, J. Tedim, M.G.S. Ferreira, and A. Cunha. 2017. “Antimicrobial activity of 2-mercaptobenzothiazole released from environmentally friendly nanostructured layered double hydroxides.” *Journal of Applied Microbiology* 1207-1218.

Kwak, S.Y., Y.J. Jeong, J.S. Park, and J.H. Choy. 2002. “Bio-LDH nanohybrid for gene therapy.” *Solid State Ionics* 229-234.

Lagaly, G. 2006. “Colloid Clay Science.” In *Handbook of clay science,* by F. Bergaya, B.K.G. Theng and G. Lagaly, 141-246. Elsevier Ltd.

Latif, Z., A. Fazal, M. Aziz Choudhary, Z. Ahmad, and M. Aslam Mirza. 2018. “Validation of Flory-Huggins Model for Phenol Adsorption by Parthenium Hysterophorus in A Batch System.” *Applied Chemical Engineering* .

Latterini, L., F. Elisei, G.G. Aloisi, U. Costantino, and M. Nocchetti. 2002. “Space-resolved fluorescence properties of phenolphthalein-hydrotalcite nanocomposites.” *Physical Chemistry Chemical Physics* 2792–2798 .

Lazaridis, N.K., and D.D. Asouhidou. 2003. “Kinetics of sorptive removal of chromium(VI) from aqueous solutions by calcined Mg-Al-CO.” *Water Research* 2875-2882.

Leroux, F., and J.P. Besse. 2001. “Polymer Interleaved Layered Double Hydroxide: A New Emerging Class of Nanocomposites.” *American Chemical Society* 3507-3515.

Li, D., F. Wang, X. Yu, J. Wang, Q. Liu, P. Yang, Y. He, Y. Wang, and M. Zhang. 2011. “Anticorrosion organic coating with layered double hydroxide loaded with corrosion inhibitor of tungstate.” *Progress in Organic Coatings* 302-309.

Li, L., R. Ma, Y. Ebina, N. Lyi, and T. Sasaki. 2005. “Positively Charged Nanosheets Derived via Total Delamination of Layered Double Hydroxides.” *Chemistry of Materials* 4386-4391.

Li, X.-H., Z.-X. Tang, and X.-Z. Zhang. 2009. “Molecular structure, IR spectra of 2-mercaptobenzothiazole and 2-mercaptobenzoxazole by density functional theory and ab initio Hartree–Fock calculations.” *Spectrochimica Acta Part A: Molecular and Biomolecular Spectroscopy* 168-173.

Libo, Y., and F. Reza. 1996. “Zero-Order Release Kinetics from a Self-Correcting Floatable Asymmetric Configuration Drug Delivery System.” *Journal of Pharmaceutical Sciences* 170-173.

Limousin, G., J.P. Gaudet, L. Charlet, S. Szenknect, V. Barthes, and M. Krimissa. 2007. “Sorption isotherms: A review on physical bases, modeling and measurement.” *Applied Geochemistry* 249.275.

Liu, C., K.G.H. Desai, X. Tang, and X. Chen. 2006. “Drug Release Kinetics of Spray-Dried Chitosan Microspheres.” *Drying Technology* 769-776.

Liu, J.-Z., L.-P. Weng, Q.-L. Zhang, H. Xu, and L.-N. Ji. 2003. “A mathematical model for gluconic acid fermentation by Aspergillus niger.” *Biochemical Engineering Journal* 137-141.

Lock, R.H., P.F. Lock, Lock M. K., E.F. Lock, and D.F. Lock. 2013. *Statistics Unlocking the Power of Data.* Wiley and Sons Inc.

Mahjoubi, F.Z., A. Khalidi, M. Abdennouri, and N. Barka. 2017. “Zn–Al layered double hydroxides intercalated with carbonate,nitrate, chloride and sulphate ions: Synthesis, characterisation and dye removal properties.” *Journal of Taibah University Science* 90-100.

Mahmoud, D.K., M.A.M. Salleh, and W.A.W.A. Karim. 2012. “Langmuir model application on solidliquid adsorption using agricultural wastes: Environmental application review.” *Journal of Purity, Utility Reaction and Environment* 200-229.

Maia, F., J. Tedim, A.C. Bastos, M.G.S. Ferreira, and M.L. Zheludkevich. 2014. “Active sensing coating for early detection of corrosion processes.” *RCS Advances* 17780-17786.

Maia, F., J. Tedim, A.C. Bastos, M.G.S. Ferreira, and M.L. Zheludkevich. 2013. “Nanocontainer-based corrosion sensing coating.” *Nanotechnology* 415502.

Makhlouf, A.S.H. 2011. “Current and advanced coating technologies for industrial applications.” In *Nanocoatings and Ultra-Thin Films. Technologies and Applications*, by A.S.H. Makhlouf and I. Tiginyanu, 3-23. Woodhead Publishing Series in Metals and Surface Engineering.

Marangoni, A.G. 2017. *Kinetic Analysis of Food Systems.* Springer International Publishing AG.

Markuszewski, R., and H. Diehl. 1980. “The Infrared spectra and structures of the three solid forms of fluorescein and related compounds.” *Talanta* 937-946.

Martins, R., T. Oliveira, C. Santos, A. Kuznetsova, V. Ferreira, F. Avelelas, A.P.F. Caetano, et al. 2017. “Effects of a novel anticorrosion engineered nanomaterial on the bivalve Ruditapes philippinarum.” *Environmental Nanoscience* 1064-1076 .

McMurray, H.N., and G. Williams. 2004. “Inhibition of filiform corrosion on organic-coated aluminum alloy by hydrotalcite-like anion-exchange pigments.” *Corrosion* 219-228.

Meng, F.W. 2005. *Study on a Mathematical Model in Predicting Breakthrough Curves of Fixed-bed Adsorption onto Resin Adsorbent.* MS Thesis, Nanjing University.

Merck, KGaA. 2019. https://www.sigmaaldrich.com/catalog/product/sigma/t0763?lang=pt&region=PT.

Michot, L.J., and F. Villiéras. 2006. “Surface area and porosity.” In *Handbook of clay science*, by F. Bergaya, B.K.G. Theng and G. Lagaly, 965-978. Elsevier.

Mohan, S., and J. Karthikeyan. 1997. “Removal of lignin and tannin color from aqueous solution by adsorption on to activated carbon solution by adsorption on to activated charcoal.” *Environmental Pollution* 183-187.

Montemor, F., D.V. Snihireva, M.G. Taryba, S.V. Lamaka, I.A. Kartsonakis, A.C. Balaskas, G.C. Kordas, et al. 2012. “Evaluation of self-healing ability in protectiv ecoatings modified with combinations of layered double hydroxides and cerium molibdate nanocontainers filled with corrosion inhibitors.” *ElectrochimicaActa* 31-40.

Munger, C.G, and L.D. Vincent. 1999. *Corrosion prevention by protective coatings.* NACE International.

Nakamura, N., and Y. Amao. 2003. “An optical sensor for CO2 using thymol blue and europeum(III) complex composite film.” *Sensors and Actuators B* 98–101.

Narashimhan, B., S.K. Mallapragada, and N.A. Peppas. 1999. “Release kinetics, data interpretation.” In *Encyclopedia of Controlled Drug Delivery*, by E. Mathiowitz, 921. John Wiley and Sons, Inc,.

Nechifor, G., D.-E. Pascu, M. Pascu (Neagu), G.A. Traistaru, and P.C. Albu. 2015. “Comparative study of Temkin and Flory-Huggins isotherms for adsorption of phosphate anion on membranes.” *UPB Scientific Bulletin, Series B* 63-72.

Neves, C.S., A.C. Bastos, A.N. Salak, M. Starykevich, D. Rocha, M.L. Zheludkevich, A. Cunha, A. Almeida, J. Tedim, and M.G.S. Ferreira. 2019. “Layered Double Hydroxide Clusters as Precursors of Novel Multifunctional Layers: A Bottom-Up Approach.” *Coatings.*

Newman, S.P., and W. Jones. 1998. “Synthesis, characterization and applications of layered double.” *New Journal of Chemistry* 105-115.

Ngawhirunpat, T., E. Goegebakan, S. Duangjit, P. Akkaramngklporn, and M. Kumpugdee-Vollrath. 2010. “Controlled release of chlorpheniramine from resonates through surface coating with Eudragit® RS 100.” *International Journal of Pharmacy and Pharmaceutical Sciences* 107-112.

Nielsen, E., G. Østergaard, and J.C. Larsen. 2014. *2-Mercapto-benzothiazole (MBT).* The Danish Environmental Protection Agenc.

Nijs, H., M. de Bock, and E.F. Vansant. 1999. "Evaluation of the microporosity of pillared [Fe(CN)6]-MgAl-LDHs." *Microporous and Mesoporous Materials* 243–253.

Norde, W. 2003. *Colloids and interfaces in life sciences.* Marcel Dekker. Inc.

Norman, G.R., and D.L. Streiner. 1998. *Biostatistics the Bare Essentials.* B.C. Decker Inc.

Ogawa, M., and H. Kaiho. 2002. "Homogeneous Precipitation of Uniform Hydrotalcite Particles." *Langmuir* 4240-4242.

Oh, J.M., S.H. Hwang, and J.H. Choy. 2002. "The effect of synthetic conditions on tailoring the size of hydrotalcite particles." *Solid State Ionics* 285-291.

O'Neil, M.J. 2001. *The Merck Index - An Encyclopedia of Chemicals, Drugs, and Biologicals.* Whitehouse Station, NJ: Merck and Co., Inc.

Openlab, Physics. 2018. *Sodium chloride (NaCl) crystal* . 22 January . http://physicsopenlab.org/2018/01/22/sodium-chloride-nacl-crystal/.

OriginLab, Corporation. 2019. *Interpreting Regression Results.* https://www.originlab.com/doc/Origin-Help/Interpret-Regression-Result.

Ozin, G.A., A. Arsenault, and L. Cademartiri. 2008. *Nanochemistry: A Chemical Approach to Nanomaterials: Edition 2.* Royal Society of Chemistry.

Panda, H.S., R. Srivastava, and D. Bahadur. 2009. "In-Vitro Release Kinetics and Stability of Anticardiovascular Drugs-Intercalated Layered Double Hydroxide Nanohybrids." *Journal of Physical Chemistry B* 15090–15100.

Parello, M.L., R. Rojas, and C.E. Giacomelli. 2010. "Dissolution kinetics and mechanism of Mg–Al layered double hydroxides: A simple approach to describe drug release in acid media." *Journal of Colloid and Interface Science* 134-139.

Pasqua, L. 2011. *Update on Silica-based Mesoporous Materials for Biomedical Applications.* iSmithers-A Smithers Group Company.

Patterson, J.M., Z. Kortylewicz, and Jr., W.T. Smith. 1984. "Thermal Degradation of Sodium Dodecyl Sulfate." *Journal of Agricultural and Food Chemistry* 782-784.

Platero, E.E., C.O. Arean, and J.B. Parra. 1999. "Synthesis of high surface area CoAl2O4 and NiAl2O4 spinels by an alkoxide route." *Research on Chemical Intermediates* 187.

Plazinski, W., W. Rudzinski, and A. Plazinska. 2009. "Theoretical models of sorption kinetics including a surface reaction mechanism: a review." *Advances in Colloid and Interfaces Science* 2–13.

Porta, P., and S. Morpurgo. 1995. "Cu/Zn/Co/Al/Cr-containing hydrotalcite-type anionic clays." *Applied Clay Science* 31-44.

Poznyak, S.K., J. Tedim, L.M. Rodrigues, A.N. Salak, M.L. Zheludkevich, L.F.P. Dick, and M.G.S. Ferreira. 2009. "Novel Inorganic Host Layered Double Hydroxides Intercalated with Guest Organic Inhibitors for Anticorrosion Applications." *ACS Applied Materials and Interfaces* 2353-2362.

Puligundla, P., J. Jung, and S. Ko. 2012. “Carbon dioxide sensors for intelligent food packaging applications.” *Food Control* 328-333.

Qiu, H., L. Lv, B-c. Pan, Q-j. Zhang, W-m. Zhang, and Q-x. Zhang. 2009. “Critical review in adsorption kinetic models.” *Journal of Zhejiang University Science A* 716-724.

Quirk, T.J., M. Quirk, and H.F. Horton. 2015. *Excel 2013 for Biological and Life Sciences Statistics A Guide to Solving Practical Problems.* Springer.

Radeva, G., E. Valcheva, and S. Veleva. 2009. “The Role of the Entropy Factor on the Adsorption of an Optical Brightener on Pulp.” *Turkish Journal of Chemistry* 241-248.

Radha, S., and P.V. Kamath. 2012. “Structural Synthon Approach to Predict the Possible Polytypes of Layered Double Hydroxides.” *Zeitschrift für anorganische und allgemeine Chemie* 2317–2323.

Rai, A.K., R. Singh, K.N. Singh, and V.B. Singh. 2006. “FTIR, Raman spectra and ab initio calculations of 2-mercaptobenzothiazole.” *Spectrochimica Acta Part A: Molecular and Biomolecular Spectroscopy* 483-490.

Ramimoghadam, D., M.Z.B. Hussein, and Y.H. Taufiq-Yap. 2012. “The Effect of Sodium Dodecyl Sulfate (SDS) and Cetyltrimethylammonium Bromide (CTAB) on the Properties of ZnO Synthesized by Hydrothermal Method .” *International Journal of Molecular Sciences* 13275-13293.

Revie, R.W., and H.H. Uhlig. 2008. *Corrosion and Corrosion Control: An Introduction to Corrosion Science and Engineering.* Wiley Interscience.

Rives, V., and S. Kannan. 2000. “Layered double hydroxides with the hydrotalcite-type structure containing Cu2+, Ni2+ and Al3+.” *Journal of Materials Chemistry* 489-495.

Rudzinski, W., and W. Plazinski. 2006. “Kinetics of Solute Adsorption at Solid/Solution Interfaces: A Theoretical Development of the Empirical Pseudo-First and Pseudo-Second Order Kinetic Rate Equations, Based on Applying the Statistical Rate Theory of Interfacial Transport.” *Journal of Physical Chemistry B* 16514-16525 .

Saha, P., and S. Chowdhury. 2011. “Insight Into Adsorption Thermodynamics.” In *Thermodynamics*, by M. Tadashi, 349-364. In Tech.

Seida, Y., Y. Nakano, and Y. Nakamura. 2001. “Rapid removal of dilute lead from water by pyroaurite-like compound.” *Water Research* 2341-2346.

Selim, H.M. 2015. *Transport and fate of chemicals in soil. Principles and applications.* CRC Press Taylor and Francis Group.

SenGupta, A.K. 2017. *Ion Exchange in Environmental Processes. Fundamentals, Applications and Sustainable Technology.* Wiley.

Serdechnova, M., V.L. Ivanov, R.M.R. Domingues, D.V. Evtuguin, M.G.S. Ferreira, and M.L. Zheludkevich. 2014. “Photodegradation of 2-mercaptobenzothiazole and 1,2,3-benzotriazole corrosion inhibitors in aqueous olutions and organic solvents .” *Physical Chemistry Chemical Physics* 25152-25160 .

Shafiei, S., Z.T. Birgani, A. Darvish, M.S. Azimi, and M. Solati-Hashjin. 2008. “Layered Double Hydroxides for Diagnostic Applications.” *Internatinal Congress of Evalution of Medical Diagnosis Modern Technologies.* ACADEMIA. 1-16.

Shawky, S., A. AboalHassan, H. Lill, D. Bald, S. F. El-Khamisy, and Ebeid-E. Z.M. 2016. “Efficient Loading and Encapsulation of Anti-Tuberculosis Drugs using Multifunctional Mesoporous Silicate Nanoparticles Running Title: Mesoporous Silicate Nanoparticles as Smart Drug Delivery System.” *Journal of Nanosciences: Current Research* 103.

Shchukin, D.G, M Zheludkevich, K Yasakau, S Lamaka, M.G.S Ferreira, and H Mohwald. 2006. “Layer-by-Layer Assembled Nanocontainers for Self-Healing Corrosion Protection.” *Advanced Materials* 1672-1678.

Siepmann, J., and F. Siepmann. 2008. “Mathematical modeling of drug delivery.” *International Journal of Pharmaceutics* 328-343.

Siepmann, J., and F. Siepmann. 2012. “Modeling of diffusion controlled drug delivery.” *Journal of Controlled Release* 351-362.

Sims, R.A., S.L. Harmer, and J.S. Quinton. 2019. “The Role of Physisorption and Chemisorption in the Oscillatory Adsorption of Organosilanes on Aluminium Oxide.” *Polymers* 410.

Singh, B., D.K. Sharma, R. Kumar, and A. Gupta. 2010. “Controlled release of thiram from neem-alginate-clay based delivery systems to manage environmental and health hazards.” *Applied Clay Science* 384-391.

Song, H., F. Jiao, X. Jiang, J. Yu, X. Chen, and S. Du. 2013. “Removal of vanadate anion by calcined Mg/AlCO3 layered double hydroxide in aqueous solution .” *Transactions of Nonferrous Metals Society of China* 3337-3345.

Sousa, I., F. Maia, A. Silva, A. Cunha, A. Almeida, D.V. Evtyugin, J. Tedim, and M.G. Ferreira. 2015. “A novel approach for immobilization of polyhexamethylene biguanide within silica capsules.” *RSC ADVANCES* 92656-92663.

Sousa, I., M.C. Quevedo, A. Sushkova, M.G.S. Ferreira, and Tedim. J. 2020. “Chitosan Microspheres as Carriers for pH-Indicating Species in Corrosion Sensing.” *Macromolecular Materials and Engineering* 1900662.

Sparks, D.L. 2003. *Environmental Soil Chemistry. Second Edition.* Academic Press.

Stanimirova, Ts., N. Piperov, N. Petrova, and G. Kirov. 2004. “Thermal evolution of Mg-Al-CO3 hydrotalcites.” *Clay Minerals* 177-191.

Stuart, B.H. 2004. *Infrared Spectroscopy: Fundamentals and Applications.* John Wiley & Sons, Ltd.

Sun, Z., L. Gu, J. Zheng, J. Zhang, L. Wang, F. Xu, and C. Lin. 2016. “A controlled release strategy of antifouling agent in coating based on intercalated layered double hydroxides.” *Materials Letters* 105-108.

Tadros, T.F. 2011. *Colloids in paints. Colloids and Interface Science Series, Vol. 6.* Wiley-VCH Verlag GmbH & Co. KGaA.

Tanaka, T., Y. Kameshima, S. Nishimoto, and M. Miyake. 2012. “Determination of carbonate ion contents in layered double hydroxides by FTIR spectrometry.” *Analytical Methods* 3925-3927.

Tedim, J., S.K. Poznyak, A. Kuznetsova, D. Raps, T. Hack, M.L. Zheludkevich, and M.G.S. Ferreira. 2010. “Enhancement of Active Corrosion Protection via Combination of Inhibitor-Loaded Nanocontainers.” *ACS Applied Materials and Interfaces* 1528-1535.

Temkin, M.I., and V. Pyzhev. 1940. “Kinetics of ammonia synthesis on promoted iron catalyst.” *Acta Physico-Chimica URSS* 327–356 .

Tosun, I. 2012. “Ammonium Removal From aueous solutions by clinoptilolite: determination of isotherm and thermodynamic parameters and comparison of kinetics by the double exponential model and conventional kinetic models.” *International Journal of Environmental Research and Public Health* 970-984 .

Toth, J. 1995. “Thermodynamical correctness of gas/solid adsorption isotherm equations.” *Journal of Colloid and Interface Science* 299–302.

Vincent, B. 2005. “Introduction to colloidal dispersions.” In *Colloid Science. Principles, methods and application*, by T. Cosgrove, 1-13. Blackwell Publisher.

Voudrias, E., F. Fytianos, and E. Bozani. 2002. “Sorption description isotherms of dyes from aqueous solutions and waste waters with different sorbent materials.” *Global NEST Scientific Environmental Journal* 75-83.

Vucelic, M., W. Jones, and G. D. Moggridge. 1997. “Cation ordering in synthetic layered double hydroxides.” *Clay and Clay minerals* 803-813.

Vulic, T.J., A.F.K. Reitzmann, and K. Lázár. 2012. “Thermally activated iron containing layered double hydroxides as potential catalyst for N2O abatement.” *Chemical Engineering Journal* 207-208.

Wang, L., A. Roitberg, C. Meuse, and A.K. Gaigalas. 2001. “Raman and FTIR spectroscopies of fluorescein in solutions.” *Spectrochimica Acta Part A* 1781–1791.

Wang, Y, H. Su, Y. Gu, X Song, and J. Zhao. 2017. “Carcinogenicity of chromium and chemoprevention: a brief update.” *OncoTargets and Therapy* 4065–4079.

Wang, Y., and D. Zhang. 2015. “Layered double hydroxides as a nanocontainer for encapsulating marine natural product antifoulant: Intercalation and tunable controlled release of cinnamate.” *Materials Research Bulletin* 205-210.

Wang, Y., W. Yang, C. Chen, and D.G. Evans. 2008. “Fabrication and electrochemical characterization of cobalt-based layered double hydroxide nanosheet thin-film electrodes.” *Journal of Power Sources* 682-690.

White, S.R, N.R Sottos, P.H Geubelle, J.S Moore, M.R Kessler, S.R Sriram, E.N Brown, and S. Viswanathan. 2001. “Autonomic healing of polymer composites.” *Nature* 794-797.

Xu, R., and Y. Xu. 2017. *Modern Inorganic Synthetic Chemistry*. Elsevier.

Yalkowsky, S.H., and Y. He. 2003. *Handbook of Aqueous Solubility Data: An Extensive Compilation of Aqueous Solubility Data for Organic Compounds Extracted from the AQUASOL dATAbASE*. CRC Press LLC, Boca Raton,.

Yang, J.-H., Y.-S. Han, M. Park, T. Park, S.-J. Hwang, and J.-H. Choy. 2007. “New Inorganic-Based Drug Delivery System of Indole-3-Acetic Acid-Layered Metal Hydroxide Nanohybrids with Controlled Release Rate.” *Chemistry of Materials* 2679-2685.

Yang, W., Y. Kim, P.K.T. Liu, M. Sahimi, and T. T. Tsotsis. 2002. “A study by in situ techniques of the thermal evolution of the structure of a Mg–Al–CO3 layered double hydroxide.” *Chemical Engineering Science* 2945 – 2953.

Yasakau, K.A., A. Kuznetsova, S. Kallip, M. Starykevich, J. Tedim, M.G.S. Ferreira, and M.L. Zheludkevich. 2018. “A novel bilayer system comprising LDH conversion layer and sol-gel coating for active corrosion protection of AA2024.” *Corrosion Science* 299-313.

Yin, H., L. Cui, S. Ai, H. Fan, and L. Zhu. 2010. “Electrochemical determination of bisphenol A at Mg–Al–CO3 layered double hydroxide modified glassy carbon electrode.” *Electrochimica Acta* 603-610.

Yin, T, M.Z Rong, M.Q Zhang, and G.C. Yang. 2007. “Self-healing epoxy composites – Preparation and effect of the healant consisting of microencapsulated epoxy and latent curing agent.” *Composites Science and Technology* 201-212.

Zadeh, M.A., J. Tedim, M. Zheludkevich, S. van der Zwaag, and S.J. Garcia. 2018. “Synergetic active corrosion protection of AA2024-T3 by 2D- anionic and 3D-cationic nanocontainers loaded with Ce and mercaptobenzothiazole.” *Corrosion Science* 35-45.

Zaggout, F.R., I.M. El-Nahhal, A.E.-F.A. Qaraman, and N: Al Dahoudi. 2006. “Behavior of thymol blue analytical pH-indicator entrapped into sol–gel matrix.” *Materials Letters* 3463–3467.

Zellner, A., H.A. Keuzenkamp, and M. McAleer. 2001. *Simplicity, Inference and Modelling: Keeping it Sophisticatedly Simple.* Cambridge University Press.

Zhang, Y., and J.R.G. Evans. 2012. “Alignment of layered double hydroxide platelets.” *Colloids and Surfaces A: Physicochemical and Engineering Aspects* 71-78.

Zhao, Y., F. Li, R. Zhang, D.G. Evans, and X. Duan. 2002. “Preparation of Layered Double-Hydroxide Nanomaterials with a Uniform Crystallite Size Using a New Method Involving Separate Nucleation and Aging Steps.” *Chemistry of Materials* 4286-4291.

Zheludkevich, M. 2009. “Self healing anticorrosion coatings.” In *Self-Healing Materials: Fundamentals, Design Strategies, and Applications*, by S.K. Ghosh, 101-139. Wiley-VCH.

Zheludkevich, M.L, I.M Salvado, and M.G.S. Ferreira. 2005. “Sol–gel coatings for corrosion protection of metals .” *Journal of Materials Chemistry* 5099-5111.

Zheludkevich, M.L., D.G. Shchukin, K.A. Yasakau, H. Mohwald, and M.G.S. Ferreira. 2007. “Anticorrosion Coatings with Self-Healing Effect Based on Nanocontainers Impregnated with Corrosion Inhibitor.” *Chemistry of Materials* 402-411.

Zheludkevich, M.L., S.K. Poznyak, L.M. Rodrigues, D. Raps, T. Hack, L.F. Dick, T. Nunes, and M.G.S. Ferreira. 2010. “Active protection coatings with layered double hydroxide nanocontainers of corrosion inhibitor.” *Corrosion Science* 602–611.

Zheng, Q., Y. Hao, P. Ye, L. Guo, H. Wu, Q. Guo, J. Jiang, F. Fu, and G. Chen. 2013. “A pH-responsive controlled release system using layered double hydroxide (LDH)-capped mesoporous silica nanoparticles.” *Journal of Materials Chemistry B* 1644-1648.

Annex

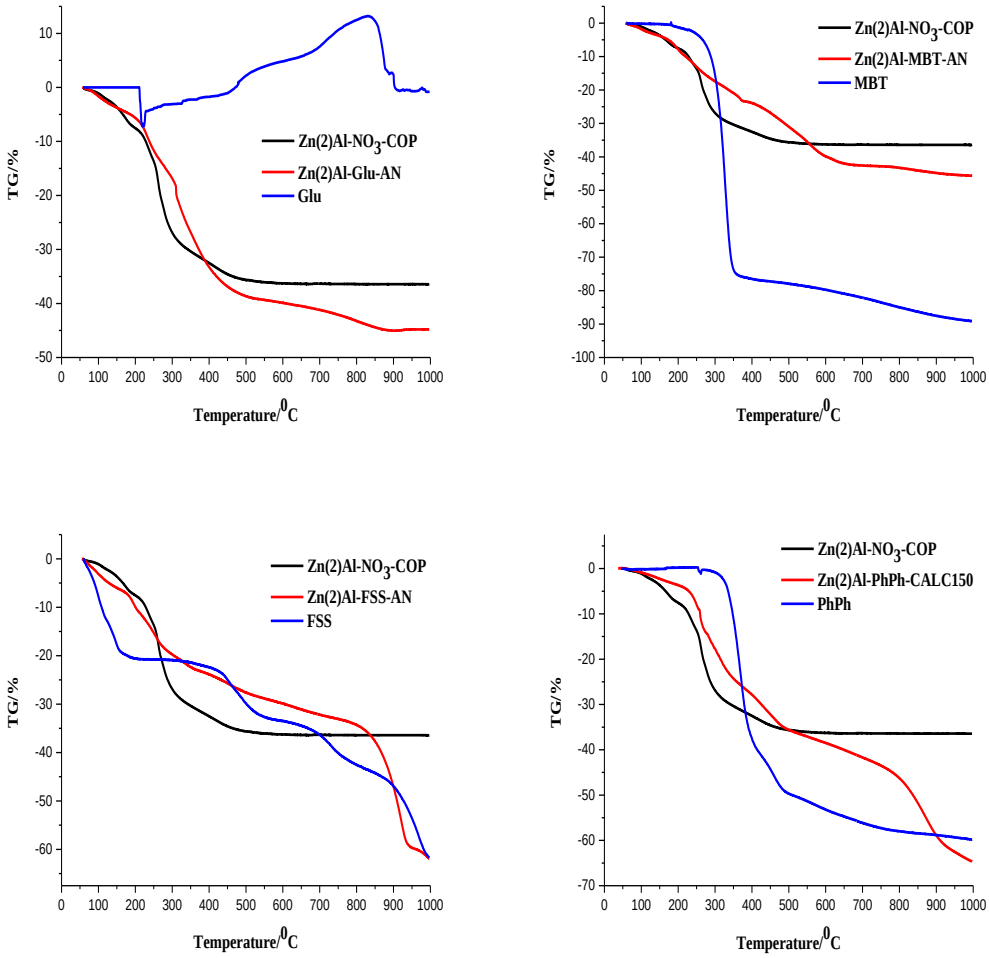

A1. Thermograms of **Zn(2)Al-NO$_3$-COP** and respective LDH loaded with active species in air

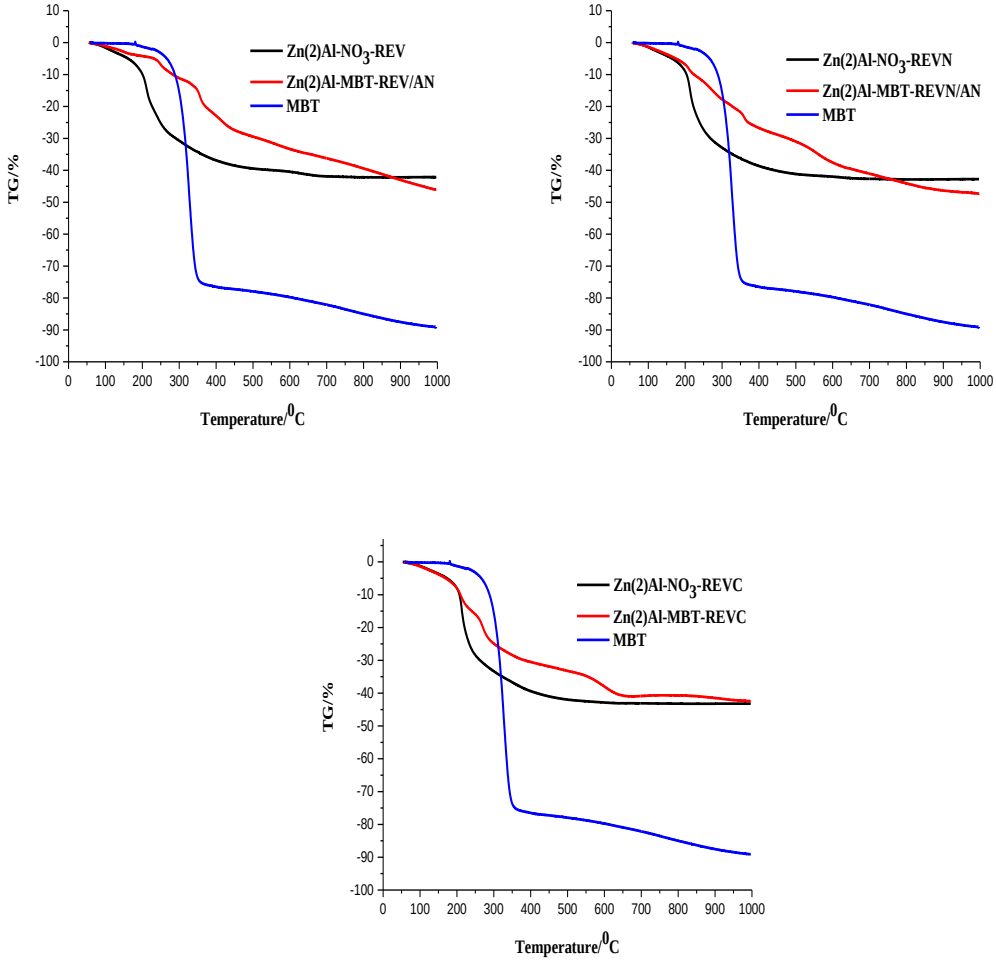

A2. Thermograms of **Zn(2)Al-NO_3-REV**, **Zn(2)Al-NO_3-REVN** and **Zn(2)Al-NO_3-REVC** and respective LDH loaded with MBT in air

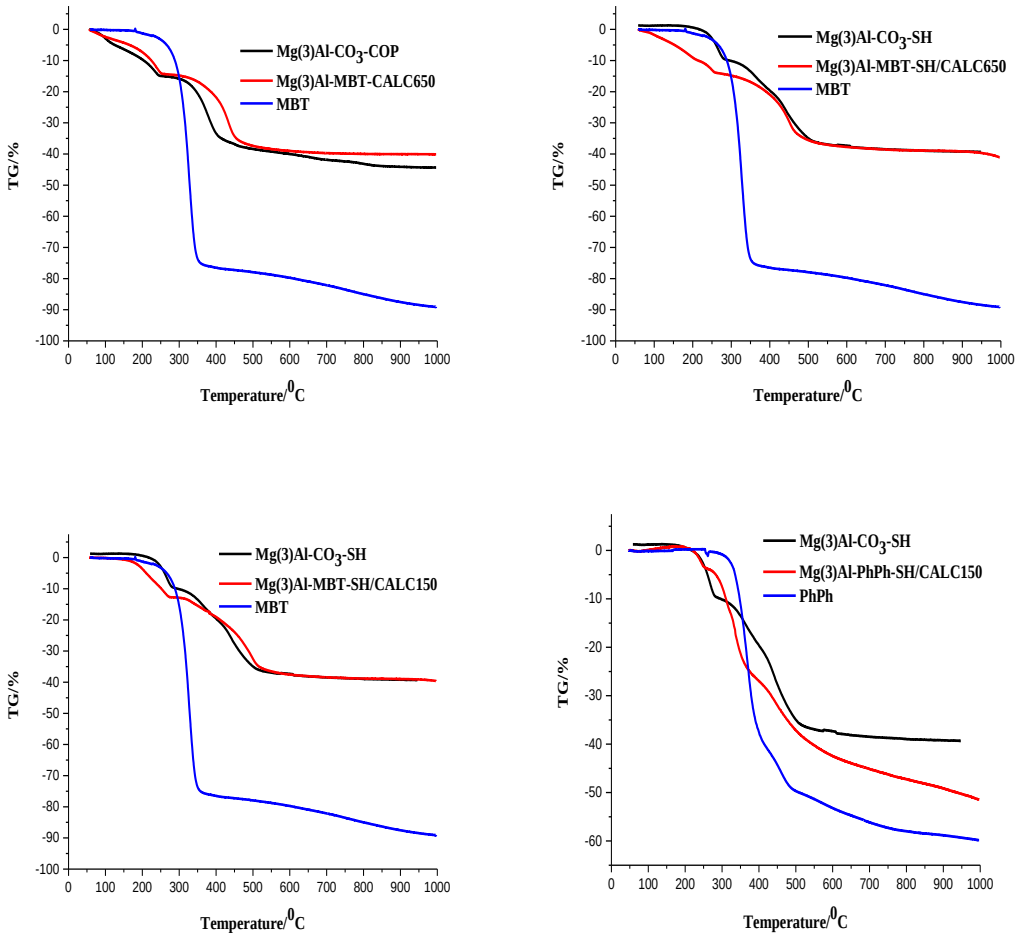

A3. Thermograms of **Mg(3)Al-CO₃-COP** and **Mg(3)Al-CO₃-SH** and respective LDH loaded with active species in air

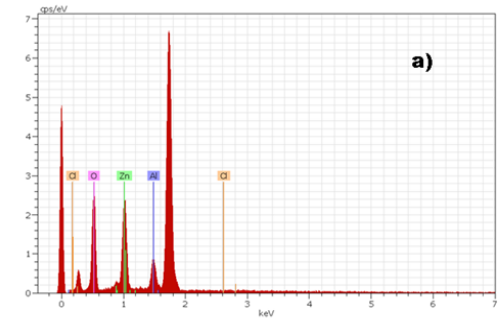

Spectrum: Acquisition

Element	Series	unn. C [wt.%]	norm. C [wt.%]	Atom. C [at.%]	Error (3 Sigma) [wt.%]
Aluminium	K-series	4.23	6.70	6.61	0.74
Oxygen	K-series	27.79	43.98	73.28	11.90
Chlorine	K-series	0.00	0.00	0.00	0.00
Zinc	K-series	31.16	49.32	20.10	4.16
Total:		63.18	100.00	100.00	

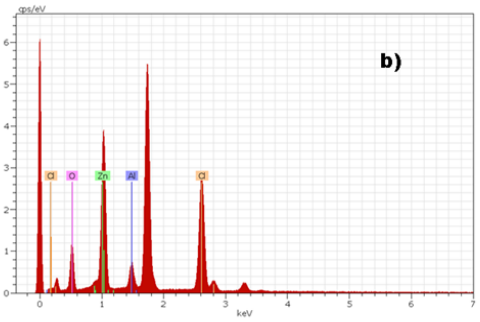

Spectrum: Acquisition

Element	Series	unn. C [wt.%]	norm. C [wt.%]	Atom. C [at.%]	Error (3 Sigma) [wt.%]
Aluminium	K-series	3.03	5.05	5.26	0.52
Oxygen	K-series	18.76	31.27	54.85	7.91
Chlorine	K-series	20.79	34.66	27.43	2.18
Zinc	K-series	17.41	29.02	12.45	2.15
Total:		59.98	100.00	100.00	

A4. EDS spectra of **Zn(2)Al-Glu-AN** before release (a) and after release (b) with 500mM NaCl trigger

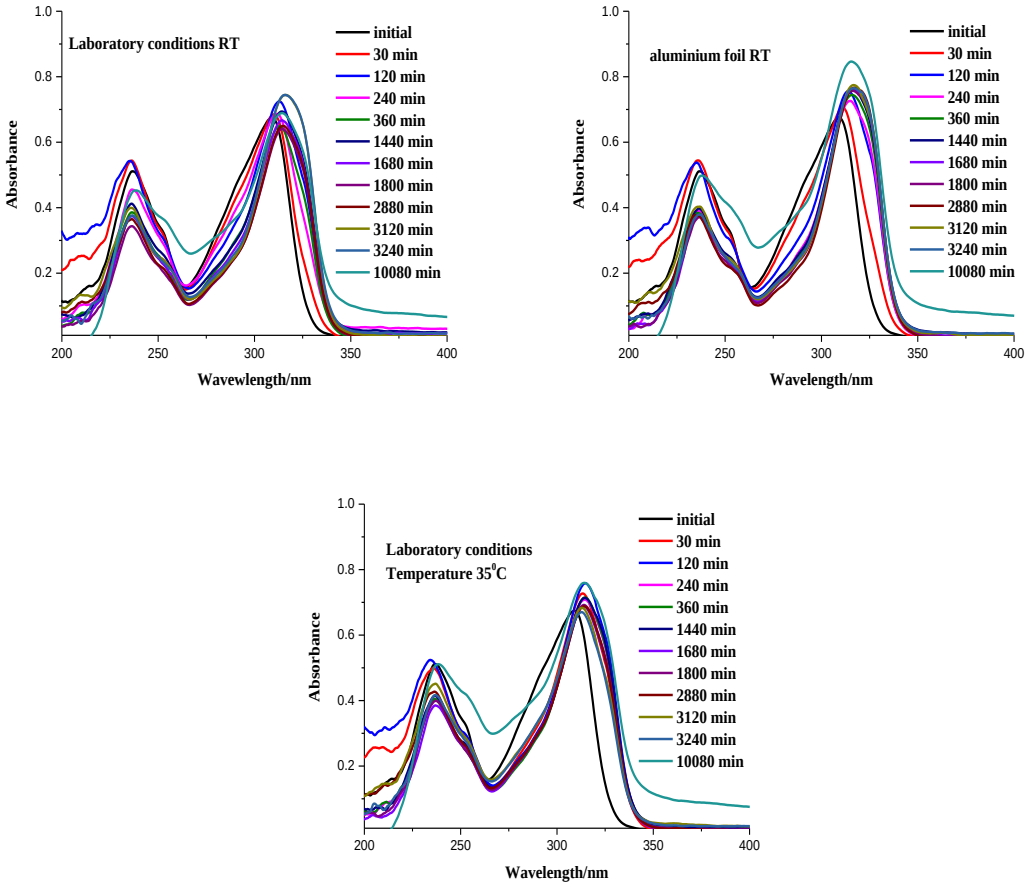

A5. MBT spectra obtained in different conditions at determined timescale

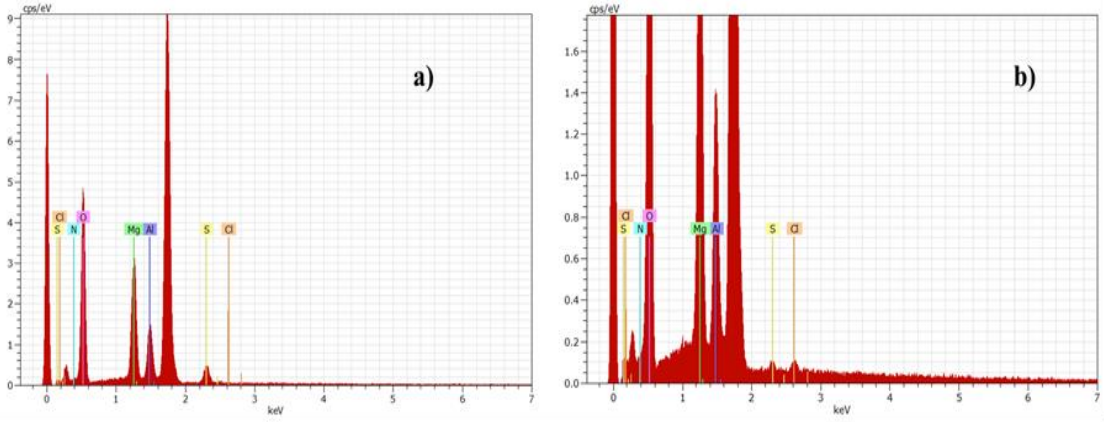

Spectrum: Acquisition

Element	Series	unn. C [wt.%]	norm. C [wt.%]	Atom. C [at.%]	Error (3 Sigma) [wt.%]
Aluminium	K-series	4.98	11.84	8.16	0.81
Nitrogen	K-series	1.04	2.47	3.28	1.08
Oxygen	K-series	25.53	60.76	70.63	9.99
Sulfur	K-series	2.58	6.14	3.56	0.41
Chlorine	K-series	0.03	0.07	0.04	0.09
Magnesium	K-series	7.86	18.71	14.32	1.36
Total:		42.02	100.00	100.00	

Spectrum: Acquisition

Element	Series	unn. C [wt.%]	norm. C [wt.%]	Atom. C [at.%]	Error (3 Sigma) [wt.%]
Aluminium	K-series	4.39	13.28	9.11	0.71
Nitrogen	K-series	0.26	0.78	1.03	0.39
Oxygen	K-series	20.67	62.52	72.34	7.66
Sulfur	K-series	0.22	0.66	0.38	0.12
Chlorine	K-series	0.27	0.82	0.43	0.13
Magnesium	K-series	7.25	21.94	16.71	1.24
Total:		33.06	100.00	100.00	

A6. EDS spectra of **Mg(3)Al-MBT-SH/CALC650** before release (a) and after release (b) with 500mM NaCl trigger

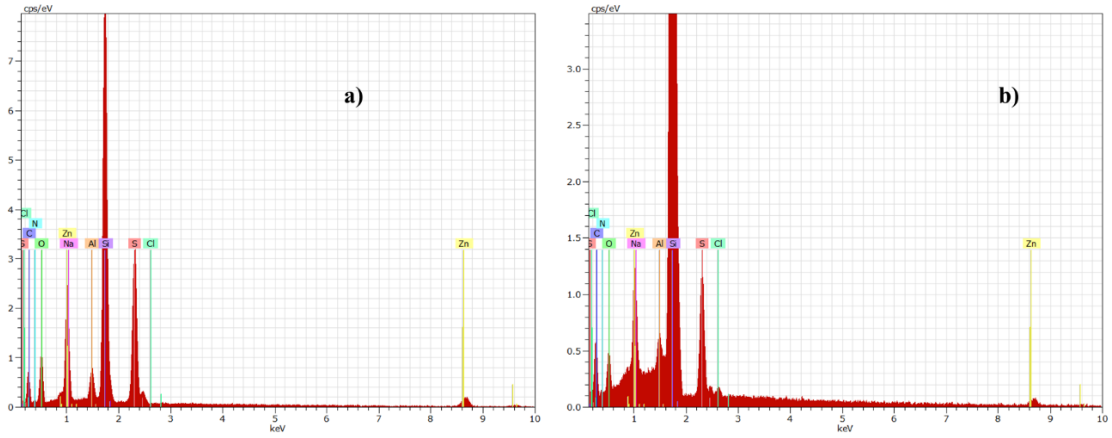

A7. EDS spectra of **Zn(2)Al-MBT-REV/AN** before release (a) and after release (b) with 500mM NaCl trigger

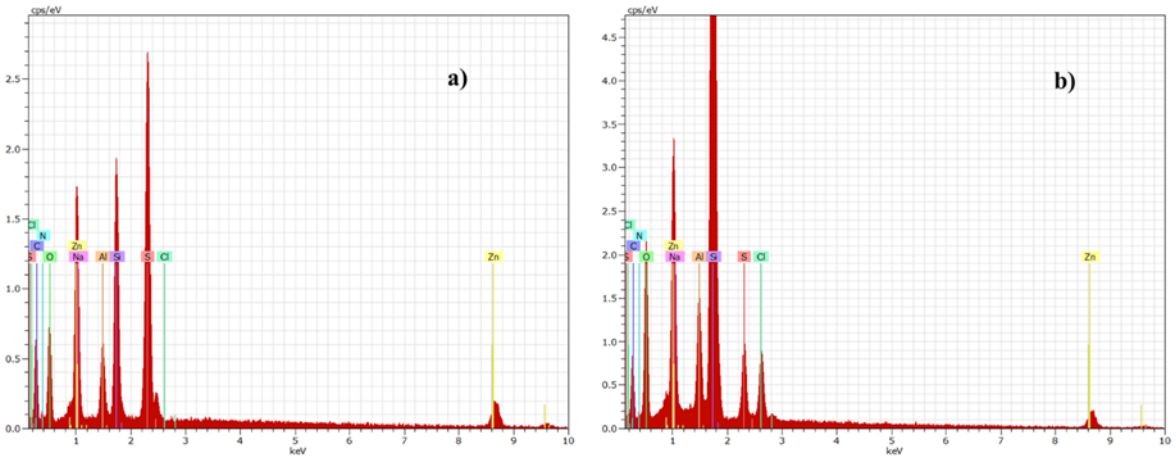

A8. EDS spectra of **Zn(2)Al-MBT-REVN/AN** before release (a) and after release (b) with 500mM NaCl trigger

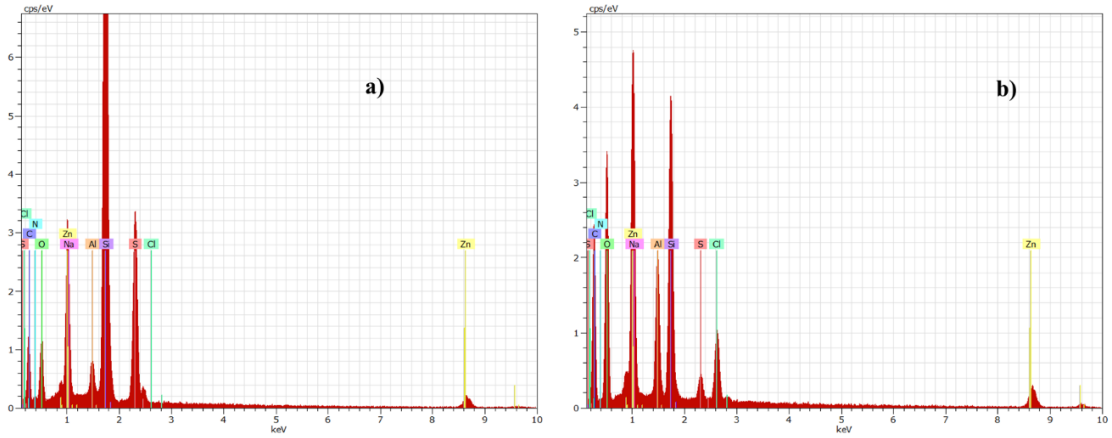

A9. EDS spectra of **Zn(2)Al-MBT-REVC/AN** before release (a) and after release (b) with 500mM NaCl trigger

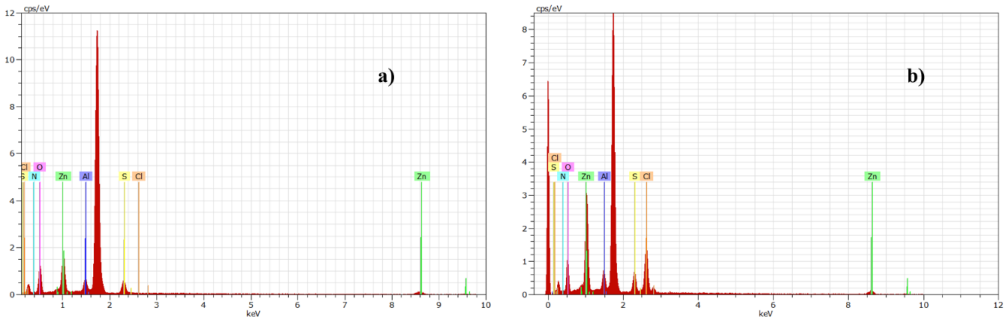

Spectrum: Acquisition

Element	Series	unn. C [wt.%]	norm. C [wt.%]	Atom. C [at.%]	Error (3 Sigma) [wt.%]
Zinc	K-series	17.48	40.32	16.11	2.48
Aluminium	K-series	2.56	5.91	5.72	0.48
Nitrogen	K-series	1.97	4.54	8.47	2.04
Oxygen	K-series	15.67	36.15	59.05	7.34
Sulfur	K-series	5.56	12.84	10.46	0.76
Chlorine	K-series	0.11	0.24	0.18	0.12
Total:		43.35	100.00	100.00	

Spectrum: Acquisition

Element	Series	unn. C [wt.%]	norm. C [wt.%]	Atom. C [at.%]	Error (3 Sigma) [wt.%]
Zinc	K-series	14.58	27.62	10.89	2.24
Aluminium	K-series	2.26	4.28	4.09	0.44
Nitrogen	K-series	3.24	6.13	11.28	3.29
Oxygen	K-series	16.77	31.76	51.17	8.41
Sulfur	K-series	4.16	7.88	6.33	0.59
Chlorine	K-series	11.80	22.34	16.25	1.35
Total:		52.80	100.00	100.00	

A10. EDS spectra of **Zn(2)Al-MBT-AN** before release (a) and after release (b) with 500mM NaCl trigger